Experimental and Numerical Modelling of Submerged Hydraulic Jumps at Low-Head Dams

Marta Lopez Egea

Thesis submitted to the
Faculty of Graduate and Postdoctoral Studies
in partial fulfillment of the requirements for the degree of

Master of Applied Science in Civil Engineering
(Water Resources)

Under the auspices of the Ottawa-Carleton Institute for Civil Engineering

Academic advisors: Dr. Ioan Nistor and Dr. Ronald Townsend

Department of Civil Engineering
Faculty of Engineering
University of Ottawa

Abstract

This study, which includes both experimental and numerical-modelling components, investigates the potentially dangerous conditions that can often occur when low-head dams (or weirs) are overtopped and 'submerged'-type hydraulic jumps subsequently form downstream of these hydraulic discharge structures. The combination of high local turbulence levels, air entrainment, and strong surface currents associated with submerged jumps can pose a significant risk to safety of boaters or swimmers. In this study, the conditions governing the formation, as well as the hydrodynamic characteristics of submerged jumps, were investigated for a wide range of flows and different boundary conditions. This research seeks to help develop improved guidelines for the design and safe operation of low-head dams.

The experimental phase of the study involved physical model testing to determine: (i) the hydraulic conditions that govern submerged jump formation, and (ii) the hydrodynamic characteristics of the submerged vortex. The numerical modelling work involved using interFoam (OpenFOAM toolbox) for simulating the experimental results. InterFoam is an Eulerian 3-D solver for multiphase incompressible fluids that employs the Volume of Fluid approach (VOF) to capture the water-air interface. The developed numerical model was subsequently validated using the experimental data collected and processed by the author of this study.

The range of tailwater depths associated with submerged hydraulic jump formation is dramatically reduced when a broad-crested weir is coupled with an elevated downstream apron, especially under high flow rate conditions. However sharp-crested weirs induced vortices which displayed reduced velocities and decreased spatial development, which were judged to be safer than broad crest lengths under the same discharge conditions. The classical formulation for the degree of submergence was not explicative when used to evaluate "how submerged the vortex was". Consequently, a new normalized formulation which compares the local tailwater depth to the lower and upper tailwater limits for the submerged hydraulic jump is proposed.

The numerical model developed for this study demonstrated the existence of residual turbulent kinetic energy at downstream sections located within the vortex's extension, at instants coinciding with the presence of a fully formed roller. This turbulent energy is arguably responsible for the stationary nature of the vortex under constant flow conditions. Residual vertical and horizontal velocities at points located within the vortex's domain are indicative of the existence of the free surface current.

Acknowledgments

I wish to express my gratitude to my supervisors, Professor Ioan Nistor and Professor Emeritus Ronald Townsend, for their continuous support, encouragement and guidance. Dr. Nistor has proved me that hard-work is the key to success; I will always be grateful to him for believing in me. Dr. Townsend's wise advice and admirable patience had contributed very much to the accomplishment of this thesis. I am also thankful to several professors in the department of Civil Engineering at the University of Ottawa: Dr. Colin Rennie, Dr. Ousmane Seidou and Dr. Majid Mohammadian for sharing their knowledge with me, for their dedication to their profession, and for providing me with invaluable insight towards the world of research.

Very special thanks to Dr. Mahmoud Al-Riffai who has served as a great mentor by sharing his knowledge and expertise on the experimental work field with me; I will never forget all the hours spent at the Hydraulic Laboratory. A special mention is dedicated to the undergraduate students Daniel Pereira and Kien Vu and the graduate student Amanj Jamal, who dedicated many hours and demonstrated patience during the data collection process. This work would have not been possible without the technical conversations, discussions, collaborations and great times spent with my colleagues during the course of my studies.

I would like to recognize the Department of Fisheries and Oceans for their financial contribution; especially I wish to acknowledge Mr. Bhuwani Paudel for making this study possible and for trusting me with this project. Furthermore I would like to extend my appreciation to the Canadian Dam Association for the recognition and the founding provided towards this research.

I am very thankful to all the people who have enlighten me and in some ways, have contributed to the fact of me being in here in this precise moment writing this thesis. I will always be grateful to my Canadian family who have fulfilled me with encouragement and love, and who took me as a daughter into their family. My deepest

appreciation also goes to my beloved partner, Cameron, who brought sunshine even to the darkest days. However, with no doubt the people who contributed to this thesis the most are my dear parents Luisa and Pepe and my brother Juan Miguel. They always remained strong when I felt weak; they taught me what the important things in life are, they have done the biggest sacrifice by letting me go; for all those reasons they are eternally carried in my heart. I would have never been the person I am without the patience and love that they dedicated to me all these years. This work is dedicated to you.

Agradecimientos

Deseo expresar mi gratitud a mis supervisores de tesis, Dr. Ioan Nistor y al Profesor Emérito Ronald Townsend, por su continuo apoyo, dedicación y animo durante el transcurso de este proyecto. Dr. Nistor me ha demostrado que trabajar duro es la clave para el éxito; siempre estaré agradecida por la confianza depositada en mí. Los sabios consejos y la admirable paciencia demonstrada por Dr. Townsend han contribuido a la finalización de esta tesis. Llevar a cabo este estudio no hubiese sido posible sin la contribución de varios profesores del Departamento de Ingenieria Civil: Dr. Colin Rennie, Dr. Ousmane Seidou and Dr. Majid Mohammadian. Ellos compartieron su conocimiento y experiencia durante innumerables clases, demostraron profunda dedicación hacia su profesión y abrieron para mi las puertas al maravilloso mundo de la investigación.

Un agradecimiento muy especial va dirigido a Dr. Mahmoud Al-Riffai quien ha ejercido como un excelente mentor, compartiendo conmigo su conocimiento y experiencia en el campo del trabajo experimental; nunca olvidaré las horas compartidas en el Laboratorio de Hidráulica. Una mecion especial va dedicada a los estudiantes de grado Daniel Pereira y Kien Vu, y al candidato a Doctor Mr. Amanj Jamal, quienes dedicaron innumerables horas y demostraron una admirable paciencia durante el proceso de recoleccion de datos. Sin lugar a duda, este trabajo no hubiese sido posible sin las conversaciones técnicas, duscusiones, colaboraciones y buenos ratos pasados con mis compañeros de trabajo durante el transcurso de mis estudios.

Deseo reconocer al Departamento de Pesca y Océanos del Gobierno Canadiense por su contribución financiera; especialmente deseo mencionar a D. Bhuwani Paudel por confiar en mi para llevar a cabo este proyecto. Adicionalmente deseo extender mi apreciación a la Sociedad Canadiense de Presas por su reconocimiento y por el apoyo economico dirigido a este proyecto.

Estoy muy agradecida a todas esas personas que en cierto modo han contribuido al hecho de que este en este preciso momento y en este preciso lugar, esté escribiendo esta tesis. Siempre estaré agradecida a mi familia canadiense por llenarme de apoyo y amor y por acogerme como a una hija en el seno de su familia. Mi mas profunda apreciación va dirigida a mi querido compañero, Cameron, quien trajo un rayo de sol incluso en los dias mas nublados. Finalmente quiero agradecer a las personas que sin lugar a duda han contribuido en mayor medida a esta tesis, mis queridos padres Pepe y Luisa, y mi querido hermano Juan Miguel. Ellos siempre han demostrado fortaleza cuando estaba débil; ellos me enseñaron cuales son las cosas importantes en la vida; ellos han hecho el mayor sacrificio dejandome marchar; por todas esas razones eternamente los llevo en mi corazón. Nunca hubiese llegado a ser la persona que soy sin la paciencia y amor que me han dedicado todos estos años. Este trabajo va dedicado a vosotros.

Table of Contents

List of Figures

List of Tables

List of Symbols

Roman letters (Italic)

A	Flume cross-sectional area (m^{2})
B	Intensive property
$\mathbf{b}$	Body forces (N/m^{3})
C_{air}	Air concentration (ND)
C_{l}	Crest length (m)
C_{w}	Rehbock weir coefficient (ND)
Ca	Cauchy number (ND)
Co	Courant number (ND)
CV	Control volume (m^{3})
∂CV	Boundaries of the control volume (m^{2})
E	Energy head (m)
E_{v}	Abscissa corresponding to the vortex's end (m)
E_{dm}	Energy dissipated by the 'drowning machine' (J)
Eu	Euler number (ND)
F	Mass flux (Kg/s.m^{2})
F_{air}	Bubble frequency (ND)
Fr	Froude number (ND)
Fr_{1}	Froude number at the gate inlet (ND)
$\mathbf{f}$	External body forces acting on the fluid (N/m^{3})
g	Gravitational acceleration (m^{2}/s)
m	Mass (Kg)
H	Upstream water head over the crest or 'freeboard' (m)
H_{0}	Approach flow energy head (m)
H_{t}	Tailwater elevation, measured from the crestplane (m)
H_{weir}	Weir height, measured from the channel's bed (m)

h_0	Gate opening of depth at the vena contracta (m)
h_3	Water depth at the downstream face of the gate (m)
$\mathbf{I}$	Identity matrix (ND)
I_v	Abscissa corresponding to the impingement point or vortex's start (m)
L	Length scale in the dimensional analysis (ND)
L_v	Vortex length (m)
P	Number of pixels
$\mathbf{p}$	Pressure Tensor (Pa)
Q	Discharge (m^3/s)
q	Unitary discharge for free flow ($m^3/m.s$)
q_f	Unitary discharge for submerged flow ($m^3/m.s$)
Re	Reynolds number (ND)
S	Degree of submergence (ND)
S_B	Mass flow associated to sink/sources in the control volume
St	Strouhal number (ND)
$\mathbf{T}$	Deviatoric stress tensor (Pa)
t	Time (s)
t_{comp}	Computational time (s)
t_{sim}	Simulation time (s)
$\boldsymbol{u}$	Velocity vector (m/s)
u_r	Artificial velocity compression term (m/s)
u_x	Horizontal component of the velocity (m/s)
u_y	Vertical component of the velocity (m/s)
u_z	Cross-sectional component of the velocity (m/s)
U_f	Velocity on the cell face (m/s)
U_{bed}	Longitudinal velocity along the bed (m/s)
$U_{surface}$	Longitudinal velocity along the surface (m/s)
V	Volume (m^3)
dV	Differential of volume (m^3)
V_0	Upstream velocity (m/s)
V_1	Vortex's supercritical velocity (m/s)

V_2	Vortex’s subcritical velocity (m/s)
V_i	Local velocity (m/s)
V_s	Surface velocity (m/s)
V_t	Downstream velocity (m/s)
X	Axis corresponding to the longitudinal direction
X_i	Abscissa corresponding to the control section i
X_r	Reduction in the *X* coordinate
Y	Axis corresponding to the vertical direction
Y_0	Upstream water level (m)
Y_1	Supercritical water level (m)
Y_2	Subcritical water level (m)
Y_b	Bed’s current minimum water depth (m)
Y_i	Local water level at control section (m)
Y_l	Submerged hydraulic jump’s lower tailwater level (m)
Y_r	Reduction in the *Y* coordinate
Y_t	Tailwater level (m)
Y_{tL}	Tailwater level associated to the transition from impinging jet to surface flow (m)
Y_u	Submerged hydraulic jump’s upper tailwater level (m)
Y_{u+}	Submerged hydraulic jump’s upper tailwater level for increasing water levels (m)
Y_{u-}	Submerged hydraulic jump’s upper tailwater level for decreasing water levels (m)
Z	Axis corresponding to the cross-directional direction
Z_r	Reduction in the *Z* coordinate
z_{floor}	Downstream apron elevation

Greek letter symbols

α_{weir}	Factor dependent on the weir’s geometry (ND)
γ	Surface tension (Kg/s^2)

δ	Dirac delta function (ND)
Γ_ϕ	Diffusivity of the property (ϕ)
ε	Turbulent energy dissipation rate (m^2/s^3)
ζ_w	Non-dimensional relative weir length parameter
θ_N	Angle formed by the nappe and the downstream pool at the impingement point (°)
κ	Turbulent kinetic energy (m^2/s^2)
λ	Scale relation between prototype and model
μ	Fluid dynamic viscosity (Pa.s)
μ_t	Turbulent dynamic viscosity (Pa.s)
ν	Kinematic viscosity (m^2.s)
ν_t	Eddy viscosity (Pa.s)
ρ	Volumetric density (Kg/m^3)
ρ_{red}	Density reduction (ND)
σ	Cauchy stress tensor (Pa)
σ_ε	Dissipation rate of the turbulent energy dissipation (ND)
σ_k	Dissipation rate of the turbulent kinetic energy (ND)
ς	Fluid Bulk viscosity (Pa.s)
ϕ	Scalar property which is temporal and spatial dependent $\phi = \phi(x, t)$
ψ	Reduction factor for submerged flow

Mathematical operators

∇	Gradient
$\nabla \cdot$	Divergence
∇^2	Laplace
$\cdot$	Vector dot product
$\partial/\partial t$	Partial derivative with respect to the time (t)

Subscripts

$\_bed$	Represents measured along the downstream apron's plane
a	Associated to the air
$black$	Associated to black pixels
i	Represents a control section i
m	Associated to the model
mix	Associated to the air-water mixture
p	Associated to the prototype
w	Associated to the water
$white$	Associated to white pixels
x	Represents along the x direction (streamwise)
y	Represents along the y direction (vertical)
z	Represents along the z direction (cross-section)

Superscripts

T	Transposed matrix

Chapter 1. Introduction

Low-head dams are overflow structures which represent one of the most widespread human influence on rivers. In Canada there are over 10,000 dams of which only 933 are categorized as large dams according to the classification criterion proposed by the International Commission of Large Dams (ICOLD). The remaining structures would belong to the group classified as 'weirs' or low-head dams, which is the focus of this study.

The highly versatile functions of these hydraulic structures explain the frequent presence of weirs and low-head dams along many streams worldwide. These structures can be installed for diverse purposes such as flow or water level regulation, water distribution for irrigation or for water supply, flow measurement, or to act as a physical barrier. Moreover, as shown in Figure 1-1, low-head dams can also be used as an effective sea lamprey control method (Lavis, et al., 2003).

Figure 1-1: Sea lamprey barrier built in Pulaski, NY in 2013. Courtesy of the Department of Fisheries and Oceans (Government of Canada).

The flow over these structures seems harmless and serene, however a serious threat hides underneath. As noted elsewhere,… "A safely executed and designed hydraulic structure does not, in itself, render a harmless water flow" (Leutheusser, 1988). Low-head dams are operated at subcritical regimes which pose a serious threat under certain flow and tailwater depths by creating a submerged hydraulic jump downstream of the structure. Additionally, as shown in Figure 1-2, the drop creates an aerated flow, which considerably reduces the actual density of the water, thereby leading to reduced buoyancy for potential victims. Furthermore, a large amount of debris gets trapped in the recirculation region. These conditions and the large amount of turbulence generated in the submerged jump (or 'roller') combine to make this vortex flow feature a "killer roller". As a result, it becomes extremely difficult for any object or human caught in the roller to escape. Low-head dam structures have been referred to in the literature as "drowning machines" (Borland-Coogan 1980). The severity of the risk depends on the characteristics of the low head dam (i.e. type, height and horizontal distance of the water drop), the water flow passing over the structure and the tailwater conditions.

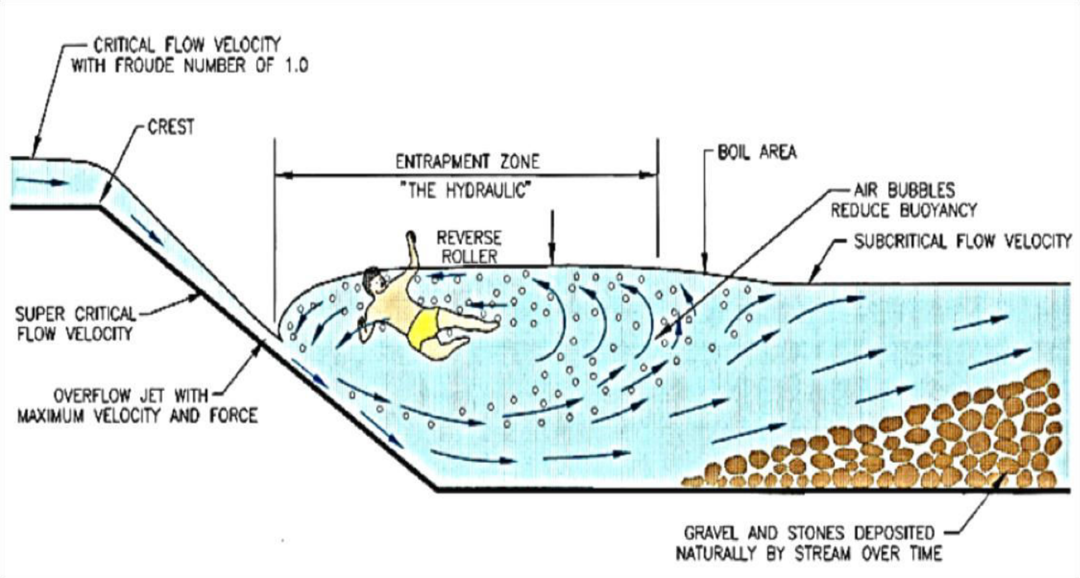

Figure 1-2: Submerged roller generated at a low-head dam. (Wright, et al., 1995)

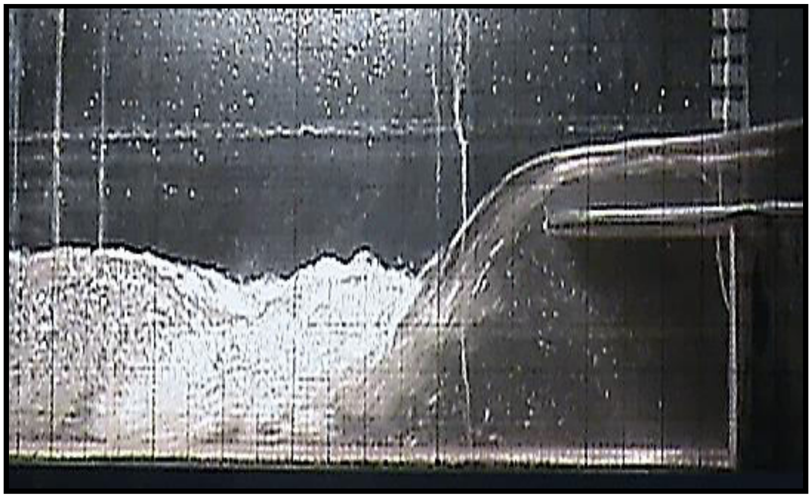

Figure 1-3: Submerged hydraulic jump experimentally simulated at the Hydraulics Laboratory at University of Ottawa.

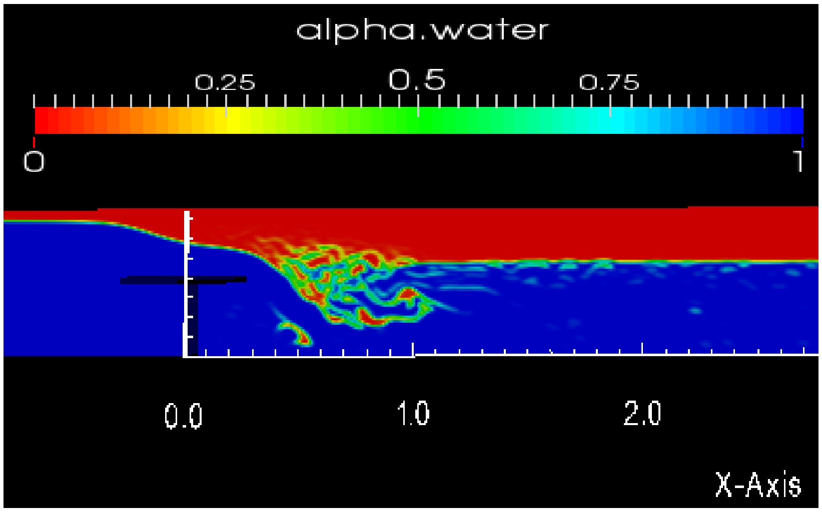

Figure 1-4: Submerged hydraulic jump numerically simulated with the CFD toolbox OpenFOAM

The risk associated with these structures is the ‘submerged’ hydraulic jump phenomenon that forms immediately downstream of the weir when the jump is ‘drowned’. This type of hydraulic jump occurs when the tailwater depth becomes greater than the sequent depth of the free hydraulic jump (Figure 1-3 and Figure 1-4). Vischer and Hager (1995) further defined two conditions for the formation of a submerged hydraulic jump: (1) the jump domain must be covered by a return flow and (2) the air entrainment must be obstructed. These two conditions represent the differences between a free and a submerged hydraulic jump. The submerged hydraulic jump has been the subject of extensive investigations (Rajaratnam 1967, Long et al., 1990). However, in most of the cases, the phenomenon was studied when generated by a sluice gate (Long, et al., 1991), where the focus is on the gate opening, the depth at the vena contracta, and the corresponding Froude numbers. Various ancillary structural devices have been employed to enhance the energy dissipation achieved by the hydraulic jump (e.g. chute blocks, baffle piers, etc.). However the particular case of sea lamprey barriers is still an ongoing area of investigation.

Several profiles have been recommended in order to dissipate the energy of the hydraulic jump, e.g. 'baffled' chutes and 'stepped' spillways, (Figure 1-5). However, in our case, the major function of the structure is not regulation of flow, or diversion of water for irrigation. The main purpose of these low head dams is to effectively act as a sea lamprey barrier, which implies particular design characteristics. As a result, the ordinary solutions to minimize the effects of submerged hydraulic jumps compromise the functionality of sea lamprey barriers. Youngs (1979) suggested that a vertical drop larger than 30 cm would be sufficient to prevent sea lampreys from upstream spawning migration. Hunn and Youngs (1980) proposed additional barrier design parameters for several flow conditions. Later, a minimum vertical drop of 45 to 64 cm in a ten years annual average spring flow was recommended to control sea lampreys migration during the spawning run (Millar & Ross, 2000). Generally, these barriers are designed to work under the range of naturally-occurring stream flow. High downstream water levels generate 'undular' jumps, while low levels cause the jump to sweep out. Flow conditions in between these two limits are responsible for the development of a submerged hydraulic jump as defined by Vischer and Hager (1995).

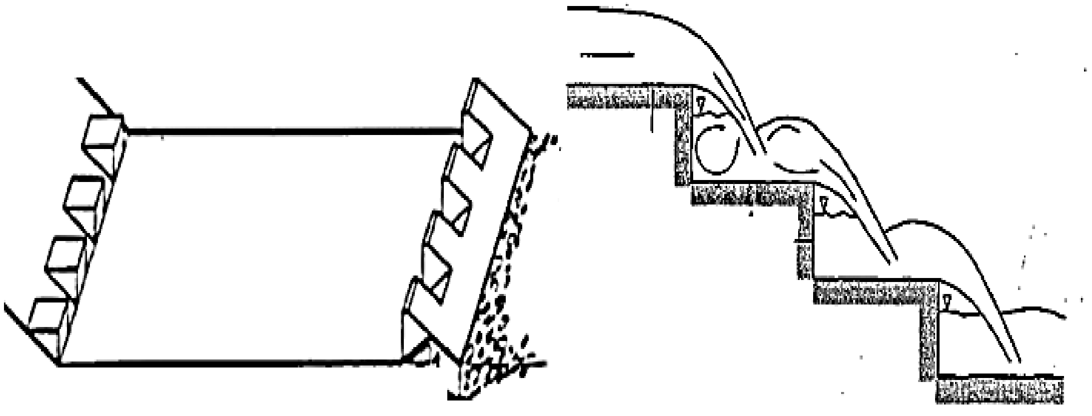

a) b)

Figure 1-5: Designs proposed to maximize energy dissipation on the downstream face of the structure. a) Baffled chute USBR type 2 stilling basin (Peterka, 1978). b) Stepped spillway operating under nappe flow condition (Rajaratnam, 1990)

1.1 Objective

The present work involves an experimental and numerical study of the influence of crest length, downstream floor elevation, tailwater depth, and discharge on submerged hydraulic jump formation and its characteristics. The aim of this investigation is to provide practical recommendations regarding the impact of broad-crested structures on the submerged hydraulic jump forming immediately downstream from low-head dams.

The goal of this comprehensive research program is to assess new design recommendations to modify the existing sharp-crested weirs which serve as sea lamprey barriers installed in many tributaries to the Great Lakes. This research program has been performed in cooperation with the Department of Fisheries and Oceans and the Great Lakes Sea Lamprey Control Center in an aim to minimize dangerous hydraulic conditions occurring at sea lamprey barriers.

Preliminary experimental tests were conducted to design a consistent testing methodology to assess the performance of each weir configuration under certain conditions of operation. The main objectives were to evaluate the effects of the crest length and the downstream apron elevation on two main aspects: (i) the tailwater levels associated with submerged hydraulic jump formation, and (ii) the dynamic characteristics of the vortex generated by the submerged hydraulic jump phenomenon.

The dual nature of this comprehensive investigation enabled an assessment of the CFD toolbox OpenFOAM for simulating this complex phenomenon. Numerical modelling has become a common practise and its popularity has increased with the advancement of the capabilities of modern computers. The numerical methods are able to accurately simulate the flow of liquids and gases and its use in the Fluid Dynamics field has been widely accepted by the scientific community. Therefore, this approach is applied with confidence to several stages of the design process. However, even in a controlled environment, the performance of the numerical model has to be assessed and calibrated such that the solution is validated.

The numerical tests were proved to truly reproduce the physical experiments conducted within the frame of this investigation. The calibration and validation processes resulted in a stable, reliable and accurate numerical model, which could then be applied to investigate the special (above-noted) aspects of this study.

1.2 Scope

Although this ongoing research program comprises a field investigation as well as the physical and numerical modeling of the hydraulic conditions immediately downstream from low-head dam structures, this thesis deals only with the physical and numerical modeling aspects of the program.

This physical model arrangement is based on the classic "weir-overflow" problem. The outcome from the experimental and numerical experiments focused on the investigation of the dynamic characteristics of the submerged vortex. Therefore the compared (i.e. 'observed in laboratory' versus 'numerically simulated') results included: (i) downstream vortex extension (ii) spatial distribution of the average bed and surface velocities within the vortex region, and (iii) density reduction within the submerged roller.

The physical arrangement was further used to investigate the occurrence of the submerged hydraulic jump condition. Moreover, in order to study the mechanisms related to the oscillatory stationary nature of the submerged vortex, the validated numerical model was used to investigate the turbulence-related parameters.

A comparison with other experimental investigations was not always possible because of the specific nature of the examined configuration. The setup and inflow conditions applied at the experimental facility accurately reproduced hydraulic conditions observed at specific sea lamprey barriers.

The submerged vortex generated downstream of low-head weirs, which is a 3-dimensional problem, was reduced to a 2-dimensional physical model in the laboratory. By approaching the problem from this standpoint, neither the effect of the glass-wall in the experimental arrangement (analogous to the river banks in the field investigations), nor the cross-flows in the numerical simulations, are considered. Therefore, this research project focused on the experimental investigation of the phenomenon in an XY plane, where the X-axis represents the direction along the streamflow, and the Y-axis denotes the vertical direction.

1.3 Contributions

This comprehensive investigation, which involved both the physical and numerical modelling of dangerous hydraulic conditions occurring at low-head dams, will provide insight into the submerged roller phenomenon and should thus lead to improved design guidelines for safer low-head dams and weirs. The experimental conditions, successfully reproduced using OpenFOAM, enhance the assessment of the impact of the low-head dam design on the submerged roller and the safe operation conditions.

The novelty of this study is in the assessment of the impact of crest-length on the characteristics of the submerged roller. Although the topics: “submerged hydraulic jump” and “broad-crested weir” have been extensively studied separately, this is the first time that both topics have been combined in the one investigation.

Moreover, the development of solution procedures for numerical models, which simulate complex multiphase flows, has occurred only in the past decade. This study represents the first approach to numerically simulate the submerged hydraulic jump occurring downstream from an overflow structure that also considers the air-water interaction. An accurate simulation of the air entrainment within the entity of the submerged roller was possible by solving the RANS equations combined with the VOF free surface tracking approach and a RAS $k - \varepsilon$ turbulence closure.

Finally, the outcomes achieved by this investigation can be extrapolated and implemented in future design alternatives, which could reduce both the occurrence and the dangerous characteristics of submerged hydraulic jumps forming downstream from sea lamprey barriers.

1.4 Outline

This thesis is organized in the following eight chapters (supplementary details are found in the Appendix section at the end of the manuscript):

Chapter 1 provides an introduction to the study, including the problem definition, the objective and goals of the investigation, the scope of the project, and potential contributions to the field of research. Chapter 2 presents an extensive literature review in the field of interest that also points to the research needs. A theoretical approach to analysing low-head dams and their risk is presented. In addition, the design constraints associated to sea-lamprey barriers (as low-head dam structures) is included. In Chapter 3, the experimental procedures, data acquisition systems, laboratory setup, sources of errors and design considerations are fully described. The experimental program is included as one of the sections of this chapter.

The theoretical concepts of the mathematical and numerical model established to simulate the complex multiphase flow, associated with the submerged hydraulic jump phenomenon, are described in Chapter 4. Details regarding the design of the computational domain and the calibration of the model are also presented in this chapter.

The results of the physical and numerical experiments are presented in the following three chapters. Chapter 5 contains the most relevant results concerning the submerged roller formation. The tailwater levels associated with the occurrence of the aforementioned phenomenon are extensively investigated for both sharp- and broad-crested configurations. An empirical formulation, which predicts the onset of the phenomenon and redefines the degree of submergence, is presented at the end of this chapter. In Chapter 6, the results regarding the dynamic characteristics of the vortex are presented. Variables, such as time-averaged bed and surface velocity within the vortex and downstream extension, are investigated. An assessment of the optimal combination of crest length and apron elevation, (to minimize the dynamic characteristics of the roller), is pursued.

Chapter 7 discusses the results derived from the numerical simulations. The spatial distribution of velocity along the channel bottom and on the surface and the time-history of the turbulent kinetic energy are presented. Details providing insight into the mechanisms involved in the generation of the submerged hydraulic jump are included. A comparison of the corresponding experimental and numerical data is also presented in this chapter. A discussion of the strengths and the weaknesses of each aspect of this investigation are presented in this section.

Lastly, Chapter 8 includes the most relevant conclusions as well as the recommendations for future research effort on this particular topic.

Chapter 2. Literature Review

This chapter presents a detailed literature review focused on previous research contributions in the field of submerged hydraulic jump induced by overflow structures. First, a description of the flow regimes occurring at overflow hydraulic structures is presented, focusing on the submerged flow regime. As particular cases of overflow structures, the low-head typology (weirs) and the specific case of sea lamprey barriers are reviewed. Next, the submerged hydraulic jump phenomenon is described mathematically. This chapter provides the start point for understanding the interaction between low-head dams and the formation of a submerged hydraulic jump downstream from these structures. A section reviewing previous physical investigations on submerged rollers forming downstream from overflow structures is included. Finally, the numerical modelling of any of the components involved on the problem under investigation (i.e. overflow structures and submerged hydraulic jump) is reviewed, presenting the most advanced contributions in the field of numerical simulations. Therefore, the main goals of this chapter are to provide with background information related to (a) physical and (b) numerical investigations involving: (i) low-head dams, (ii) submerged hydraulic jumps, and (iii) the dangerous hydraulic conditions associated to the development of submerged hydraulic jumps immediately downstream from low-head dams.

2.1 Flow regimes on overflow structures

Dams are hydraulic structures which represent a vital constituent of the infrastructure system assuming a relevant role as a life-sustaining element for the population (AASHTO, 2005). These structures impound water, wastewater or other liquid substances upstream in order to serve various functions such as flood control, water supply, irrigation, water level control, etc. According to the Bureau of Reclamation of the Unites States, dams can be categorized based on three main aspects: use, hydraulic design, and material of construction. The classification based on its hydraulic design defines two typologies: overflow and non-overflow structures (USBR, 1960). Overflow or overtopping dams are defined as structures which are designed to discharge flow over their crests. This design results in structures which are overflowed.

The design of overflow structures encompasses several profiles such as sharp-crested, broad-crested, ogee-shaped, etc. Assuming a vertical downstream face, two types of flow regimes associated to overtopping hydraulic structures are described in literature: free flow and submerged flow (USBR, 1960). The tailwater level determines the flow regime governing the discharge over the weir. Both regimes have been extensively studied and specific typologies of each category of flow regime have been proposed by several authors.

Free flow regime was understood at earlier dates than submerged flow. Initial investigations focused on estimating the discharge coefficient for submerged flows (Rehbock, 1929) (Villemonte, 1947), however at that time, the flow dynamics downstream from these structures were not fully understood yet (Rajaratnam and Muralidhar 1969). Free flow regime occurs when the tailwater level is lower that the crest height. Under this condition, the discharge is not affected by the downstream water level (Y_t) being only a function of the upstream head over the crest (H). In the past, experimental investigations focused on fully understanding the variables involved on the flow motion on this flow regime. The specific discharge (q) for the free flow regime on overtopping structures was found to be a function of the head of water over the crest. Hence, in the case of flow overtopping, the specific flow discharge over a dam is defined by the discharge equation shown below:

$$q = \frac{2}{3} C_w \sqrt{2gH^3} \tag{2.1}$$

There are several suggestions for the discharge coefficient. The Rehbock weir discharge coefficient C_w was defined as follows (Rehbock 1929):

(2.2) $$C_w = 0.6035 + 0.0813\left(\frac{H}{H_{weir}}\right)$$

Where the variable H_{weir} represents the height of the weir, measured from the bed to the highest level of the crest. Furthermore, the submerged flow regime occurs when the downstream water level reaches values approximately in the range of the crest height(H_{weir}), or above. Under this regime, the unitary discharge over the structure is affected by the upstream head over the crest (H) and the downstream water level (Y_t) and the tailwater elevation measured from the crest's plane (H_t), as seen in Figure 2-1.

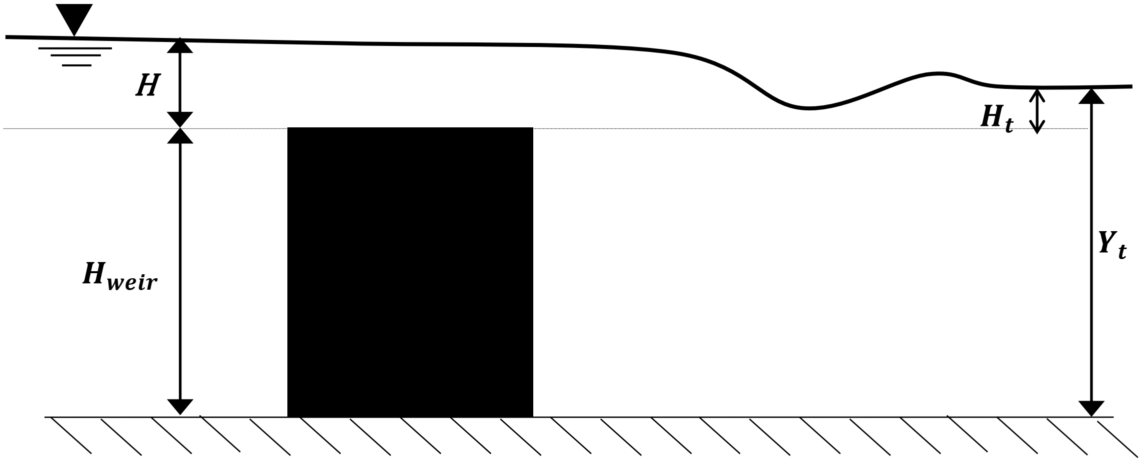

Figure 2-1: Submerged flow regime. Definition of variables involved on the unitary discharge.

In 1996, Wu and Rajatranam performed a total of 35 experiments considering six weir heights and several discharges for each height (freeboards). The submerged regime was fully investigated and several subcategories of submerged flow regimes were identified by the authors (Wu and Rajaratnam, 1996). A reduction factor (ψ) was defined to modify the unitary discharge for free flow regime, such that the unitary discharge can be calculated on submerged flow regimes (q_f), according to:

(2.3) $$q_f = \psi \cdot q, \qquad 0 \leq \left(\frac{H_t}{Y_t}\right) \leq 0.95$$

The reduction factor (ψ), as a function of the non-dimensional tailwater elevation over the crest, defined as the ratio (H_t/H). Figure 2-2 shows the relation between these two variables.

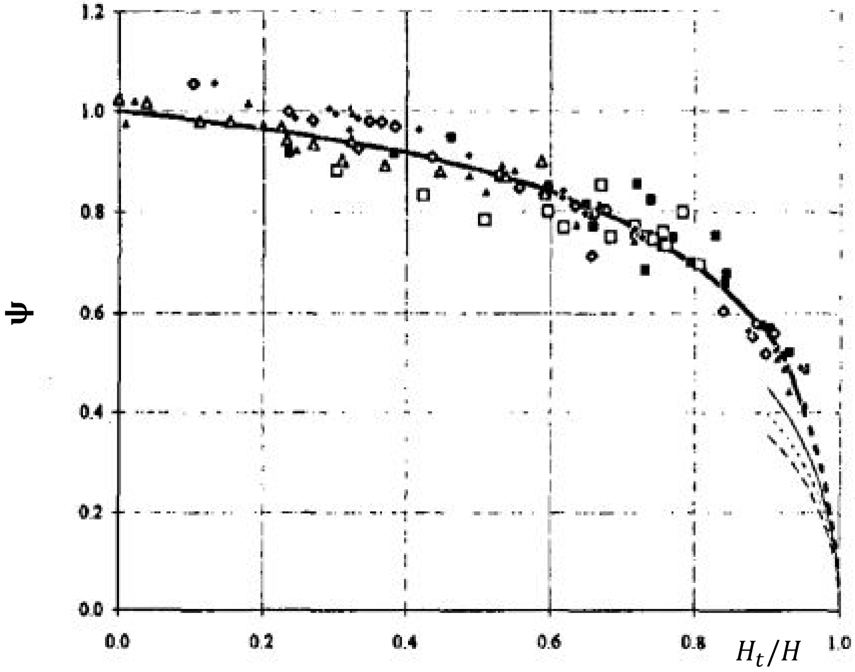

Figure 2-2: Reduction factor (ψ) as a function of the non-dimensional submergence (H_t/H). (Wu and Rajaratnam 1996)

Hysteresis effects associated to the tailwater level (Y_{tL}) which created the transition between the impinging jet and the surface flow regime (boundary between the two flow regimes) was observed by Wu and Rajaratnam (1996). This hysteresis was related to the direction of the change of the water level. In other words, the transition between free and submerged flow depended on how it was achieved; either by increasing the tailwater level (Curve 2), or by decreasing it (Curve 1), as seen in Figure 2-3.

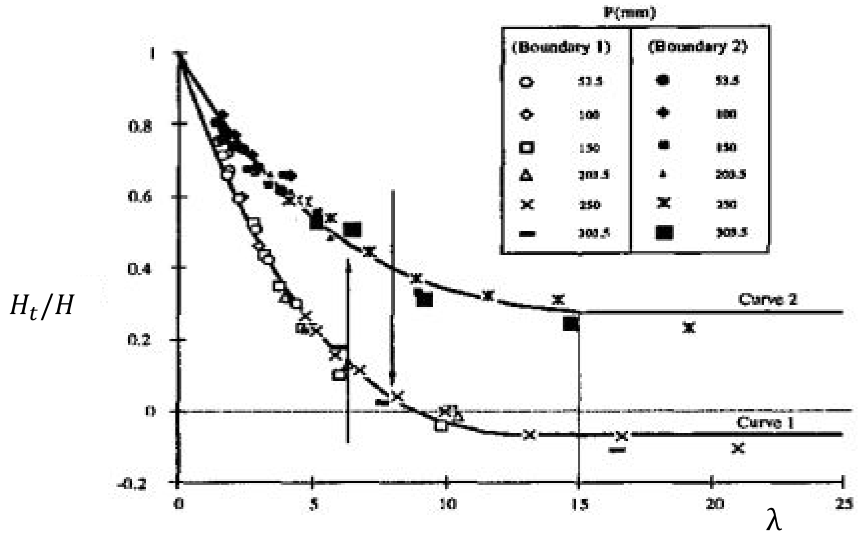

Figure 2-3: Transition between free and submerged flow regimes. (Wu and Rajaratnam, 1996)

The previous figure shows the ratio (H_t/H) versus the parameter λ on the abscissa axis. The non-dimensional submergence parameter (λ), is defined as:

$$\lambda = \sqrt{g(H - H_t)} \cdot \frac{Y_t}{q} \tag{2.4}$$

This non-dimensional submergence allowed the comparison of the flow rates and weir heights, by accounting for the freeboard on the weir and the submergence, represented by the difference $(H - H_t)$.

The tailwater depth associated to the transition between free and submerged flow was defined as "Modular Limit" (Y_{tL}) (Hager and Schwalt 1994). This index is defined by the authors as:

$$Y_{tL} = \frac{Y_t}{H + H_{weir}} \tag{2.5}$$

For the experimental conditions, the curves represented on Figure 2-3 would be associated to the Modular Limit, according to the definition given by equation (2.5). The region between Curve 1 and Curve 2 is understood as a transitional area where either regime could occur.

It is understood that Curve 2 shown in Figure 2-3 would correspond to increasing tailwater levels and Curve 1 to decreasing water levels. The gap area in between Curves 1 and 2 does not necessarily represent that either of the two flow regimes could occur, as indicated by Wu and Rajataranam (1996). This region is related to the different mechanisms involved in the transition from free to submerged flow regime and vice-versa (from submerged to free). Therefore the effect of increasing or decreasing the tailwater level affects the modular limit.

2.1.1 Low-head dams

A weir is a hydraulic overtopping structure which in general offers the same functions as a dam, but of smaller magnitude (height and length). Figure 2-4 elaborates on classification of dams by size. The term low-head dam is associated to weirs which in addition have the function of acting as a barrier. Sea lamprey barriers are an example of low-head dams.

Weirs and low-head dams belong to the category of small dams. The International Commission of Large Dams provided generic guidelines to classify small dams on a bulletin focused on this typology of structures (Committee on Small Dams, 2011). The proposed classification defines small dams as structures characterized by a height (measured from the bed level to the maximum crest level) within the range $2.5m < H < 15m$ and satisfying $H^2\sqrt{V} < 200$, where V represents the storage volume in millions of cubic meters at the maximum operating level. The $H^2\sqrt{V}$ relation is represented (colour coded) for several magnitudes in Figure 2-4. The original definition of large dams according to ICOLD, is represented by the red line in Figure 2-4.

In any case, these are generic minimum specifications and some local administrations and entities might define additional conditions. In Canada, the Canadian Dam Association (CDA) is an organization which intends to address the dam safety issue from a national perspective, reaching consultants, engineers and dam owners. At this point the dam regulation is a provincial issue which is dealt by the territorial jurisdiction in charge. Therefore, a federal regulation does not exist in Canada. In Ontario, the Ministry of Natural Resources and Forestry is the institution responsible for dam management within the province.

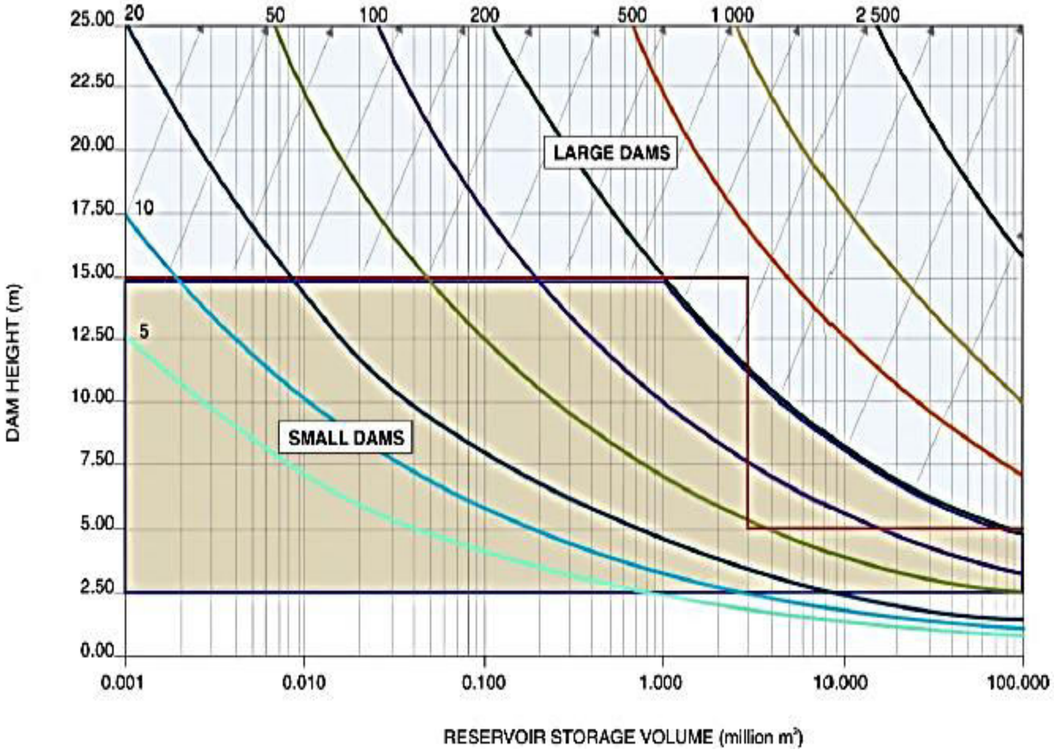

Figure 2-4: Classification of small and large dams, as a function of the dam height (H), storage volume (V) and $H^2\sqrt{V}$ relation. (Committee on Small Dams, 2011)

2.1.2 Sea Lamprey barriers

The sea lamprey (*Petromyzon Marinus*), originally from the Atlantic Ocean, is an invasive species in the Great Lakes. They were introduced through the Welland canal since its completion in 1829, and were first observed in Lake Erie in 1921, followed by Lake Huron and Michigan and finally Lake Superior in the 1940s (Crowe, 1975). This parasitic species preys on fish and as a consequence of its intrusion, a harmful effect on the fish community was observed. As a response, the Great Lakes Fisheries Commission (GLFC) was formed in 1955 to control the sea lamprey population and manage fish communities. The programs carried out by this entity are supported by the Department of Fisheries and Ocean Canada (DFO) as the Canadian agent and the United States Fish and Wildlife Services (USFWS) as the US agent.

Sea lampreys migrate upstream in the lake tributaries to spawn. In the past, a control program based on pesticides to kill larvae has reduced the lamprey population to

10% of historical levels (Smith & Tibbles, 1980). The GLFC has since then looked for alternative solutions due to the high cost of pesticides, the negative impact to other aquatic species and the access limitations to ravine systems. In addition to pesticides, other solutions rely on barriers, which prevent the access of the sea lampreys to spawning habitats where reproduction occurs. The sea lampreys successfully spawn in 430 of the 5,750 Great Lake tributaries which represent an invasion of around 10% of the entire hydrological system (Morman, et al., 1980). A specimen of sea lamprey is shown in Figure 2-5.

Figure 2-5: Specimen of sea lamprey. Great Lakes Environmental Assessment and Mapping Project (Picture courtesy of T. Lawrence)

In 1979, Youngs carried out experimental research with live specimens and found that none were able to overcome a 30 cm difference between the weir crest and the pool surface. In 1980, Sawyer recommended the application of integrated pest management (IPM) to manage the problem of sea lamprey population in the Great Lakes. This interdisciplinary method included biological and chemical methods. As a consequence, low-head dams were used in conjunction with other techniques as recommended by Sawyer in order to effectively combat the sea lamprey pest.

Typical barriers are 1 to 2 meters high concrete barriers, which extend across the stream installed with the vital objective of maintaining the minimum required vertical drop of 30 cm during the sea lamprey migration season (April – June). Different materials such as steel sheet piles are conventional, depending on the location and the geotechnical characteristics of the soil material at the foundation level. These barriers are assumed to be effective if "positioned on sea lamprey habitat potential rivers, controlling up to 90% of the sea lamprey population" (Lavis, et al. 2003).

The modern low-head dams used as lamprey barriers are typically composed of a fixed-crest height and overhanging lip which maintains the vertical drop of minimum 30 cm from the headwater upstream to downstream pool during the sea lamprey migration period (Lavis, et al. 2003). Most fixed-crest designs incorporate a jumping pool for migratory fish passage, minimizing the ecological impacts of these barriers on the ecosystem.

The optimal control of sea lampreys relies not only on the height of the dam, but on the proper location of the barriers in order to minimize the area where the pesticides have to be used. For this reason, barriers are usually located near the river mouth, as close to the lakes as possible. These areas traditionally coincide with highly populated and urbanized locations which attract tourists and visitors, such as Duffins Creek in Lake Ontario. Both factors enlarge the human risk associated to the harmful hydraulic conditions forming downstream of sea lamprey barriers. In order to reduce the risk of potential drowning in these areas several measures have been taken such as education of local population, warning signs in the areas and finally a modification of the physical barriers in order to minimize risky conditions downstream. The objective of this project is to identify the hydraulic conditions downstream and the factors involved and evaluate alternative designs assuring the functionality as a sea lamprey barrier and minimizing the development of submerged hydraulic jump.

Sea Lamprey Barriers: Design Parameters

In 1950, Applegate conducted extensive field observations on the Ocqueoc River in Michigan at different dams and stated that the same lampreys could "jump above two feet in the vertical direction" or "leap a maximum of four feet in a frontward slightly upward direction at the base of natural drops". Sea lampreys were observed to develop the ability to find migration paths on logging dams passing over obstacles by finding holes or irregularities on the structure (Applegate, 1950).

Later, Wigley continued with this line of investigation in 1959. He studied the behavior of lampreys in Cayuga Lake Inlet in New York and found that 1 foot (≈30 cm) barrier would work as a partial barrier in order to mitigate lamprey migration (Wigley, 1959). At a later date, field investigations were carried out by Youngs at the same location than Wigley (the Cayuga Lake). The purpose of this study was to determine the maximum vertical height that a migrating adult sea lamprey could overcome. Sea lampreys were exposed to different height ranging from 2 to 30 cm. Several water flow conditions and barrier heights were tested using more than 1,000 adult lampreys trapped on site. Of all specimen analyzed (some lampreys were used more than once), none was able to ascend a 30 cm height. He determined that the upstream migration of sea lampreys might be effectively prevented by using low vertical barriers. Consequently, the essential factor to consider during design is the vertical drop between the barrier crest and the downstream pool elevation, which is a function of the water conditions downstream. He concluded that a water barrier of at least 30 cm is effective for preventing the pass of sea lampreys, which were observed to be very weak at jumping, but very good at swimming (Youngs 1979). The general behavior observed by Youngs (1979) corroborates the previous observations carried out earlier by Wigley (1959), demonstrating than a 30 cm vertical drop between the upstream and the downstream is enough to prevent the spawning of sea lampreys.

Therefore, the effective design of sea lamprey barriers relies on the appropriate selection of the structure height according to the before mentioned standards, such that the resulting barrier successfully guarantees the minimum vertical drop. The crest elevation is described as the "height which provides a flow condition presenting a barrier to lampreys except during a n^{th} year flow event within the spawning period" (Millar and

Ross 2000). The value for the variable n^{th} is defined for different locations by using hydrological analysis of the catchment area, however problems arise when a combination of environmental circumstances such as a flood flow event could allow the passage of lampreys. Several methods for determining the crest height are available, however the engineer's decision is essential and depends fundamentally on the scope of the project. One of the methods suggested by Millar and Ross in 2000, is the empirical method which has been widely used and is the point of reference for any analysis. This is derived from the experiments aforementioned carried out by Youngs in 1979 and assumes 45 to 61 cm (18 to 24 in.) water level drop at mean annual flow conditions, formulated as follows:

$$(2.6) \qquad Crest\ Height\ =\ Stage\ at\ Mean\ Annual\ Discharge + Offset$$

Where the offset is associated to the [46 – 61 cm] water level range. This formulation involved a professional judgment of the engineer to accommodate variations in river morphology between alternative sites. This model performed well on small water streams with mean annual flows in the range [0.5 – 3 m^3/s] and where the downstream conditions feature good gradient characteristics.

Other researchers have explored alternative methods to physical barriers and mechanical and electromechanical barriers have been proved to act as effective control measurements (Hunn and Youngs, 1980). These alternative designs were recognized as a significant contribution to the "attempts to control the population of sea lampreys in the upper Great Lakes". Based on this principle, alternative barriers designs are available now, such as electrical, velocity barriers and designs featuring an adjustable crest in which the crest heights changes according to the tailwater depth.

2.2 Hydraulic jumps

At this point, the human safety is still under debate, and is a key point in effective sea lamprey management (McLaughlin, et al. 2007). Every year, several casualties associated to low-head dams occur. The dangerous hydraulic conditions formed downstream have been studied thoroughly (Leutheusser and Fan, 2001). The authors identified that under a certain tailwater depth range, a submerged hydraulic jump formed causing a horizontal vortex with the high free surface velocities responsible for several fatalities every year in North America.

The hydraulic jump phenomenon attracted the curiosity of many researchers in the past. In 1958, the first measurements of the turbulence structure in hydraulic jumps were attempted for classical jumps (Rouse, Siao and Nagaratnam 1958). In 1972, Resch and Leutheusser measured the turbulent structure of hydraulic jumps as a function of the flow upstream by means of hot-film techniques for two different inflow Froude numbers (Fr_1=2.8, Fr_1=6). They tested two conditions: fully developed upstream flow and potential upstream flow. They found that the turbulence distribution (evaluated by the turbulence intensity and the Reynold stresses) were affected by the characteristics of the upstream flow (Resch et Leutheusser, 1972).

The submerged hydraulic jump has been the subject of extensive investigations (Rajaratnam, 1967), (Long, Steffler and Rajaratnam, 1990) but in most of the cases, the phenomenon was studied when generated by a sluice gate (Long, et al., 1991) where the focus is on the gate opening, the depth at the vena contracta, and the corresponding Froude number. This approach is contrasted with the weir overflow setup (Figure 2-6).

The first experimental investigation on submerged hydraulic jumps, as a three-dimensional phenomenon, relied on Laser Doppler Anemometry (LDA) measurements taken along the streamwise, widthwise and vertical directions (Long, Steffler and Rajaratnam 1990). The sluice gate setting designed by the authors to experimentally assess the properties of the submerged hydraulic jump served as the frame for future investigation on this field of research. Later experimental investigations have used the same setup investigating the phenomenon created by a sluice gate, but only a few investigated the submerged hydraulic jump created by an overtopping structure (Leutheusser and Fan, 2001).

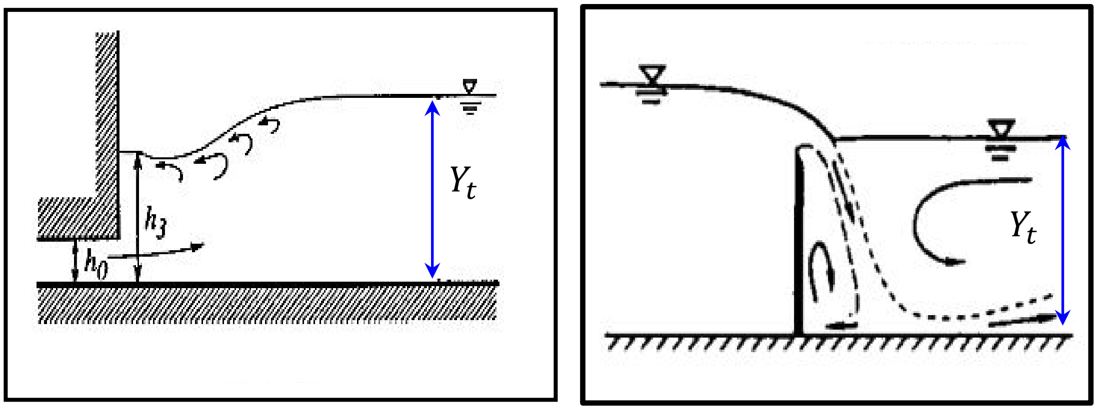

a) b)

Figure 2-6: a) Sluice gate setup (Ohtsu, Yasuda and Ishikawa, 1999). b) Weir overflow setup (Wu and Rajaratnam, 1996)

2.2.1 The free hydraulic jump

The 'free' or classical hydraulic jump is a phenomenon which enables the flow to dissipate the excess of the energy while is transitioning from a supercritical inflow regime, upstream from the structure, to a subcritical state downstream. At an overflow structure, this excess on the energy balance is related to the transition from (i) an upstream section whose characteristics are determined by the discharge and structure height and (ii) a downstream section whose characteristics are imposed by the hydrologic system.

Figure 2-7 illustrates the standard geometry for a classical hydraulic jump, where the toe of the jump is just touching the falling nappe. The initial depth is represented by the supercritical depth (Y_1) and the final water level is represented by the subcritical depth (Y_2). Over the length of the hydraulic jump, the flow transforms from supercritical to subcritical; the high levels of turbulence and noise observed in classical hydraulic jumps (innate to this phenomenon) are the mechanisms available in the flow nature to achieve this transition. The sequent depths on a classical free hydraulic jump are related, for a rectangular horizontal channel in absence of friction, by the Bélanger equation:

$$\frac{Y_2}{Y_1} = \frac{1}{2}\left(-1 + \sqrt{1 + 8{F_1}^2}\right) \tag{2.7}$$

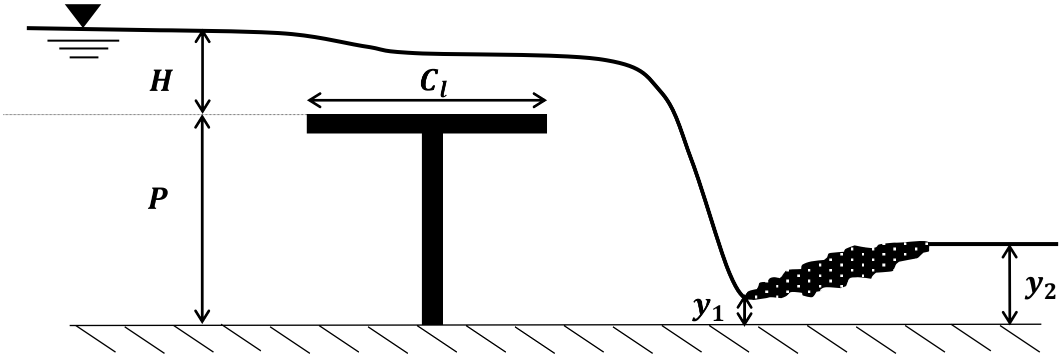

Figure 2-7: Graphical representation of the submerged hydraulic jump formed downstream from overflow structures

Where the Froude number at the inflow section on the jump (Fr_1) stands for the non-dimensional relation between the local inflow average velocity (V_1) and the supercritical depth (Y_1). Therefore, the Froude number at the inflow section provides information regarding the characteristics of the flow "feeding" the jump.

$$F_1 = \frac{V_1}{\sqrt{gY_1}} \tag{2.8}$$

At the same time, local average velocity (V_1) is defined as $V_1 = q/Y_1$ from the mass conservation equation, as a function of the discharge for unit width (q). At overflow structures, the hydraulic jump typology depends on the water level conditions downstream for a given discharge. The category submerged hydraulic jump will occur when the tailwater depth (Y_t) reaches values above the subsequent depth for the classical hydraulic jump (Y_2). This situation is associated to the dangerous events previously described.

2.2.2 The submerged hydraulic jump

The classical hydraulic jump is referred to as 'optimum' because of its ability to dissipate the largest amount of energy. The "degree of submergence" (S) compares the local tailwater depth to the subsequent depth of the vortex, providingan indication of how submerged the vortex is. This variable, essential to qualitatively evaluate the characteristic of the submerged vortex, is defined as follows (Govinda Rao and Rajaratnam, 1963):

$$(2.9) \qquad S = \frac{Y_t - Y_2}{Y_2}$$

Several situations are identified for different values of the degree of submergence:

- If $S = 0$, the hydraulic jump is stable leading to a classical hydraulic jump.
- If $S < 0$, the jump is swept out downstream.
- If $S > 0$ the jump is submerged.

Therefore, for a 'classical' hydraulic jump, the downstream subcritical depth (Y_2) and the local tailwater depth of the channel (Y_t) are equal leading to a null value for the degree of submergence. This project is focused on tailwater depths which satisfy the condition of positive degrees of submergence, leading to the development of the above mentioned submerged hydraulic jump condition. This condition implies that the local tailwater depth becomes larger than the sequent depth of the jump. Several authors pointed out to the fact that as the jump's submergence increases, there is a decrement on the jet mixing, resulting in a reduction of the energy dissipated in comparison with free hydraulic jumps (Habibzadeh, 2013). Therefore, as the degree of submergence increases the jump becomes less efficient, translating into a reduced capacity to dissipate energy (Vischer and Hager, 1995). From a design standpoint, the submerged hydraulic jump presents the advantage of developing a reduced sensitivity to tailwater variations being confined to the same downstream region, in comparison with the free hydraulic jump which displaces along the downstream region as a function of the local tailwater level. However the submerged hydraulic jump is a less efficient mechanism to dissipate energy and consequently, the downstream region affected by the jump is larger in comparison with the free jump. As a result, a longer stilling basin must be considered if the downstream is working under submerged conditions (Habibzadeh, 2013).

The authors of this manuscript identified some limitations derived from the classical definition of the degree of submergence (S) proposed in 1963 by Govinda Rao and Rajatranam which, to the best knowledge of the authors, have not ever been discussed by previous literature:

- The degree of submergence (S) is not explicative and can't be used to compare across cases.
- In order to calculate the degree of submergence according to the classical relation, it is necessary to know beforehand the sequent subcritical depth for the free hydraulic jump (Y_2). Obtaining this subsequent depth may be impractical or difficult under some experimental conditions or on site. Additionally, its numerical calculation might rely on the use of the empirical Bélanger equation which at the same time, is a function of the supercritical depth (Y_1).
- The maximum tailwater level able to create a submerged hydraulic jump (Y_{u+}), is not considered by the classical formulation for the degree of submergence. Consequently, the current definition only compares the local tailwater depth (Y_t) with the sequent subcritical depth for the free hydraulic jump (Y_2), seen as the minimum tailwater level for submergence.
- Finally, obtaining this supercritical depth feeding the roller for overflow structures is a challenge. Under a submerged hydraulic jump condition, the downstream pool and reverse current on it affect the entry of the impinging jet. As a result, the characteristics of the supercritical sequent depth (Y_1) feeding the submerged hydraulic jump get affected by the downstream conditions.

An explanatory example regarding the weaknesses of the classical definition of the degree of submergence can be found on the research performed by Leutheusser and Fan (2001). The authors carried out some experimental work involving the investigation of submerged hydraulic jumps on rectangular sharp-crested weirs. The test conditions consisting of five experimental series are shown in Table 2-1. The test conditions recorded two different types of degree of submergence, for the ‘flip’ and ‘flop’ conditions. The condition ‘flip’ is referred to the maximum tailwater level associated to a submerged hydraulic jump formation under increasing tailwater depth conditions. On the other hand, the ‘flop’ condition refers to the to the maximum tailwater level creating a submerged hydraulic jump under decreasing tailwater levels.

Table 2-1: Summary of experimental test conditions and key measurements. (Leutheusser and Fan, 2001)

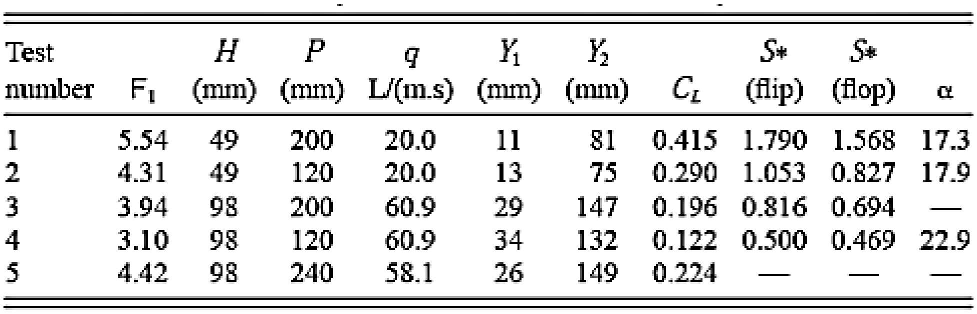

Test number	F_1	H (mm)	P (mm)	q L/(m.s)	Y_1 (mm)	Y_2 (mm)	C_L	$S*$ (flip)	$S*$ (flop)	α
1	5.54	49	200	20.0	11	81	0.415	1.790	1.568	17.3
2	4.31	49	120	20.0	13	75	0.290	1.053	0.827	17.9
3	3.94	98	200	60.9	29	147	0.196	0.816	0.694	—
4	3.10	98	120	60.9	34	132	0.122	0.500	0.469	22.9
5	4.42	98	240	58.1	26	149	0.224	—	—	—

The degrees of submergence recorded by the authors range between [1.79-0.50] for the flip and between [1.568-0.469] for the flop. However, reaching either the ‘flip’ or the ‘flop’ implies that the submerged hydraulic jump is fully submerged and tailwater levels above this value would induce the transition from submerged hydraulic jump to ‘undular’ jump (in the case of the ‘flip’). Consequently, a proper definition of this degree of submergence would obtain a value of 100% (or 1 in a normalized scale) for the degree of submergence associated to either ‘flip’ or ‘flop’.

In 1990, an experimental investigation of submerged hydraulic jumps determined for the first time the dynamic characteristics of submerged hydraulic jump using LDA. The results of this study are shown in Figure 2-8, revealing negative horizontal velocities along the free surface at sections affected by the submerged jump.

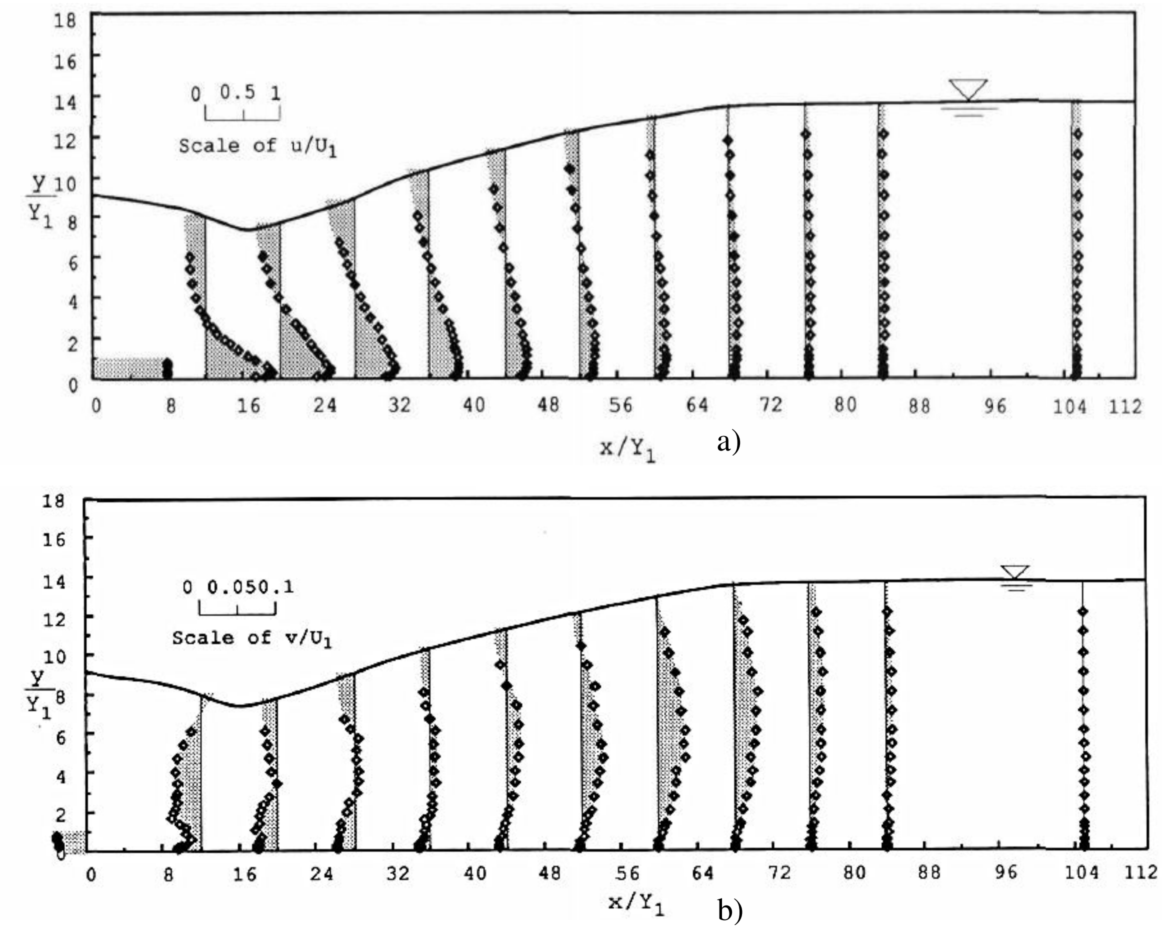

Figure 2-8: Velocity distribution over the depth for $Fr_1 = 8.19$ and $S = 0.24$.
a) Horizontal velocity. b) Vertical velocity. (Long, Steffler and Rajaratnam, 1990)

In 2001, a new investigation provided insight into the dynamic characteristics of the roller. The results involving the surface velocity (V_s) as a function of the degree of submergence and the energy lost by the “drowning machine” (ΔE_{dm}) are presented in Figure 2-9. The dashed lines are derived from an equation proposed by the authors to estimate the upstream velocity of the free surface (Leutheusser and Fan, 2001). The equation is proposed as a function of the total power loss of the submerged hydraulic jump based on a simple model of a forced vortex. This model gives an approximation, however it is not able to accurately simulate the flow processes involved in the turbulent submerged hydraulic jump. The coefficient α is selected to match the experiments, as a calibration parameter. This formulation can be used as a comprehensive way to predict the maximum upstream velocity, and it is defined as follows:

$$(2.10)\qquad \frac{V_s}{V_1} = \left[\frac{16\Delta E_{dm}/Y_t}{\alpha(S+1)(\sqrt{1+8{F_1}^2}-1){F_1}^2}\right]^{1/3}$$

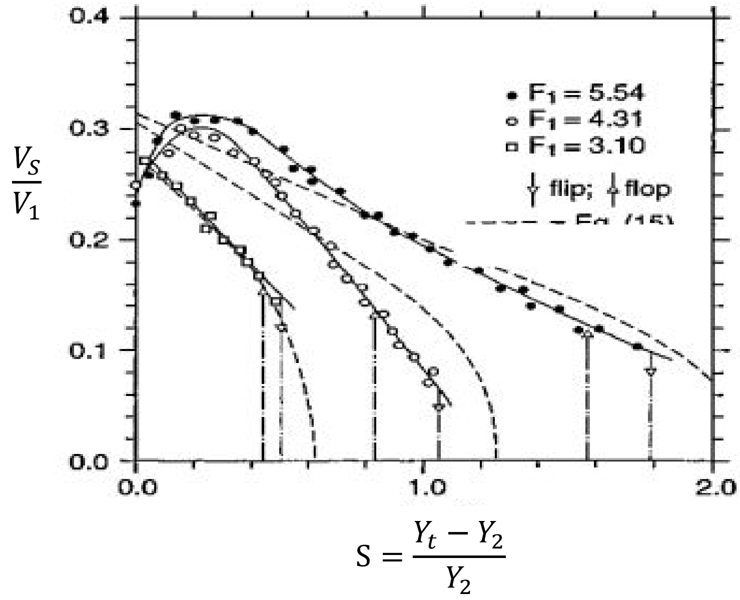

Figure 2-9: Relation between the non-dimensional countercurrent free surface velocity and the degree of submergence, corresponding to experimental conditions summarized in Table 2-1. (Leutheusser and Fan, 2001)

The experimental results of Leutheusser and Fan are summarized by Figure 2-9. It is observed that the counter-current superficial velocity reaches a maximum of one third of the unsubmerged supercritical flow velocity (V_1) for several Froude numbers and weir characteristics. Other remarks involve the constant ratio between the upstream depth (Y_0) and the critical tailwater level (Y_u) at which the flip and flop form. The transition between submerged hydraulic jump and surface roller or vice-versa occurs at the following ratios:

- The term flips refers to the transition from submerged hydraulic jump to surface roller for increasing tailwater levels. For nappe flip, the critical submergence tailwater level satisfies ratios of $Y_0 / Y_{u+} = 1.10$

- The term flops refers to the transition from surface roller to submerged hydraulic jump for decreasing tailwater levels. For nappe flop, the critical submergence tailwater level satisfies ratios of $Y_0 / Y_{u-} = 1.19$

As a result, the tailwater level required to achieve the flip is larger than for attaining the flop. This can be explained in terms of the dissimilar nature of the 'flip' and 'flop' phenomena. The 'flip' phenomenon occurs when the submerged vortex transforms into an 'undular' jump, therefore transitioning from a stationary roller to a moving oscillatory wave. On the other side, the 'flop' gets reduced to a problem of wave instability, materialized by the transition from an 'undular' jump, to a submerged roller.

Other points discussed by Leutheusser and Fan, which are of interest for this research, is the fact that mild degrees of submergence are associated to more dangerous vortices. Figure 2-9 reveals how the non-dimensional surface velocity (V_s / V_1) starts increasing for degrees of submergence close to 0, reaching a peak. From that maximum, the relation decreases with increments on the degree of submergence.

2.2.3. Hydraulic conditions for development of submerged jump

Specific combinations of flow discharge, downstream water depth and vertical drop are associated with the development of a submerged hydraulic jump. The tailwater depth determines the mechanism of dissipation of energy of the hydraulic jump. At the same time, the downstream water level is a variable naturally imposed under normal operation conditions by the downstream primary water body, such as the lake or the river at which the tributary flows. Therefore, the tailwater level depends on several factors such as downstream river slope, roughness, section, rainfall intensity, in-stream structures and catchment area. (Leutheusser and Fan, 2001)

In 1996, Wu and Rajaratnam studied the submerged flow regimes at a vertical drop for tailwater levels above the crest height. The depth of the tailwater downstream determines the flow type over the weir for a given discharge. Figure 2-10 shows different types of hydraulic jump. In the range of downstream tailwater levels $0 < Y_t < a$, a classical or 'free' hydraulic jump forms. As the tailwater level reduces within this range, the hydraulic jump is repelled from the structure in the downstream direction. Water levels in the range $a < Y_t < b$ are associated with a submerged hydraulic jump, representing the range of water levels which are the focus of this study. Within the depth range $b < Y_t < c$ a surface roller would form. Finally, water levels above the previous case $Y_t \geq c$ would generate a surface jet.

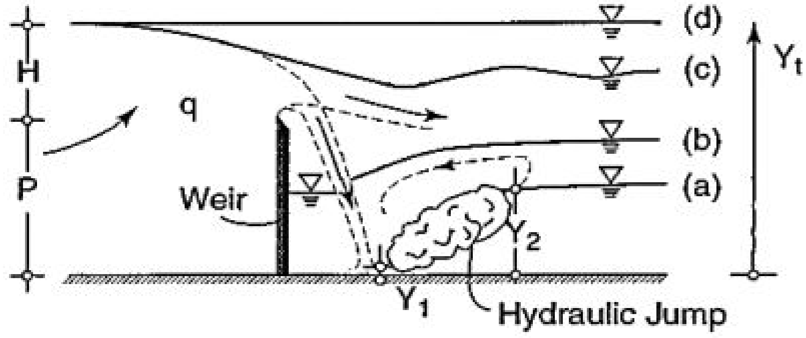

Figure 2-10: Diagram of the Various States of Weir Flow. Adapted from (Wu and Rajaratnam, 1996)

Furthermore, the authors distinguished between submerged flow (Figure 2-11-a) and surface flow (Figure 2-11-b-c-d). The water profiles for the submerged and surface flow regimes further described by Wu and Rajatranam are illustrated in Figure 2-11:

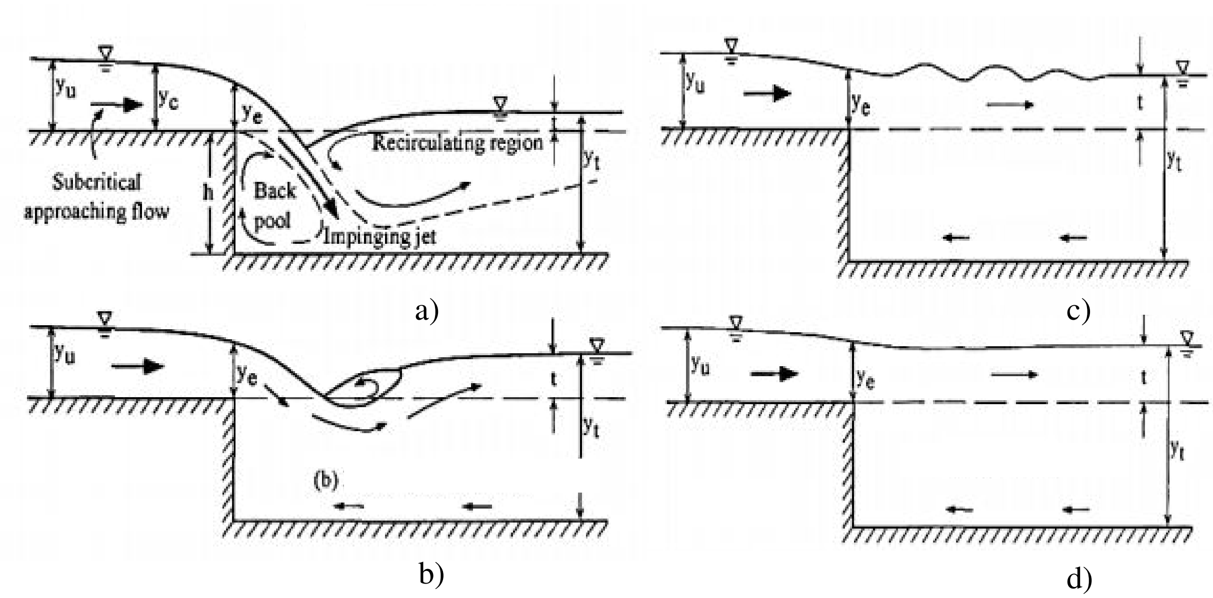

a) c)

b) d)

Figure 2-11: Submerged flow regimes for rectangular sharp-crested weirs (a) Impinging Jet; (b) Breaking Wave; (c) Surface Wave; (d) Surface Jet. (Wu and Rajaratnam, 1996)

An impinging jet (Figure 2-11-a) is associated to tailwater levels smaller than the crest height. In this case, the nappe hits the downstream pool as a plunging flow, generating a downstream recirculation pool, creating a submerged hydraulic jump. As the tailwater rises, the incoming flow lifts from the bed forming a surface flow. Three sub-regimes are identified in the surface flow category (for increasing tailwater levels): breaking wave, surface wave and surface jet. These different stages are seen in Figure 2-11 (Wu and Rajaratnam, 1996), (Wu and Rajaratnam, 1998).

In summary, the submerged hydraulic jump phenomenon occurs under submerged flow regime when the hydrological tailwater depth exceeds the jump's subcritical depth. This event is very common in low overflow structures. The submerged hydraulic jump produces a horizontal vortex with high countercurrent free surface velocities. Consequently, the dangerous hydraulic conditions observed at overflow structures are associated to the formation of this phenomenon.

2.3 Low-head dams: Dangerous Hydraulic Conditions

Several authors identified the presence of dangerous hydraulic conditions downstream of low head dams (Hotchkiss, 2001) and this issue was addressed by a movie titled "The Drowning Machine" (Borland-Coogan, 1980). The hydraulic jump becomes submerged and develops into a horizontal vortex with a high rolling velocity associated to a counter current which develops in an apparently serene surface. This phenomenon is magnified by the presence of a plunging nappe which entrains air during the fall. As a result, the water density gets reduced as well as the buoyancy of any potential victim entrapped in the recirculation region. This incident has been identified as the cause of several fatalities, and until 1991 this phenomenon was "virtually unknown in hydraulic engineering literature" (Leutheusser and Birk, 1991).

2.3.1. Dynamic characteristics of submerged rollers forming downstream of overflow structures

In 2001, Leutheusser and Fan dedicated their research to quantify the high velocities representative of different situations, by quantifying the hydraulic processes involved in these events. In order to do so, experiments evaluated the performance of overflow structures, modeled by sharp-crested rectangular plate weir. In the simulations the different types are not considered because this factor is not essential. The results matched their previous research (Leutheusser and Birk, 1991) and the velocity was estimated to be approximately one third of the supercritical inflow velocity of the classical jump. The worst case scenario was associated with small degree of submergence, defined as the relation between the depth at the end of the hydraulic jump and the tailwater depth.

The vortex formation depends on the tailwater depth, the fall height (structure height) and the emerging flow. According to several authors, the location of the submerged roller is restricted to under the downstream pool and above the upper nappe of the falling jet, where the water is recirculated. As a result, the downstream appears calm and harmless. The vortex velocity was measured initially by Leutheusser and Birk (1991) who experimentally determined that the upstream directed velocity can reach values of up to 2 m/s, a high value considering that the maximum swimming human velocity performed by an Olympic swimmer is about the same magnitude (2 m/s). Leutheusser and Birk (1991) and Hotchkiss (2001), suggested that the falling nappe would exert a force of approximately 1.5 times the weight of the victim. Consequently, this dynamic force would submerge the potential victim.

2.3.3 Classical solution to minimize submerged hydraulic jumps

In order to minimize dangerous hydraulic conditions immediately downstream from low-head dams, the structure needs to be carefully designed. Various methods have been proposed in order to maximize the dissipation of energy associated to the hydraulic jump. Measurements such as downstream steps or dented baffle chutes would efficiently accomplish this function; however it would compromise the functionality of the weir as a sea lamprey barrier. None of these measures would assure the minimum vertical drop required to be effective.

Leutheusser and Birk in 1991 recommended either to increase the height of the structure enough to form a proper hydraulic jump instead of a submerged jump or to introduce the "cascade effect" on the structure in order to dissipate the energy, the latter being more recommended due to its environmentally friendly nature and their capability to adapt and be effective under different hydraulic conditions. Figure 2-12 shows an example of a baffled-chute.

Derived from the analysis of flow characteristic of the weirs, Leutheusser and Birk recommended the installation of baffle-block chute for breaking up the vortex. This design considers a 1V:2H slope with alternative baffles to dissipate energy along the chute length. A flow discharge of $q = 26.3\,\mathrm{l/m.s}$ was cited as the design discharge by the authors. The authors proved that the dangerous condition associated to the formation of the submerged vortex was in all cases eliminated because of the presence of the baffles.

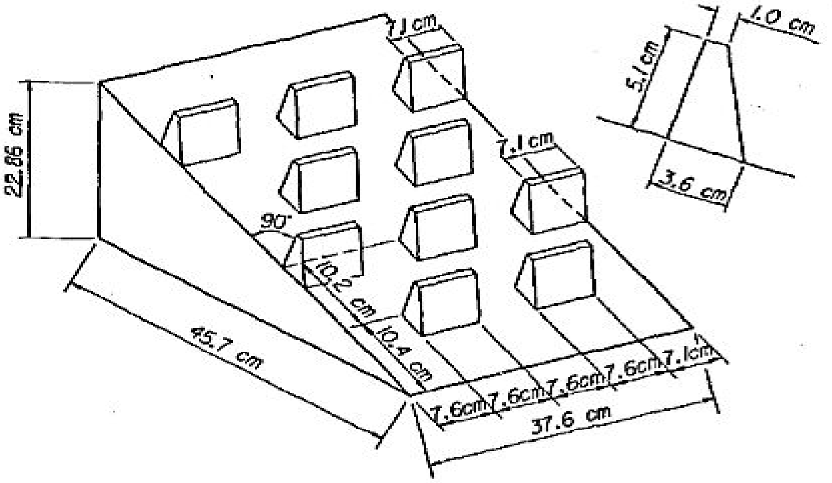

Figure 2-12: Example of baffled-chute. The dimensions correspond to the U. S. Bureau of Reclamation Basin IX. (Leutheusser and Birk, 1991)

This solution was later discussed by Hotchkiss and Comstock (1992). The authors noticed that the baffle chute basin design proposed by Leutheusser and Birk (1991) was not as effective as initially presented in terms of safety for swimmers and boaters. This solution dissipated the frontal vortex, however the navigation through the baffles for any potential victim would entail a danger on its own. Additionally, the amount of debris entrapped on the structure would lead to an even more dangerous event at the same time that the functionality and integrity of the structure would become compromised. A series of experiments were carried out to illustrate the flow patterns through a baffled chute and the results were published as a discussion of the article published one year before by Leutheusser and Birk (Hotchkiss and Comstock,1992).

The experiments conducted by Hotchkiss and Comstock to prove their theory consisted of the test of some cases not considered in the initial manuscript by Leutheusser and Birk who suggested the Basin IX chute design as seen in Figure 2-12 as a solution to 'drownproof' low overflow structures. Two discharge conditions different to the design discharge were tested, both with discharges larger than the design one. At the same time, two different tailwater depths were tested for each experimental discharge. The experimental results validated their theory about the potential dangerous conditions for swimmers occurring at the fall of baffled chutes.

2.4 Numerical modeling of a "drowning machine"

A validated numerical model presents many advantages over physical investigations. Experimental studies are time consuming and expensive and less flexible for implementing changes in geometry or flow characteristics. However, the existence of experimental data is essential to achieve a validated numerical model able to produce reliable simulations. The implementation of geometry modifications, changes along the boundary conditions or initial conditions can easily be implemented in a numerical environment. The high complexity, of both the weir overflow and the submerged hydraulic jump problems, explains the few contributions within the frame of combined experimental and numerical investigations. Successful numerical studies focusing on the simulation of a "drowning machine" (result of a submerged hydraulic jump forming downstream from an overflow structure) are non-existent at the moment.

The case of a submerged hydraulic jump created by a sluice gate was successfully numerically reproduced for the first time in 1991 (Long, Steffler, & Rajaratnam, 1991). At this point the investigation on the internal structure of the hydraulic jump case was better understood and some numerical investigations were already performed (Madsen and Svendsen' 1983), (McCorquodale and Khalifa' 1983).

The main challenges associated to the numerical simulation of the submerged hydraulic jump are associated to the changing geometry of the free surface and the modeling of air entrainment. The authors confronted these issues by implementing an offset control method able to adapt the mesh to a changing geometry (free surface) combined with a hybrid scheme and the 'SIMPLE' (Semi-Implicit Method for Pressure-Linked Equations) algorithm to solve the 3D Navier-Stokes equations (Caretto, et al. 1972). The 'SIMPLE' method achieves the solution in sequential "guess-and-correct" operations. Each iteration starts with an estimated pressure distribution enabling the calculation of a velocity field which satisfy the linearized momentum equations. Then, the mass conservation equation is applied to correct the velocity and pressure fields such that all the equations are satisfied. Additionally a standard two-dimensional RAS $k - \varepsilon$ turbulence model was added to the mathematical model. As a result, Long and his colleagues were able to successfully recreate a submerged hydraulic jump. Their numerical results compared to previous experimental data are presented in Figure 2-13.

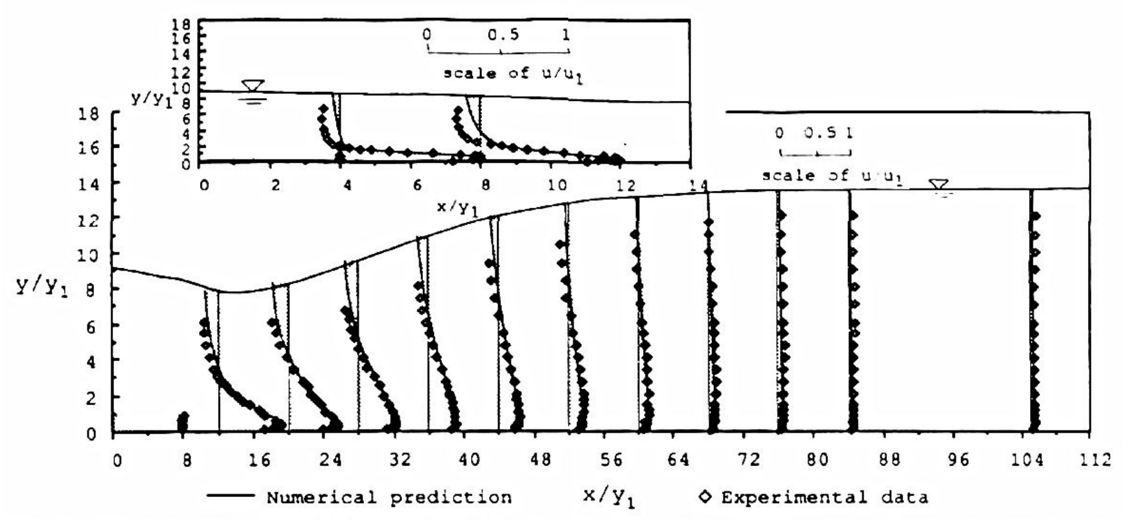

Figure 2-13: Comparison of longitudinal velocity distribution between experimental and numerical data for $F_1 = 8.19$ and $S = 0.24$. (Long, Steffler and Rajaratnam 1991)

Long et al. presented the first numerical simulation of submerged hydraulic jumps in 1991, achieving a prediction which was closely related to the experimental results of the flow structure performed one year before (Long, Steffler and Rajaratnam, 1990). However the governing equations were for steady state flow and the offset method to track the changing free surface had important limitations to predict a changing surface.

The initial implementation of the fractional Volume of Fluid (VOF) on numerical simulations was proposed by (Hirt, 1981) enabling the prediction of complex free boundary conditions. In 1994 Qingchao and Drewes investigated an improved simulation of the submerged hydraulic jump created by a sluice gate. The development consisted of the implementation of governing equations for unsteady flow condition (partially implicit discretization techniques) and the use of the VOF technique to track the free surface. The turbulence model $k - \varepsilon$ previously used (Long, Steffler and Rajaratnam, 1991) was considered to close the RANS equations. The time-evolution of the free surface and spatial distribution of velocity and turbulence-related parameters for the already developed submerged hydraulic jump is presented in Figure 2-14. The authors concluded that the inflow Froude number and the energy dissipation rate are proportional. Another observation is that the turbulence energy is mainly dissipated within the region affected by the roller.

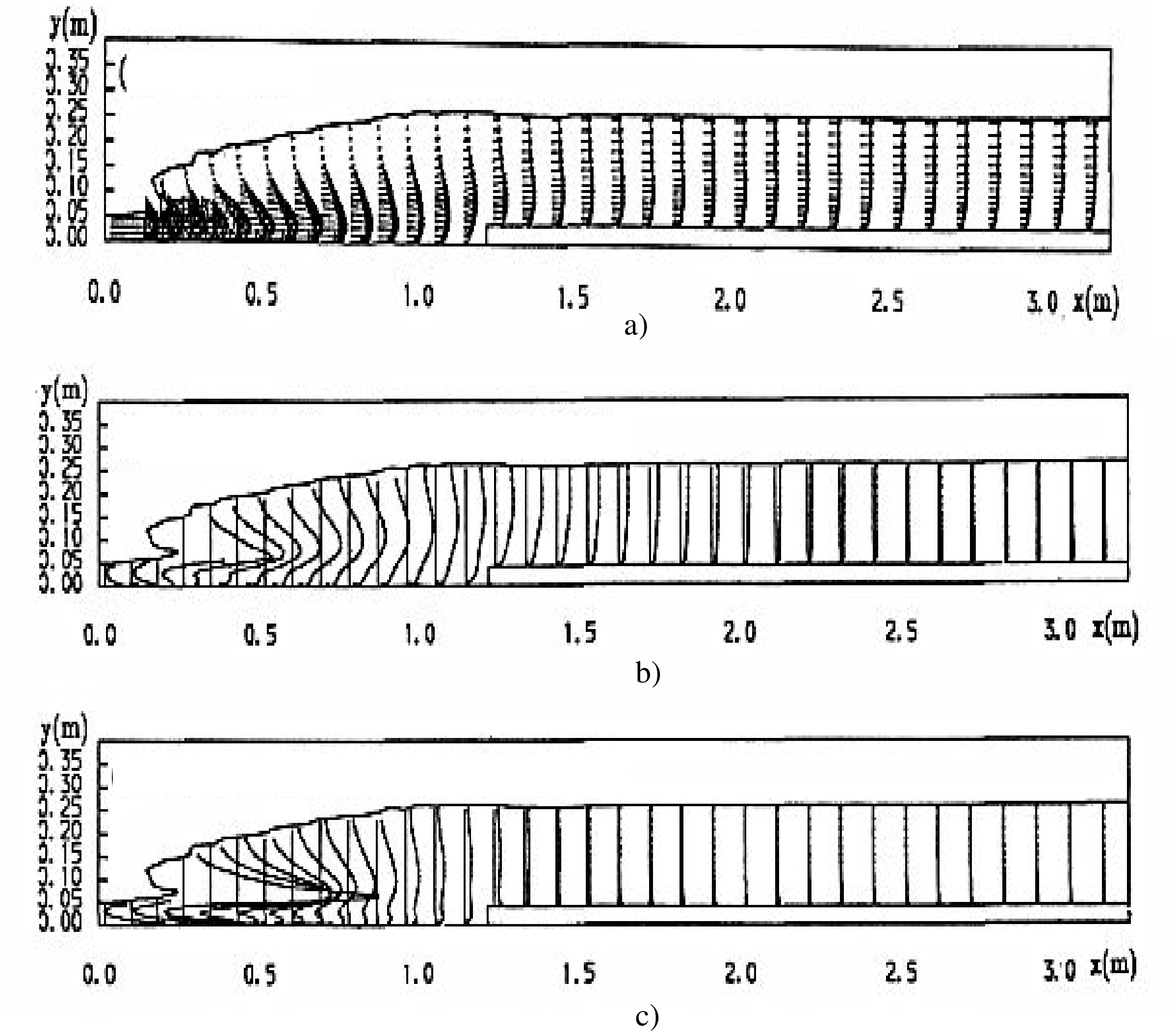

a)

b)

c)

Figure 2-14: Distribution of flow quantities for a submerged jump. $Fr_1 = 4.3,\ t_{sim} = 3.291$ s. a) Velocity vector. b) Turbulent kinetic energy. c) turbulence dissipation rate (Qingchao and Drewes, 1994)

The line of investigation opened in 1994 by Qingchao and Drewes served later authors who took advantaged from a model considering unsteady state and the VOF method. The exact conditions experimentally tested in 1991 by Long and his colleagues were numerically reproduced in a 2-D simulation (Ma, Hou and Prinos, 2001) achieving a very close agreement between the experimental and numerical data. These authors argued that the inclusion of air entrainment would highly improve the numerical calculations. Their results are shown in Figure 2-15.

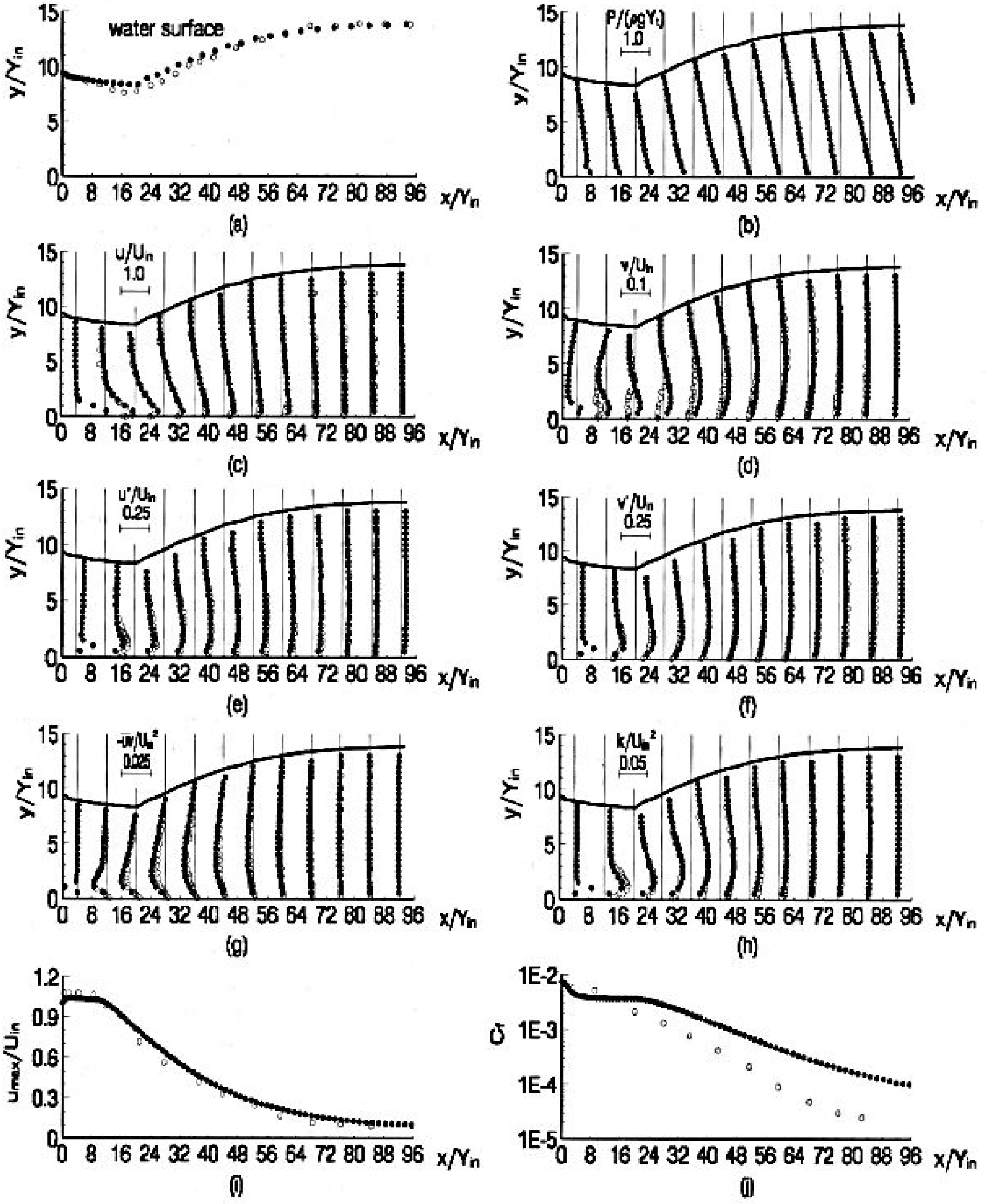

Figure 2-15: Flow quantities for a submerged jump $Fr_1 = 8.19$ $S = 0.24$. Filled dots refer to computed values (Ma, Hou and Prinos 2001) and hollow dots to experimental measurements (Long, Steffler and Rajaratnam 1990)

The current study investigates the simulation of submerged hydraulic jump by using an open source, computational fluid dynamics platform known as OpenFOAM. The interFoam solver which solves the RANS equation for a multiphase flow is considered.

Consequently, this approach is similar to the previous studies but with the advantage of considering the air entrainment. This solver has been proved to accurately predict a 2D hydraulic jump created by a sluice gate, as seen in Figures 2-16 and 2-17 (Romagnoli, Portapila, & Morvan, 2009). The simulated values for the streamwise component of the velocity and the kinetic turbulent energy closely reproduced experimental investigations in the field.

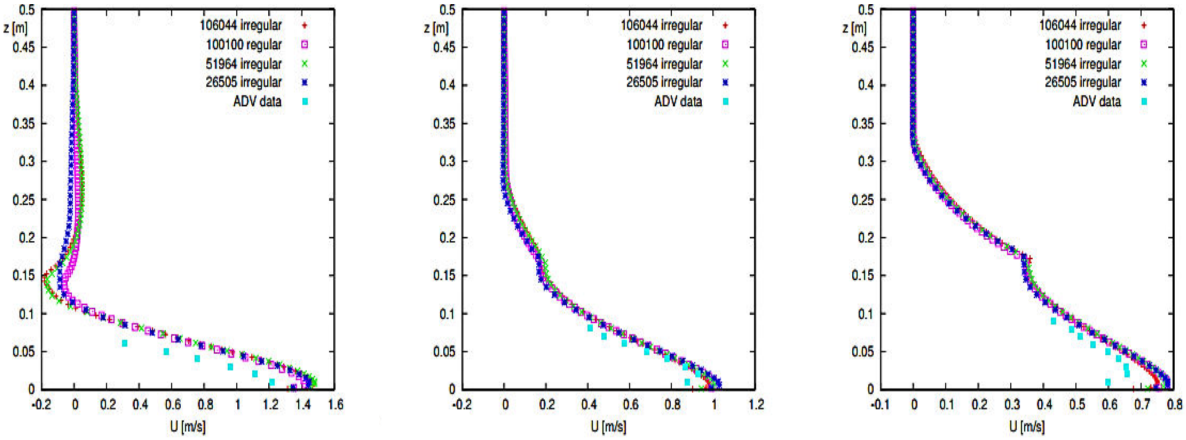

Figure 2-16: Average horizontal velocity for several meshes and downstream locations; a) $x/(Y_2 - Y_1) = 1.12$, b) $x/(Y_2 - Y_1) = 3.52$, $x/(Y_2 - Y_1) = 5.92$. (Romagnoli, Portapila, & Morvan, 2009)

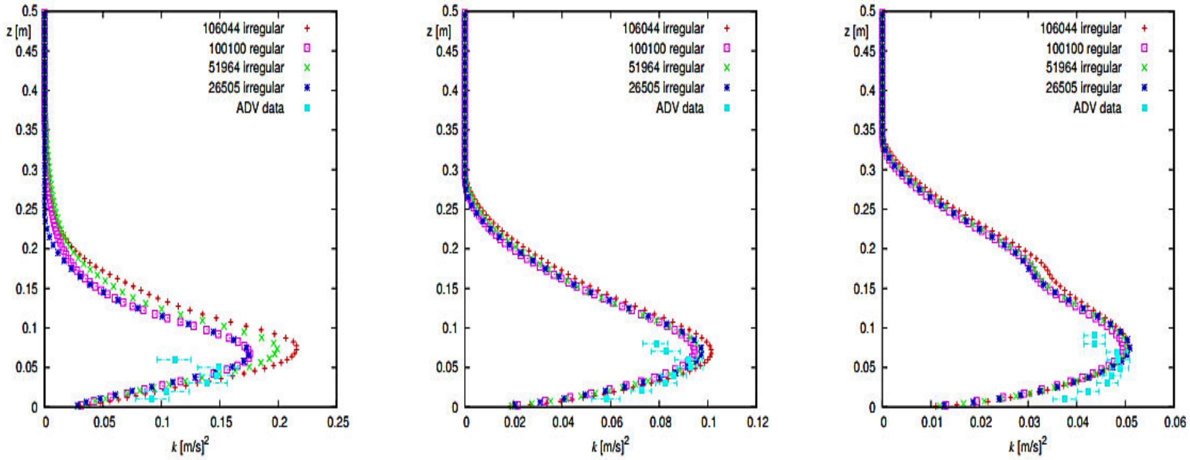

Figure 2-17: Turbulent kinetic energy for several meshes and downstream locations; a) $x/(Y_2 - Y_1) = 1.12$, b) $x/(Y_2 - Y_1) = 3.52$, $x/(Y_2 - Y_1) = 5.92$. (Romagnoli, Portapila, & Morvan, 2009)

The second element which must be addressed by the numerical simulation is the reproduction of the hydraulic conditions generated on overflow structures. The dangerous hydraulic conditions are generated by both: the overflow structure and a resulting submerged hydraulic jump, however an accurate reproduction of both elements is pursued. Additionally, this research considers the submerged hydraulic jump phenomenon generated by an overflow structure instead of a sluice gate.

In this hydraulic application the numerical model must include the Navier-Stokes equations to fully reproduce the phenomenon. The classical shallow water equations (SWE) are discarded because of its formulation depth-averaging the flow characteristics. This simplification assumes hydrostatic pressure distribution and zero velocity along the vertical direction (Lv, Zou and Reeve, 2011)

In 2009, the numerical simulation of a sharp-crested weir in a rectangular channel was achieved by using the $k - \varepsilon$ turbulence model and the VOF scheme to solve the two-dimensional Reynolds averaged Navier-Stokes equations (Qu, et al. 2009). The PISO algorithm (Pressure-Implicit with Splitting of Operators), developed by Issa in 1986, enabled coupling of the pressure and velocity variables. As a result, the PISO algorithm (Issa 1986) is an essential part of the solution process to discretize the governing equations. The already discretized algebraic equations were solved with a Stone-based tri-diagonal solver. The water profile numerically simulated by Qu et al. (at two freeboard elevations) is compared to previous experimental data in Figure 2-18.

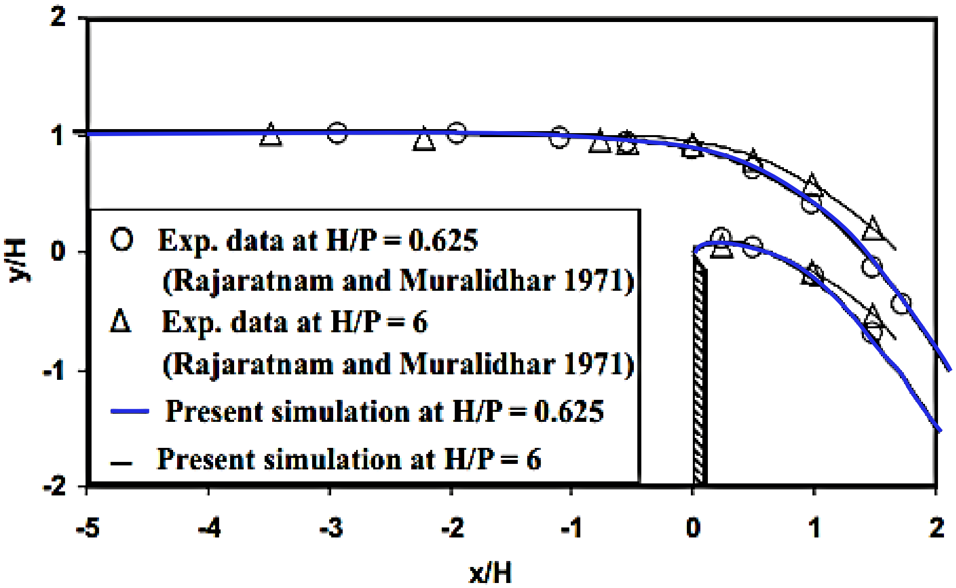

Figure 2-18: Water surface profiles near the nappe region. (Qu, et al. 2009)

In 2010, the numerical simulation of free flow over a sharp-crested weir was achieved by using the Langragian Smooth Hydrodynamic Particle method to solve the mathematical scheme (Ferrari, 2010). The governing equations are represented by the full weakly compressible Navier-Stokes equations and the Tait equation of state for water, which provides the relative pressure field under the hypothesis of weakly compressible fluid and neglecting the atmospheric pressure. A high quantitative agreement with physical investigation was obtained but at a very high computational cost.

Figure 2-19 presents the pressure field and the streamline of the free flow obtained for this simulation at four different time steps.

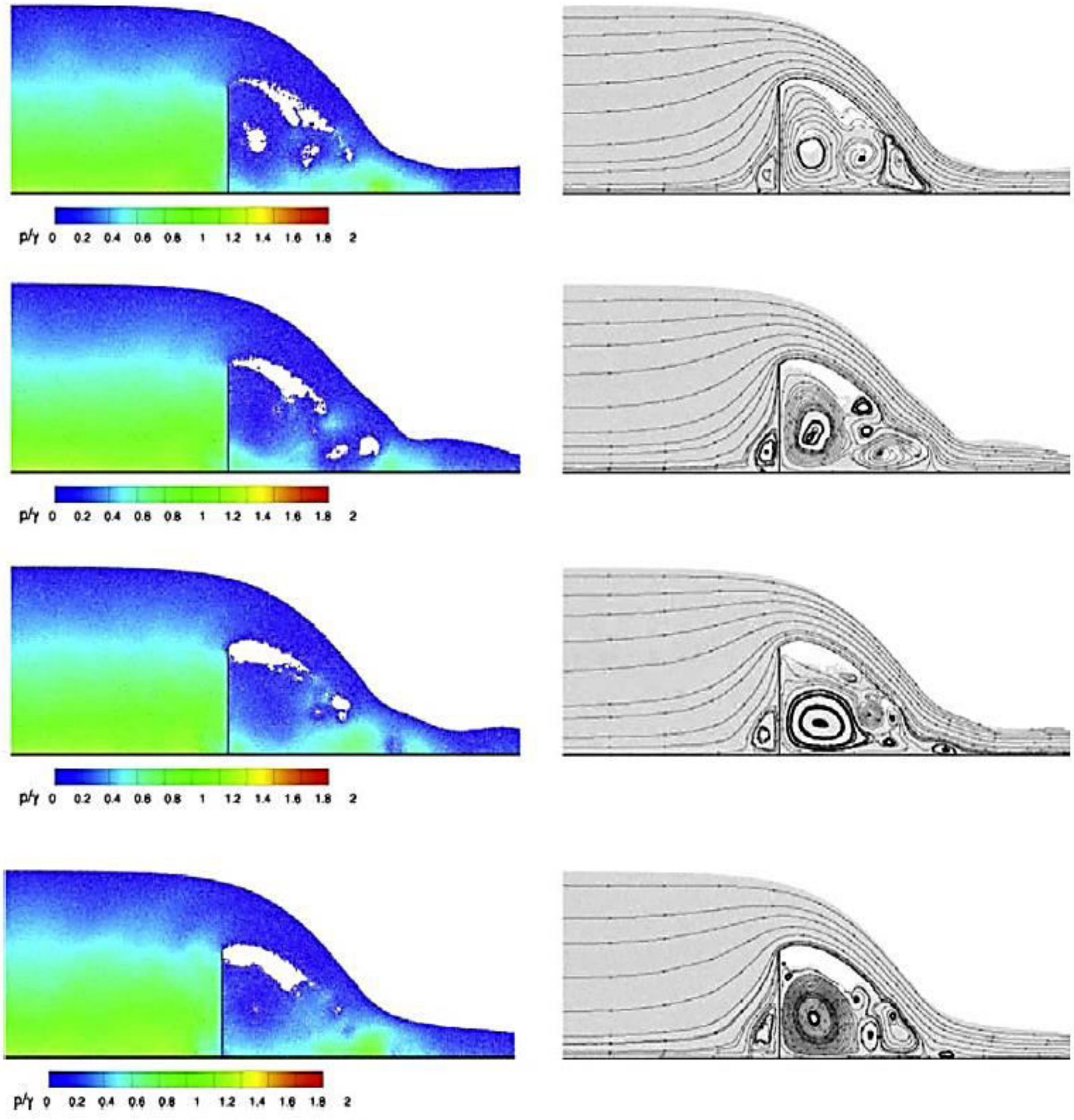

a) b)

Figure 2-19: Visualization of free flow overtopping a sharp-crested weir. (a) Pressure field. (b) Streamlines. The numerical results correspond to SPH numerical simulation with 500,000 particles. (Ferrari 2010)

In 2009, a hybrid scheme to track the free surface as a combination of the Level Set and the VOF methods referred as LS/VOF was developed (Lv, Zou, et al., 2009). In 2001, this hybrid method was applied to simulate the interface at weir overflow for sharp-and broad-crested structures (Lv, Zou and Reeve, 2011). Both methods were developed to track the free surface are based on the transport equation and are considered as sharp interface methods On the case of the fractional volume of fluid method, the property transported is the fractional volume of fluid function, α. This function reaches a value of $\alpha = 1$ for volumes containing water, $\alpha = 0$ for volumes filled with air and values within $0 < \alpha < 1$ for the free surface. On the other hand, the level set method considers the smooth level set function φ into the transport equation. This function gives the normal distance to the free surface, therefore points located at the interface have a value of $\varphi = 0$. This method was proved to accurately reproduce the free flow over sharp- and broad-crested weirs for several freeboards, as seen in Figure 2-20.

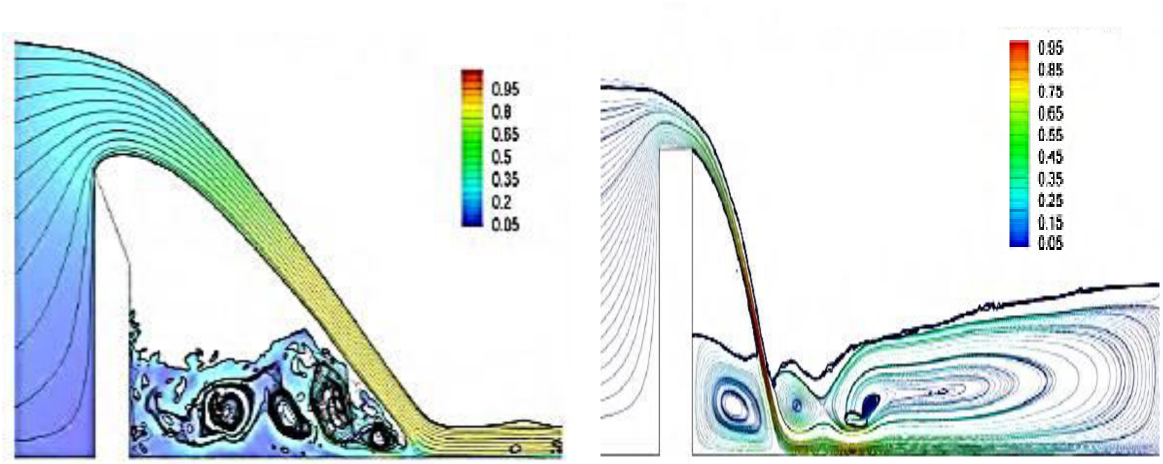

a) b)

Figure 2-20: Normalized horizontal velocity and streamlines of the flow field using a hybrid LS/VOF interface tracking method. a) Classical hydraulic jump b) Submerged hydraulic jump (Lv, Zou and Reeve, 2011)

The accuracy of the VOF method is highly dependent on the free surface reconstruction scheme and under complex scenarios, the process of interface reconstruction from the volumes of fluid is not an easy task. On the other side, the level set method has the disadvantage of not conserving the mass in the system well under complex interface geometries achieving non-physical behavior of the fluid. The hybrid LS/VOF method benefits from the advantages of both methods and minimizes its drawbacks. The velocity field, air entrainment and very complex vortical motions are resolved by this method.

2.5 Conclusion

The insights of both, the internal structure of the submerged hydraulic jump and the dynamics of free flow over weirs, have been pursued by the scientific community. Physical and numerical investigations have been applied to both of these concepts. The submerged hydraulic jump is characterized by high counter-current free surface velocities and high levels of air entrained within the core of the vortex. The degree of submergence (S) was found to highly affect the dynamic characteristics of the roller (Leutheusser and Fan, 2001). Moreover, the submerged hydraulic jump occurs typically either on a spillway chute or behind a sluice gate (Vischer and Hager, 1995), however more attention has been dedicated to the sluice gate case. In that scenario the inflow conditions are controlled at the vena contracta (Fr_1), instead of an overtopping structure, where the combined effect of the falling nappe and the violent collision with the downstream pool affect the inflow conditions and the dynamic characteristics of the submerged roller.

The ‘free’ flow over sharp and broad-crested weirs was extensively studied in literature, but authors focused on the hydrodynamic properties of the flow over the crest. However, the effect of the crest length on downstream characteristics of the submerged hydraulic jump forming downstream from these types of structures has been studied neither physically nor numerically. Lastly, the modern technologies enable the development of numerical models which are able to solve the governing equations of complex and turbulent flows simulating the air entrainment. The development of techniques to track the interface such as the VOF, combined with numerical algorithms to solve the Navier Stokes equations establish a robust numerical scheme suitable to simulate the problem under consideration.

Chapter 3. Experimental Procedure

3.1 Physical Model

All experiments focused on the effects on weir hydraulics brought about by (i) modification to the sharp crest commonly used in sea lamprey barriers in the Great Lakes region, and (ii) changes to the setting of the apron elevation immediately downstream of the structure.

All experimental runs were performed in the Hydraulics Laboratory at the University of Ottawa. The experimental work was carried out in a 13 m-long horizontal glass-walled flume, having a rectangular (0.385m-wide x 0.75m-deep) cross-section. The weir model was constructed of maple wood and Plexiglas and was sealed with waterproof silicone. The model weir was 0.257m high x 0.06m wide. The interchangeable crests of the model all had a thickness of 0.02 m and their lengths ranged from 0.06 m to 0.55 m. The model was located 3.0m from the flume's entrance section (9.85m from the flume's exit section) and was sealed to the flume's bottom and glass walls to prevent water infiltration along the connections. This location ensured: (i) generation of 'fully-developed' flow upstream of the model, and (ii) flow conditions immediately downstream of the model were not unduly influenced by the 'drawdown' water-surface profile (M2-curve) effect generated near the flume's outlet control gate. Figure 3-1 displays the experimental setup.

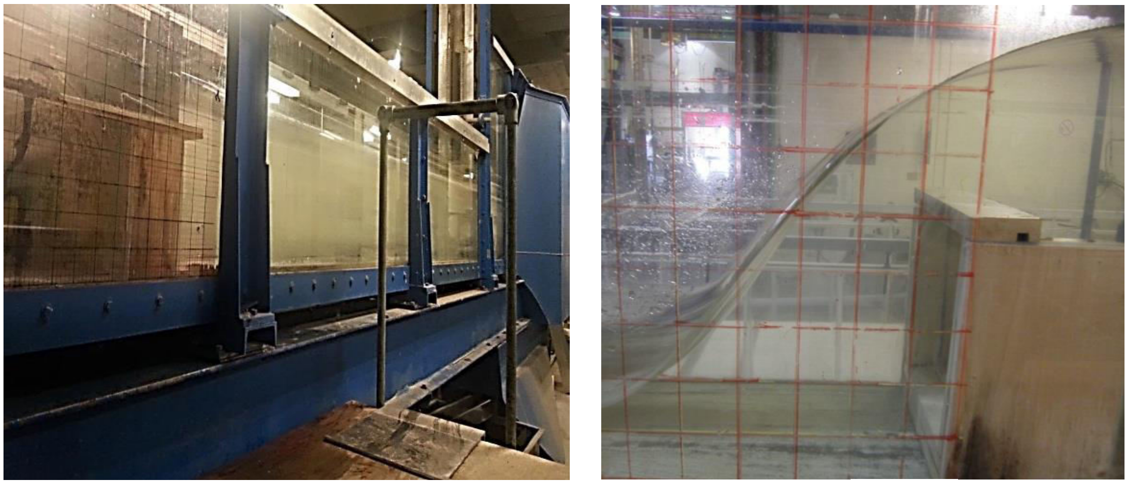

a)

b)

Figure 3-1: Experimental setup: a) side view of the glass-walled flume where the experimental tests were performed (looking upstream); b) close-up to the model

As shown in Figure 3-2, the tailwater depth in the flume was controlled by a sharp-crested weir located at the flume’s outlet section, the height of which could be adjusted by a crank. As noted above, the flume’s test section was located far enough upstream from the outlet weir that flow conditions developed at the former were not adversely affected by the ‘drawdown’ (i.e. ‘M2’-type) water-surface profiles generated just upstream of the latter.

.

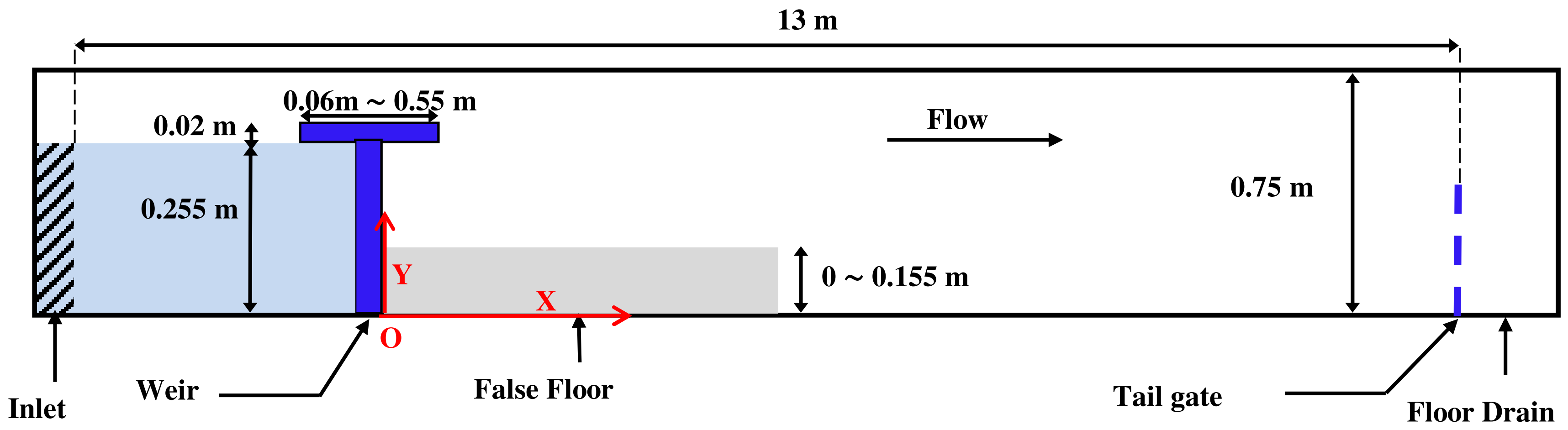

a) Side elevation

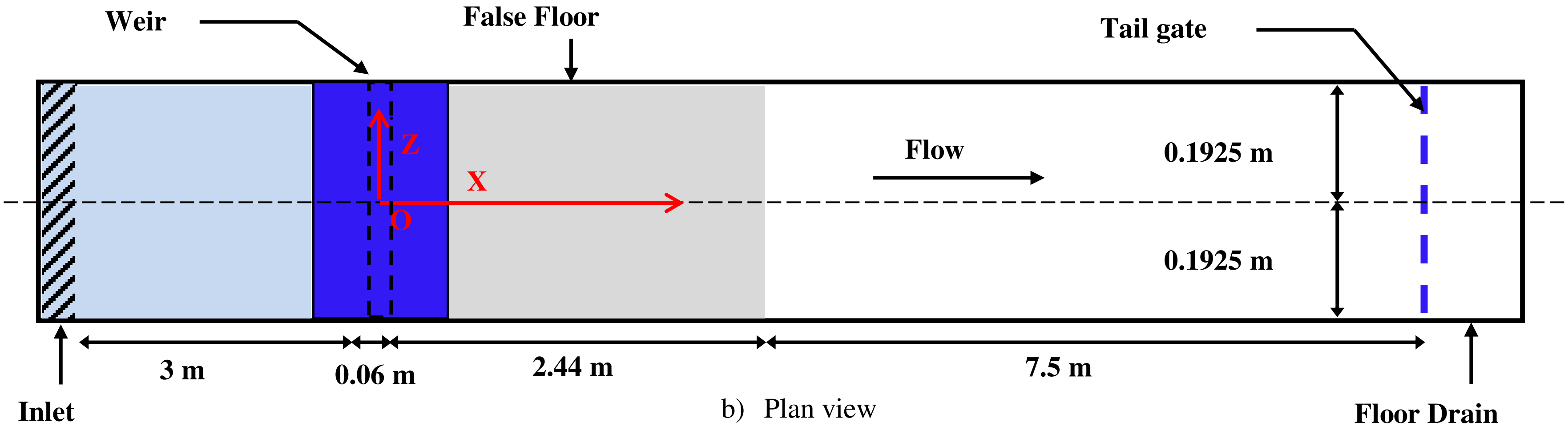

b) Plan view

Figure 3-2: Sketch of the experimental setup

3.1.1 Spatial reference

The axes were assumed as follows: X-axis along the longitudinal direction of the flow, Y-axis along the vertical direction, and Z-axis in the lateral direction. The lateral confinement of the flume was such that it restricted the laboratory investigation to that of a 2-D type. Consequently, all the measurements were taken along the middle plane of the flume. The global reference system was taken at the origin, O, which was located as indicated in Figure 3-2:

$$O:(X,Y,Z) = (0,0,0) \sim (downstream\,face, bed\ elevation, middle\ on\ the\ flume)$$

3.1.2 Scaling criteria

A full dynamic similarity is not possible between scale models and prototypes. For this reason, models are always a compromise (Khatsuria, 2005) and an exhaustive analysis to determine the more relevant parameters is important when designing the physical characteristics of the model.

The physical relation between the hydraulic parameters determines the most suitable scale for relating the hydraulic model to its prototype. In order to satisfy these similarity conditions, one or more relations are used to downscale the prototype and design the hydraulic model (Hughes, 1993). The most appropriate scaling criterion can be determined by selecting the two most relevant or major forces dominating the hydraulic problem. As Hughes points out, in any flow problem the inertial forces are always important. Determining the second major force acting within the hydraulic problem leads to the identification of the appropriate scale criterion required to design the model. In hydraulic problems, some of the most common forces acting within the hydraulic domain are: viscid (viscosity), gravitational, surface tension, elastic, pressure, and temporal (Hughes, 1993). Some of the classical scaling criteria resulting from combining the inertial forces with these other force result in the following dimensionless parameters:

- Reynolds number, Re, used in viscous-dominated hydrodynamic problems.
- Froude number, Fr, used in gravity-dominated hydrodynamic problems.
- Cauchy number, Ca, used in problems where elastic – compressive forces are dominant.

- Euler number, Eu, suitable for problems that focus on hydrodynamic pressure .
- Strouhal number, St, defined by the relation between the temporal and convective inertial forces. This relation is suitable for problems governed by instability and/or large oscillations.

Hydraulic environments can be described by more than two physical relationships between dominant forces, thereby resulting in more than one scaling criterion. However, it is impractical to consider more than one scaling relation. Most free surface hydraulic models are gravity-dominant, therefore a Froude scaling criterion prevails over the viscous-dominant Reynolds model, or any other dimensionless criterion.

As this experimental investigation deals with an overflow-type structure, Froude number equality is required in this instance (Prashun, 1992). Other scaling effects, such as those associated with friction, turbulence and air entrainment, should be accounted for through the application of corrective factors (Khatsuria, 2005). The Froude number (gravity-dominant) scaling criterion is expressed as:

$$Fr = \sqrt{\frac{F_{inertial}}{F_{gravitational}}} \tag{3.1}$$

Where the inertial force is defined as:

$$F_{inertial} = mass\ x\ acceler._{convec} = (\rho V)\left(U_0 \frac{\partial U_0}{\partial L}\right) = (\rho L^3)\left({U_0^2}/{L}\right) \tag{3.2}$$

$$= \rho L^2 {U_0}^2$$

And the gravitational force is expressed as:

$$F_{gravitational} = mass\ x\ acceler._{gravitational} = (\rho V)(g) = \rho L^3 g \tag{3.3}$$

Consequently, the Froude scaling criterion can be reduced to:

$$Fr = \sqrt{\frac{\rho L^2 {U_0}^2}{\rho L^3 g}} = \sqrt{\frac{{U_0}^2}{Lg}} = \frac{U_0}{\sqrt{Lg}} \tag{3.4}$$

The relation between the length (L) of the model, (subindex $_{,m}$) and the prototype, (subindex $_{,p}$) is related to the scaling factor (λ), defined as:

(3.5) $$\lambda = \frac{L_p}{L_m};$$

For a Froude scale, the basic variables involved in flow motion are related to the scaling factor, as follows:

(3.6) $$Fr_p = Fr_m; \quad v_p = v_m\sqrt{\lambda}; \quad Q_p = Q_m\lambda^{5/2}$$

The model simulated the hydraulic conditions found on a real stream according to data provided by the DFO. By considering the discharge at the prototype and the flow range provided by the pump at the tilted flume in the laboratory facilities, the appropriate reduction factor was selected. Furthermore, the aforementioned (limited) physical width of the laboratory facility required consideration of additional scaling criteria to satisfy the "distorted geometry" aspect of the resulting physical model (Chanson, 1999); (Khatsuria, 2005). The reduction factors, (subindex $_{,r}$) selected for designing the distorted-scale model are presented below:

(3.7) $$X_r = 6; \quad Y_r = 6; \quad Z_r = 12$$

In summary, in this hydraulic problem involving weir overflow, the forces associated with surface tension and elastic compression are small in comparison with the gravitational forces which dominate the flow regime in the model. Therefore, a distorted Froude scaling law is used in the experimental investigation to simulate the flow characteristics and also reduce the effects derived from using a narrow flume.

3.2 Experimental program

The experimental program was designed to evaluate (i) the factors governing the formation of the submerged vortex feature (surface roller), and (ii) the hydrodynamic characteristics of the submerged vortex. The investigation focussed primarily on qualitative assessment of the effects of crest length and downstream apron elevation on the characteristics of the submerged vortex. The experimental program proceeded in two stages.

3.2.1 Stage 1: Occurrence of submerged hydraulic jump

For the initial investigation, the tailwater range associated with the formation of a submerged hydraulic jump was analyzed. Variable downstream water levels (Y_t) were used to identify the transitions between different forms of hydraulic-jump (i.e. 'free' jump, 'submerged' jump and 'undular' jump) associated with different (Y_t).

To establish the lower ('fully-developed' jump) boundary condition in the testing program, first the water surface elevation in the downstream ('tailwater') channel was slowly raised until a selected 'free flow' discharge condition over the weir produced a fully-developed jump immediately downstream of the structure. Next, the water surface elevation in the downstream channel was incrementally increased until this 'fully-developed' jump condition suddenly changed to a 'submerged jump' condition. The tailwater depth, which triggered this sudden change in the jump's form (i.e. from 'fully developed' to 'submerged'), became the 'lower boundary' tailwater depth condition (Y_l) in the testing program. Clearly, for the selected flow condition, a submerged jump will not form in the downstream channel when the tailwater depth is set below Y_l. To establish the upper boundary condition for this particular series of tests, the water depth in the tailwater channel was slowly increased above Y_l until the 'single-roller' submerged jump condition suddenly changed to one where a series of smooth surface waves replaced the (single) submerged roller. The value of the tailwater channel depth, where this sudden transition occurred, was identified as Y_{u+}. Thus, for the given flow condition, tailwater depths above Y_{u+}will produce a series of smooth surface waves, rather than a single submerged roller (vortex). A third flow- transition boundary condition was also identified for this flow by slowly decreasing the tailwater channel depth from any value above Y_{u+}. For the 'decreasing tailwater depth' scenario, the depth where the aforementioned series of smooth surface waves suddenly switches back to a single submerged roller is identified as Y_{u-}. For all flow conditions considered, Y_{u+} is always greater that Y_{u-}. The different boundary thresholds described above are shown in Figure 3-3.

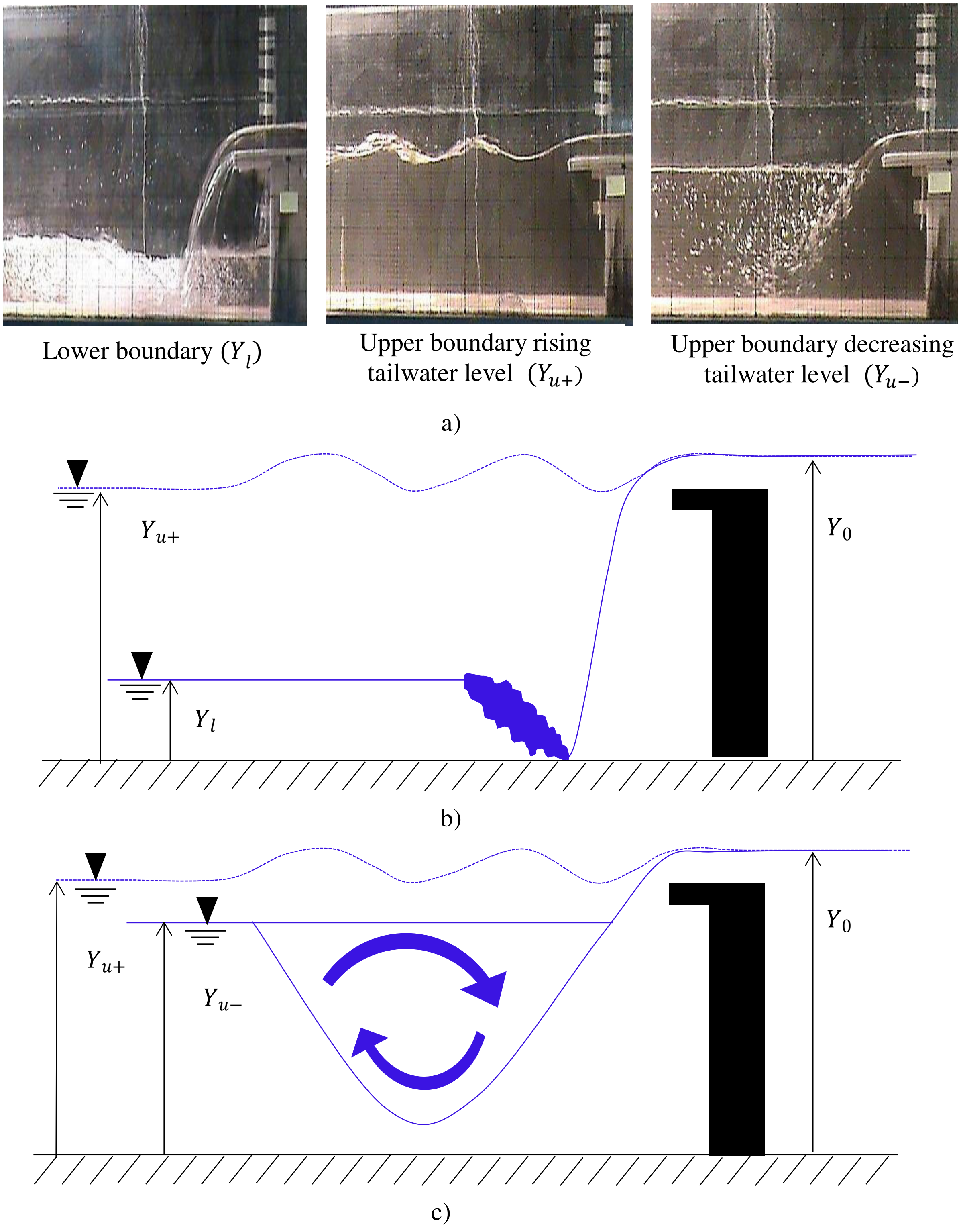

Figure 3-3: The boundary conditions established for the testing program: (a) photos of the Y_l, Y_{u+} and Y_{u-} conditions; (b) sketch of the boundaries identified for increasing tailwater levels, and (c) sketch of the boundaries for decreasing tailwater levels.

A total of 333 experimental runs were performed within the frame of this experimental stage, of which 111 samples of data corresponded to each transition (Y_l, Y_{u+}, Y_{u-}), respectively. An overview of the experimental conditions tested in the model is shown in Table 3-1. Four different test series corresponding to various downstream channel elevations were considered. Furthermore, six to ten subseries associated with modifications of the crest length were conducted for each floor elevation. Lastly, different flow rates were further investigated for every test combination. The scenarios performed for this study are summarized in Table 3-1.

Table 3-1: Test program: Vortex Occurrence

Floor elevation (cm)	Crest length (cm)	Flow rate - Model (l/s)	Variables objective
0	6, 8, 12, 16, 20, 24, 30 35, 45, 55	10, 20, 30, 40, 50	Y_l, Y_{u+}, Y_{u-}
+10.5	6, 8, 12, 16, 20, 24, 30 35, 45, 55	10, 30, 50	Y_l, Y_{u+}, Y_{u-}
+15.5	6, 12, 24, 35, 45, 55	10, 30, 50	Y_l, Y_{u+}, Y_{u-}
+5.5	6, 12, 24, 35, 45, 55	10, 30, 50	Y_l, Y_{u+}, Y_{u-}

The objective of this stage focused on identification of the submerged hydraulic jump tailwater limits for positive and negative increments of the downstream water level (i.e. identification of Y_l, Y_{u+}, Y_{u-} for each condition). Additionally, control sections located upstream and downstream were used to measure the local velocity and the water depth for each experimental run at these control sections. The results of the experimental stage are presented in Chapter 5. The physical processes involved on the submerged hydraulic jump phenomenon and its connection with the variables flow rate, crest length and downstream elevation were further investigated by means of the experimental data collected in this stage.

3.2.2 Stage 2: Characteristics of the submerged hydraulic jump

A secondary experimental test program was undertaken to evaluate the vortex characteristics of submerged-type jumps. The characteristics of the vortex flow were investigated for different levels of submergence (experimental series corresponding to

Test 1-a in Table 3-2). Preliminary results indicated that mild degrees of submergence caused a larger energy loss, which is in agreement with the results obtained by other researchers (Rajaratnam, 1967) (Leutheusser & Fan, 2001). For the remaining experimental series, the level of submergence was fixed at a mild level (submergence in the range 20% - 50%). Details of the experimental conditions tested in this stage are shown in Table 3-2.

Table 3-2: Test program - Vortex Characteristics

Test #	Floor elevation (cm)	Crest length (cm)	Flow rate (l/s)	Degree of submergence
1-a	0	6, 35, 45, 55	10	Mild, medium, high, submerged
1-b			30, 50	Mild, Submerged
2	+10.5	6, 55	10, 30, 50	Mild
3	+15.5	6, 55	10, 30, 50	Mild
4	+5.5	6, 55	10, 30, 50	Mild

Once the input conditions were established and the submerged vortex was deemed to be stable, detailed measurements of various parameters were taken to assist in the ‘analysis’ exercise that followed. A total of 50 runs were performed within the frame of this second experimental stage. A graduated grid, which extended over the zone occupied by the vortex-type flow, was inserted on the flume’s glass wall and was used to determine flow velocities at the nodes of the grid. There were two challenging aspects in setting this data-acquisition framework up: (1) the submerged vortex extension varied with the input conditions; and (2) the downstream limit of the vortex flow feature could not be easily (visually) identified. Therefore, post- processing of the experimental data was necessary in order to determine the ‘boil’ point of the submerged hydraulic jump. The boil point (or ‘neutral’) point is defined as the point where the overtopping water jet splits and either continues moving downstream, or is recirculated in an upstream direction as part of the counter-current flow (see Figure 3-4).

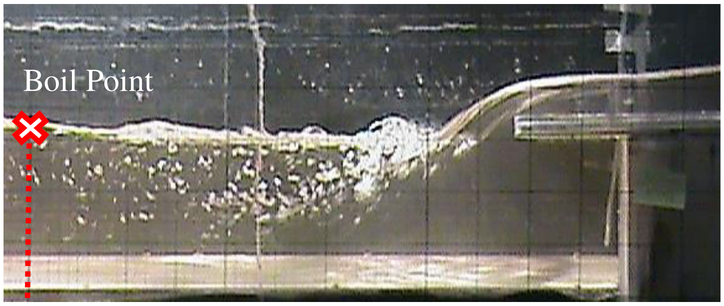

Figure 3-4: Boil (or ‘neutral’) point identified at the submerged hydraulic jump.

The location of the jump’s neutral point is one of the key parameters in regards to evaluating the performance of different crest profiles, (in connection with reducing hazardous vortex conditions, as well as reducing the velocity of the jet current).

The establishment of fixed vertical control sections, spaced at 0.2-m intervals and covering the entire vortex domain, facilitated the detailed analysis of the vortex hydrodynamics. In those cases when a broad-crested weir was used, the downstream channel floor elevation setting was at its lowest (i.e. zero), and the flow rates were large, the number of control sections ranged from 2 to 12.The vertical spacing of the control points was obtained by dividing the local water depth at the control section into equal segments. Velocity data were collected at three different depths ($Y_i/3,\ 2Y_i/3,\ Y_i$), where Y_i refers to the local water elevation at the vertical control section (i). An illustration of the arrangement is shown in Figure 3-5.

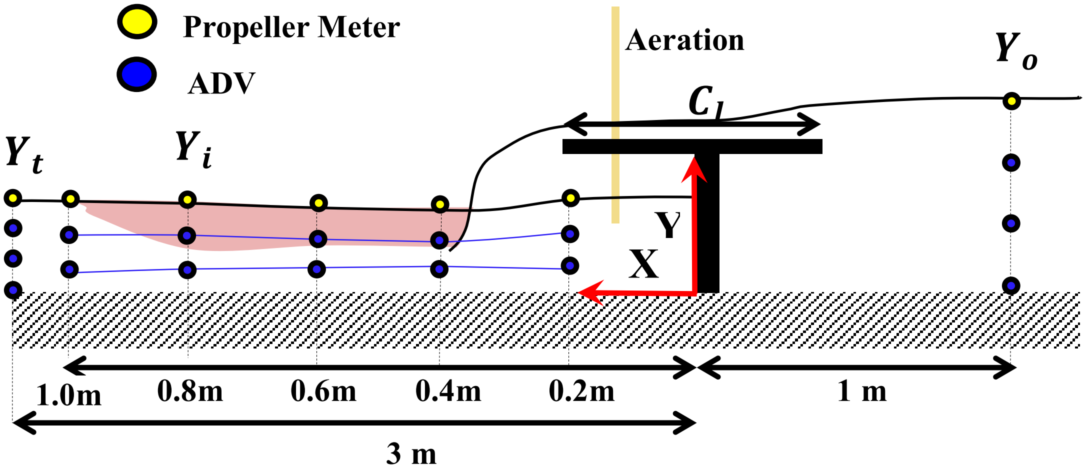

Figure 3-5: Diagram showing data acquisition points in the test. The coloured points (i.e. yellow or blue) indicate the device used (Propeller Meter or ‘ADV’)

3.2.3 Limitations derived from the experimental setup

The instrumentation used in the acquisition of experimental data suffered from the following limitations: The performance of the down-looker ADV was poor in areas of the flow field where air entrainment volumes were large. Consequently, in areas where the ADV did not ensure correlation of measurements above 60% (including points along the air/water interface), a Propeller Meter was used instead. Furthermore, in order to better define the velocity profiles, supplementary velocity measurements were collected along the vertical axis whenever possible. In those areas where both the ADV and Propeller Meter measured data were deemed to be unreliable, other flow-simulation techniques were employed to assist in analysing the flow field. A description of specific issues encountered during the simulations, and their resolution, are described below:

***Flow Visualization**:* A clear visualization of the complex flow patterns in these highly-turbulent flow fields was not possible. The mixing process was very fast and a clear identification of the extent of the flow field affected by the vortex was not possible. Potassium permanganate dye was added to the upstream flow, in an attempt to highlight the main recirculation pattern downstream of the structure. However, the level of turbulence downstream of the model weir was such that the entire water body was quickly coloured and no distinct vortex-type pattern could be observed

Aeration of the nappe: For a sharp-crested weir design and for free-discharge weir operation, initial experimental runs showed an insufficient aeration of the flow below the overflow nappe, in comparison to the prototype. This is a common situation observed in certain types of overflow weirs and spillways (Chanson, 1993). The lack of aeration caused a reduction of the pressure below the nappe. For low discharge conditions and sharp- or short-crest lengths, a hysteric cyclic response of the falling nappe was observed. For a given discharge, the pressure built up within an air volume confined below the falling nappe, which was incrementally compressed by a thickening nappe. The trapped air bubble was ultimately released once the air pressure became very high (and consequently, the air volume very small), and during the air escape, a new air bubble was captured. This problem was corrected by artificially forcing aeration of the nappe. This was achieved by inserting a perforated plastic pipe, which was opened to the atmosphere and connected to the negative pressure region formed below the falling nappe.

Accuracy of the water flow supply: The inflow pump was set at the target flow rate by means of an electronic-type digital controller. Before testing began, it was observed that, for a set discharge, the submerged hydraulic jump was somewhat unstable, re: its position in the flume. This unsteadiness was thought to be partly due to the feature's inherent instability and possibly also due to fluctuations in the inlet flow rate. The possible causes responsible for this unsteady behaviour are:

- Inability of the pump to introduce a constant discharge rate
- Inaccuracy of the digital flow meter
- Reactive flow adjustment: The pump's auto-regulated valve reacted to the measurements collected by the digital flow meter, a posteriori.

In order to minimize this inaccuracy of the water supply, two alternatives were considered. (1) Introduce an upstream 'head' tank that is able to provide a constant flow rate for each condition. (2) Run the tests with the already installed devices and account for the inaccuracy of the flow. The first alternative was not compatible with the interior reservoir already built inside the flume and major modifications were required (i.e. a solution outside of the time frame and budget of the project). The second alternative was selected, and the digital flow measurements were compared against data collected at the V-Notch installed in the outlet tank. It was observed that the average flow was accurately measured, but not the instantaneous discharge. Since all the measurements are time-averaged, the average flow data was taken as representative of the condition evaluated.

3.3 Nominal range of input variables

3.3.1 Discharge over the structure

The water discharge values selected in the experimental work covered the full range of river flow discharge observed in the main Great Lakes tributaries, where the sea lamprey barriers are installed. The extrapolation of the conclusions found in this study to other hydraulic barriers installed in the region is a key point of the current research project. In order to select an appropriate flow range for the laboratory tests, the maximum capacity of the pump, which supplies flow to the study flume, was considered. This pump produced a maximum flow of 100 l/s in our flume, which had a rectangular cross-section, area $A = 0.28875m^2$ $(0.75m\ x0.385\ m)$. Therefore, the maximum possible unit-width flow rate generated by the pump was $q = 0.26m^2/s$. This maximum flow rate was used to downscale a generic barrier.

For the current experimental research, the flow rate ranged between 10 and 50 l/s. These values were equivalent to unitary flow rates in the range $0.026 - 0.130\ m^2/s$ in the flume. For the distorted Froude scale $(\lambda_x = \lambda_y = 6; \lambda_z = 12)$, this flow rate range is equivalent to a unitary flow of 0.147 and 0.735 m^2/s at the barrier.

3.3.2 Non-dimensional crest length

Several crest lengths C_L were tested for the above-mentioned flow rates to evaluate its impact on the formation and characteristics of the submerged hydraulic jump. According to Hager and Schwalt, broad-crested weirs are less susceptible than sharp-crested ones, regarding the development of submerged flows, and consequently they are less sensitive to variations of the tailwater depth (Hager & Schwalt, 1994).

The crest classification is a function of the discharge over the crest and the longitudinal length of the weir's crest. The maximum and minimum crest lengths selected for the experimental investigation were determined by considering the maximum and minimum flow rate over the structure. Horton was the first to conduct exhaustive studies on the subject of flow over weirs (Horton, 1907). The non-dimensional relative weir length parameter (ζ_w) was defined as the ratio of the approach flow energy head (H_0), to the crest length, (Govinda Rao & Muralidhar, 1963), expressed as:

$$(3.8) \qquad \zeta_w = \frac{H_0}{C_l}$$

The definition of these variables is illustrated in Figure 3-6 below:

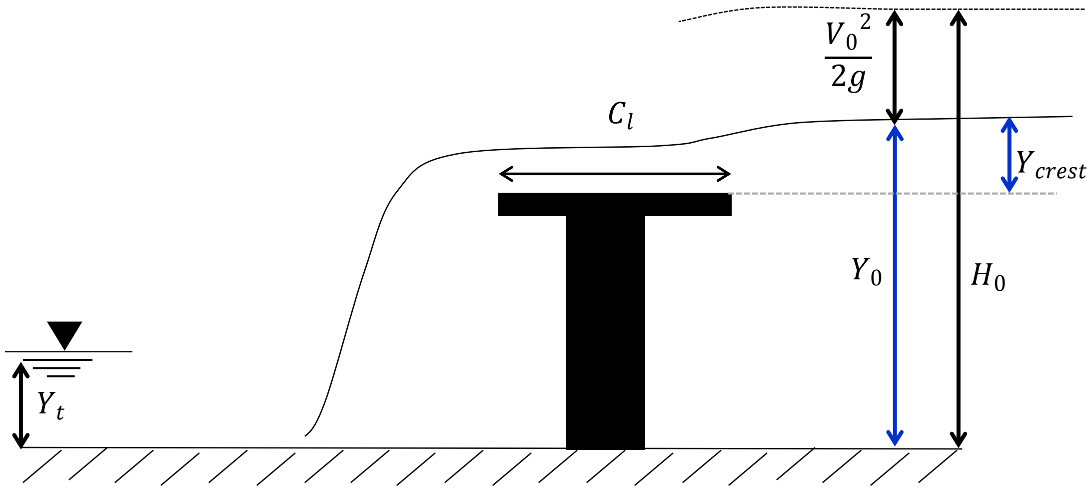

Figure 3-6: Variables involved in relative crest length (ζ_w) variable, based on the definition proposed by Govinda Rao & Muralidhar (1963).

The non-dimensional relative weir length (ζ_w), serves to classify the flow over the weir (Govinda Rao & Muralidhar, 1963):

- $0 < \zeta_w \leq 0.1$, for long crested weirs
- $0.1 < \zeta_w \leq 0.4$, for broad-crested weir
- $0.4 < \zeta_w \leq 1.5$, for short-crested weir
- $1.5 < \zeta_w$, for sharp-crested weir

This weir flow classification was applied to design the crest lengths used in the experiments, (see Table 3-3). The experimental observations confirmed the weir flow classification identified in the literature, and allowed the necessary modification of the original model in order to test the sharp- (installed on site) and broad- (proposed) crested weirs. In our experiments, broad-crested weirs were tested to evaluate the effect of crest length on the submerged hydraulic jump formation and on the dynamic characteristics of the roller.

Table 3-3: Weir flow classification according to the relative crest length, ζ_w (Govinda Rao & Muralidhar, 1963).

Q C_L	10 (l/s)	20 (l/s)	30 (l/s)	40 (l/s)	50 (l/s)
6 (cm)	Short	Sharp	Sharp	Sharp	Sharp
8 (cm)	Short	Short	Sharp	Sharp	Sharp
12 (cm)	Short	Short	Short	Short	Sharp
16 (cm)	Short	Short	Short	Short	Short
20 (cm)	Broad	Short	Short	Short	Short
24 (cm)	Broad	Short	Short	Short	Short
30 (cm)	Broad	Broad	Short	Short	Short
35 (cm)	Broad	Broad	Short	Short	Short
45 (cm)	Broad	Broad	Broad	Broad	Short
55 (cm)	Broad	Broad	Broad	Broad	Broad

3.3.3 Downstream channel elevation

Various ancillary structural devices have been employed to enhance the energy dissipation achieved by the hydraulic jump (e.g. chute blocks, baffle piers, etc.). Because the purpose of the sea lamprey barrier is to prevent the migration of invasive species upstream, the maximum downstream bed elevation is constrained and a minimum vertical drop between the downstream water level and the weir crest elevation must be provided during migration season (Millar & Ross, 2000) (Hunn & Youngs, 1980). Consequently, the particular case of sea lamprey barriers is still an ongoing area of investigation in the field of designs able to minimize the submerged hydraulic jump without compromising its function.

Protective structures, such as stilling basins or aprons, are sometimes built downstream from spillways to protect the channel bed from excessive erosion and scour created by the formation of a hydraulic jump. Since the nature of these protective structures can be reactive (built a posteriori, after the occurrence of erosive processes and scour at the structure's bed), the inclusion of these elements is not always considered in the initial design. Therefore, the effect of raising the bed level downstream of the weir structure was considered in the current study.

3.4 Measurements

3.4.1 Stage 1: Submerged roller formation

The variables controlled during the experimental investigations were:

- Flow rate or discharge (Q)
- Crest length(L_c)
- Downstream apron elevation (z_{floor}):

Measurements taken during each test focused on the collection of:

- Tailwater level (Y_t): This variable was collected at three transitional states; (1) the lower water level at which a submerged hydraulic jump formed (Y_l), (i.e. representing the transition from free to submerged hydraulic jump), (2) for increasing tailwater levels, the maximum water level associated with the continuing formation of a submerged hydraulic jump (Y_{u+}), and (3) for decreasing tailwater levels, the maximum water level able to trigger the generation of a submerged hydraulic jump from a series of smooth surface waves (Y_{u-}).
- Downstream velocity (V_t): At the downstream control section $(x = +3.0m)$ and measured at three different elevations
- Upstream water level (Y_0)
- Upstream velocity (V_0): At the upstream control section $(x = -1.0m)$ and measured at three different elevations
- Local velocity (V_i): Measured at several sections, covering the entire domain affected by the roller.
- Digital imagery of each condition

3.4.2 Stage 2: Submerged roller characteristics

The parameters controlled during these investigations included those for Stage 1, plus the following:

- Tailwater level(Y_t): By controlling this variable, the degree of submergence was imposed for each experimental scenario.

The measured variables within the frame of the second stage of the experimental investigation included those for Stage 1, plus the following:

- Longitudinal profile of the water free surface (Y_i):, collected along the middle axis on the flume, in a time-average form. This longitudinal profile extends from the upstream to the downstream (including the crest), covering the entire extension affected by the vortex. Control sections spaced $0.2\ m$ served as the fixed locations where the measurements were performed

- Velocity measurements on submerged roller. Several depths served as a reference for the data collection at each control section ($X_i = 0.2\ m$). At least three depths were considered at each control section for the velocity collection. In particular, two variables were carefully taken for all locations: (1) longitudinal bottom velocity (U_{bed}) and (2) longitudinal free surface velocity ($U_{surface}$).

- Length of the vortex (L_v): Visual observation of the downstream abscissa corresponding to the maximum longitudinal extension of the vortex.

- Impingement point: Visual observation of the downstream abscissa corresponding to the location where the impinging free falling nappe meets the downstream water level.

3.5 Instrumentation

Water discharge was measured using an in-line electronic flow meter and validated with the aid of a sharp-crested V-notch located in the discharge tank of the flume. Time-averaged discharge measurements were found to have an accuracy ranging between ± 2-5% (lower accuracy readings -5%- by the propeller meter occurred at high discharge conditions). The tailwater depth was controlled by an adjustable-height gate located at the end of the flume and was measured using a point gauge mounted over the edge of the flume. Within the test section, depth was measured using a rail-mounted point gage which had an accuracy of ±0.1 mm. Velocities within the vortex flow field were measured using an Acoustic Doppler Velocimeter (ADV) and an Propeller Meter. Two sets of tests were performed using the same experimental setup: (1) investigation of the condition of submerged hydraulic jump, and (2) examination of the submerged hydraulic jump characteristics. A description of the devices used to measure each variable is provided below:

- **Water depth**

A series of fixed control sections were considered $(X_i = 0.2\,m)$. At each section, the depth of the water was measured by means of a point gauge. A grid of 1cm x1cm resolution printed over an acetate sheet was installed on the glass-wall of the sided flume to help with the depth measurements and with the location of the control sections.

Additionally digital images of each condition were recorded. This digital material was geo-referenced and transformed by use of Geographical Information System techniques (GIS) and superimposed with the water profile sketched from the data measurement. As a result, the water profile for each test became graphically fully defined and validated by the digital information.

- **Velocity**

Velocities were collected by using two different devices: an ADV and a Propeller Meter. The usage of two devices is derived from the limitations of each one for collection of the target variable in the given environment. An initial pretest was undertaken to evaluate the performance of each device for measurement of the velocity in the different sections and elevations within the vortex. Initially, both devices were used to measure velocity under stable conditions, and both devices recorded the same values. However, under highly turbulent conditions, the ADV did not perform well because of the air entrainment and the turbulent and unstable nature of the flow. For the propeller meter, the measurements provided insight into the time-averaged velocity component along the flow direction (longitudinal component). However the device was not able to provide additional information associated with other velocity components or turbulence levels.

Nortek Vectrino ADV - Down Looker: This Acoustic Doppler Velocimeter is able to automatically collect a large amount of data at each control point. The data include the velocities (in all directions) and turbulence for a time series. The ADV used in the data collection is shown in Figure 3-7-a). The ADV configuration was set at a sampling rate of 200Hz, a nominal velocity range of +/-0.3 m/s, 1.8 mm transmit length and a sampling volume of 7.0 mm.

The ADV requires all the receptor beams and sensor to be 5 cm submerged in water. The measurements are estimated for a volume a certain distance from the sensor, depending on the settings (frequency of the signal or the acoustic wave length and volume sampled).

Due to the above limitation, the instrument did not measure the countercurrent velocity of the vortex along the free surface. This is a key variable for assessment of the characteristics of the vortex and the drowning hazard derived from its formation. Additionally, the correlation of the measurements along the time series was proved to be low in turbulence zones because of the large amount of air entrained (above 30%). At locations where high levels of air bubbles were present, some of the settings of the ADV were modified in order to achieve a larger correlation.

Propeller Meter: This device measures the time-averaged flow velocity by noting the number of rotations per second of a propeller located at the nose of the device. Two different propellers were used, depending on the location of the device (the nominal ranges of the velocities for each propeller were different). This instrument used in the experimental tests is shown in Figure 3-7 b).

This device belongs to the class of ‘rotor’ current meters. The moving flow exerts a pressure on the blades of the propeller and the number of revolutions is counted by an electronic device. A calibration formula is given, which allows the user to convert the number of revolutions of the propeller into a velocity measurement.

Due to the nature of the device, the data are averaged over the period during which the data is collected (vs. time series provided by the ADV). Additionally, it was observed that, in certain locations, the current would momentarily change its direction (standing water zones). As the revolutions are added by this device (independent–of the direction in which they are occurring), the flow velocity was overestimated in these zones of the flow field. Visual observation of the behaviour of the currents in these same areas permitted identification of ‘neutral’ points, characterized by an average net velocity of zero.

Figure 3-7: Instrumentation. a) Down looker Acoustic Doppler Velocimeter (ADV) installed over a metallic frame on the flume. b) Propeller meter.

<u>Other instrumentation</u>

- Rail-mounted point gauge position at the centreline
- Piezometer at the discharge tank on the V-Notch
- Grid installed on the glass-walled flume

3.5.1 Reliability of the measurements

The reliability of our results depended highly on the quality of the data collected. The accuracy of the various measurements taken during this investigation depends on both the nature of the variable being measured as well as the device selected for that particular measurement. The experimental setup was designed such that the relative error is minimized and consequently, the reliability of our predicted scenarios is maximized. Table 3-4 lists the alternative procedures used in measuring the different study variables.

Table 3-4: Measured variables and the instrument/device associated with its collection

Variable	**Alternatives**	
Water Depth	Pointer gauge	Photography+ Grid
Velocity	Propeller Meter	ADV
Flow Rate	Flow meter	V-Notch
Spatial Variables	Meter line	Grid

This performance-related study was time-averaged and also space-dependent, (i.e. the performance of each device was analyzed at different locations in the domain). Table 3-5 shows the sensitivity of each device to the study variables.

Table 3-5: Sensitivity of each device to the discharge (Q), vertical location (Y), crest length (C_L), degree of submergence (S) and downstream location (X)

Variable	**Q-depend.**	**Y-depend.**	**C_L-depend.**	**S-depend.**	**X-depend.**
Pointer gauge	-	-	-	-	-
ADV	X	X	-	X	X
Propeller Meter	-	X	-	X	X
Photography	-	-	-	-	X
Flow Meter	X	-	-	-	-
Meter line	-	-	-	-	-
Grid	-	-	-	-	-
V-Notch	-	-	-	-	-

Variable non-dependent devices

For those devices whose performance was not dependent on any of the controlled variables (i.e. pointer gauge, V-Notch, meter line, grid), the accuracy of the measurement was related to the precision of the device. These factors are noted below:

- Pointer Gauge: Precision = +/- 1mm
- Meter line: The scale for the meter line was mm.
- Grid: This was manually drawn on an acetate sheet installed on the glass wall to facilitate the digital analysis of pictures and videos taken during the experimental runs. The size of the grid was 1cm x 1cm, and consequently the measurements derived from the digital analysis have a maximum resolution of 1 cm. This affects measurements of the vortex length and the water depth. The measurements were taken at the flume's wall.
- 90° V-Notch: For this device the empirical formula used was:

(3.9) $Q = 13.7H^{5/2}$

This formula relates the head of flow over the notch (H) (measured in cm) to the flow rate (measured in cm^3/s) by using a power relationship. Consequently, for the larger flow rates, the precision of the piezometer plays a more important role, highly influencing the accuracy of the flow measurement. For the largest flow considered in the test $(Q = 50l/s)$, an error of 1 mm in the measurement of the head (H) leads to a 0.47l/s absolute error in the flow rate. Consequently, the maximum relative error is 0.01% for this device.

Variable-dependent devices

The accuracy of each device depends on the variable measured, the specific experimental run, and the location of the control point. Each device is individually analyzed:

- Acoustic Doppler Velocimeter: The ADV did not perform well for measurements taken along the free surface and in locations having large amounts of air entrained (e.g. medium depths, close to the weir). The settings for the ADV were modified (frequency, sample volume) adapting them to values able to achieve larger correlations. For cases where correlation was smaller than 60%, the propeller Meter was used instead. According to the manufacturer, the device provides velocity measurements with a maximum error of 0.1mm/s, However, the data series was further ‘de-spiked’ and processed into an averaged velocity value. Consequently, the local average velocity value would accumulate a lower error than 0.1mm/s.

- Propeller Meter: This measurement device did not perform well at points located near the boiling point of the vortex (sections located at large abscissas). These locations were characterized by a nearly null-averaged longitudinal velocity and instantaneous flows, which were observed to change direction (moving either towards the downstream or towards the upstream, respectively). Moreover, according to the information provided by the manufacturer, the revolutions per second measured by the device had an accuracy of +/-1mm/s.

- Photography: Digital imagery was corrected by using the grid installed on the flume, which had a resolution of the order of 1.0cm.

- Automatic flow meter: Accuracy depended on the discharge handled by this unit. The discharge measurements were taken downstream of the unit and were then used to correct the valve opening installed upstream of the unit (automatic mode). The upstream depth and the velocity were recorded at three locations. It was found that the relative error of the flow meter ranged between 2.5% and 5%. The V-notch installed in the downstream discharge tank was used to verify these measurements. Consequently, the maximum absolute error associated with the flow meter measurements is 5% of the maximum flow rate ($Q = 50l/s$), leading to a maximum error of $Q = 2.5l/s$.

<u>Relative error of controlled variables</u>

In summary, the absolute error depends not only on the accuracy of the measuring devices and techniques, but also on the variables examined. The maximum absolute error and relative error for each device is summarized in Table 3-6.

Table 3-6: Maximum absolute and relative error associated with each measuring instrument/procedure used

Instrument	Variable Affected	Max Absolute Error	Variable (representative value)	Relative Error
Pointer gauge	Y-Depth	1 mm	20 cm	0.005%
ADV	V-velocity	0.0001 m/s	0.05 m/s	0.2%
Propeller Meter	V-velocity	0.001 m/s	0.05 m/s	0.2%
Photography	L-length	1cm	20 cm	0.007%
Flow Meter	Q-flow	2.5 l/s	Max 50 l/s	5%
V-Notch	Q-flow	0.47 l/s	Max 50 l/s	0.01%
Meter Line	Y-Depth	1cm	20 cm	0.05%
	L-length	1cm	80 cm	0.013%
Grid	Y-Depth	1cm	20 cm	0.05%
	L-length	1cm	80 cm	0.013%

Chapter 4. Description of Numerical Experiments

This chapter describes the numerical methodology and its implementation in the OpenFOAM toolbox to simulate the fluid dynamics of the weir overflow problem with an imposed tailwater depth. The numerical approach to the problem consists of two components: a model and a solution procedure (Rusche 2002). The model is represented by a set of mathematical equations which describe the physical processes involved in the fluid motion and its dynamics. The solution procedure establishes the methods to obtain an approximate solution for the mathematical model, including the spatial and temporal discretization of the equations which describe the problem. Both aspects of the numerical methodology are described in this section.

In addition, details associated to the numerical model setup, its calibration and its sensitivity to certain parameters is included in this chapter. A detailed analysis of the several computational domains tested to reproduce numerically the hydraulic conditions observed in the physical setup is presented. The purpose of this analysis was to optimize the design of the computational domain in order to minimize the computational cost associated to the execution of numerical runs and to provide with a flexible design enabling an easy implementation of changes on the crest length, downstream water level, and on the downstream apron elevation assessed in this study. The large amount of physical runs, involving changes in geometry, justified an extensive investigation on the selection of the best implementation of the computational domain in an environment of changing geometry.

The calibration of the model was ultimately achieved by selecting the values for mesh resolution, transport properties and turbulence related parameters, which better reproduced the physical observations. A detailed sensitivity analysis explored the impact of these code-related parameters on the numerical results.

4.1 Mathematical Model

4.1.1 Reynolds Transport Theorem

The mathematical model considers the RANS equations (Reynolds Averaged Navier-Stokes) which are applied to the two incompressible, immiscible, isothermal fluids which describe the problem (water and air in this study), using the conventional VOF (Volume of Fluid) free surface tracking approach (Rusche, 2002), combined with a RAS '$\mathrm{k}-\mathrm{\varepsilon psilon}$' turbulence closure. Therefore, the motion of a fluid is described by the Reynolds averaged Navier-Stokes equations, which represent the governing equations in this study. These equations arise from applying Newton's Second Law to the fluid under motion. The theorem which provides the mathematical context for the abovementioned formulation was proposed by Osborne Reynolds in 1903 and represents the basis for continuum mechanics.

The Reynolds Transport Theorem (RTT) theory corresponds to the first axiom in his paper published in 1903, in which this mathematician expresses that any change in the quantity of any entity within a control volume can only be achieved in one of the two possible ways (Reynolds 1903):

- By destruction or production of the property within the surface
- By the passage of the entity (or property) through the boundaries

This theorem which is applied to any intensive property (B) within a control volume (CV), it establishes that "the sum of the changes over time for the intensive property B inside a control volume is equal to the amount of property loss/gained through the boundaries of the control volume, plus the amount of property created/consumed by the sources or sinks, respectively, inside the control volume" (Reynolds 1903). The integral formulation for the theorem can be expressed as follows:

$$(4.1) \qquad \frac{d}{dt}\int_{CV} B dV = -\int_{\partial CV} B(\boldsymbol{u}\cdot\boldsymbol{n})\, dA - \int_{CV} S_B dV$$

Where $\boldsymbol{u}$ represents the velocity vector $\boldsymbol{u} = (u_x, u_y, u_z)$ and $\boldsymbol{n}$ represents the vector normal to the surface. The closed surface associated to the control volume in the fluid is referred as CV, and ∂CV represents the boundaries of the control volume. The term (S_B) accounts for the mass flow of the property (B) within the control volume. Some mathematical transformations are applied to the previous expression to convert it into a partial differential relation.

The first step implies the application of the Divergence Theorem, to transform the term associated to the boundaries of the control volume, to the control volume itself. Intuitively, a set of sources and sinks within a control volume would regulate the flow of fluid inside the control volume and consequently through the boundaries of the enclosed volume. Consequently, the vector field controlling the fluid flow throughout the boundaries $(\boldsymbol{u})$ can be expressed as the vector's field divergence $(\nabla \cdot \boldsymbol{u})$ which represents the effect of the sinks and sources. Consequently the first term on the right-hand-side (RHS) of equation (4.1) is rewritten as:

$$\int_{\partial CV} B(\boldsymbol{u} \cdot \boldsymbol{n})\, dA = \int_{CV} \nabla \cdot (B\boldsymbol{u})\, dV \tag{4.2}$$

As a result, this theorem relates the flux of a vector field though the boundary to the behavior of the vector field inside the enclosed volume. Another mathematical transformation is undertaken by applying the Leibniz integral rule to the term on the left-hand-side (LHS) on equation (4.1). This rule relates the derivative of the integral to the partial derivative, consequently:

$$\frac{d}{dt}\int_{CV} B dV = \int_{CV} \frac{\partial B}{\partial t} dV \tag{4.3}$$

Finally, the transport Theorem (RTT) is rewritten as follows:

$$\int_{CV} \frac{\partial B}{\partial t} dV = -\int_{CV} \nabla \cdot (B\boldsymbol{u}) dV - \int_{CV} S_B dV \tag{4.4}$$

Rearranging the terms, the expression yields:

$$\int_{CV} \left[\frac{\partial B}{\partial t} + \nabla \cdot (B\boldsymbol{u}) + S_B\right] dV = 0 \qquad (4.5)$$

Equation (4.5) represents the simplified integral form of the Reynolds Transport Theorem within a closed control volume. If this equation is valid for any volume, the RTT is finally rewritten on its differential form as follows:

$$\frac{\partial B}{\partial t} + \nabla \cdot (B\boldsymbol{u}) + S_B = 0 \qquad (4.6)$$

This is the most common expression of the RTT theorem and represents the transport equation for any entity of the moving fluid within the control volume. On its nature, this relation can be applied to any property that follows a conservation law, such as mass, linear momentum and energy. This expression establishes the start point to develop the mathematical equations which describe the motion of fluids.

4.1.2 Continuity equation

The continuity equation is achieved by imposing the RTT to the property mass, as an extensive entity dependent on the control volume $(m = \rho V)$. Its corresponding intensive entity, independent of the volume (V), results in the variable density (ρ), which is selected as the intensive property to be conserved by the Reynolds Transport Theorem as indicated:

$$B = \frac{\partial m}{\partial V} = \frac{\partial (\rho V)}{\partial V} = \rho \qquad (4.7)$$

The RTT is rewritten for mass conservation, applying the mass definition shown equation (4.7) to the generic expression of the RTT shown by equation (4.6):

$$\frac{\partial \rho}{\partial t} + \nabla \cdot (\rho \boldsymbol{u}) + Q = 0 \tag{4.8}$$

Where the term Q refers to the mass flux associated to sources and sinks. By expanding the divergence term, equation (4.8) is rewritten as:

$$\frac{\partial \rho}{\partial t} + \rho \nabla \cdot \boldsymbol{u} + \boldsymbol{u} \nabla \cdot \rho + Q = 0 \tag{4.9}$$

Some assumptions are taken into consideration at this stage. First, the flow is assumed incompressible and the fluid homogeneous (constant density). Under those circumstances, there are no changes of the density within the control volume $(\nabla \cdot \rho = 0)$ or with time $(\partial \rho / \partial t = 0)$. Second, it is assumed that there are no sources or sinks responsible for mass creation/consumption in the control volume $(Q = 0)$. Since the unique physical mechanism for mass additions is associated to chemical or nuclear reactions, this assumption is valid in this study. The final expression for mass conservation is:

$$\nabla \cdot \boldsymbol{u} = 0 \tag{4.10}$$

This mathematical expression represents the differential form of the mass conservation equation inside a volume of control for an incompressible flow.

4.1.3 Momentum conservation equations

The Navier-Stokes equations result from the application of the RTT to Newton's Second Law. In other words, this equation establishes the conservation of linear momentum $(m\boldsymbol{u})$ within the control volume. The intensive property associated to the momentum conservation results in:

$$B = \frac{\partial(linear\ momentum)}{\partial V} = \frac{\partial(\rho V \boldsymbol{u})}{\partial V} = \rho \boldsymbol{u} \tag{4.11}$$

If this definition is substituted in the generic equation (4.6) for the RTT, the conservation of momentum formulation results in:

$$(4.12)\quad \frac{\partial(\rho \boldsymbol{u})}{\partial t} + \nabla \cdot (\rho \boldsymbol{u}\boldsymbol{u}) + Q = 0$$

This expression features a dyad in the second term ($\boldsymbol{u}\boldsymbol{u}$). The previous formulation is expanded term by term as follows:

$$\text{First term in LHS}\quad \frac{\partial(\rho \boldsymbol{u})}{\partial t} = \rho\frac{\partial \boldsymbol{u}}{\partial t} + \boldsymbol{u}\frac{\partial \rho}{\partial t}$$

$$\text{Second term in LHS}\quad \nabla \cdot (\rho \boldsymbol{u}\boldsymbol{u}) = \boldsymbol{u}\boldsymbol{u}\nabla\rho + \rho\nabla \cdot (\boldsymbol{u}\boldsymbol{u}) = \boldsymbol{u}\boldsymbol{u}\nabla\rho + \rho[\boldsymbol{u} \cdot \nabla\boldsymbol{u} + \boldsymbol{u}\nabla \cdot (\boldsymbol{u})]$$

Including the definition for these two terms, equation (4.12) is expressed as:

$$(4.13)\quad \rho\frac{\partial \boldsymbol{u}}{\partial t} + \boldsymbol{u}\frac{\partial \rho}{\partial t} + \boldsymbol{u}\boldsymbol{u}\nabla\rho + \rho\boldsymbol{u} \cdot \nabla\boldsymbol{u} + \rho\boldsymbol{u}\nabla \cdot (\boldsymbol{u}) + Q = 0$$

Rearranging and grouping the terms including ρ and $\boldsymbol{u}$:

$$(4.14)\quad \rho\left[\frac{\partial \boldsymbol{u}}{\partial t} + \boldsymbol{u} \cdot \nabla\boldsymbol{u}\right] + \boldsymbol{u}\left[\frac{\partial \rho}{\partial t} + \boldsymbol{u}\nabla\rho + \rho\nabla \cdot (\boldsymbol{u})\right] + Q = 0$$

Assuming incompressible flow and homogeneous fluid ($\rho = cte$), the terms accounting for changes of the density with time $\partial\rho/\partial t$, or location $\nabla\rho$ would equal to zero. Additionally, conservation of mass ($\nabla \cdot \boldsymbol{u} = 0$) is assumed. The conservation of linear momentum reduces to the following expression:

$$(4.15)\quad \rho\left[\frac{\partial \boldsymbol{u}}{\partial t} + \boldsymbol{u} \cdot \nabla\boldsymbol{u}\right] + Q = 0$$

The term (Q) is associated to the linear momentum developed by sources or sinks within the control volume. This can be substituted by the term b, which represents the body forces associated to these elements per unit volume.

$$(4.16) \quad \rho\left[\frac{\partial \boldsymbol{u}}{\partial t} + \boldsymbol{u} \cdot \nabla \boldsymbol{u}\right] = b$$

The independent term associated to the body forces (b) resulting of the conservation of momentum is further assessed. This term is analyzed by using the Cauchy Momentum Equation, which implies the conservation of momentum from a non-relativistic standpoint in any continuum. The body forces term is decomposed into the divergence of the stress tensor of the fluid (σ) and other body forces acting on the fluid (f) which includes the gravity and other external forces. This decomposition is presented in tensorial notation as follows:

$$(4.17) \quad \mathrm{b} = \nabla \cdot \sigma + \mathrm{f}$$

The Cauchy stress tensor (σ) relates the components of the fluid stress in the three directions of the Cartesian plane. This tensor is further decomposed into the principal term which includes the pressure along each Cartesian direction (p), indicative of the axial stresses in the fluid, and a deviatoric stress tensor (T), which accounts for the shear stresses:

$$(4.18) \quad \sigma = -\mathrm{p} \cdot \mathrm{I} + \mathrm{T}$$

Where the identity matrix is represented by (I). In agreement with this definition of the Cauchy stress tensor, the hydrostatic pressure is accounted by the principal stress term. By applying the divergence to the Cauchy stress tensor, the body forces of the fluid can be defined as:

$$(4.19) \quad \mathrm{b} = -\nabla \mathrm{p} + \nabla \cdot \mathrm{T} + \mathrm{f}$$

Some assumptions, inherent to this particular case study, must be applied to the deviatoric stress tensor (T), which ultimately controls the viscous terms of the flow under motion. Assuming isotropy in the continuum (no change of the fluid properties along the space), the tensor satisfy the following condition:

$$T_{ij} \sim (\frac{\partial \mathrm{u}_x}{\partial \mathrm{y}} + \frac{\partial \mathrm{u}_y}{\partial \mathrm{x}} + \frac{\partial \mathrm{u}_z}{\partial \mathrm{z}} \delta_{ij})$$

Assuming Newtonian fluid (internal stress linearly related to the fluid strain), the deviatoric stress tensor (T) is expressed as a function of the viscosity of the fluid (μ), the bulk viscosity of the fluid (ς):

$$T_{ij} = \mu(\frac{\partial \mathrm{u}_x}{\partial \mathrm{y}} + \frac{\partial \mathrm{u}_y}{\partial \mathrm{x}} + \frac{\varsigma}{\mu}\frac{\partial \mathrm{u}_z}{\partial \mathrm{z}} \delta_{ij})$$

The bulk viscosity is defined, depending on the case, as:

$$\varsigma \approx -\frac{2}{3}\mathrm{\mu} \text{ or } 0$$

In cases associated to bulk viscosity $\varsigma = 0$, the deviatoric stress tensor is expressed as:

$$(4.20) \quad \mathrm{T} = \mathrm{\mu}(\nabla \boldsymbol{u} + (\nabla \boldsymbol{u})^T)$$

And the divergence for the deviatoric stress tensor is ultimately formulated as:

$$(4.21) \quad \nabla \cdot \mathrm{T} = \nabla \cdot [\mathrm{\mu}(\nabla \boldsymbol{u} + (\nabla \boldsymbol{u})^T)]$$

The hypothesis of incompressible fluid and homogenous material leads to considering that the fluid viscosity (μ) is a constant as well. Therefore, equation (4.21) is rewritten as:

$$(4.22) \quad \nabla \cdot \mathrm{T} = \nabla \mathrm{\mu} \nabla^2 \boldsymbol{u}$$

The resulting Navier-Stokes equations are expressed below in differential notation, for the assumption that the only external body force acting on the fluid is the gravity as:

$$(4.23) \qquad \rho\left[\frac{\partial \boldsymbol{u}}{\partial t} + \boldsymbol{u}\cdot\nabla\boldsymbol{u}\right] = -\nabla \mathrm{p} + \mu\nabla^2\boldsymbol{u} + \rho g$$

The left-hand side terms refer to the fluid motion by including respectively: the unsteady acceleration term $(\partial\boldsymbol{u}/\partial t)$ and the convective acceleration term $(\boldsymbol{u}\cdot\nabla\boldsymbol{u})$. On the right-hand-side, the first term accounts for the gradient of the normal pressure forces inside the fluid (∇p), the second term relates to the viscosity forces $(\mu\nabla^2\boldsymbol{u})$ and the third one is associated to other forces acting on the system, like gravity (ρg). This equation is expanded and expressed in Cartesian coordinates [x,y,z], where (u_x, u_y, u_z) represent the velocity components along each direction:

$$\rho\left(\frac{\partial u_x}{\partial t} + u_x\frac{\partial u_x}{\partial x} + u_y\frac{\partial u_x}{\partial y} + u_z\frac{\partial u_x}{\partial y}\right) = -\frac{\partial \mathrm{p}}{\partial x} + \mu\left(\frac{\partial^2 u_x}{\partial x^2} + \frac{\partial^2 u_x}{\partial y^2} + \frac{\partial^2 u_x}{\partial z^2}\right) + \rho g_x$$

$$\rho\left(\frac{\partial u_y}{\partial t} + u_x\frac{\partial u_y}{\partial x} + u_y\frac{\partial u_y}{\partial y} + u_z\frac{\partial u_y}{\partial y}\right) = -\frac{\partial \mathrm{p}}{\partial y} + \mu\left(\frac{\partial^2 u_y}{\partial x^2} + \frac{\partial^2 u_y}{\partial y^2} + \frac{\partial^2 u_y}{\partial z^2}\right) + \rho g_y$$

$$\rho\left(\frac{\partial u_z}{\partial t} + u_x\frac{\partial u_z}{\partial x} + u_y\frac{\partial u_z}{\partial y} + u_z\frac{\partial u_z}{\partial y}\right) = -\frac{\partial \mathrm{p}}{\partial z} + \mu\left(\frac{\partial^2 u_z}{\partial x^2} + \frac{\partial^2 u_z}{\partial y^2} + \frac{\partial^2 u_z}{\partial z^2}\right) + \rho g_z$$

This set of equations in combination with the continuity equation (4.10), are used to fully describe the fluid movement in the control volume for a given fluid.

4.1.4 Phase fraction equation

The two fluid formulation of the Volume of Fluid Method (VOF) is used as a free surface capturing technique, by applying the concept of the fractional volume of fluid to the cells defining the domain (Hirt and Nicols, 1981). This method combines the previously described Navier-Stokes equations with an additional equation obtained by applying the Reynolds Transport Theorem to the "phase fraction" or 'indicator' function (α). This methodology tracks the interface between two fluids at each time step, enabling a numerical simulation of multiphase problems. Therefore, this method defines the interface by means of a ‘volume tracking method’ instead of providing with a “sharp boundary” definition (Rusche 2002). Therefore, the interface is considered as a transition zone where a mixture of both phases –air and water- occurs. This theory is implemented in the OpenFOAM toolbox to conduct the numerical simulation.

Mathematically, this formulation is possible by introducing in the equation system a function which accounts for the fraction of volume; the indicator function (α) (Rusche 2002). This function is associated to each phase within the system becoming a part of the Langragian invariant (Hirt and Nicols, 1981). The indicator function describes the fractional amount of each fluid at each point, by giving values to α within the nominal range [0-1]. It is described as follows:

$$\text{Indicator Function } (\alpha) \begin{cases} \alpha = 0 & \text{For a point fully inside Fluid A} \\ 0 < \alpha < 1 & \text{For a point with Fluid A and Fluid B} \\ \alpha = 1 & \text{For a point fully inside Fluid B} \end{cases}$$

For the case under consideration, where the only two fluids considered are water and air, ‘fluid A’ is taken as air and ‘fluid B’ as water. The indicator function is rewritten as:

$$\text{Indicator Function } (\alpha) \begin{cases} \alpha = 0 & \text{For air} \\ 0 < \alpha < 1 & \text{For a point in the transition zone} \\ \alpha = 1 & \text{For water} \end{cases}$$

Mathematically, the transition zone corresponds to any cell where the indicator function obtains values different from 0 or 1. This occurs mainly in the free surface, where a sharper transition between the two fluids occurs. However, this same formulation enables the mathematical simulation of air entrainment. Consequently, other locations within the water domain different from the free surface are susceptible to the presence of air, corresponding to small bubbles or larger air packets. This indicator function is an essential part of the mechanism which describes the interaction between the phases water and air. Therefore, the transport equation for the indicator function is added to the mathematical scheme designed to describe the fluid dynamics of the system.

$$(4.24) \quad \frac{\partial \alpha}{\partial t} + \nabla \cdot (\boldsymbol{u}\alpha) = 0$$

As described by previous authors (Rusche, 2002) (Romangnoli, 2009), the basic fluid properties of the fluids are reformulated in the frame of this method, such that the proportion of air and water in the cell, for a given time, is taken into consideration when solving the flow motion. Therefore, the volumetric density (ρ) and dynamic viscosity (μ) are reformulated. The subindexes w and a refer respectively, to water and air.

$$(4.25) \quad \rho = \alpha * \rho_w + (1 - \alpha) * \rho_a$$

$$(4.26) \quad \mu = \alpha * \mu_w + (1 - \alpha) * \mu_a$$

Moreover, the indicator function has been reformulated by using a bounded compression to account for the compression of the free surface (Rusche, 2002). This new advanced approach is implemented into the mathematical scheme further considered in OpenFOAM. The bounded compression of the free surface relies on the incorporation of an artificial velocity compression term (u_r), which is added to the phase fraction function affecting only to points located near the interface. The objective of this term is to compress the interface towards a sharper one, achieving a larger definition of the interface. This relative velocity or 'compression velocity' is defined as:

$$(4.27) \quad \boldsymbol{u}_r = \boldsymbol{u}_w - \boldsymbol{u}_a$$

This velocity represents the relative velocity between the water and air fractions at cells where both fractions coexist. The main advantage of this method is to create a more defined boundary at the contact between the two fluids. The inclusion of this term minimizes the numerical diffusion created by the discretization of the convection term in the momentum equation. The redefined expression for the phase fraction equation is formulated as:

$$\frac{\partial \alpha}{\partial t} + \nabla \cdot (\boldsymbol{u}\alpha) + \nabla \cdot (\boldsymbol{u}_r \alpha (1 - \alpha)) = 0 \tag{4.28}$$

The factor $\alpha\ (1 - \alpha)$ in the equation above is not null only for $\alpha \neq 0\ or\ \alpha \neq 1$. Consequently, the compression velocity plays a role only in cells occupied by a combination of air and water, affecting only the cells near the surface and to locations where any form of air entrainment occurs. Finally, the velocity $(\boldsymbol{u})$ at each cell is redefined such that the term accounts for the velocity and phase fraction of each fluid within each cell.

$$\boldsymbol{u} = \alpha \boldsymbol{u}_w + (1 - \alpha)\boldsymbol{u}_a \tag{4.29}$$

This definition of velocity is considered in the mass and momentum conservation which describe the fluid motion (equations 4.10 and 4.23). As a result, a strong coupling between the classical VOF method and the two-fluid model is achieved.

4.1.5 Turbulence closure

The previous system requires some turbulence closure in order to describe a determined mathematical system. Since the governing Navier-Stokes equations are solved in an averaged form (RANS) by the numerical solver, and additional term corresponding to the Reynolds stresses is incorporated into the averaged equations. Hence a turbulence model suitable for this mathematical scheme must be added to the system. From all of the existent turbulence models, the RAS type (Reynolds-Average Simulation) is suitable for the abovementioned averaged governing equations. Additionally, the ‘DES’ (Detached Eddy Simulation) could be considered for its hybrid nature (using Large Eddy Simulation ‘LES’ near the walls and Reynolds-Average RAS in the rest of the domain).

The computational costs associated to filtering the governing equations to calculate the effect of the turbulence at sub-grid scales ‘LES’ is much higher than running the standard $\mathrm{k}-\varepsilon$ RANS model. In 2003, Cheng et al. compared both methods for predicting the flow over a matrix of cubes and found that while the overall predicted mean characteristics of flow were quite similar, ‘LES’ approach offered a better characterization of turbulence around the obstacle simulating the flow separation at sharp edges and recirculation vortices with higher accuracy (Cheng, et al. 2003). The main objective of this study is to qualitatively identify the hydraulic characteristics occurring downstream from low-head dams. Therefore, a detailed simulation of the turbulence around the wall does not represent the main focus of this study.

The RAS turbulence model is based on the concept of the “eddy viscosity” (ν_t) introduced by Joseph Boussinesq in 1887. He related the Reynolds stress to the mean characteristics of the flow, by using the eddy viscosity. A RAS approach was selected to minimize the computational cost while offering results as reliable as the ‘LES’ approach for the velocity and pressure at the points of interest. From all the RAS models encountered in literature and implemented on the OpenFOAM toolbox ($\mathrm{k}-\varepsilon\mathrm{psilon}$, $\mathrm{k}-\mathrm{Omega}$, $\mathrm{k}-\mathrm{OmegaSST}$, $RNG\ \mathrm{k}-\varepsilon$, etc.), the standard $\mathrm{k}-\varepsilon\mathrm{psilon}$ turbulence model was chosen. This model was selected based on its use in the OpenFOAM tutorial which considers a weir overflow problem. The similarity between these two problems served to make this decision.

The standard $\mathrm{k}-\varepsilon\mathrm{psilon}$ model incorporates two new variables, which are assumed to be transported by the flow. Consequently, the turbulence model achieves the closure of the flow motion problem by including the transport equations for these two variables: the turbulent kinetic energy (k), and the turbulent energy dissipation (ε). The sensitivity of the model to the turbulence closure is further discussed in this chapter. The transport equations for these two variables were first introduced in 1972 (Jones and Launder 1972), and are expressed as:

$$(4.30)\qquad \frac{\partial k}{\partial t}+\nabla\cdot(\boldsymbol{u}k)=\frac{1}{\rho}\nabla\cdot\left[\left(\frac{\mu_t}{\sigma_k}+\mu\right)\nabla k\right]+\frac{\mu_t}{2\rho}|\nabla\boldsymbol{u}+(\nabla\boldsymbol{u})^T|^2-\varepsilon$$

(4.31) $$\frac{\partial \varepsilon}{\partial t} + \nabla \cdot (\boldsymbol{u}\varepsilon) = \frac{1}{\rho} \nabla \cdot \left[\left(\frac{\mu_t}{\sigma_\varepsilon} + \mu \right) \nabla \varepsilon \right] + C_1 \frac{\varepsilon}{\kappa} \frac{\mu_t}{2\rho} |\nabla \boldsymbol{u} + (\nabla \boldsymbol{u})^T|^2 - C_2 \frac{\varepsilon^2}{\kappa}$$

Where the dynamic turbulent viscosity (μ_t) is defined as:

(4.32) $$\mu_t = \rho C_\mu \frac{\mathrm{k}^2}{\varepsilon}$$

The constants σ_k and σ_ε represent the diffusion rates for the variables k and ε, respectively and are derived from the concept of turbulent mixing length (Prandtl 1925). Additional empirical constants are C_1, C_2 and C_μ. For high Reynolds numbers, and based on experimental work on free turbulent flows, the values for these constants are defined as follows (Launder and Spalding 1974):

Table 4-1: Proposed values for the turbulent constants in the $\mathrm{k} - \varepsilon\mathrm{psilon}$ model (Launder and Spalding 1974)

C_1	C_2	C_μ	σ_k	σ_ε
1.44	1.92	0.09	1.0	1.3

These values for the constants are the ones included in OpenFOAM in the $\mathrm{k} - \varepsilon$ turbulence model by default. These constants are accessible though the source code and its modification can be easily implemented (kEpsilon.H)

4.1.6 Equations system

The mathematical scheme which represents the governing equations for the flow motion in this study includes the following equations:

$$(4.10) \qquad \nabla \cdot \boldsymbol{u} = 0$$

$$(4.24) \qquad \frac{\partial(\rho \boldsymbol{u})}{\partial t} + \nabla \cdot (\rho \boldsymbol{u}\boldsymbol{u}) - \mu \nabla^2 \boldsymbol{u} = -\nabla \mathrm{p} + \rho g$$

$$(4.28) \qquad \frac{\partial \alpha}{\partial t} + \nabla \cdot (\boldsymbol{u}\alpha) + \nabla \cdot (\boldsymbol{u}_{\mathrm{r}}\alpha(1-\alpha)) = 0$$

$$(4.30) \qquad \frac{\partial \mathrm{k}}{\partial t} + \nabla \cdot (\boldsymbol{u}\mathrm{k}) = \frac{1}{\rho}\nabla \cdot \left[\left(\frac{\mu_t}{\sigma_k} + \mu\right)\nabla \mathrm{k}\right] + \frac{\mu_t}{2\rho}|\nabla \boldsymbol{u} + (\nabla \boldsymbol{u})^T|^2 - \varepsilon$$

$$(4.31) \qquad \frac{\partial \varepsilon}{\partial t} + \nabla \cdot (\boldsymbol{u}\varepsilon) = \frac{1}{\rho}\nabla \cdot \left[\left(\frac{\mu_t}{\sigma_\varepsilon} + \mu\right)\nabla \varepsilon\right] + C_1\frac{\varepsilon}{\kappa}\frac{\mu_t}{2\rho}|\nabla \boldsymbol{u} + (\nabla \boldsymbol{u})^T|^2 - C_2\frac{\varepsilon^2}{\kappa}$$

4.2 Finite Volume Discretization

The establishment of a solution procedure to resolve the set of partial differential equations which comprise the governing equations for the problem relies on discretization techniques which are applied to: (i) the equations, (ii) the time, and (iii) the space. Therefore, the discretization techniques intend to obtain a solution which is formed by a set of values which satisfy the equations at specific locations and times.

The discretization of equations relies on mathematical techniques to transform the partial differential equations into a set of algebraic equations; the time discretization is achieved by setting a time step in which the equations are solved. Finally, the discretization of the space divides the domain into cells where the solution is seen, and establishes the boundary conditions within the computational domain. Space and time discretization are closely related by the Courant number. Moreover, the discretization parameters highly affect the convergence of the solution. Each element to be discretized (i.e. equations, time and space) and the techniques used, will be presented in this section.

4.2.1 Equation discretization

The discretization techniques, applied to the spatial and temporal dimensions, are part of the solution process to obtain the numerical solution to the mathematical set of equations which describe the physical phenomenon.

In the finite volume method, the standard form of the continuity, momentum and phase fraction are integrated over the control volume and time. These equations, as expressed in the previous section, are derived from the application of the Reynolds Transport Theorem to different properties. The generic form of the transport equation for a scalar property which is spatial and temporal dependent $[\phi = \phi(x,t)]$, adopts the following expression:

$$\underbrace{\frac{\partial \rho\phi}{\partial t}}_{\text{Temporal derivative}} + \underbrace{\nabla\cdot(\rho\boldsymbol{u}\phi)}_{\text{Convection term}} - \underbrace{\nabla\cdot\left(\rho\Gamma_\phi\nabla\phi\right)}_{\text{Diffusion term}} = \underbrace{S_\phi(\phi)}_{\text{Source term}} \tag{4.33}$$

Where the diffusivity of the property is represented by Γ_ϕ. The transport equation for the scalar property (ϕ) is integrated over the time and over the space, on a control volume around point (V_M), in which the point M represents its centroid. The integral formulation of the transport equation is expressed as:

$$\int_t^{t+\Delta t}\left[\frac{\partial}{\partial t}\int_{V_M}\rho\phi dV + \int_{V_M}\nabla\cdot(\rho\boldsymbol{u}\phi)dV - \int_{V_M}\nabla\cdot\left(\rho\Gamma_\phi\nabla\phi\right)dV\right]dt \tag{4.34}$$

$$= \int_t^{t+\Delta t}\left(\int_{V_M} S_\phi(\phi)\,dV\right)dt$$

The integral form of the transport equation represents the standpoint for the discretization technique. This is a second-order equation which requires a minimum second-order accuracy discretization. The discretization method adopted by the interFoam solver is second-order accurate in space and time, which intends to transform the differential equations into algebraic expressions. The accuracy of the discretization technique will depend on the spatial and temporal variation of the property $\phi(x,t)$

between two consecutive points and time steps. Assuming that the magnitude of the property is known at time t ($\phi_{,t}$) and at the point M (ϕ_M). The linear variation of the property in space and time is considered for a second-degree accurate discretization as follows:

$$\phi(x) = \phi_M + (x - x_M) \cdot (\nabla\phi)_M \tag{4.35}$$

$$\phi(t + \Delta t) = \phi_{,t} + \Delta t(\frac{\partial \phi}{\partial t})_{,t} \tag{4.36}$$

4.2.2 Spatial discretization

The total space is discretized into control volumes where the equations are evaluated and the solution is calculated. These control volumes coincide with the numerical cells in the computational domain. The flow characteristics are evaluated at the cell centers and related to the flux through the cell faces.

Therefore, the spatial discretization pursues (i) to transform the integral of the partial differential equations over the control volume into a set of linear equations (ii) to relate the integral over the control volume to the value of the property at the cell and the flux through its faces and (iii) to estimate the cell value at its neighbours from the known cell values and flux through the cell faces. Once the equation has been discretized in space, the semi-discretized form of the transport equation is expressed as follows:

$$\begin{aligned} &\int_t^{t+\Delta t} \left[\left(\frac{\partial \rho \phi}{\partial t} \right)_M V_M + \sum_f F\, \phi_f - \sum_f \left(\rho \Gamma_\phi \right)_f \mathrm{S} \cdot (\nabla \phi)_f \right] dt \\ &= \quad \int_t^{t+\Delta t} (\ S_u\, V_M + \ S_P\, V_M \phi_M)\, dt \end{aligned} \tag{4.37}$$

The numerical boundary conditions imposed to the domain are categorized into two main types: (i) Dirichlet and (ii) Von Neumann boundary conditions. The first type imposed a fixed value for the variable along the boundary. The second type establishes a gradient of the variable in the normal direction to the boundary. The physical boundaries are later discussed in the solution procedure section.

4.2.3 Temporal discretization

The temporal discretization for temporal derivatives and for time integrals is achieved by calculating the difference between the value of the properties, at the cell, in two consecutive time steps $(t, t+\Delta t)$ and dividing by the length of the time step:

$$\left(\frac{\partial \rho\phi}{\partial t}\right)_M = \frac{(\rho\phi)_M^{t+\Delta t} - (\rho\phi)_M^{t}}{\Delta t} \tag{4.38}$$

For time integrals, the temporal discretization is achieved by integration of the property and its evaluation at the times steps which represent the limits to the temporal integral:

$$\int_t^{t+\Delta t} \phi(t)\, dt = \frac{(\phi)^t + (\phi)^{t+\Delta t}}{2}\, \Delta t \tag{4.39}$$

Finally, the discretized expression in space and time (Marquez Damian, S.) of the generic transport equation is expressed as:

$$\begin{aligned} &\frac{(\rho\phi)_M^{t+\Delta t} - (\rho\phi)_M^{t}}{\Delta t} V_M + \frac{1}{2}\left(\sum_f F\,{\phi_f}^{t} + \sum_f F\,{\phi_f}^{t+\Delta t}\right) \\ &-\frac{1}{2}\left(\sum_f \left(\rho\Gamma_\phi\right)_f \mathrm{S}\cdot {(\nabla\phi)_f}^{t} + \sum_f \left(\rho\Gamma_\phi\right)_f \mathrm{S}\cdot {(\nabla\phi)_f}^{t+\Delta t}\right) \\ &= \; S_u\, V_M + \frac{1}{2}\left(\; S_P\, V_M {\phi_M}^{t} + \; S_P\, V_M {\phi_M}^{t+\Delta t}\right) \end{aligned} \tag{4.40}$$

4.3 Solution Procedure

The solution procedure of OpenFOAM toolbox requires the definition of three main elements: (i) the computational domain and boundary conditions (ii) the initial conditions and (iii) the specification of the governing equations, the discretization methods and the algorithms selected to solve them. In this section the implementation of each element in OpenFOAM is described.

4.3.1 Computational Domain

4.3.1.1 Geometry

The physical arrangements which were tested as part of the experimental investigation of this study are emulated in the computational investigation. All details related to the setup of physical model are described in depth in Chapter 3. A schematic plan view of the described arrangement is shown in Figure 4-1.

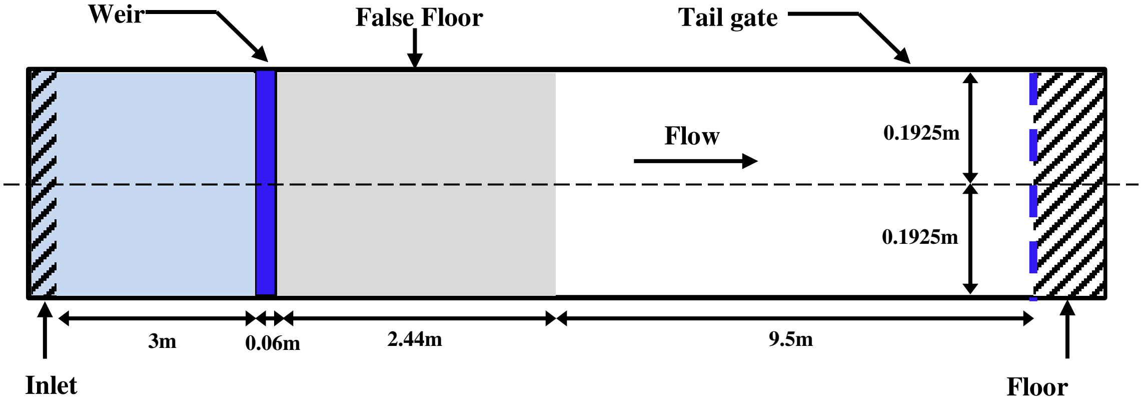

Figure 4-1: Plan view of the experimental setup

4.3.1.2 Optimal design of the Computational Domain

The computational domain was designed to emulate the hydraulic conditions occurring immediately downstream from the low-head dam and to reproduce the physical setup. Elements included in the physical configuration, such as the glass-walled flume, the upstream flow inlet and the downstream control gate, were considered for the design of the computational domain. Several design alternatives for the numerical testing were performed in order to: (i) optimize the design in terms of computational cost of the simulations, and (ii) easy implementation of geometry modifications within the computational domain (i.e. changing crest length and downstream apron elevation). The computation domain design thus followed an iterative process in order to meet these objectives. The computational domain was characterized by the following attributes:

a) Addition of a downstream collection tank: This tank allowed for a free fall of the water after overtopping the downstream gate. The outlet boundary conditions were applied to the furthest downstream vertical wall of the collection tank. As a result, these strong outlet conditions did not affect the characteristics of the flow within the region of interest.

b) Virtual 2-D analysis within a 3-D environment: The OpenFOAM computational environment provides 3D modelling. During the experimental stage, the physical measurements were collected along the middle plane of the horizontal flume. Therefore, the simulation of the flow characteristics along the channel's cross section is not of interest for the simulation. In order to simplify the numerical model into a 2-D calculation, the numerical domain considered a unique cell which covered the entire domain along the plane YZ, defined as the plane whose normal vector coincides with the streamwise direction X.

c) Domain definition by vertices/hexahedrons: In OpenFOAM the domain is designed by defining vertices and its connections, creating control volumes. The boundary conditions are applied to the faces of these volumes. The domain's initial design considered the definition of 11 control volumes (A to K), and 44 vertices, as seen in Figure 4-2. The fluid characteristics along cells faces which were shared by two control volumes were consistent between adjacent hexahedrons. Hence, continuity of the solution was achieved. Thus, it was noted that as the number of control volumes increased, the convergence along the boundaries was drastically reduced, seen in terms of higher limitations imposed to the flow between neighbor hexahedrons. Consequently, alternative methods to define the geometry, which enabled the definition of the domain by using fewer vertexes, were pursued further.

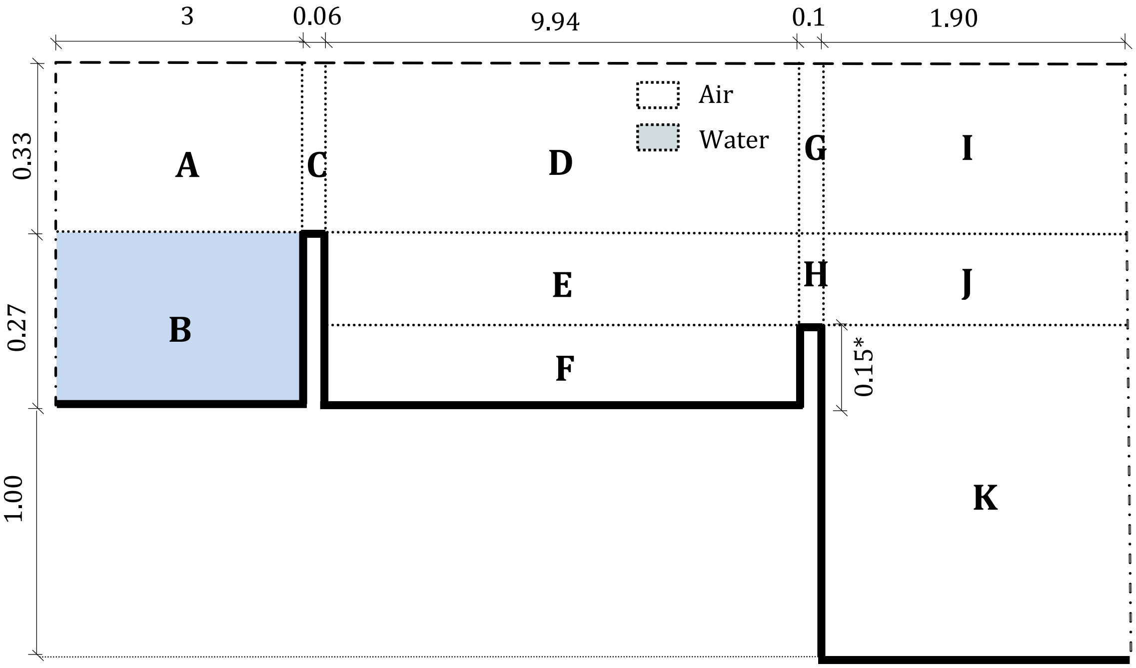

Figure 4-2: Numerical domain defined by using 44 vertices and 11 hexahedrons. Measurements in meters. Not to scale.

d) <u>Convergence achieved by simplification of the domain's definition</u>: Alternatives to the domain design were investigated in order to reduce the number of patches to be merged (shared faces along the volumes) and the number of vertices. This implementation was very beneficial especially for broad crest and elevated apron configurations, which required a larger amount of vertices (and hexahedrons) to define the computational domain. The alternative design relied on the definition of the domain as one unique hexahedron (8 vertices vs. 44 vertices) from which the obstacles were removed, by means of the tool *topoSet*. Afterwards, the new boundaries (associated to the exposed faces in the clipped volume), were assigned with the same boundaries as the walls. This new design improved the performance of the simulations, by reducing the computation time for the sharp crest case, or by achieving convergence in the case of broad-crested weir as a result of the relaxation of the constraints in the system. Figure 4-3 shows the resulting computational domain using this technique.

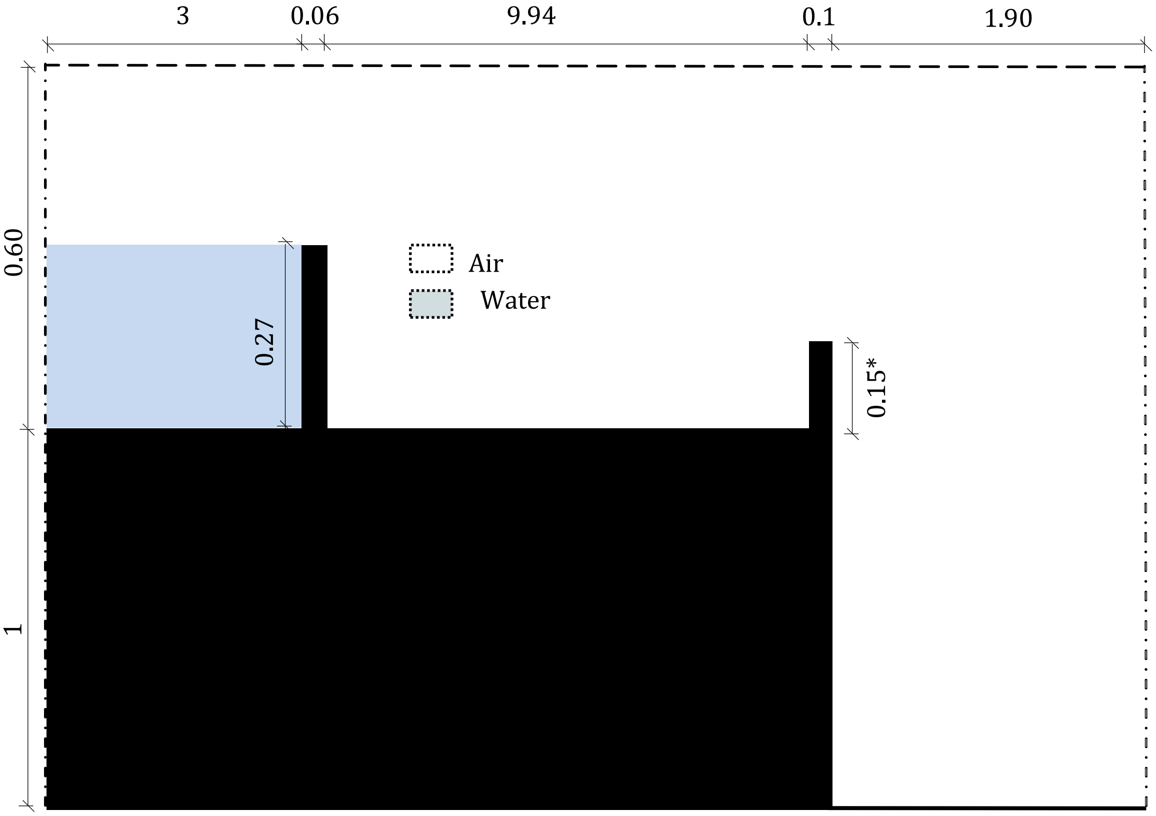

Figure 4-3: Numerical domain defined by removing the obstacles from the numerical domain. Measurements in meters. Not to scale.

4.3.1.3 Physical Boundary Conditions

There are four different types of boundary conditions, which are imposed at the domain physical borders, such that the model reproduces the observed conditions. These physical boundary conditions, represented by the atmosphere, inlet, outlet and wall, are associated to specific cell faces within the domain. The vertical side walls were defined as a default face patch, which is an empty type boundary condition. Therefore, the numerical model neglected the effect of the side walls. Moreover, each physical boundary condition was associated with specific numerical conditions imposed respectively, to the velocity $(\boldsymbol{u})$ and pressure $(\boldsymbol{p})$ fields. This association was easily implemented by the use of patches in the numerical model. The numerical boundary conditions related to each patch are summarized in Table 4-2.

Table 4-2: Relation between numerical and physical boundary conditions

Boundary Condition	**U**-condition	**P**-condition
Atmosphere	$\nabla u = 0$	$p = 0$
Inlet	$Variable\ with\ Q$	$\nabla p = 0$
Outlet	$\nabla u = 0$	$\nabla p = 0$
Wall	$u = 0$	$\nabla p = 0$

The resultant geometry described in the numerical model, as well as the physical location where the boundary conditions are imposed are summarized below in Figure 4-4. The shaded areas represent volumes which are removed from the domain, corresponding to walls or obstacles. It is bounded by the yellow line in Figure 4-4, which is the wall where the non-slip condition was implemented. The numerical domain visualized in ParaFOAM is seen in Figure 4-5.

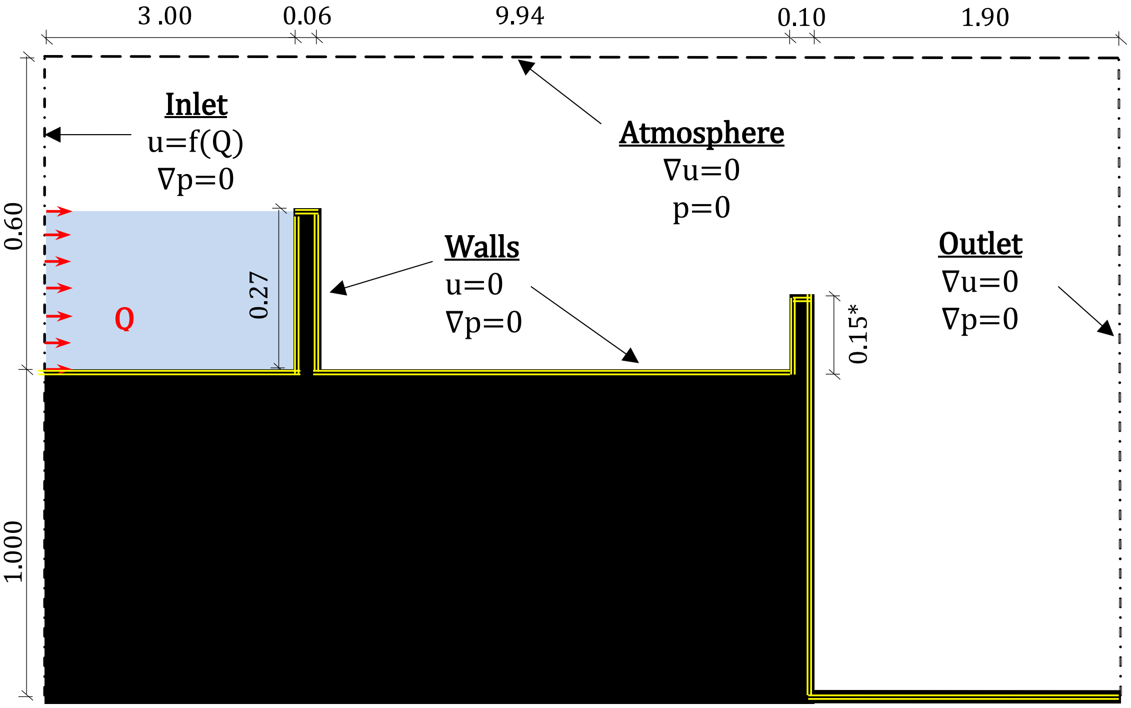

Figure 4-4: Numerical and physical boundary conditions. Measurements in meters. Not to scale.

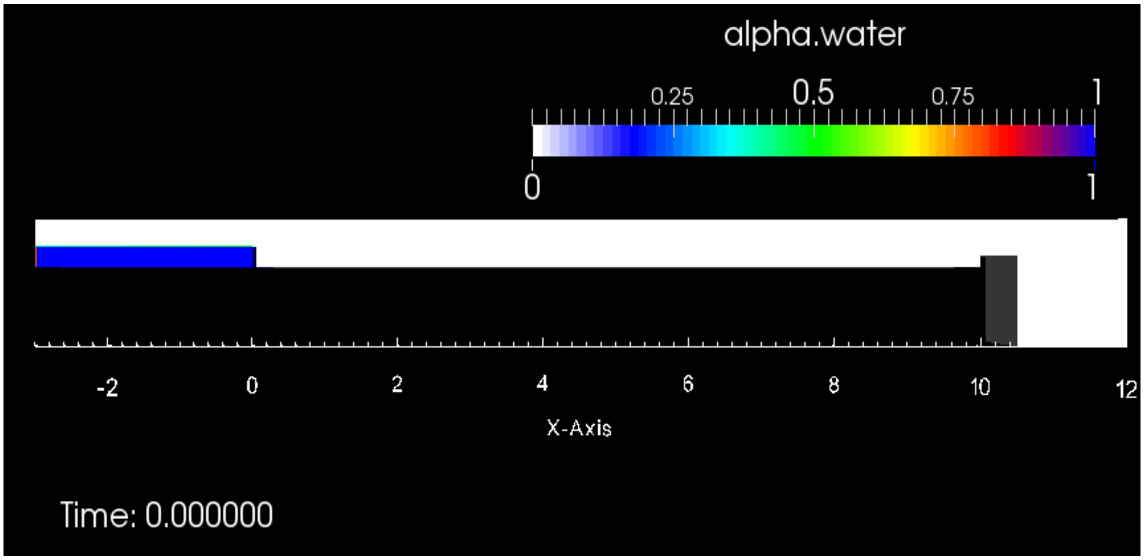

a)

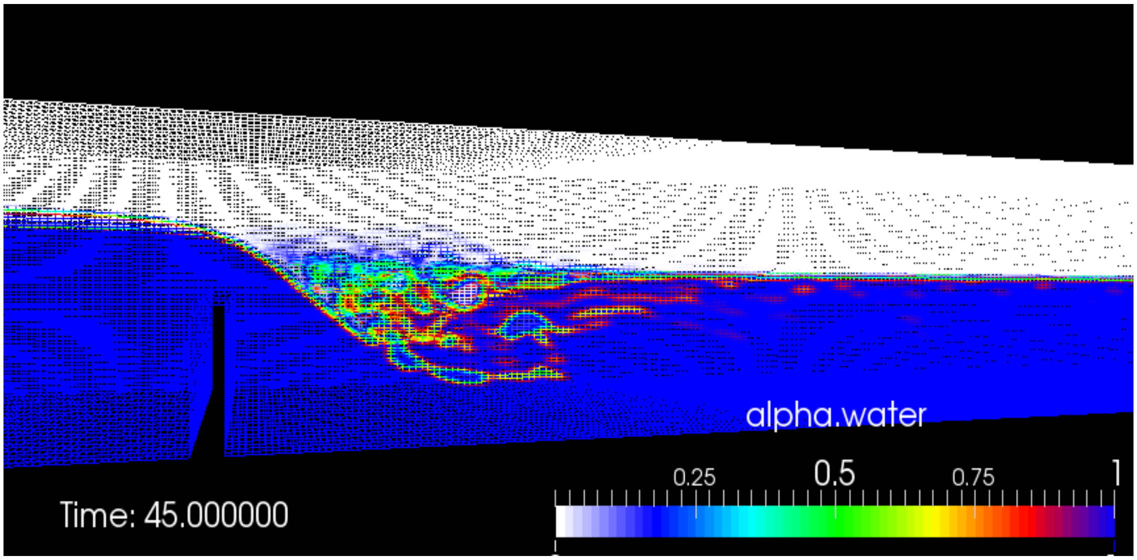

b)

Figure 4-5: Numerical domain visualized in ParaFOAM. a) Full domain; b) Zoom on the dam and the immediate downstream region.

4.3.2 Time implementation

There are two time discretization schemes which are implemented in OpenFOAM in order to achieve convergence and stability of the solution: the adaptive time-step control and the temporal sub-cycling feature.

4.3.2.1 Adaptive time-step control

The adaptive time-step control implementation, enforces the solution stability by adapting the time step, before each iteration, as a function of the instantaneous Courant number. Using the velocity at the cell face $({U_f}^{n-1})$ and the time step (Δt^{n-1}) obtained at the previous time step, the maximum Courant number for the next time step can be calculated (Co^n), according to the following expression.

$$(4.41) \qquad Co^n = {U_f}^{n-1} . \frac{\Delta t}{\Delta x}$$

The Courant number is essential for achieving stability when solving partial differential equations by numerical methods. This number allows for the correct selection of the time step (Δt^n) for a given cell size and for the calculated velocity. The concept behind this non-dimensional number is that the time step for the simulation must be inferior to the time that the fluid would spend traveling from one cell to the adjacent one. More refined cell grids would require smaller time steps to achieve stability. Once the Courant number for the nth time step is calculated (Co^n), the time step for the current iteration is adapted according to the following expression, described by Marquez Damian:

$$(4.42) \qquad \Delta t^n = min\left\{\frac{Co_{max}}{Co^n} \Delta t^{n-1}, \left(1 + \lambda_1 \frac{Co_{max}}{Co^n}\right) \Delta t^{n-1}, \lambda_2 \, \Delta t^{n-1}, \Delta t_{max}\right\}$$

Where the parameters $\lambda_1$and λ_2 ensure that the time step adaptations are stable reducing cyclic loops.

4.3.2.2 Temporal sub-cycling

OpenFOAM allows temporal sub-cycle dividing the total time step (Δt) into sub-cycles characterized by smaller time steps (Δt_{sc}) at which the phase fraction (γ) and the mass flux $(F_{sc,i})$ is calculated (Marquez Damian, S.). The advantages derived from this implementation are a more accurate solution for the phase fraction (more reliable free surface estimation) and the possibility to increment the global time step for solving other governing equations (resulting in a decrement of the computational cost). For a given number of sub-cycles (n_{sc}) the time step at the sub-cycle is calculated according to:

$$\Delta t_{sc} = \frac{\Delta t}{n_{sc}} \tag{4.43}$$

Once the time step characteristic of the sub-cycle has been determined, the total mass flux corresponding to the global time step is calculated as an addition of the computed mass flux at each sub-cycle according to the following expression:

$$F = \rho \cdot U_f \cdot S_f = \sum_{i=1}^{n_{sc}} \frac{\Delta t_{sc}}{\Delta t} \cdot F_{sc,i} \tag{4.44}$$

4.3.3 Solving process

4.3.3.1 OpenFOAM

OpenFOAM is a CFD toolbox that runs on the Linux operating system, with commands initiated within the terminal. Each test-case requires creation of a directory where all the data associated to the problem is stored. Initially, only three subdirectories are contained inside the problem directory: *`/0`*, *`/constant`* and *`/system`*. The solution process requires following the steps specified below in the terminal in order to run the numerical model:

- Step 1: Create Mesh

The mesh is created by the command `blockMesh` on the terminal. The entire computational domain is defined by a hexahedron which is divided into the specified number of cells in the x, y and z axis. The vertices and faces that define this hexahedron are listed in the *blockMesh* text file. The obstacles in the domain were defined by using an alternative method to define the hexahedrons, in order to easily implement changes in the geometry of the computational domain.

- Step 2: Remove obstacle from the domain

The obstacles are represented by the weir itself, the weir crest, the downstream gate which controls the tailwater level, and the elevation of the downstream apron. In order to remove the obstacles from the computational domain specified above, the command `topoSet` is executed. This command removes the specified boxes from the previous domain. The obstacles were described in a file contained in the main directory with an extension *setSet.* The set of cells corresponded to the geometry of the boundaries.

- Step 3: Redefine the new boundaries as walls

By removing the obstacles from the domain, new physical boundaries were created. These faces do not have any numerical boundary associated yet. The elements removed from the domain represent the face of the obstacles. Thus, the new boundaries will be treated as walls, which was associated to a previously defined patch called *lowerWall*. The command executed on the terminal follows the subsequent syntax:

```
subsetMesh –overwrite c0 –patch lowerWall
```

The command `subsetMesh` is used to select the group of cells corresponding to the new boundaries created by the `topoSet` command. The rest of the command indicates to consider on these boundaries the numerical conditions of the *lowerWall* patch.

- Step 4: Set initial location of the water volume

A volume of water behind the weir is set at the initial condition. If nothing is specified, the full domain is full of air. The command `setFields` locates the water according to the directory *setFieldsDict* located on the `/system` subdirectory.

- Step 5: Run the governing equations

At this stage, the model is perfectly defined and the governing equations can be solved. The solver selected for this simulation is executed on the terminal through the command `interFoam.` This solver belongs to the library of the OpenFOAM toolbox and it solves the Navier-Stokes equations. The multiphase consideration is possible because of the additional transport equation added to the mathematical scheme.

4.3.3.2 InterFoam

InterFoam is the numerical solver used to resolve the governing equations in our numerical model. The solver begins reading some specific files and setting the values for the fluids' properties. The reference pressure is set as a hydrostatic pressure associated to the column of water. Once the calculation is initialized the main loop starts. Firstly, the time steps and Courant numbers are calculated, and the adaptive time control technique implemented. For a specific time step, the fraction equation is solved by using the MULES integration technique (Multi-dimensional Limiter for Explicit Solution), to guarantee the smoothness of the air-water interface. The version of OpenFOAM used in this simulation is OpenFOAM v. 2.3.0, which includes a new semi-implicit version of the MULES method fully described in OpenFOAM's user manual (OpenFOAM 2014), which allows achieving convergence even for larger values of the Courant number. The mass flux and the density of the cells are obtained for the given time step. With this information, the momentum predictor is calculated to obtain the velocity field, followed by the PISO loop. Once this step is finished, if the final time is not reached, the main loop is repeated until reaching the end of the simulation.

4.3.3.3 PISO Algorithm

The PISO algorithm (Pressure Implicit with Splitting of Operator) was first introduced by Issa in 1986. The PISO procedure solves the Navier-Stokes equations by coupling the velocity and the pressure. This algorithm represents an extension of the SIMPLE algorithm (Patankar and Spalding 1972). PISO was developed to calculate the transport processes in three-dimensional flows, fully accounting for the cross-sectional processes. The SIMPLE algorithm suggested calculating an approximate velocity field (based on an estimation of the pressure field) which is later corrected in order to satisfy the continuity equation. This approach served as a base to develop the PISO procedure, which is implemented in the interFoam solver. The PISO algorithm considers the following steps:

- First, a predictor step, which solves the discretized momentum equation, is used to find the velocity field. The pressure field from the previous step is used in this predicting stage. This step is called the momentum predictor, obtaining an approximation of the velocity field.
- Following the initial predictor step, the PISO procedure considers two corrective steps. The first one consists on the estimation of the pressure field from the pressure equation, using the approximated velocity field. This step is known as the pressure solution. This new pressure field is used to calculate the conservative mass flux through the cell faces. Then, the velocity field is corrected using the corrected pressure field. This correction is performed in an explicit manner, eliminating the errors of this corrective step. This stage, referred as the explicit velocity correction, provides with the corrected velocity field.
- The PISO loop for correction of the velocity is repeated as many times as specified in the toolbox dictionary. The variable `nCorr` controls the number of cycles repeated to correct the velocity field.
- If the time has not reached the final time yet, the cycle begins calculating the new moment predictor and repeating the PISO loop until the final time iteration.

4.4 Calibration of Parameters

This section provides the results of the sensitivity analysis executed for the numerical investigation. The main goal of this analysis is to calibrate the numerical model as well as to fully understand the impact of some parameters on the numerical results and on the solving process operated by the interFoam solver.

The physical experiment selected to perform the calibration considered a base case. This physical arrangement is characterized by Q=50 l/s and a non-elevated downstream apron and a 6cm crest length. In addition to having a larger amount of experimental data for the aforementioned condition, a more reliable set of measurements was taken at this condition and also a larger downstream extension was affected by the vortex, resultant of a larger flow rate. In contrast to other experimental investigations, which are characterized by a fixed experimental arrangement, this study considers several crest lengths and downstream floor elevations, which induce a modification of the physical geometry and a changing computational domain.

The experimental runs selected for further comparison with the numerical tests enabled a qualitative and quantitative evaluation of the effect of the value of the principal variables on the characteristics of the downstream submerged vortex. The occurrence of the vortex, associated to the first experimental stage, was not further considered by the numerical approach. This stage considered a total of 333 runs which focused on the identification of the tailwater depths associated to the transition from 'free' to submerged and from 'submerged' to 'undular' hydraulic jumps. The arrangement designed within the frame of the numerical approach required running the simulations (t_{sim}) for a minimum of 40 seconds. This computation took, in average, a run time of 37.5 hours (t_{comp}). The very high computational cost associated to each numerical simulation did not make feasible a further application of the numerical approach to verify the findings achieved in the first experimental stage (hydraulic conditions associated to the formation of a submerged roller).

4.4.1 Preliminary selection of sensitive parameters

This subsection presents the selected values for the base case of the sensitivity analysis. These parameters were selected based on the nature of the CFD model, the numerical formulation of the selected solver, the discretization schemes adopted, and trial and error tests performed to truly reproduce the experimental conditions.

The sensitivity analysis intended to study the impact of the modification of the value for each individual parameter on the numerical model. The impact of changes to each parameter on the results achieved by the model enabled the evaluation of the sensitivity of the model to that specific parameter. The optimal value was discovered through this process, allowing a calibration of the numerical model. The selected parameters for the base case and its values are summarized in Table 4-3.

Table 4-3: Selected values for the base case in the sensitivity analysis

Parameter	Value
Mesh resolution	1.25cmx0.61cm
Water Kinematic viscosity (ν)	1×10^{-6} m^2/s
Air Kinematic viscosity (ν)	1.48×10^{-5} m^2/s
Discretization scheme	Linear
Turbulence Model	$k - \varepsilon$
Time-stepping (Δ_{time})	0.001
Maximum Courant number ($maxCo$)	0.2

Not all of the parameters involved on the model were considered in the sensitivity analysis. The specific case for weir overflow included in the OpenFOAM toolbox represented the start point of the numerical simulation, which was modified to emulate the experimental conditions by imposing a downstream water level. Following the investigations performed by Castillo et al. (2014) and Rogmanoli et al (2009), in which OpenFOAM was used to simulate the hydraulic jump condition, the interFoam solver was selected to perform the simulation of the submerged hydraulic jump. The sensitivity of the numerical model to the parameters is included in Table 4-3 and evaluated in the following subsections.

4.4.2 Mesh resolution

The mesh resolution indicates the size of the cells within the computational domain. In this simulation the mesh resolution was considered constant in the x and y axes, corresponding to the horizontal and vertical directions. The cross-section was neglected and one unique cell was considered along the z axis. Moreover, the side walls were defined as empty planes such that the flow was not affected by them. The mesh size is closely related to the time steps, highly affecting the Courant number. Therefore, it was found that the mesh size highly affected the convergence of the solution. Table 4-4 describes the characteristics of the meshes assessed in this sensitivity analysis.

Table 4-4: Total number of cells and computational times for various mesh resolutions.

Case	Mesh size (Δx, Δy)	X_{cells} (n°)	Y_{cells} (n°)	Number of Cells (n°)	t_{comp} (hours)
Mesh_0	1.25cmx0.6cm	1200	260	312,000	38.55
Mesh_1	2cmx2cm	750	80	60,000	12.60
Mesh_2	5cmx2.5cm	300	64	19,200	0.87
Mesh_3	5cmx5cm	300	32	9,600	0.26

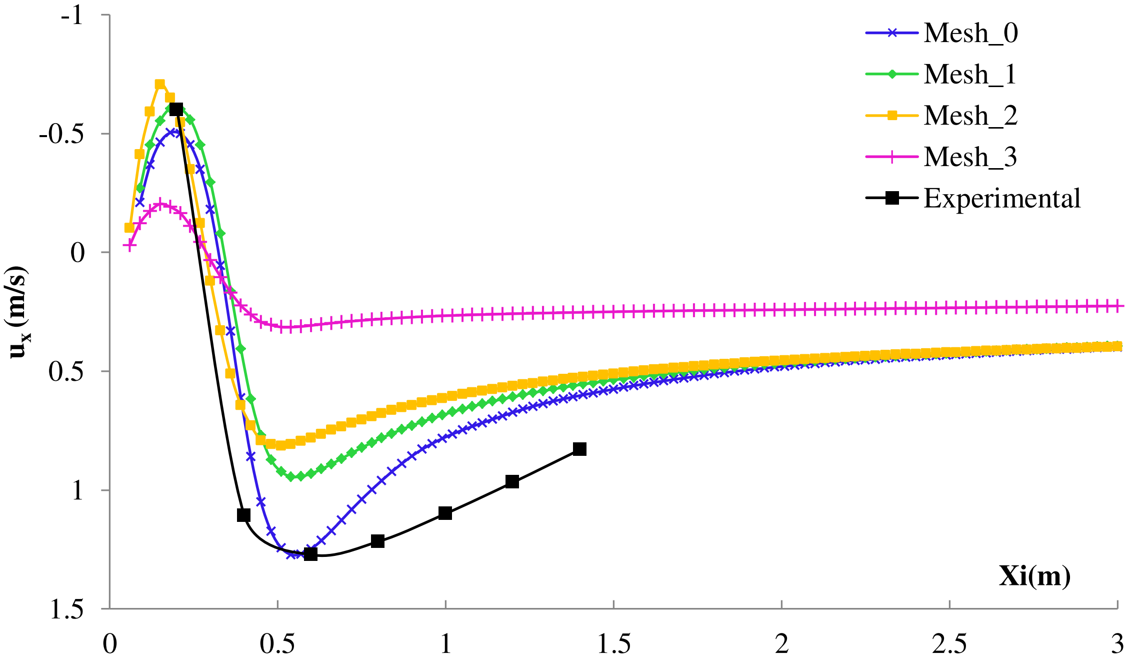

Figure 4-6: Model sensitivity to the mesh resolution; spatial distribution of the velocity along the bed $(y = 0.03\ m)$

Figure 4-6 shows that the impact of the mesh resolution on the bed velocity is very significant. As the mesh refines, the velocity along the channel's bed increases improving the accuracy of the simulation. The numerical reproduction of the velocity peak (in magnitude and downstream location) served to assess the model's performance. The smaller mesh size was able to precisely predict the bottom velocity peak, providing a good agreement with the experimental results. Therefore, it was determined that the smaller mesh size $(1.25cm\ x\ 0.61cm)$ was fine enough to achieve reliable results. The sensitivity analysis did not consider finer meshes because of the large computational resources required to perform the numerical simulation. The spatial distribution of the bed velocity shows a slight disagreement between experimental and numerical data. The numerical model underpredicts the velocity which might be caused by the inaccurate simulation of air entrainment processes and air-water regions in the roller.

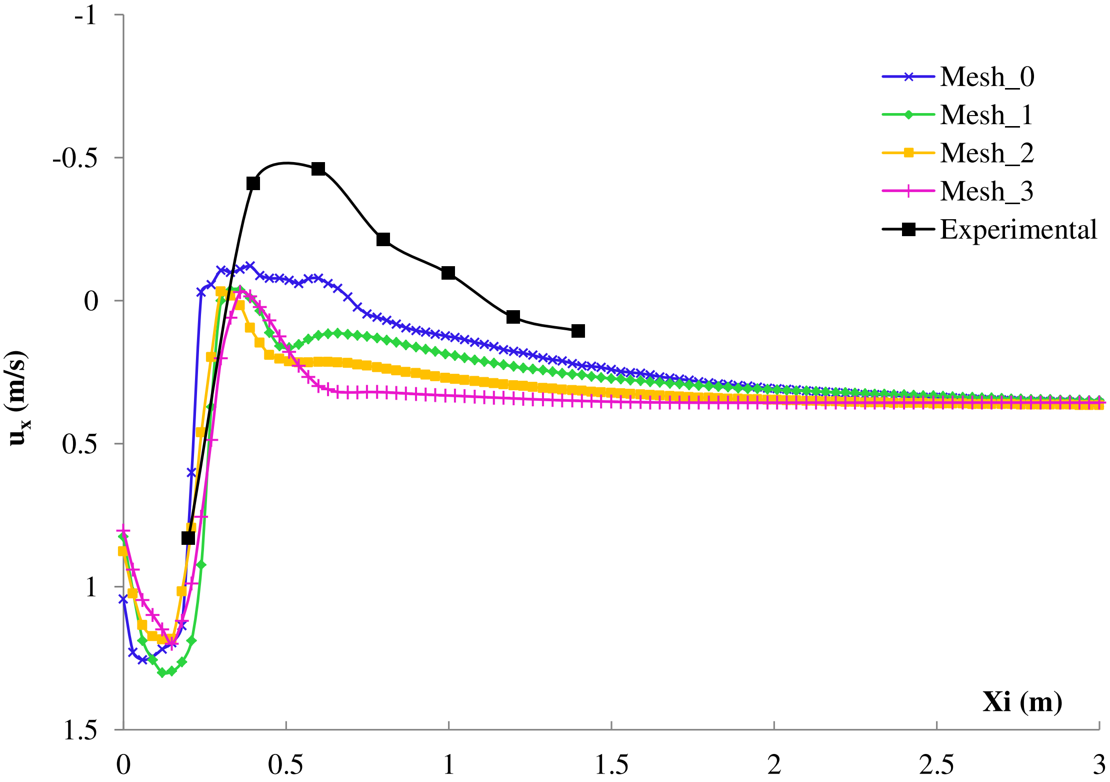

Figure 4-7: Model sensitivity to the mesh resolution; spatial distribution of the velocity along the surface $(y = 0.3\ m)$

Similar to the previous observations regarding the impact of the mesh size on the bed velocity, Figure 4-7 shows that the mesh resolution has a significant impact on the spatial distribution of the surface velocity. For large cell sizes, it seems that the predicted magnitude of the velocity along the surface is underestimated in the downstream region affected by the vortex (between 0 and 1.5 meters). As the cell size is decreased, the numerical model is able to better capture the counter-current velocity observed along the surface. This velocity, numerically predicted for several mesh resolutions, converges as the abscissa increases, towards the outside portion of the extension affected by the roller.

This observation leads to conclude that a fine mesh is required in order to capture the submerged hydraulic jump phenomenon. It is expected than a mesh finer than the one considered in this study, would provide larger values for the negative velocity along the free surface. The computational constraints did not allow testing finer meshes.

As expected, the computational time increased with the mesh size. The computational time was found to increase exponentially, as a function of the particle number (see Table 4-4). The smaller size considered in the sensitive analysis was proved to predict the velocities (surface and bed) relatively well. In general terms, the numerical simulations seem to underestimate the velocity, however the trend followed by the velocity seem to be properly simulated.

4.4.3 Transport properties

This parameter affects the physical processes involved on the simulation of this specific problem. The Froude scaling criterion, selected to downscale the physical model, indicates that the problem is dominated by the gravitational forces. The numerical modeling of gravitational-dominated problems is highly dependent on the density (ρ) and kinematic viscosity (ν) of the fluids under consideration, i.e. water and air, and the surface tension factor (γ). The values for the base case were taken from the weir overflow tutorial included in the OpenFOAM toolbox. The sensitivity of the model to the transport properties of the fluids was further assessed. The density of water and air were maintained constant during the simulation, at the values of $\rho = 1000\ kg/m^3$ for water, and $\rho = 1\ kg/m^3$ for air. Table 4-5 shows the numerical scenarios that were selected for comparison, in which the 'Visc_0' scenario represents the base case.

The selected transport properties assess the sensitivity of the model to the kinematic viscosity of water ('Visc_1' scenario), air ('Visc_2' scenario) and surface tension of the water ('Visc_3" scenario), respectively.

Table 4-5: Transport properties of fluids selected for sensitivity analysis scenarios.

Case	ν_{water} (m^2/s)	ν_{air} (m^2/s)	γ (Kg/s^2)	t_{comp} (hours)
Visc_0	1E-6	1.48e-5	0.07	38.55
Visc_1	1E-5	1.48E-5	0.07	39.69
Visc_2	1E-6	1.48E-4	0.07	53.14
Visc_3	1E-6	1.48e-5	0.035	42.49

Figure 4-8 and Figure 4-9 show that the choice of the fluid viscosity (ν) and the surface tension (γ) have little influence on the vortex's bed and surface velocities. It is noted though, that the scenario 'Visc_2' predicts a peak velocity which slightly differed in space in comparison with the other simulations. The required simulation time was considerably larger for this condition, as shown in Table 4-5.

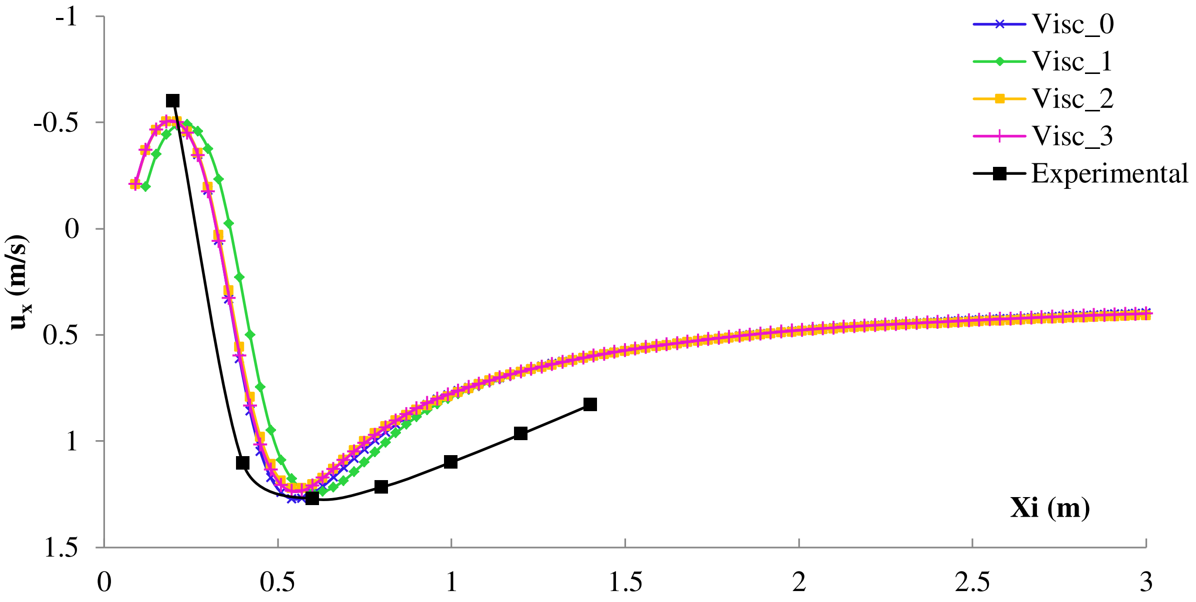

Figure 4-8: Model sensitivity to the fluids properties; spatial distribution of the velocity along the bed $(y = 0.03\ m)$

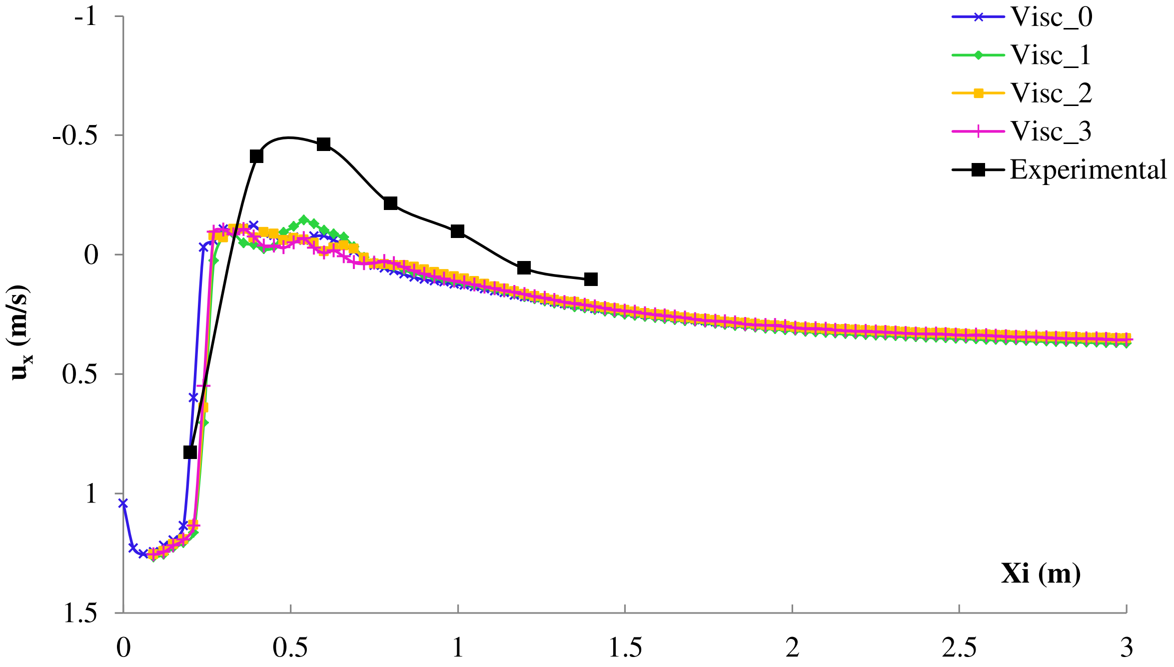

Figure 4-9: Model sensitivity to the fluids properties; spatial distribution of the velocity along the surface $(y = 0.3\ m)$

4.4.4 Turbulence model

The turbulence model selected in the base case is the $k - \varepsilon psilon$ model, as described in section 4.1.5. The sensitivity to the turbulence model was evaluated by comparing it against three other turbulence models: $k - omega$ and laminar. The selected numerical values for the $k - \varepsilon psilon$ and $k - omega$ scenarios coincided with the default numerical values included in the OpenFOAM toolbox. The laminar turbulence model crashed at $t_{sim} = 6s$, when the water was overtopping the downstream weir attempting to exit the domain. Figure 4-10 c) shows how the water particles lose their cohesion after overtopping the downstream gate, causing the simulation to fail. The submerged roller is a highly turbulent phenomenon; therefore the failure of the model under laminar flow regime hypothesis was expected.

Table 4-6: Turbulence models tested

Case	Parameters	t_{comp} (hours)
$k - \varepsilon psilon$	$k = 4.14E - 3$ $\varepsilon = 4.39E - 5$	38.55
$k - omega$	$k = 0.24$ $\omega = 1.78$	30.69
Laminar	N/A	N/A

Therefore the sensitivity to the turbulence model is reduced to an assessment of the performance of the $k - \varepsilon psilon$ and the $k - omega$ models, included in Figure 4-11 and Figure 4-12. Both models performed well at predicting the bed and surface roller velocities. The $k - \varepsilon psilon$ model simulated the roller better by capturing the velocity peak along the bed, while the $k - omega$ closure predicted better the flow velocity at sections located downstream from the effect of the vortex, achieving a smoother solution.

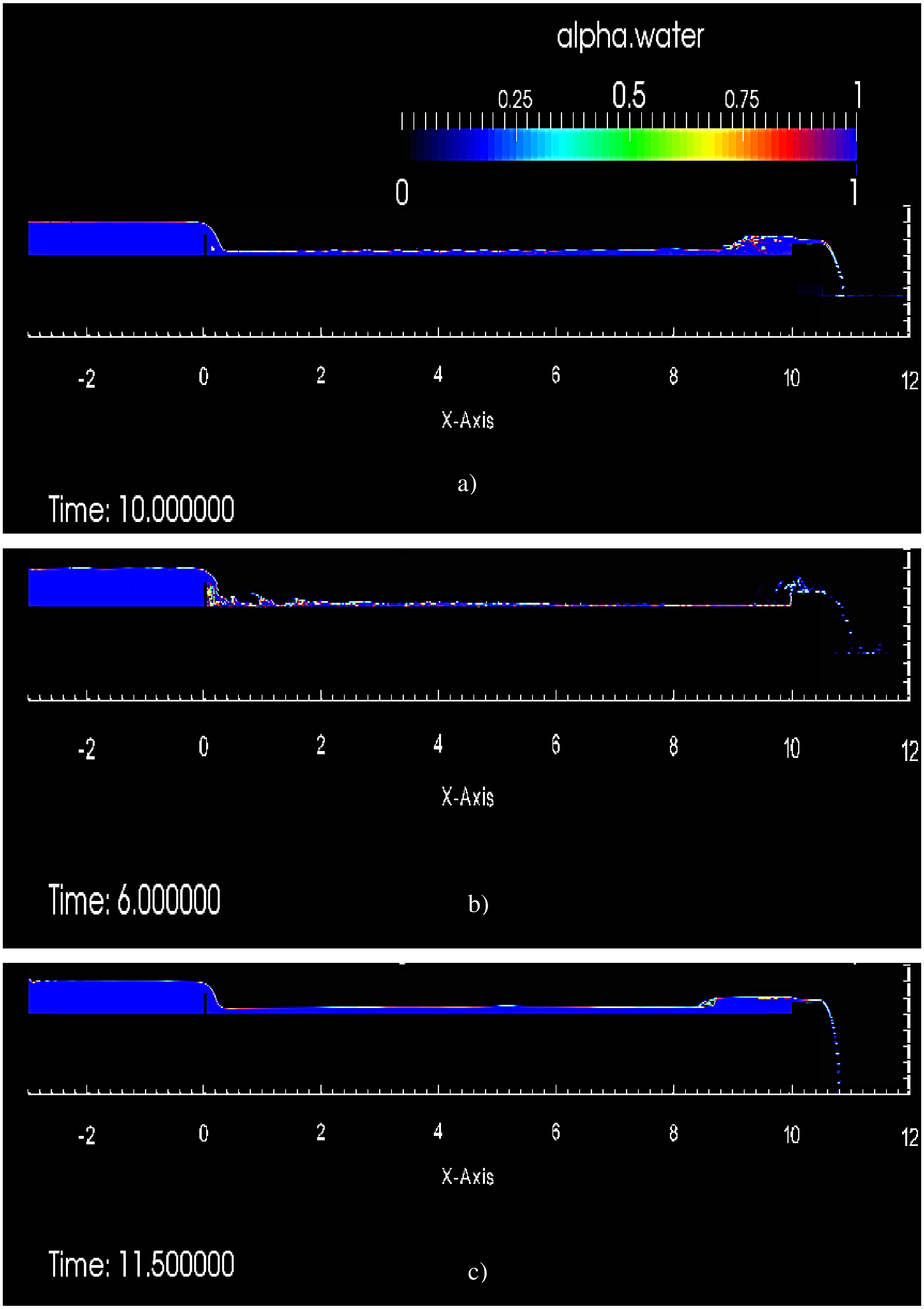

Figure 4-10: Model sensitivity to the turbulence model;

a) $k - \varepsilon psilon$, b) $k - omega$ and c) laminar

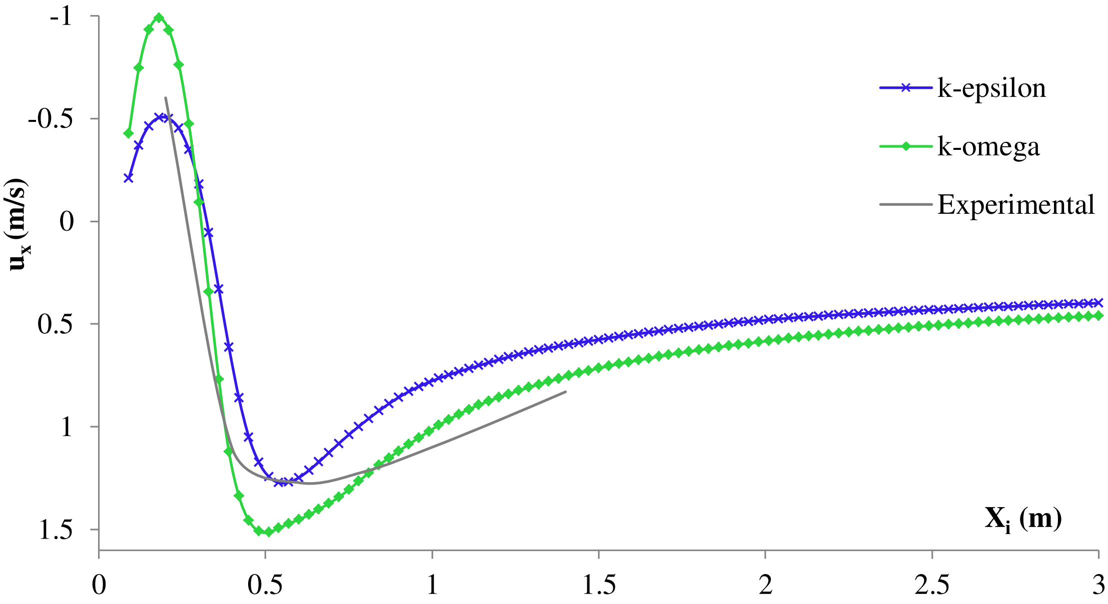

Figure 4-11: Model sensitivity to the turbulence model; spatial distribution of the velocity along the bed $(y = 0.03\ m)$

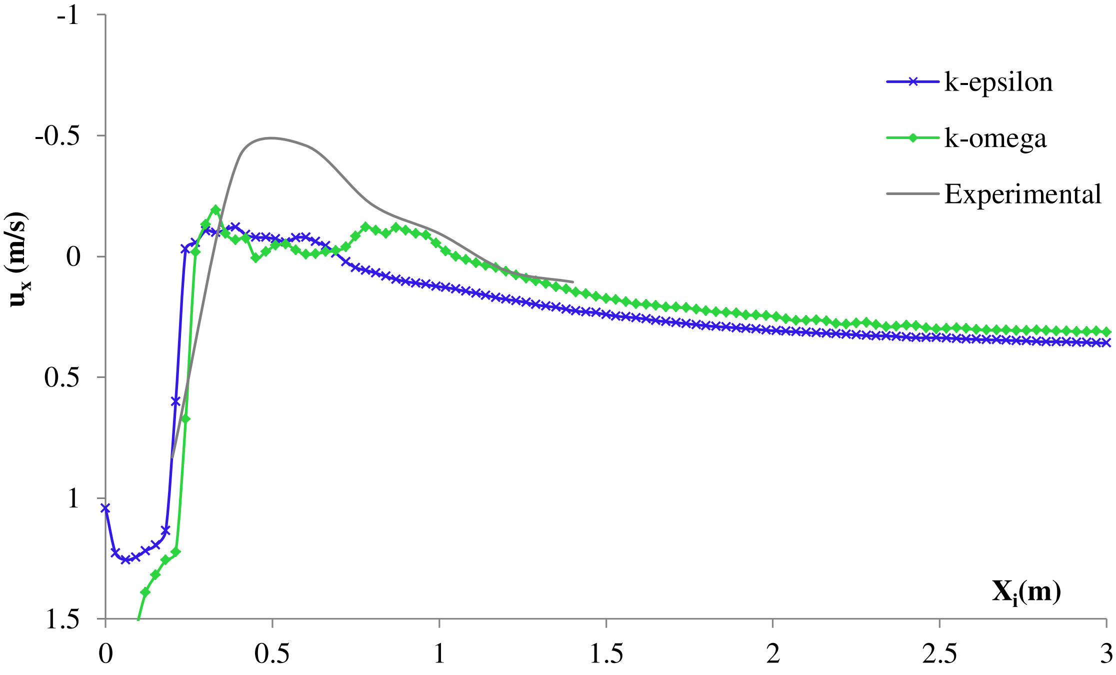

Figure 4-12: Model sensitivity to the turbulence model; spatial distribution of the velocity along the surface $(y = 0.3\ m)$

4.4.5 Discussion

The sensitivity analysis presented in this section helped to evaluate the effect of certain parameters on the numerical results.

It was found that the mesh resolution highly affected these results, especially the surface velocity. It was determined that fine meshes are required to capture the magnitude and location of the velocity peak. The model's sensitivity to the air and water transport properties (kinematic viscosity and surface tension) is negligible. However, the numerical model is quite sensitive to the selected turbulence model; the $k - \varepsilon psilon$ model performed the best at predicting the magnitude and the location of velocity peaks, while the $k - omega$ turbulence model predicted the channel's dynamic variables better at downstream sections located out of the area of influence of the submerged roller. The turbulent nature of the submerged hydraulic jump is why the laminar model performed well. In this case fundamental hydrodynamic principles were broken causing the model to crash.

Chapter 5. Occurrence of submerged vortex

The primary objective of the experimental investigation is to determine the range of downstream water levels associated to the 'submerged'-type hydraulic jump. This knowledge will determine whether the structure is operating under dangerous hydraulic conditions. This chapter outlines a novel approach to the submerged roller phenomenon identifying (i) the physical variables which govern the submerged roller phenomenon and (ii) proposing an improved definition of the degree of submergence as a function of the physical variables aforementioned. The experimental arrangement was modified in order to assess the effect of crest length, downstream apron elevation and discharge on the minimum and maximum tailwater levels associated to the development of the submerged hydraulic jump. This led to the definition of lower (Y_l) and the upper boundaries (Y_u) for the submerged vortex.

5.1 Submerged hydraulic jump's lower boundary

The lower boundary for the submerged hydraulic jump (Y_l) represents the minimum water level capable to produce a submerged hydraulic jump. Physically, this tailwater level is associated to the transition between the 'free' and 'submerged' types of hydraulic jump.

5.1.1 Crest length effect

Visual observations show that the transition occurred at approximately the same tailwater depth for a given discharge. The lower boundary for all discharges and all crest lengths considered for a non-elevated downstream apron is represented in Figure 5-1, as a function of the relative weir length parameter (ζ_w)

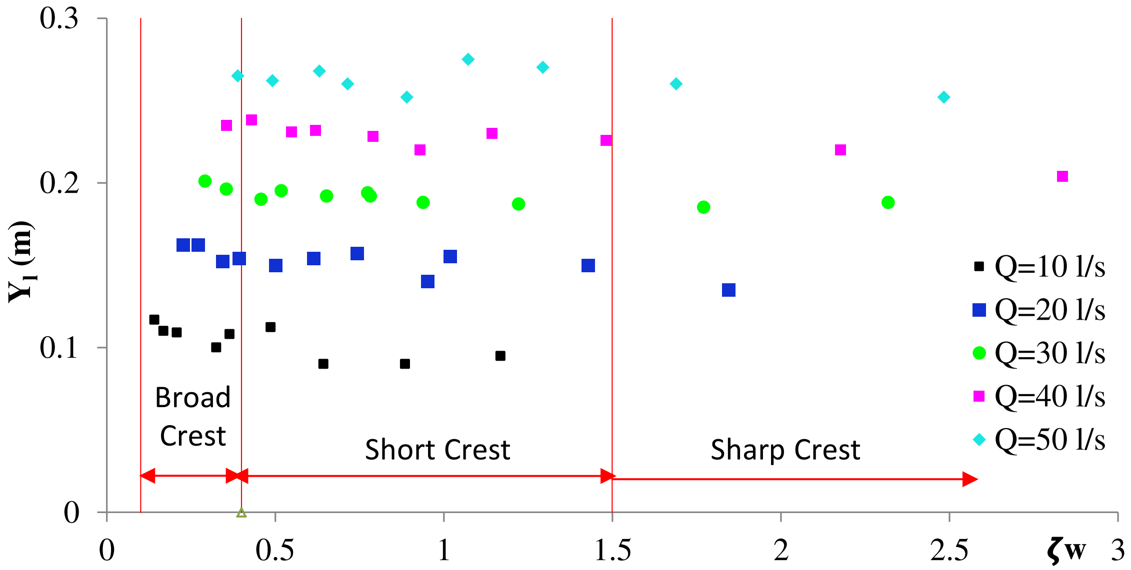

Figure 5-1; Tailwater depth corresponding lower boundary (Y_l), as a function of the non-dimensional relative weir length (ζ_w) and the discharge (Q).

Higher flow rate conditions increased the lower boundary (Y_l). In the broad-crested region (left side of Figure 5-1), the five flow discharges tested (Q=10, 20, 30, 40 and 50 l/s) are clearly differentiated as quasi-horizontal lines with equal spacing. Indeed, this pattern reveals a strong correlation between the lower boundary and the discharge in the broad crest region. Moreover in the same region, for the smallest flow rate considered (Q=10 l/s), the lower boundary was identified at around 11cm measured from the bottom of the channel. For the maximum discharge (Q=50 l/s) the lower boundary increased up to 26 cm.

The scattering of the experimental data increases as we move from the broad crest region towards the short- and sharp crest regions (from left to the right in Figure 5-1). The data sets associated to the five discharge series cannot be tracked in the previous figure outside of the broad-crested region. This dispersion can be explained by considering the more turbulent nature of the flow chute over the structure, when narrower crests are installed (i.e. ‘short’ and ‘sharp’ crests, respectively).

For low discharge conditions (corresponding to data points located at the bottom region of Figure 5-1) the crest length shows a larger impact on the submerged jump’s lower boundary: as the weir crest shortens, the lower boundary slightly decreases. The opposite behaviour is observed for high flow rate data sets (associated to points located on the top region on Figure 5-1); as the crest shortens, the submerged jump's lower boundary seems to increase. From now on, the discharge is represented in terms of the freeboard or upstream water level (Y_0). This variable, which is usually controlled and monitored on-site in real streams, is used in the posterior analysis of the experimental data.

5.1.2 Apron elevation effect on lower boundary (Y_l)

If the tailwater level associated to the lower (Y_l) and upper boundaries (Y_u) is plotted against the upstream water level (Y_0), for the entire data set (333 experimental runs), it appears to be correlation for the data set, as observed in Figure 5-2. The data points located at the bottom of Figure 5-2 reveal strong correlation and are further investigated in this section.

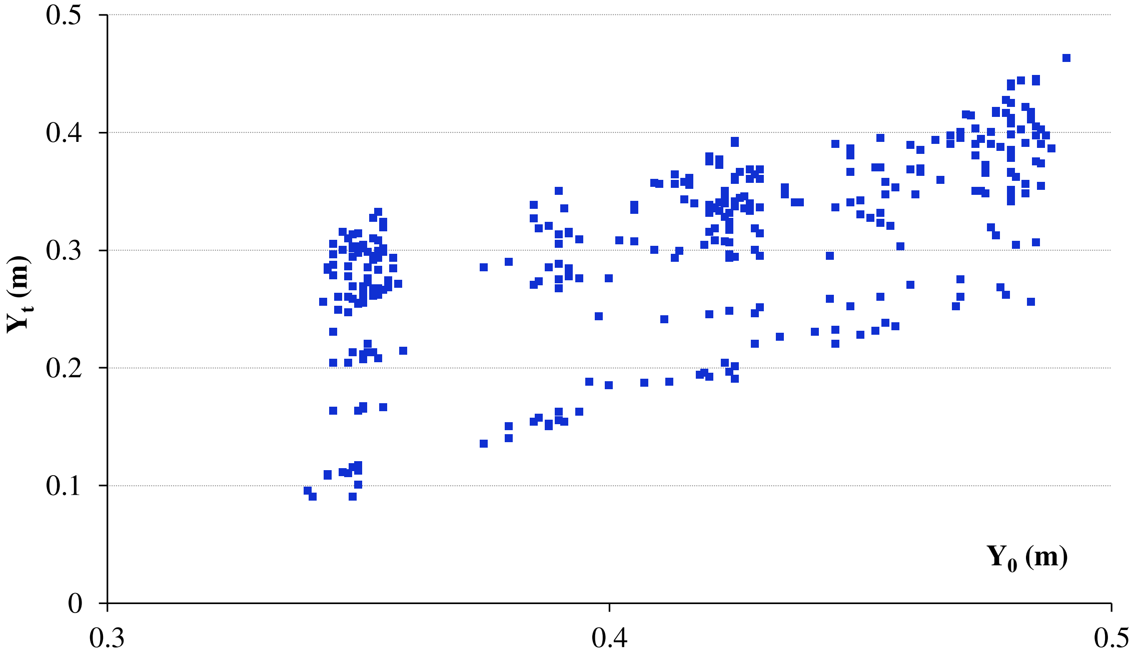

Figure 5-2: Relation between tailwater depth, Y_t, and upstream water depth, Y_0, for all transitional stages

Several floor elevations were considered. It was determined that the lower boundary increased when the downstream apron was elevated. It was observed that the lower boundary was reached at approximately the same depth, for a given discharge condition, but measured from the plane of the downstream apron. Therefore, a new variable was introduced ($\mathrm{Y_{t\_bed}}$), which represents the tailwater level, measured from the downstream floor plane, or apron, as represented in

Figure 5-3. The numerical relation between these two variables is:

$$Y_t = z_{floor} + Y_{t\_bed} \tag{5.1}$$

The apron's elevation is accounted for by the variable (z_{floor}). The experimental runs performed on the frame of submerged vortex occurrence are shown in Figure 5-4, which relates the newly defined variable (Y_{t_bed}) to the upstream water level, revealing a strong correlation of data points representing the lower boundary of the submerged hydraulic jump.

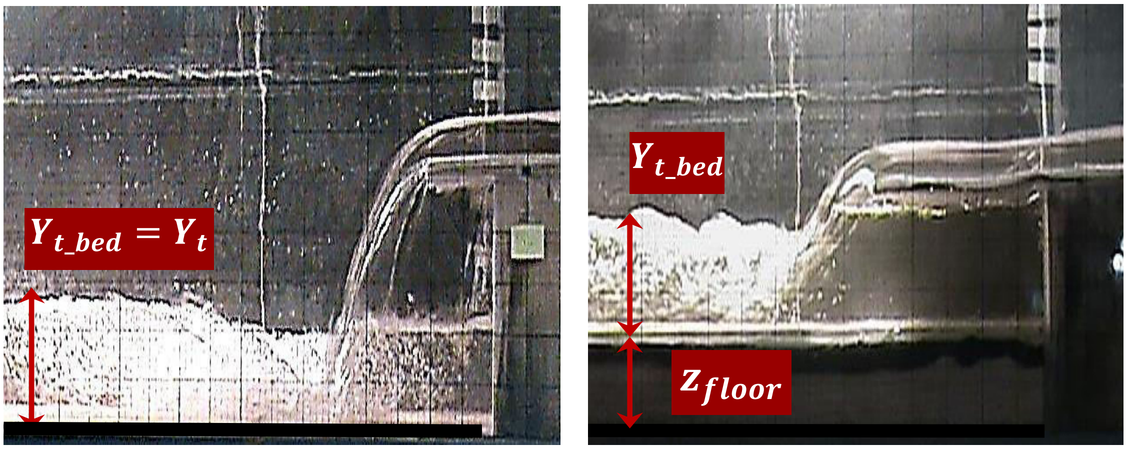

Figure 5-3: Graphical definition of the variables tailwater level (Y_t) and tailwater level measured from the apron's plane (Y_{t_bed})

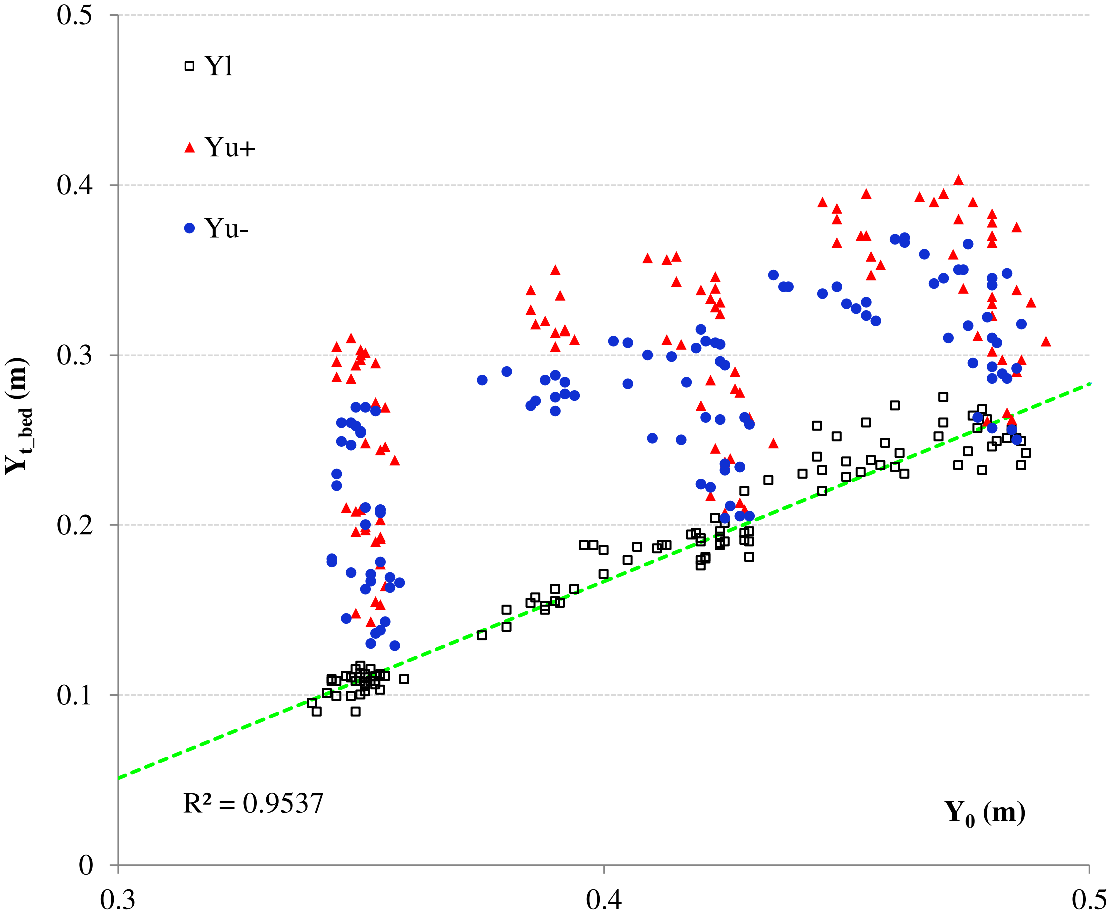

Figure 5-4: Relation between the tailwater level measured from the downstream floor (Y_{t_bed}) and the upstream depth (Y_0).

Figure 5-4 reveals the strong relation between the tailwater level (measured from the apron's plane) and the upstream level for the lower boundary of the submerged hydraulic jump. Therefore, the submerged hydraulic jump's lower boundary measured from the apron's plane (Y_{l_bed}) can be expressed in terms of the aforementioned variables. The expression is formulated as:

$$(5.2) \qquad Y_{l\_bed} = 1.16 * Y_{crest}$$

Where the variable (Y_{crest}) represents the upstream water depth, measured above the weir crest. This equation is modified into a generic expression which is expressed in absolute terms, providing the minimum tailwater level forming a submerged-type hydraulic jump, expressed from a reference plane located at the bed of the channel, as seen in

Figure 5-3. Therefore, the mathematical equation (5.2) is modified according to the relation (5.1). The submerged hydraulic jump's lower boundary is expressed, for this experimental investigation, as:

$$Y_l = 1.16 * Y_{crest} + z_{floor} \tag{5.3}$$

This relation enables the prediction of the lower boundary with a very high accuracy especially for cases of low flow rate in the stream. The variables Y_{crest} and z_{floor} are measured from the same plane, corresponding to the channel's bed. As seen in Figure 5-4, the scattering of the data points increased with the discharge (increases from left to right). The proposed relation, represented by the green trend line in Figure 5-4, predicts the lower boundary with a higher accuracy at low discharge condition than at high flow rates. In any case, the proposed relation (5.3) shows a tendency to slightly under predict the lower boundary at high flow rates. The measurement and collection errors, in combination with the accuracy of the measurement devices might be the source of this disagreement. Finally, Figure 5-4 does not seem to present a strong correlation between the upstream water level (Y_0) and the upper boundaries (Y_{u+} and Y_{u-}).

5.2 Submerged hydraulic jump's upper boundary

The upper boundary, referred as (Y_u), corresponds to the maximum water level associated to the submerged roller formation, or minimum hydraulic tailwater depth responsible for generating a surface wave referred in literature as an 'undular' hydraulic jump. The 'undular' jump forms during low supercritical inflow Froude numbers, and is characterized by undulations of the water surface (Chow, 1959). This upper boundary represents the transition from 'free' to 'submerged' flow regime, which was investigated by Wu and Rajaratnam for sharp-crested weirs (1996). Additional information regarding the experimental data concerning the lower and upper boundaries is included in Appendix A.

5.2.1 Initial considerations

This submerged hydraulic jump's upper boundary (Y_u), can be reach by two different scenarios as described below:

- Increasing the tailwater level: When the downstream water level is incrementally raised from a submerged jump condition, the vortex will eventually 'flip' forming a surface roller. The tailwater flow depth associated to the upper boundary for increasing tailwater levels is referred as (Y_{u+})
- Decreasing tailwater level: Under an initial scenario of a 'undular' type hydraulic jump, when the tailwater level is incrementally decreased, the surface waves will eventually become unstable, plunging and forming a new submerged vortex. This process is referred in literature as the vortex 'flop'. The downstream water depth associated to the upper boundary, for decreasing tailwater levels, is referred as (Y_{u-})

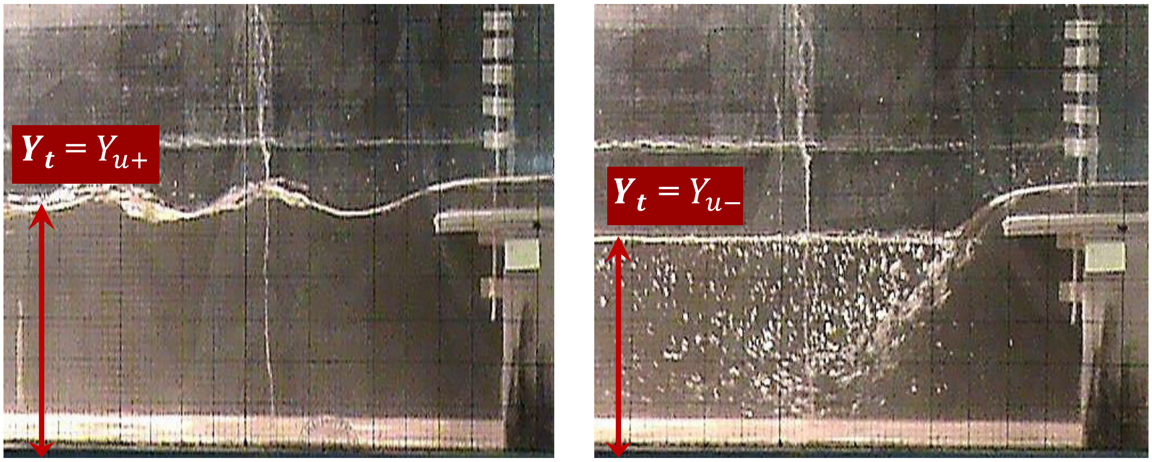

a) b)

Figure 5-5: Upper boundaries for the submerged hydraulic jump. a) Upper boundary for increasing tailwater levels (Y_{U+}). b) Upper boundary for decreasing tailwater levels (Y_{U-}).

Both upper limits (Y_{u+}) and (Y_{u-}) have properties inherent to the nature of the mechanism that produces them. Moreover, the upper boundary Y_{u+} is reached at higher downstream water levels than the Y_{u-} boundary. Experimental observations demonstrated the fact $Y_{u+} > Y_{u-}$, in agreement with Leutheusser & Fan (2001). The difference between these two values is explained in terms of the ventilation of the nappe and the physical mechanisms behind the formation of the submerged jump in each case.

Since $Y_{u+} > Y_{u-}$, the tailwater range prone to submerged hydraulic jump condition $[Y_l - Y_u]$ is larger for increasing than for decreasing water levels leading to the worst case scenario for development of submerged rollers. Therefore, the upper limit for increasing tailwater levels (Y_{u+}), was selected for further consideration in this study.

5.2.2 Crest length effect on the upper boundary

The transition between submerged hydraulic jump and undular roller seem to be reduced to a wave instability problem. The slightly unsteady flow provided by the pump was responsible for inducing the undular wave too early (at lower water levels) in certain runs, inducing a premature instability of the wave. Figure 5-6 represents the relation between the upstream water level (Y_0) and the local tailwater depth (Y_t), for the entire data set. The upper boundary for increasing water levels (Y_{u+}) occurs at larger flow depths than for decreasing water levels (Y_{u-}). The scattering of the experimental data increases with the discharge, represented by Y_0, revealing a larger dispersion of the experimental measurements on the right part of Figure 5-6.

This scattering of the data sets was further investigated. The effect of the crest length on the upper boundary was evaluated, as shown in Figure 5-7. The upper boundary for increasing water levels Y_{u+}, (represented by the red data series on Figure 5-6), was plotted as a function of the crest length on Figure 5-7.

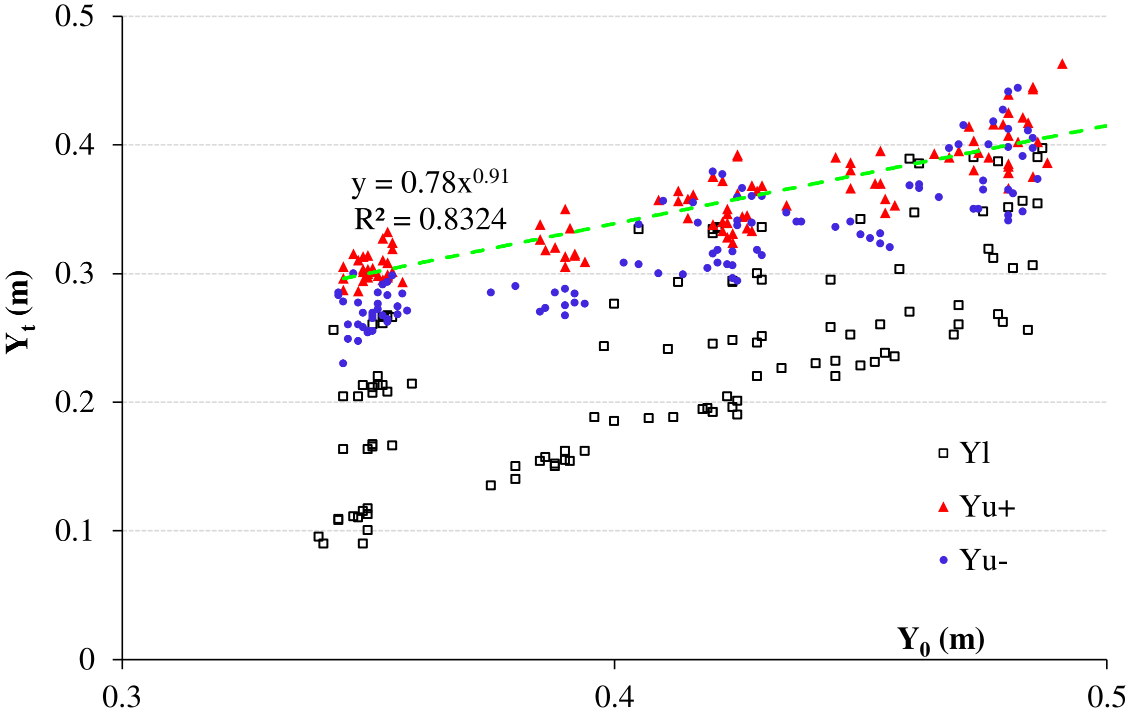

Figure 5-6: Upper boundaries as a function of the local tailwater depth (Y_t).

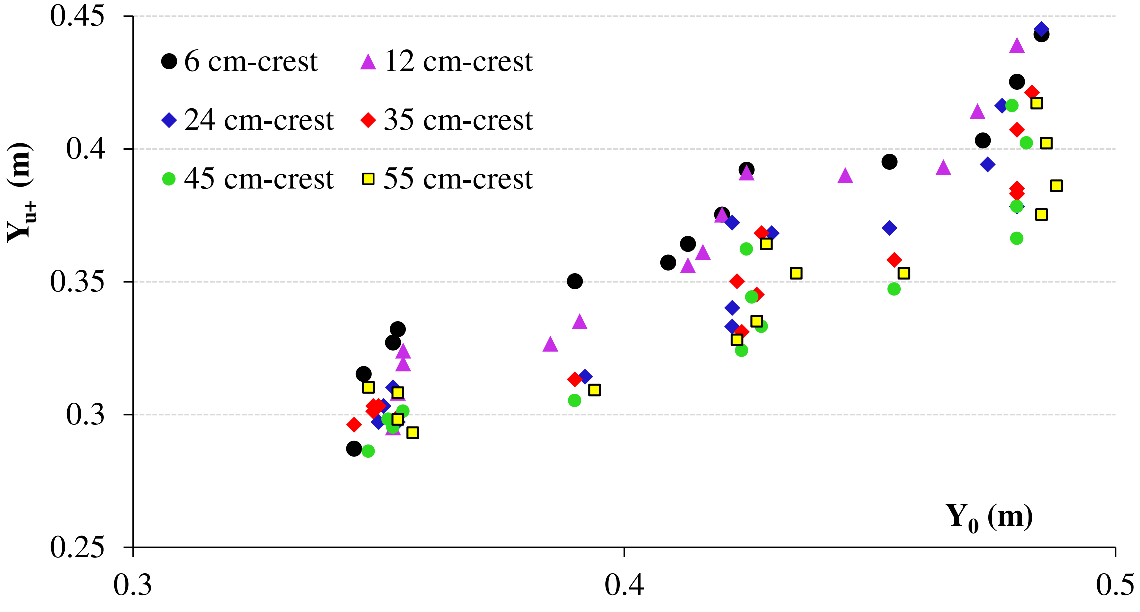

Figure 5-7: Upper boundary (Y_{u+}) investigated as a function of the crest length.

Broad-crested weirs required smaller flow depths to reach the upper boundary than sharp-crested weirs, thereby impacting the net tailwater range ($Y_{u+} - Y_l$) associated with the occurrence of submerged hydraulic jumps. The trend presented by the 6-cm series (represented by the black data set in Figure 5-7) achieved higher Y_{u+} values than for the 55-cm crest (represented by the yellow series in Figure 5-7). Series in between (i.e., 12cm, 24 cm, 35 cm, and 45 cm), seem to agree with this trend.

The scattering of the results was affected by the flow rate; as the discharge increases, the dispersion of the data sets increase. The interpretation given to this finding is that the downstream floor elevation has a higher than expected impact on the upper boundary, especially under high flow rates. Figure 5-8 reveals that the lower boundary (Y_l) is not affected by the crest length, in agreement with the numerical definition of this limit which does not account for the crest length (see section 5.1).

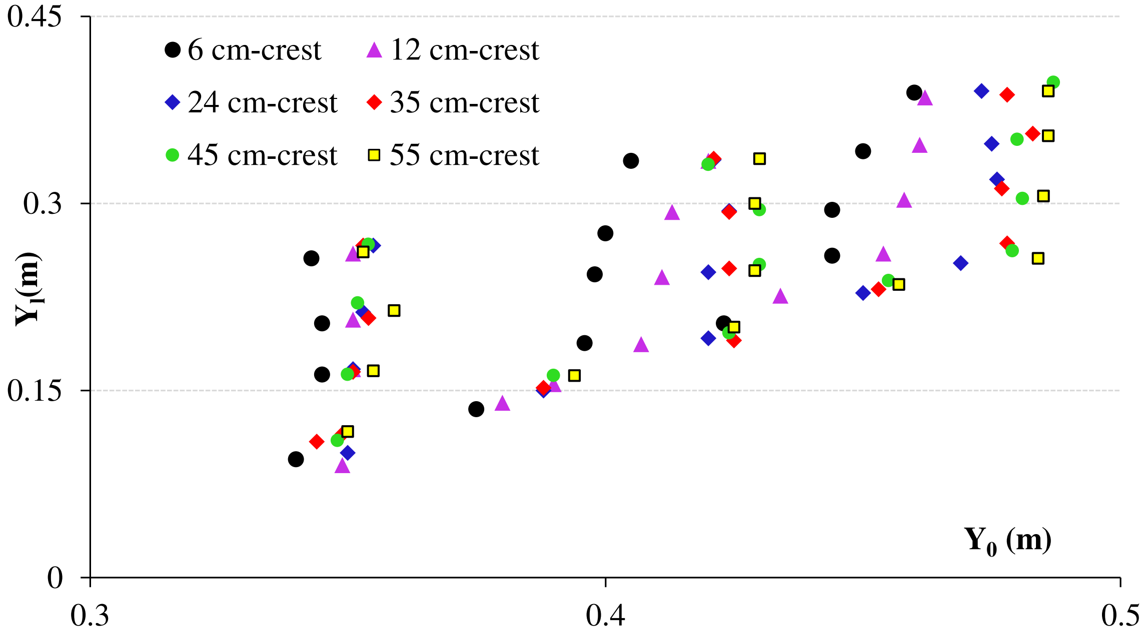

Figure 5-8: Lower boundary (Y_l) investigated as a function of the crest length.

In conclusion, broad crest showed a better performance than sharp-crested weirs at reducing the upper boundary and therefore, the range of tailwater depth associated with the formation of a submerged hydraulic jump. As a result, the risk of sharp-crested weirs operating under dangerous hydraulic conditions could be minimized by installing wider crests (i.e. broad crests).

5.2.3 Apron elevation effect on upper boundary (Y_{u+})

Preliminary hypothesis pointed to a negative impact of the downstream apron's elevation on the submerged roller's upper boundary (Y_{u+}). This can be explained based on the fact that once the upper boundary is reached, the submerged flow regime occurs. Moreover, the upper boundary is associated to the physical transition from 'free' to 'submerged' flow regime; and therefore the downstream is ultimately dependent on the upstream conditions, independently on the apron's elevation.

Figure 5-9 shows that the downstream floor's elevation mildly affects the upper boundary. The trend lines for each floor elevation share a common point at the minimum discharge (on the left of Figure 5-9) and from here they diverge; the highest downstream floor elevation requires the largest tailwater depth for reaching the upper boundary achieving the biggest correlation. As the downstream floor elevation decreases, the required transitional tailwater depth (Y_{u+}) and the accuracy of the trend line for each series decreases.

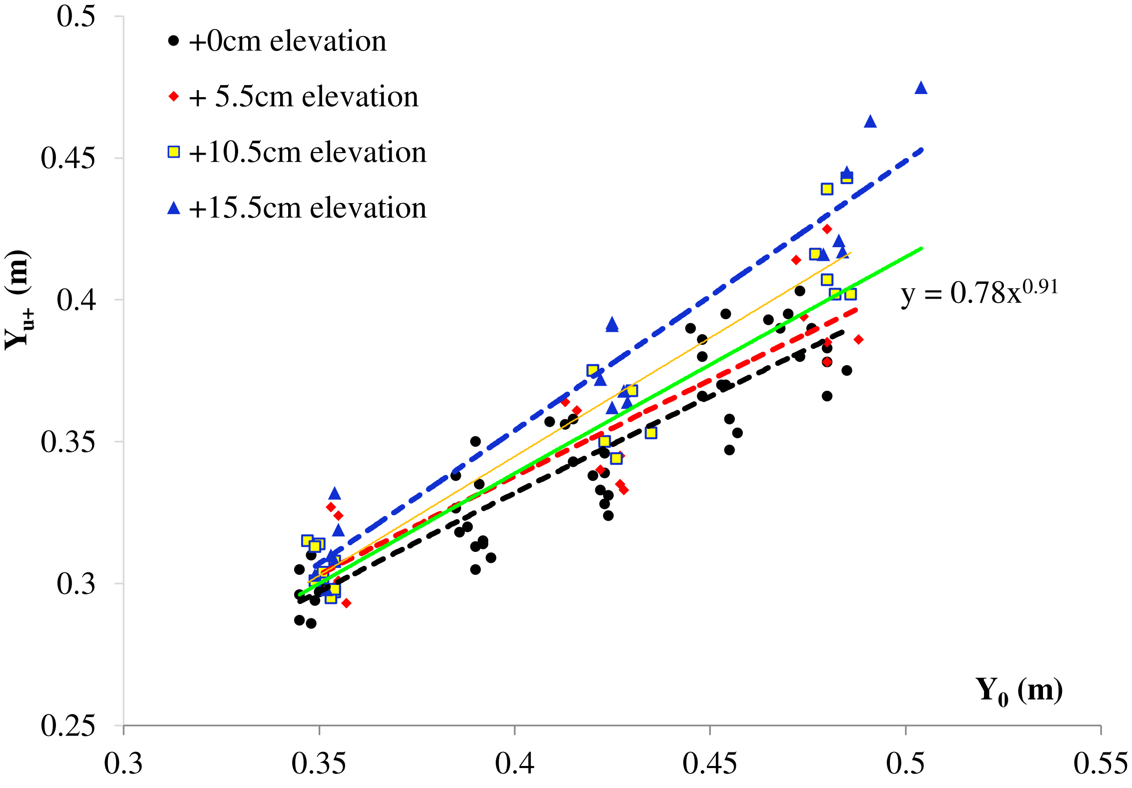

Figure 5-9: Upper boundary as a function of the downstream apron elevation.

Therefore Figure 5-9 shows the trend lines for each data set, which corresponded to a power relation to predict the upper boundary as a function of the upstream depth (Y_0), which represent the base of the power function. The expression which better fits the entire data (obtained using the least squares regression technique) is expressed mathematically as:

$$(5.4) \qquad Y_{u+} = 0.78 * {Y_0}^{0.91}$$

Where the constant (0.78) is seen as a calibration factor dependent of the geometry of the dam. The simplicity of this empirical expression stems from its nature; the upper boundary is expressed as a function of the main variable affecting this transition for a given weir height: the upstream water depth.

However it was concluded, in Section 5.2.2., that the tailwater depth at which the upper boundary is reached is affected by the crest length, especially at high flow rates. Both, sharp crest lengths and elevated aprons are associated to larger Y_{u+}. These variables are combined, in order to obtain a more complex expression to predict the upper boundary, indicated by equation (5.5). The accuracy of this alternative formulation is achieved by compromising its simplicity. This expression, which successfully accounts for the abovementioned variables, was determined by using the least squares regression analysis and takes the form of:

$$(5.5) \qquad Y_{u+} = \alpha_{weir} * \left[{Y_0}^{(1-0.05*\left[\frac{H_{weir}-z_{floor}}{H_{weir}}\right]-0.03*[\xi_w]} \right]$$

The power function was driven by the correlation trends provided in Figure 5-9. The downstream apron elevation and crest length play an essential role in the calculation of the upper boundary. Both variables are included in the exponent of the power function. The correction factor (α_{weir}) inherent to the geometry of each specific weir is used to provide a correction of the upper boundary. The correction factor for this specific case reaches a value of $\alpha_{weir} = 0.78$. This expression also considers the crest length through the inclusion of the non-dimensional crest length (ξ_w), defined by equation (3.8).

Therefore, this formulation provides a good simulation of the combined effect of the variables directly involved in this specific problem, accounting for the length of the crest, the downstream elevation of the channel bed or apron, and taking into consideration the specific characteristics of the dam. The latter formulation (Eq. 5.5) is able to accurately capture the fluctuations of the upper boundary caused by the range of conditions considered by the data set.

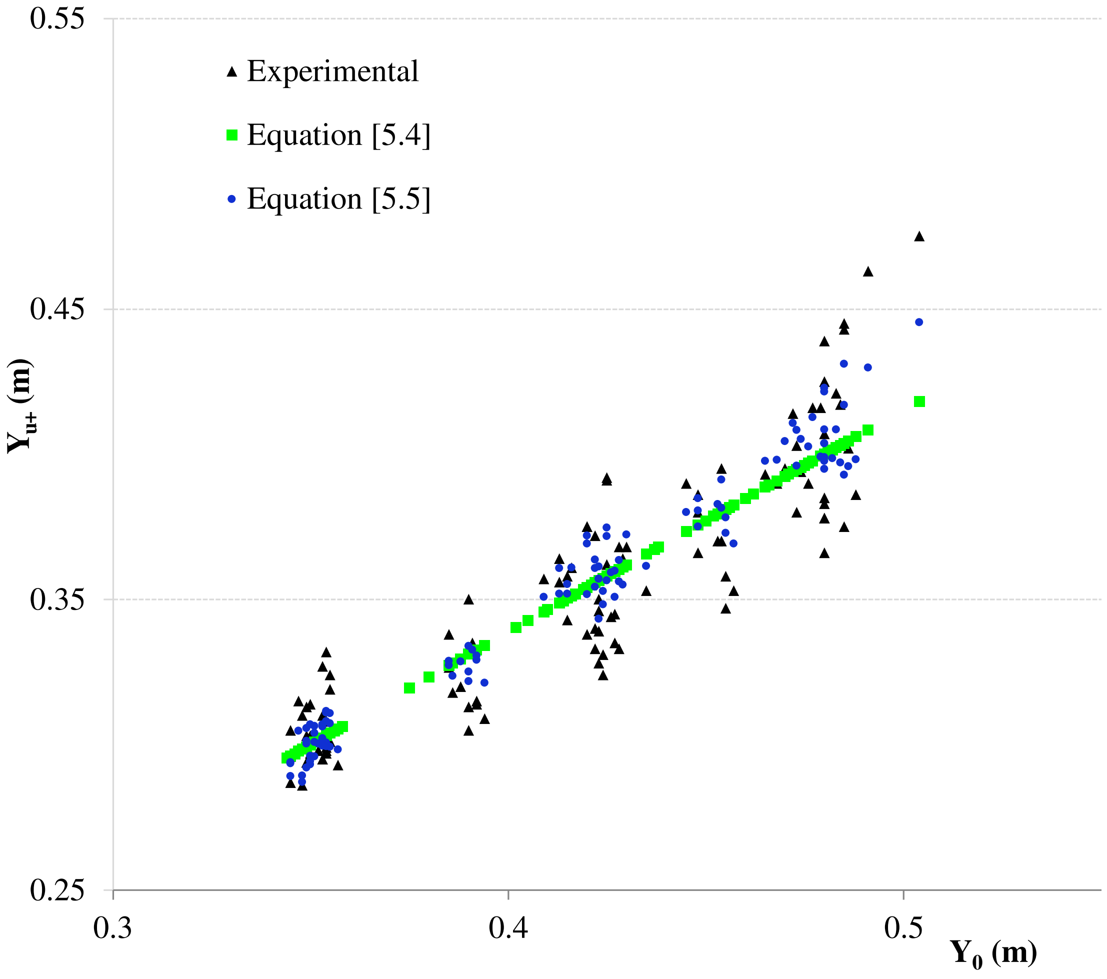

Figure 5-10: Comparison of experimental data and empirical proposed formulation (5.4) and (5.5) for the upper boundary.

The scatter plots showing the performance of Equations 5.4 and 5.5, to predict the observed upper boundary indicates the accuracy of the latter to estimate this limit (Figure 5-12) over the simplified equation (see Figure 5-11).

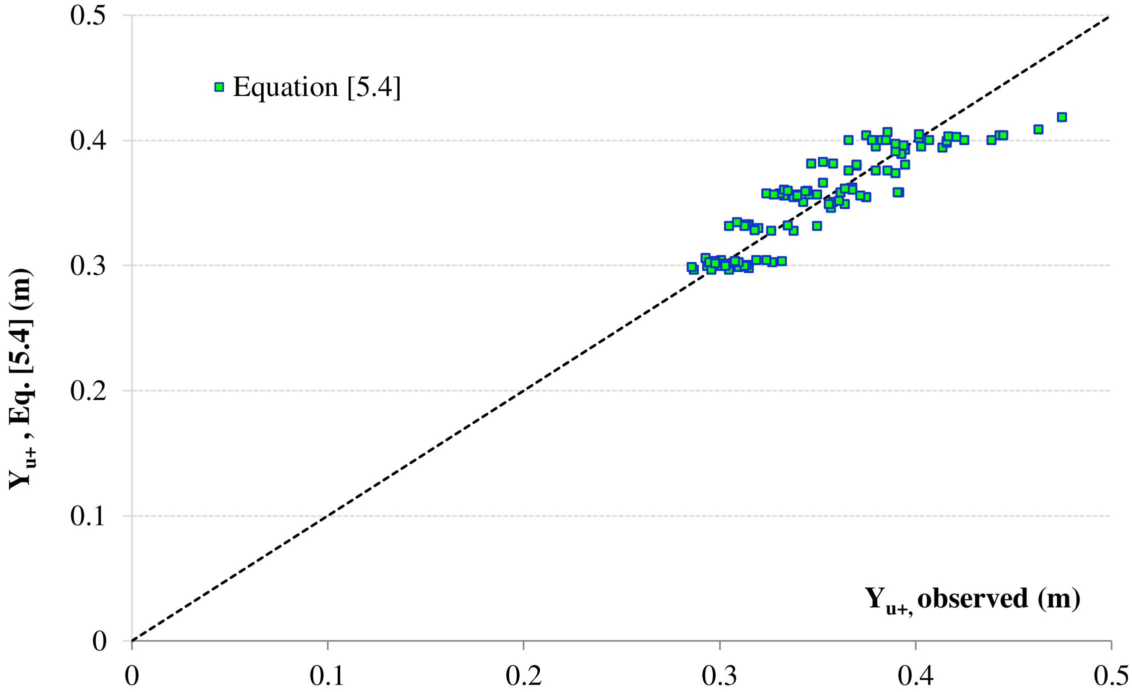

Figure 5-11: Scatter plot showing equation [5.4] vs. the observed tailwater level for the upper boundary ($Y_{u+,\text{observed}}$)

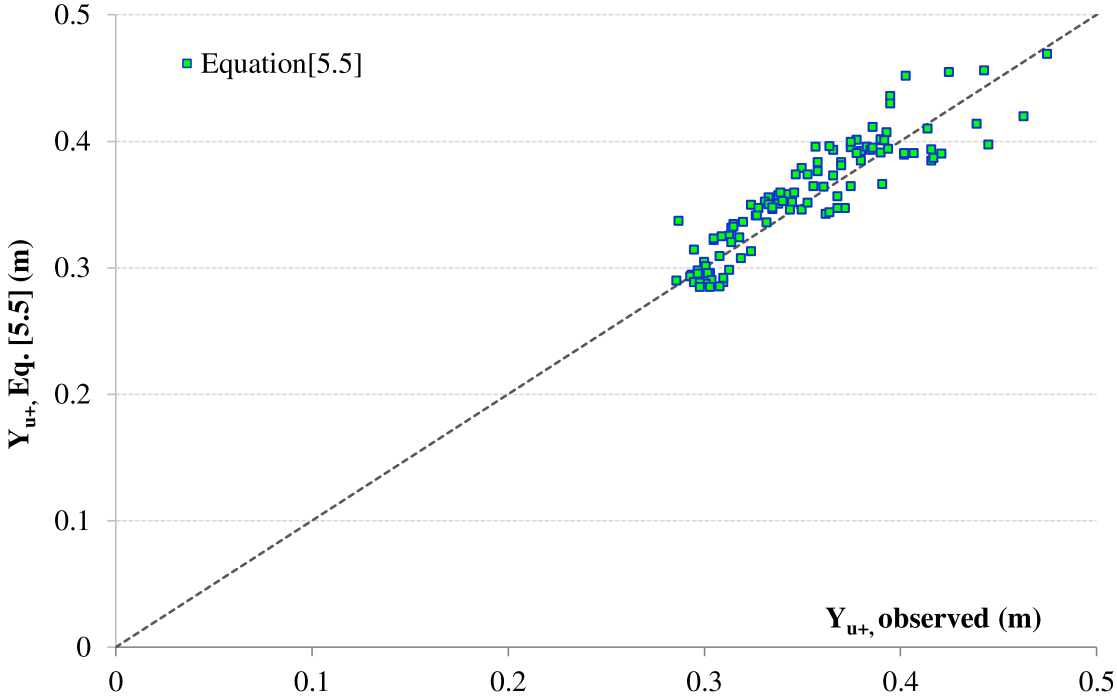

Figure 5-12: Scatter plot showing equation [5.5] vs. the observed tailwater level for the upper boundary ($Y_{u+,\text{observed}}$)

5.2.4 Vortex 'Flip' and 'Flop'

The transition from 'submerged' hydraulic jump to 'undular' roller (Y_{u+}) , induced the 'flip' of the vortex toward the free surface. This 'undular' jump is characterized by surface waves generated by downstream flow conditions with pressures different than the hydrostatic (Montes & Chanson, 1998). Oppositely, assuming the condition of 'undular' type jump, if the tailwater depth is decreased, the boundary (Y_{u-}) is reached, and the free surface waves become unstable, break, and the vortex 'flops', becoming submerged again. These boundary thresholds have been related to the upstream depth in order to assess the implications on the submerged hydraulic jump formation of increasing and decreasing, respectively, the downstream tailwater level.

In this experimental study, the authors show that the crest length and floor elevation do have an effect on the ratio $[Y_0/Y_t]$. It was found that the upper boundary for the flip (Y_{u+}), was always reached at higher water levels than for those occurring in the case of the flop (Y_{u-}). Previous work, suggested that the ratio of upstream depth Y_0 to tailwater depth Y_t was a constant value (Leutheusser & Fan, 2001), with approximate values of $[Y_0/Y_t] \approx 1.10$ for the flip and $[\mathrm{Y_0/Y_t}] \approx 1.19$ for the flop. The mathematical difference between these two numbers is explained in terms of the incomplete ventilation of the roller when the tailwater level is decreased (Leutheusser & Fan, 2001), (Tschantz & Wright, 2011).

The values for the ratio $[\mathrm{Y_0/Y_t}]$ obtained by the current experimental investigation are presented in Figure 5-13 for the vortex's 'flip' and 'flop' respectively:

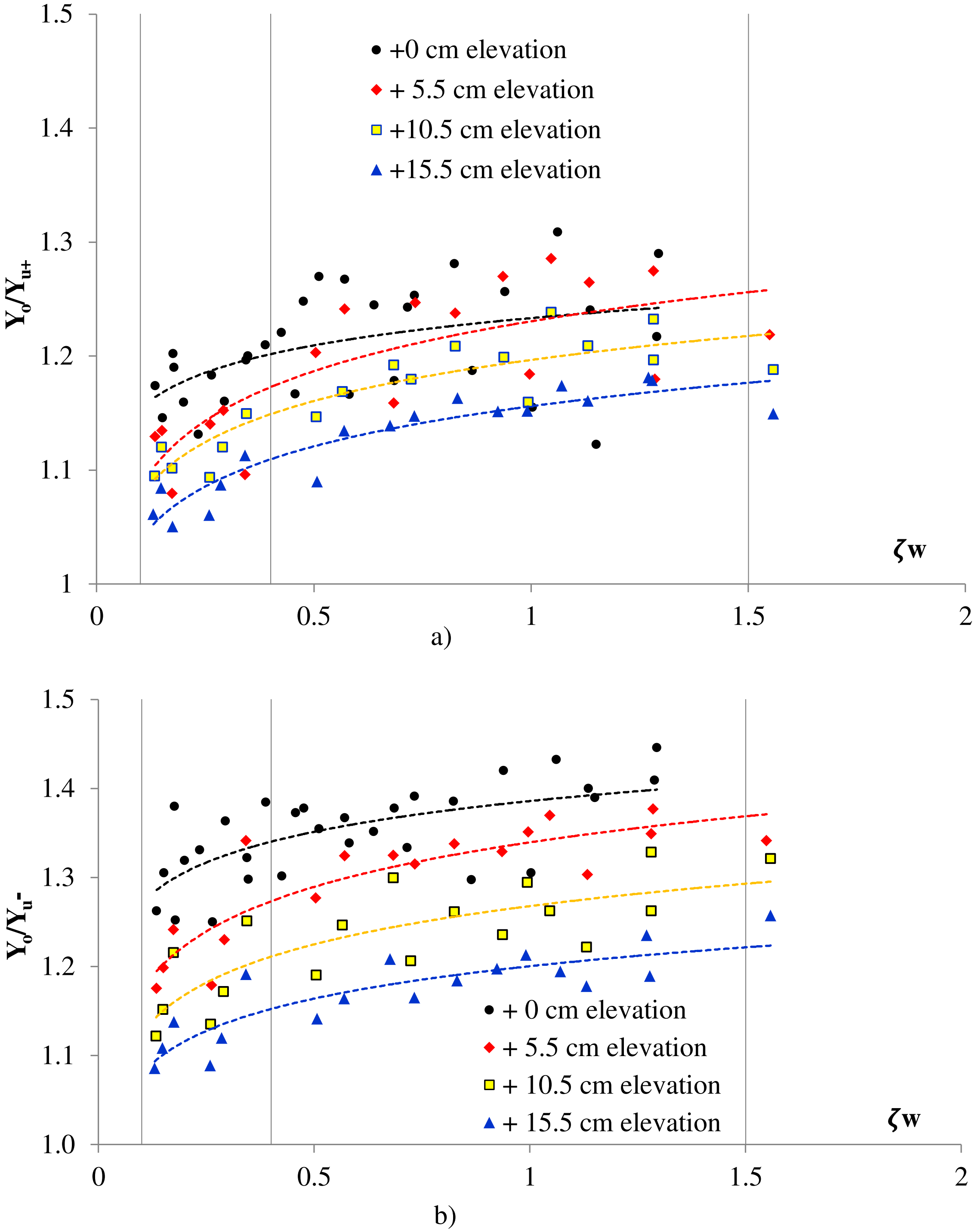

Figure 5-13: Non-dimensional tailwater depth as a function of the non-dimensional crest length (ζ_w). (a) Vortex flip (Y_{u+}). (b) Vortex flop (Y_{u-}).

The range of non-dimensional tailwater depths $[Y_0/Y_u]$ for the 'flip' Figure 5-13 a) is smaller than for the case of the vortex 'flop' Figure 5-13 b). In terms of magnitude, the previous figure also reveals that the 'flip' occurs at lower values of the ratio $[Y_0/Y_u]$ than the 'flop'. For a given discharge (constant Y_0), lower values for the ratio $[Y_0/Y_u]$ are translated into larger values of the upper boundary (Y_u). Consequently, the 'flip' occurs at larger tailwater depths than the 'flop.'

As the crest length increases, represented by lower values of the non-dimensional crest length (ζ_w), the tailwater associated to the transition (either Y_{u+} or Y_{u-}) decreases.

The net tailwater range associated to dangerous hydraulic conditions is summarized, as a function of the crest length and the downstream apron's elevation, in Figure 5-14. The yellow region represents the tailwater range which would create a classical or 'free' hydraulic jump type. The blue region is associated to surface rollers or 'undular' jump condition. The red region represents the submerged hydraulic jump domain. Therefore downstream water levels occurring within this region would induce potentially dangerous hydraulic conditions. The lower limit for the red region (physical boundary between the yellow and the red areas) is associated to the lower boundary (Y_l), while the upper limit to the red region (physical boundary between the red and blue areas) materializes the upper boundary (Y_{u+}).

Figure 5-14 represents the aforementioned limits for the low flow condition $((Q = 10l/s)$ and proves how a combination of an elevated floor and a broad crest achieve lower tailwater levels for the submerged roller's upper boundary.

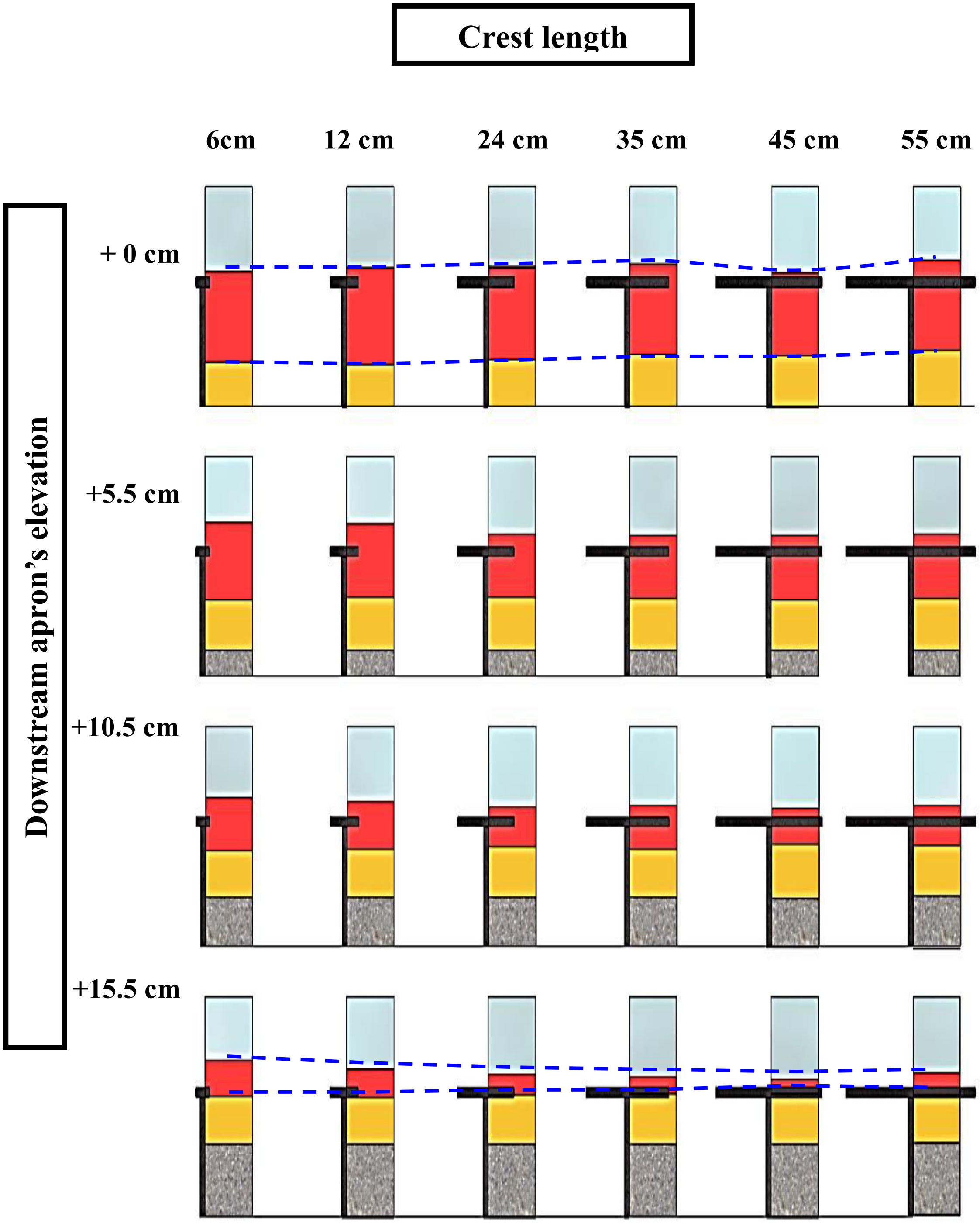

Figure 5-14: Transitional states for low discharge (10l/s) . (Yellow): Free hydraulic jump. (Red): Submerged hydraulic jump. (Blue): Surface roller.

5.2.5 Energy dissipated by the submerged vortex tailwater limits

The energy lost through the submerged roller was computed by considering a fixed upstream and downstream section. From this assumption, the energy dissipation rate therefore corresponds to the combined effect of the water overtopping the weir and the energy dissipated by the vortex formation. Figure 5-15 compares the energy loss against the ratio Y_0/Y_{t_bed}. The energy dissipated was computed by considering the water level and the averaged velocity at the upstream and downstream sections for each water depth associated to each transitional state (Y_l, Y_{u+}, Y_{u-}). Applying the energy conservation equation between the upstream and downstream sections, the dissipated energy is calculated as:

$$E_{dissipated} = \frac{E_{upstream} - E_{downstream}}{E_{upstream}} = \frac{\left(Y_0 + \frac{V_o{}^2}{2g}\right) - \left(Y_t + \frac{V_t{}^2}{2g}\right)}{Y_0 + \frac{V_o{}^2}{2g}} \tag{5.6}$$

Where the variables V_o and V_t represent the averaged velocity on the upstream and downstream sections respectively, and g represents the gravity constant. Figure 5-15 reveals that more energy is dissipated when the tailwater depth equals the submerged hydraulic jump's lower boundary. Visual observations agreed with this finding. A larger amount of entrained air, turbulence, noise and chaotic trajectory of water particles was observed when the tailwater level was set at the lower boundary in comparison with the upper boundary.

These findings reveal partial agreement with the results observed by Leutheusser and Fan (2001), indicating once more that energy dissipation decreases as the degree of submergence increases. However, Figure 5-15 shows the energy dissipated by the minimum and maximum tailwater levels inducing the submerged hydraulic jump, but it does not provide information regarding the energy dissipated by intermediate tailwater levels.

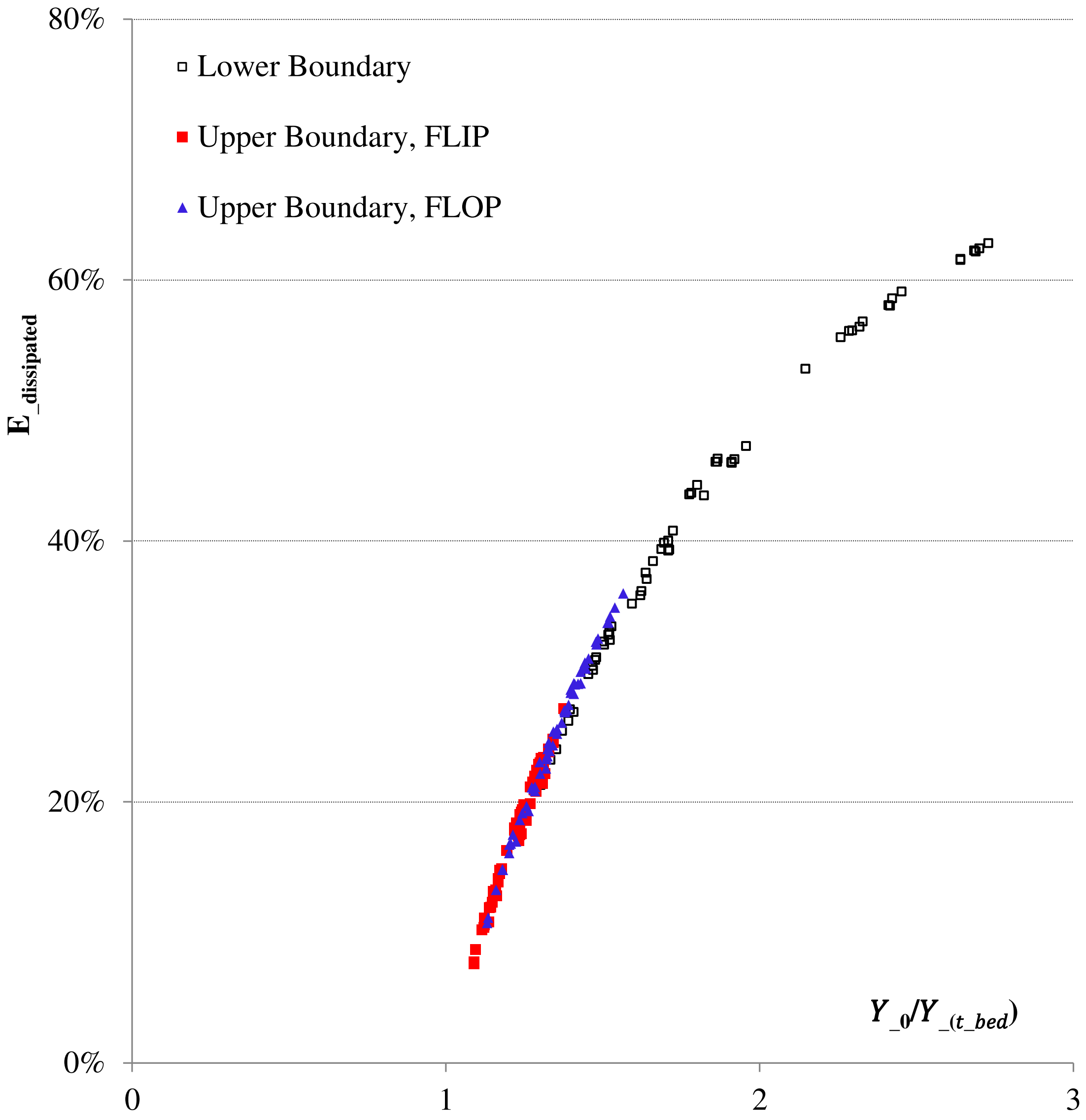

Figure 5-15: Energy dissipation rate for each transition as a function of Y_0/Y_{t_bed}

5.3 Redefinition of the degree of submergence (S)

The original definition of the degree of submergence (S), compares the local tailwater depth to the subsequent depth of the vortex, providing with an indicator of how submerged the vortex is (Govinda Rao & Rajaratnam, 1963), (Rajaratnam, 1967). This variable, which is defined by equation (2.9), presents some weaknesses which were discussed in section 2.2.1. According to this definition, the submergence (S) scores values larger than 0 for the submerged hydraulic jump condition, however, the number does not have an indicative meaning. Therefore a more submerged vortex would not necessarily obtain a larger value for the degree of submergence.

This experimental study has defined the boundaries for the submerged jump, which served to propose alternative definitions. The degree of submergence (S) has been redefined and expressed in normalized terms. This alternative definition compares the local tailwater depth, Y_t to the dangerous tailwater range associated to the formation of a submerged hydraulic jump $(Y_{u+} - Y_l)$. For increasing tailwater levels, the submergence is defined as:

$$(5.7) \qquad S = \frac{Y_t - Y_l}{Y_{u+} - Y_l}$$

This expression defines the degree of submergence as a percentage by comparing the local tailwater level to the range in which the submerged roller forms.

The definition of the degree of submergence, based on the experimental results obtained in this study, is expressed as:

$$(5.8) \qquad S = \frac{Y_t - (1.16 * Y_{crest} + z_{floor})}{\left(\alpha_{weir} * \left[{Y_0}^{\left(1-0.05*\left[\frac{H_{weir}-z_{floor}}{H_{weir}}\right]-0.03*[\xi_w]\right)} \right]\right) - (1.16 * Y_{crest} + z_{floor})}$$

The tailwater depth associated to the lower (Y_l) and the upper boundaries (Y_{u+}), are substituted according to equations (5.3) and (5.5). This definition, which compromises the simplicity of the equation in favour of its accuracy, provides the degree of submergence as a function of the physical characteristics of the weir $(H_{weir}, z_{floor}, \alpha_{weir}, \xi_w)$ and the hydraulic characteristics of the flow (Y_t, Y_{crest})

5.4 Conclusions

The submerged jump's lower boundary (Y_l) represents the minimum water level capable to produce a submerged roller. The lower boundary is therefore associated to the transition from 'free' to 'submerged' hydraulic jump. The impact of the crest length on the lower boundary depends on the flow rate: for low discharges, as the crest shortens, the lower boundary decreases. For high flow rates the opposite behavior is observed.

The lower boundary is also affected by the downstream apron's elevation: as the apron is raised, the submerged jump's lower limit is raised proportionally. Consequently the lower boundary, measured from the apron's plane (Y_{t_bed}), is constant for a given discharge. A mathematical expression (5.3) was developed to predict this lower boundary (Y_l), as a function of the upstream flow depth over the crest (Y_{crest}) and the downstream apron's elevation (z_{floor}).

The submerged jump's upper boundary corresponds to the maximum water level associated to the submerged roller formation, or minimum hydraulic tailwater depth responsible for generating a surface wave referred as 'undular' hydraulic jump. Broad-crested weirs required smaller depths to reach the upper boundary than sharp-crested ones, thereby impacting the net tailwater range $(Y_{u+} - Y_l)$ associated with the occurrence of submerged hydraulic jumps. The downstream apron's elevation mildly affects the upper boundary and elevated floors slightly increased the upper boundary.

Two equations were proposed to predict the upper boundary (Y_{u+}): (i) a simple power relation (5.4) which is a function of the upstream depth (Y_0) only and is dependent on the model, and (ii) an integral expression which improves the accuracy of the prediction by compromising its simplicity (5.5) and can be extrapolated to other setups.

It is also concluded that the crest length and the apron elevation do have an effect on the ratio $[Y_0/Y_t]$, and therefore on the vortex's 'flip' and 'flop' phenomenon. In agreement with literature, the 'flip' was always reached at higher water levels (Y_{u+}) than for the 'flop' (Y_{u-}). However, the crest length and apron elevation seem to affect the ratio $[Y_0/Y_t]$ in disagreement with previous investigations which suggested constant values of the ratio $[\mathrm{Y_0/Y_t}]$ estimated at $[\approx 1.10,]$ for the 'flip' and $[\approx 1.19]$ for the 'flop' (Leutheusser & Fan, 2001), (Tschantz & Wright, 2011).

The original definition of the degree of submergence (S) which compares the local tailwater depth to the subsequent depth of the vortex, is not explicative. The degree of submergence (S) is redefined in this chapter by equations (5.7) and (5.8) and expressed in normalized terms, by comparing the local tailwater depth, (Y_t) to the dangerous tailwater range associated to submerged hydraulic jump $(Y_{u+} - Y_l)$.

Chapter 6. Hydrodynamic characteristics of the submerged vortex

The comprehensive experimental program assessed the impact on the dynamic characteristics of the vortex through the following variables: (i) the degree of submergence, (ii) the water discharge, (iii) the crest length, and (iv) the downstream apron elevation. The investigation on the vortex dynamic characteristics centres on the analysis of the digital photographs and the physical measurements taken for the conditions described in the second stage of the experimental program (section 3.2.2). The vortex characteristics refer to dynamic aspects of the roller such as: the spatial distribution of vortex averaged velocities along the channel bed and the free surface, the downstream extension affected by the submerged vortex and the changes induced in the angle formed by the falling nappe with the downstream pool. In addition, a qualitative assessment of the air entrainment within the roller for a series of experimental arrangements was conducted.

This analysis served to draw analogies between the air-water regions defined for 'free' hydraulic jumps (Chanson & Brattberg, 2000) and those identified for the 'submerged' type jump.

6.1 Submergence: Effect on vortex characteristic

The characteristics of the vortex were compared against the degree of submergence. A series of tests performed for a constant low flow rate (10 l/s), constant crest length (6 cm), and changing tailwater levels enabled this assessment. The characteristics of each experimental run are described in Table 6-1. The degree of submergence was calculated according to the proposed formulation (5.9) developed in this study. Figure 6-1 shows the effect of the degree of submergence on the spatial distribution of the averaged surface velocity.

Table 6-1: Degree of submergence calculation

Test Code	Crest (mm)	Y_0	Y_t	Y_l (Eq. 5.3)	Y_{u+} (Eq. 5.5)	S (Eq. 5.9)
130607_1	6	0.344	0.123	0.0943	0.295	14%
130610_1	6	0.347	0.153	0.0978	0.297	28%
130611_1	6	0.346	0.202	0.0966	0.296	53%
130611_2	6	0.344	0.249	0.0943	0.295	77%

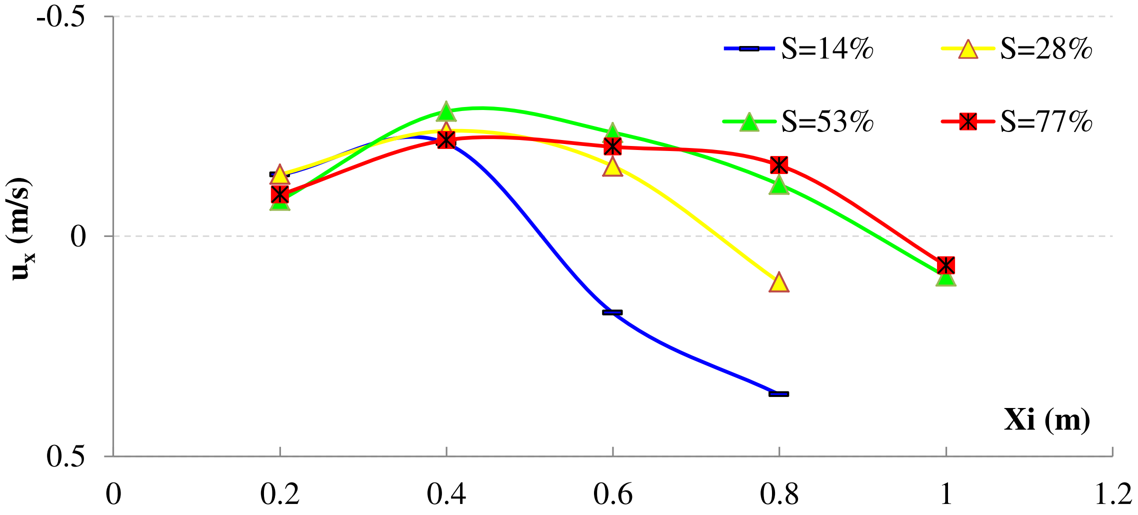

Figure 6-1: Effect of the degree of submergence on the surface velocity, u_x, corresponding to experimental data summarized in Table 6-1

It was observed that the degree of submergence did not affect the maximum value of the counter-current velocity, as seen in Figure 6-1. However, the submergence seems to affect the spatial dissipation of the surface velocity. As the submergence increases, the surface velocity curve becomes flatter for increasing abscissas(X_i). Consequently, the free surface velocity is spatially maintained as the degree of submergence increases, affecting a larger downstream extension. For degrees of submergence above 50%, the surface velocities reveal an asymptotic behaviour. Therefore, it is concluded that the downstream extension affected by the vortex increases with the degree of submergence (S) in the range of submergence [0-50%].

6.2 Flow rate: Effect on the vortex characteristics

The water discharge affected the vortex characteristics as expected: larger flow rates created vortices which occupied a larger downstream extension, and which were characterized by higher velocities, as shown in Figure 6-2. Therefore, high flow rate conditions created vortices which were judged to be more dangerous.

For an increasing discharge, the falling nappe increased its thickness over the crests and its velocity. Moreover, it was observed that the angle formed by the nappe with the downstream pool at the impingement point was affected by the discharge.

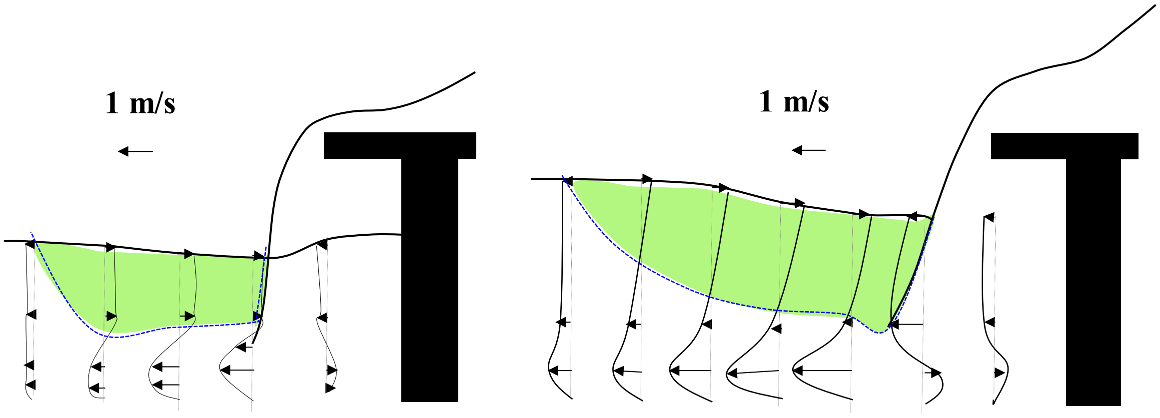

a)

b)

Figure 6-2: Characteristics of the submerged vortex formed downstream. a) 55 cm crest, Q = 10 l/s (130626_2); b) 55 cm crest, Q=50 l/s (130722_1)

6.2.1 Nappe Angle

The depth of water flowing over the weir crest directly affected the nappe angle (θ_N). Indeed as the discharge increased, the angle formed by the falling nappe with the downstream pool decreased, as seen in Figure 6-3. The nappe angle affected the vertical location where the submerged roller formed: as the discharge increased, the vortex lifted towards the free surface, affecting only to the upper portion of the downstream region. A direct relation between the discharge(Q), the nappe angle (θ_N) and the minimum thickness of the bed current (Y_b), was observed (see Figure 6-3).

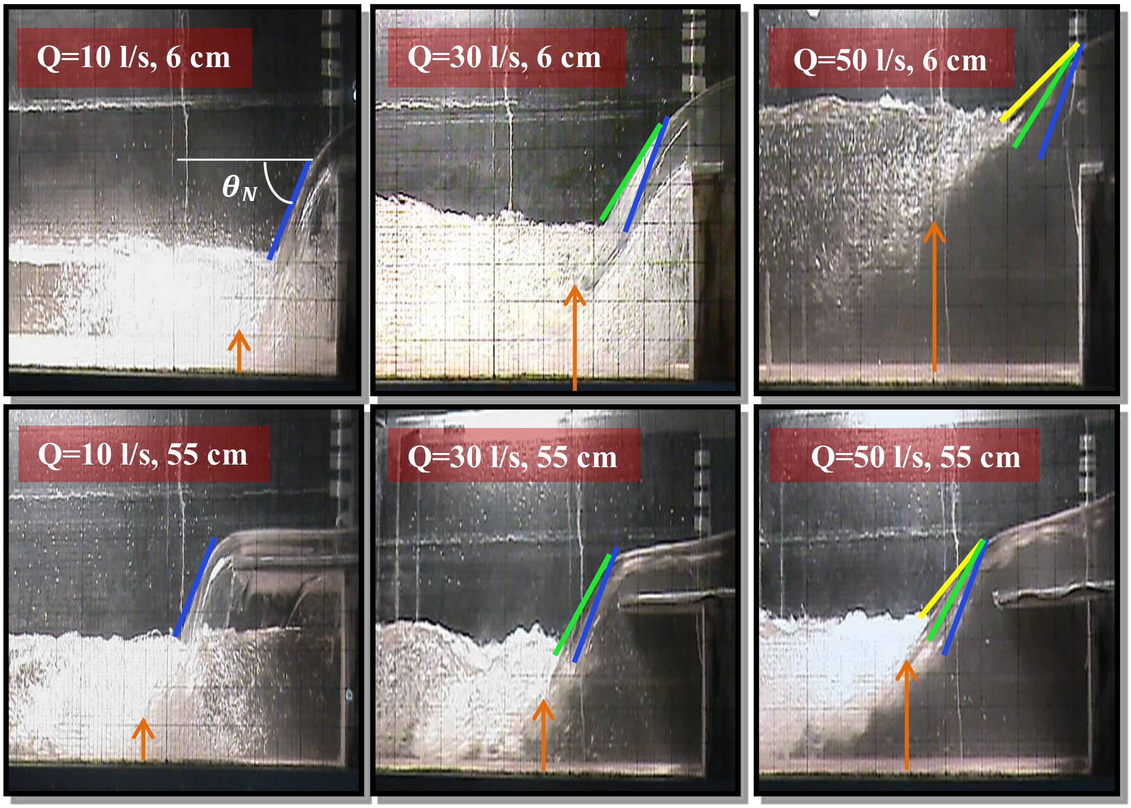

Figure 6-3: Nappe angle (θ_N), and minimum bed "thickness" (Y_b), as a function of the flow rate (blue Q=10 l/s, green Q=30 l/s, yellow Q=50 l/s. Above: sharp-crest; Below: broad-crest.

This current along the channel bed, which is analogous to a plane "wall jet", is induced by the falling nappe striking the channel bed. The thickness of the bed current (Y_b) is ultimately responsible for feeding the submerged roller by transferring the bed current's momentum to downstream sections. As the discharge increases, the nappe angle becomes milder, as seen in Figure 6-3, by comparing the blue, green and yellow lines, which represent the angle of incidence of the nappe with the downstream pool. Therefore, the bed current depth (Y_b) increases with the discharge, resulting into a larger roller, in terms of velocities and affected extension.

The crest length appears to have negligible effect on the discussed parameters, as observed comparing the top and bottom series in Figure 6-3. However, the crest length affects the location of the impingement point, which is pushed further downstream by wider crests.

6.3 Crest length: Effect on vortex characteristics

The effect of the crest length on the characteristics of the submerged vortex is determined in this section. Figure 6-4 presents the velocity profiles and area affected by the recirculation flow (in red) for 6 and 55cm crest lengths under low flow rate conditions (Q=10 l/s). The conclusions extrapolated from this representation are in agreement with medium and high flow rate results. Broad crest lengths were observed to push the vortex further downstream, as a consequence of a falling nappe which was chuted further in comparison with a sharp-crested design. In addition, a secondary recirculation vortex located below the crest and in between the nappe and the downstream face of the weir, is created for the 55cm crest, as seen in Figure 6-4-b). Moreover, the axis of the submerged vortex is quasi horizontal for broad crests, resulting into velocity profiles which are less skewed than those created by sharp crests. As a result, the downstream area affected by the reverse current is larger in extension and depth for the 55cm configuration.

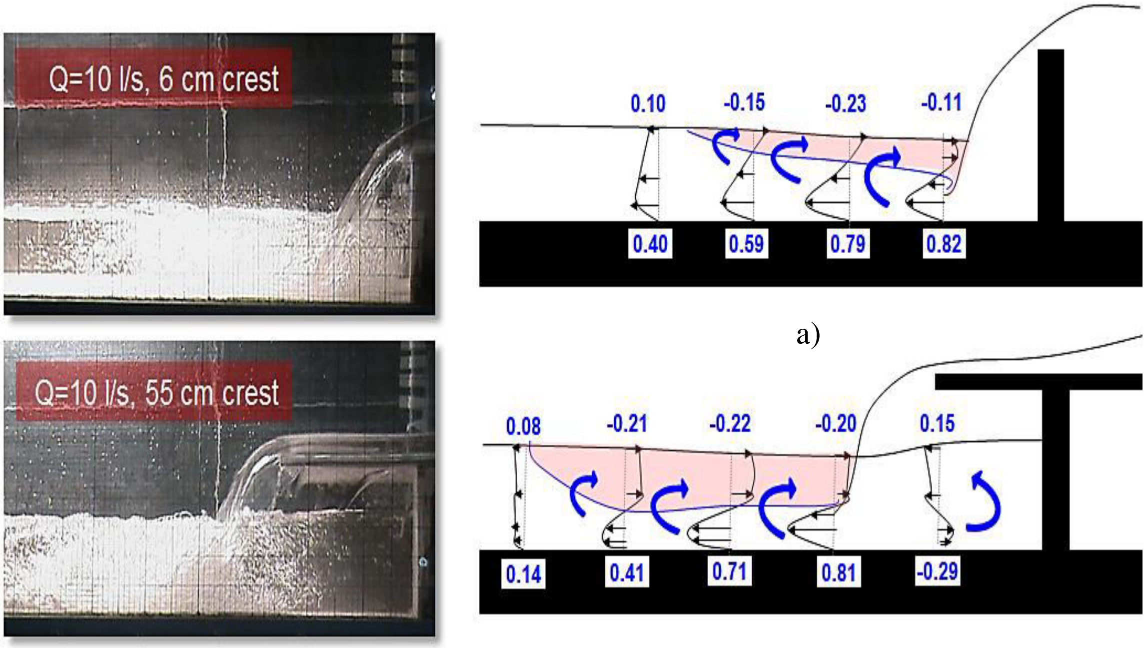

a)

b)

Figure 6-4: Effect of the crest length on the velocity profiles for Q=10l/s. Velocity measurements in m/s. a) 6cm crest (130610_1). b) 55cm crest (130626_2)

The performance of each design is individually assessed in terms of the hydrodynamic characteristics of the submerged roller.

Sharp crest configuration: The impingement process is more turbulent and entrains a larger amount of air. Larger amounts of energy are dissipated by the falling nappe when it strikes the downstream pool’s surface at the impingement point. Furthermore, sharp-crested designs lead to a reduction of the available energy which is able to feed the submerged vortex. Consequently, the roller’s extension and dynamic characteristics are reduced in comparison with alternative designs. The surface velocity reached its maximum magnitude at sections located at approximately the centre of the vortex, in the streamwise direction. At the same time, the surface velocity is heavily dissipated along the horizontal direction. As a result, there is a smaller downstream extension affected by the reverse surface current.

Broad crest configuration: The crest overflow and the nappe’s impingement processes were observed to be smoother than for sharp crest designs resulting in a reduced amount of air entrainment and turbulence. The development of the critical depth over the weir crest produces a smoother transition from the upstream to the downstream conditions, minimizing the energy dissipated by the crest overflow process. As a result, a larger amount of energy to form and feed the vortex is available. The supercritical velocity along the channel bed was slowly diminished spatially, inducing velocity profiles which revealed negative pressure on the recirculation zone. The vortex presents a quasi-horizontal axis, which translates into a larger recirculation region (in the horizontal and vertical directions).

In conclusion, broad-crested weirs produced submerged vortices characterized by higher velocities and larger downstream extensions. The hydraulic conditions identified for the sharp crest design served to judge this structure as a safer configuration than the broad crest for any potential victims entrapped in the recirculation region.

6.4 Apron elevation: Effect on vortex characteristics

An elevated downstream floor induced vortices characterized by smaller extension and velocities (bed and surface), which in all cases were judged to be safer.

Theoretically, for a given total energy at a fixed downstream section, an elevated downstream floor translates into a greater component of the potential energy and therefore, a smaller component of the kinetic energy term. Consequently, for the same amount of total energy downstream, a non-elevated floor would be associated to a null value for the potential energy and a large kinetic energy component, which is ultimately responsible for generating the submerged hydraulic jump. The effect of the apron elevation on the bed and surface velocities is presented in Figure 6-5 and 6-6. These figures represent the high discharge condition (Q=50 l/s), which is associated to the worst case scenario. Appendix B includes the graphical representations for the remaining flow conditions considered in this study.

Figure 6-5 shows that the shape of the bed velocity curve (continuous line) is not affected by the elevation of the downstream floor. The velocity peak is decreased as the apron is raised, but the form of the curve is constant for all data series. These findings are in agreement with the broad crest configuration, which is presented in Figure 6-6.

The surface velocity is more susceptible to any change in the system; the time-averaged spatial distribution shows that both the shape and the velocity peak are affected by the apron elevation. A general trend indicating that elevated aprons reduce the dynamic characteristics of the vortex for both, sharp- and broad- crest configurations, is found. Therefore, a non-elevated downstream apron leads towards a more dangerous vortex for any potential victim entrapped in the recirculation region.

The results presented in Figure 6-5 and Figure 6-6 are in agreements with those presented in section 6.3; the surface current extends to larger abscissa for broad in comparison with sharp crest configurations.

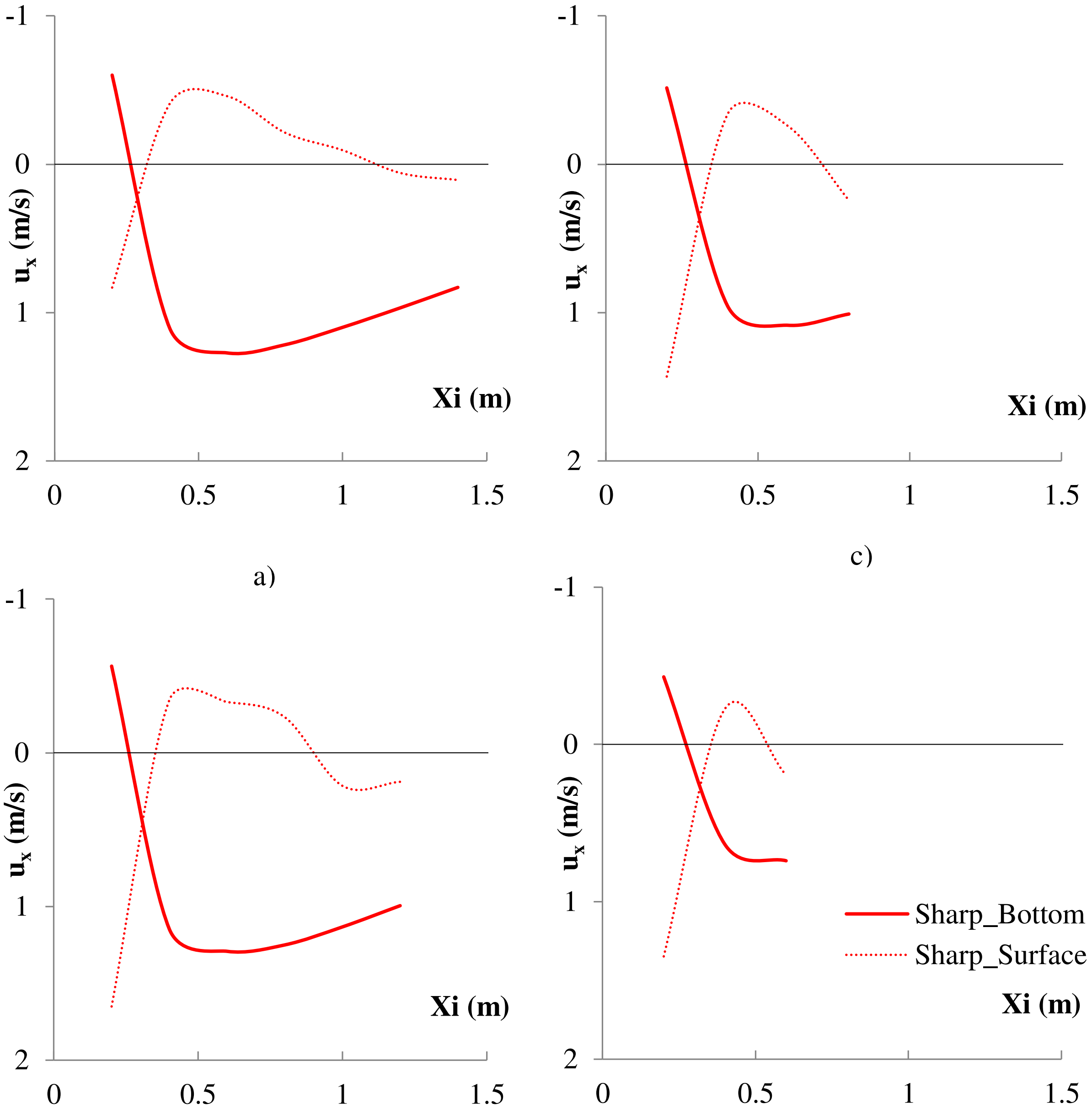

a)

c)

b)

d)

Figure 6-5: Spatial distribution of the surface and bed velocities for 6 cm crest and 50 l/s; a) $z_{floor} = 0cm$, (130715_2); b) $z_{floor} = 5.5cm$, (130827_1); c) $z_{floor} = 10.5cm$, (130807_1); d) $z_{floor} = 15.5cm$, (130816_2)

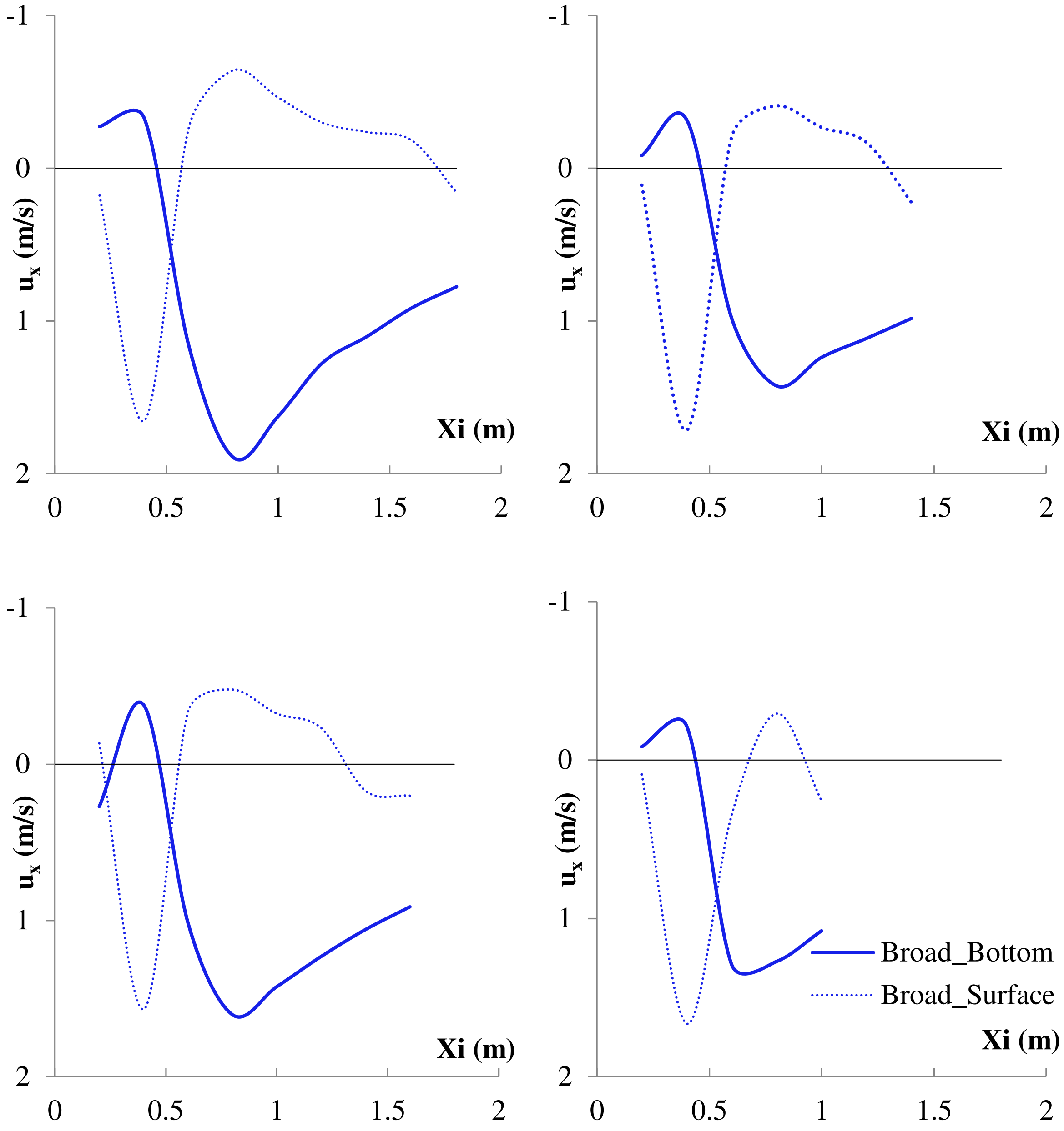

Figure 6-6: Spatial distribution of the surface and bed velocities for 55 cm crest and 50 l/s; a) $z_{floor} = 0cm$, (130722_1); b) $z_{floor} = 5.5cm$, (130826_2); c) $z_{floor} = 10.5cm$, (130806_3); d) $z_{floor} = 15.5cm$, (130816_1)

The impingement point is represented in Figure 6-5 and Figure 6-6 by the intersection of bed and surface velocity curves at the lowest abscissa. Comparing the location of the impingement for both crest lengths, it is seen that the 55cm crest series reach the impingement point at higher abscissas, in agreement with the results shown in section 6.3.

In conclusion, the downstream floor elevation affects broad- and sharp crest configurations in the same form; the dynamic characteristics of the vortex are minimized when the downstream floor is elevated.

6.5 Extension of the submerged roller

Two sources of data were considered to assess the vortex extension: (i) experimental data collected in the flume based on visual observations in combination with digital images and (ii) calculated data derived from the velocity measurements, which is based on the graphical representations shown in Figures 6-5 and 6-6, and those included in the Appendix B.

The end location of the region affected by the submerged roller (E_v) is related to the location of the impingement point (I_v). The latter is defined as the abscissa corresponding to the distance, measured from the downstream face of the weir, where the vortex begins. Therefore, the vortex length (L_v) is associated to the longitudinal vortex extension, measured between the impingement point (I_v) and the end point (E_v).

The impingement (I_v) and end (E_v) points are related to the vortex's length by the expression:

$$E_v = I_v + L_v \tag{6.1}$$

From the safety standpoint, two domains are defined in the downstream domain as a function of the downstream location of interest (X):

- If $X > E_v$ → **No risk** (abscissa outside of the range of action of the vortex).
- If $X \leq E_v$ → **Recirculation risk** (abscissa inside the region affected by the submerged roller, where a free surface counter-current exist).

A graphical schematic representation of the downstream extension affected by the vortex is included in Figure 6-7. Experimental results show that the visual identification of the end location of the vortex (E_v) is not accurate, and in most of the cases, the downstream affected extension is overpredicted. Therefore this analysis, which compares the visual observations data with the collected measurements, provides insight into the errors associated to the visual estimation of the affected downstream extension.

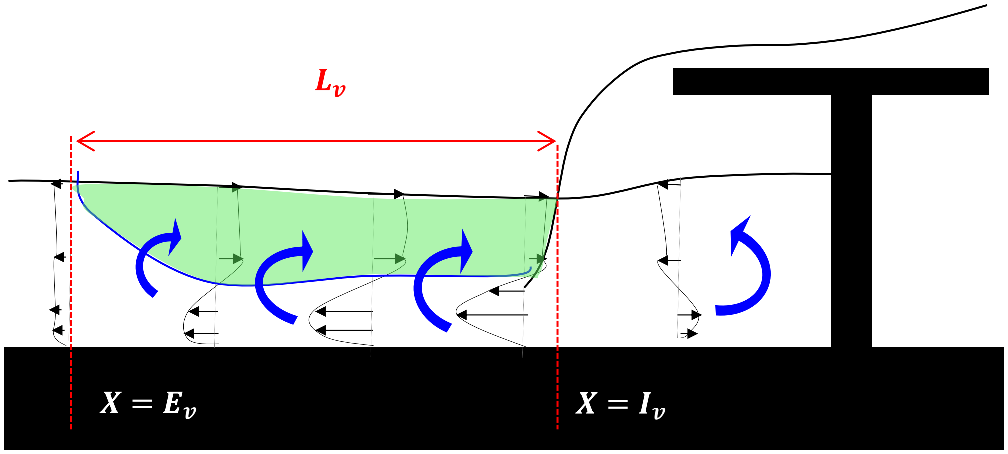

Figure 6-7: Extension affected by the vortex and identification of downstream regions

The procedure pursued to compare the experimentally calculated and observed values for the vortex extension based on two sources of information: (i) the calculated vortex extension based on velocity measurements and (ii) the observed vortex extension based on digital imagery.

6.5.1 Calculated method

The variables were obtained from the graphical representation of the spatial distribution of the bed and surface velocities. The minimum abscissa corresponding to the intersection of the surface velocity (represented by the dashed line in Figure 6-8) with the zero velocity line, indicates the beginning of the vortex $\rightarrow X = I_v$. The maximum X coordinate corresponding to the second intersection of the surface velocity with the zero velocity line indicates the end of the region affected by the vortex $\rightarrow X = E_v$. Downstream locations beyond this point $(X > E_v)$, are not affected by the free surface counter-current.

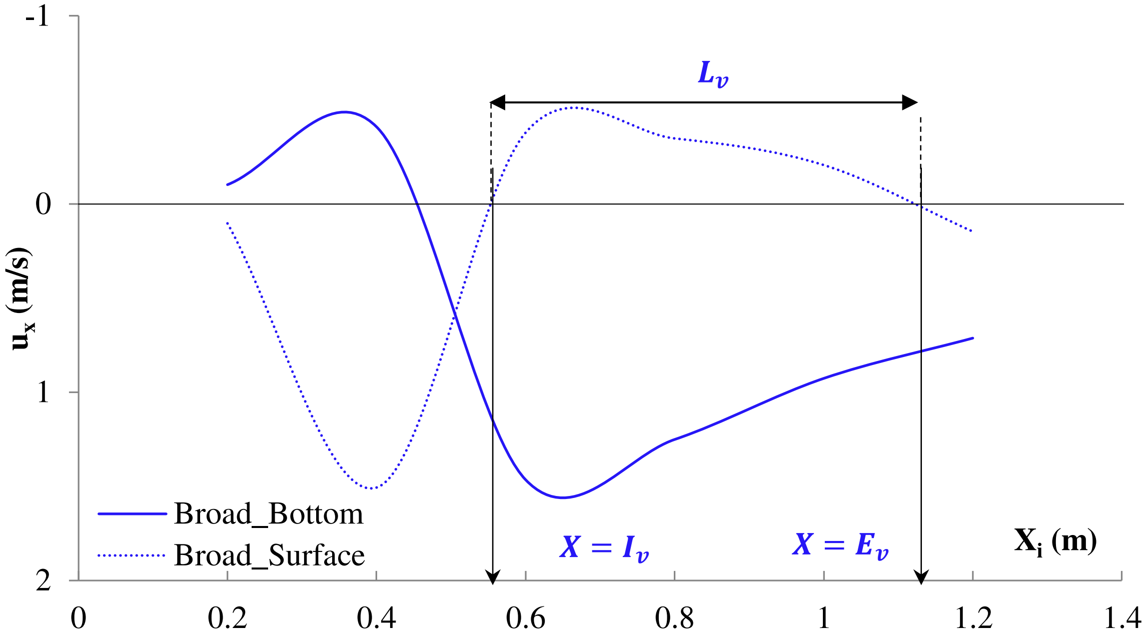

Figure 6-8: Identification of the vortex's extension based on the 'calculated method' for the test case 'M130806_2' (see Appendix B)

6.5.2 Visual method

In the visual method the variables were obtained based on the observation during the experimental runs, or the posterior analysis of the digital imagery. The identification of the impingement (I_v) and end $(E_v{}')$ points are associated to the locations indicated in Figure 6-9:

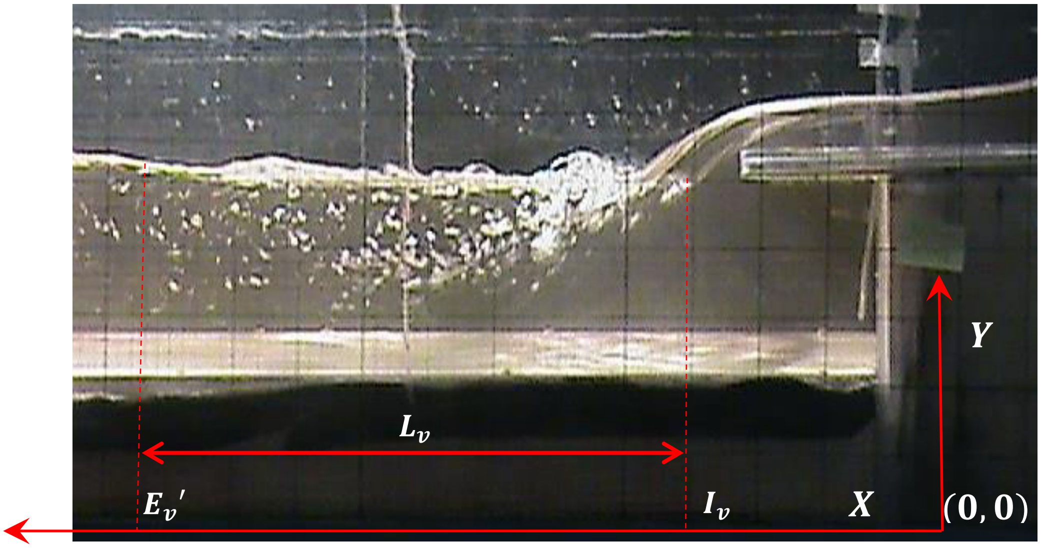

Figure 6-9: Identification of the vortex extension variables from the “visual method”

The beginning of the vortex $(X = I_v)$, was materialized by the point of intersection of the falling nappe with the downstream pool. The end of the vortex $(X = E_v')$, corresponded to the downstream location where the air bubbles did not show recirculation. As seen in Figure 6-9, there is a point where the air bubbles rose towards the free surface following a vertical trajectory, without being dragged back towards the weir, by a surface current. This location represented the end of the vortex. As in the calculated method, the vortex length L_v is mathematically calculated using the expression (6.1).

6.5.3 Comparison of calculated and visual prediction of vortex extension

The results comparing the calculated and observed vortex extension for several arrangements is presented in this section. The control variable selected to assess the differences between the visual and calculated method is the ratio between the downstream floor elevation (z_{floor}) and the weir height (H_{weir}).

For the minimum discharge $(Q = 10\ \mathrm{l/s})$ it is found that elevated aprons, represented by high values of the ratio z_{floor}/H_{weir}, reduce the extension affected by the submerged vortex, as seen in Figure 6-10. The extension of the vortex decreases drastically for downstream apron elevations above 40% of the total dam height. The solid lines in Figure 6-10 represent the results obtained by the visual method which seems to slightly overestimate the extension of the vortex. Moreover the calculated method, represented by dashed lines in Figure 6-10, predicts smaller values for the end of the vortex (E_v). Sharp-crested weirs induce a vortex that significantly affects a smaller downstream region, in comparison with the broad-crested arrangement. Table 6-2 includes the values for the extension related variables obtained for low flow rate.

Table 6-2: Experimental data concerning the vortex extension for Q=10 l/s

Condition			**Calculated**			**Observed**		
Z_{floor}	Crest	Z_{floor}/H_{weir}	I_v	E_v	L_v	I_v	E_v’	L_v
0	B	0.0%	0.27	0.94	0.67	0.37	1.00	0.63
0	S	0.0%	<0.2	0.72	>52	0.14	0.77	0.63
5.5	B	19.9%	<0.2	0.92	>0.72	0.35	1.10	0.75
5.5	S	19.9%	<0.2	0.68	>0.48	0.11	0.81	0.70
10.5	B	37.9%	0.23	0.91	0.68	0.36	1.07	0.71
10.5	S	37.9%	<0.2	0.68	>0.48	0.11	0.71	0.60
15.5	B	56.0%	0.3	0.72	0.42	0.41	0.83	0.42
15.5	S	56.0%	<0.2	0.49	>0.29	0.09	0.44	0.35

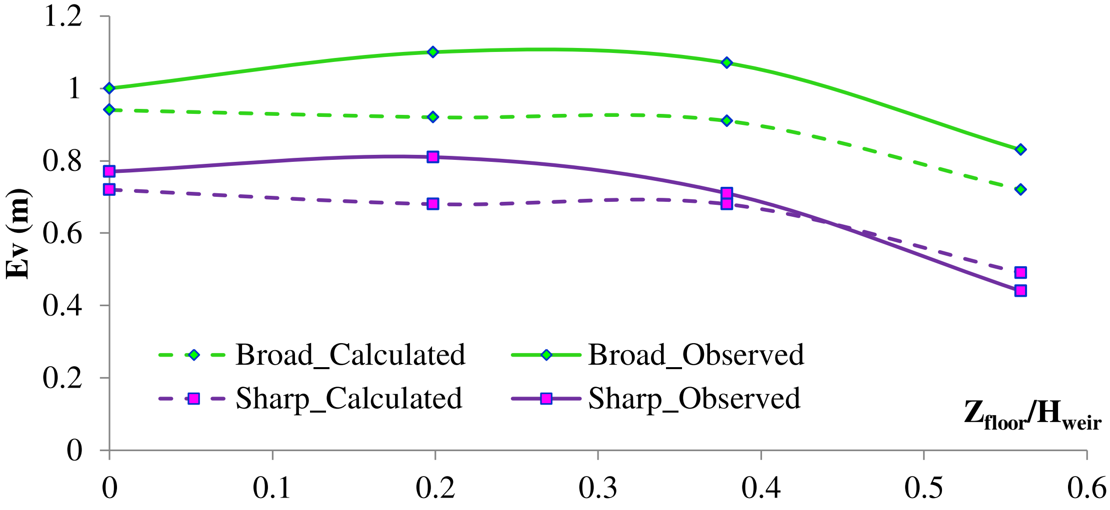

Figure 6-10: Vortex extension vs. non-dimensional apron elevation for Q=10 l/s

Appendix C shows the comparison between the two aforementioned methods to determine the vortex extension for medium ($Q = 30\ \mathrm{l/s}$) and high ($Q = 50\ \mathrm{l/s}$) flow rate conditions which, in general terms, show agreement with those found for low discharge.

Figure 6-11 summarizes the behaviour of the two crest lengths investigated, merging the results obtained for the low, medium and high flow conditions. The downstream elevation ranged between 0% and 55% the total weir's height. By elevating the downstream floor, the vortex extension reduces to a minimum of two thirds of the original vortex extension.

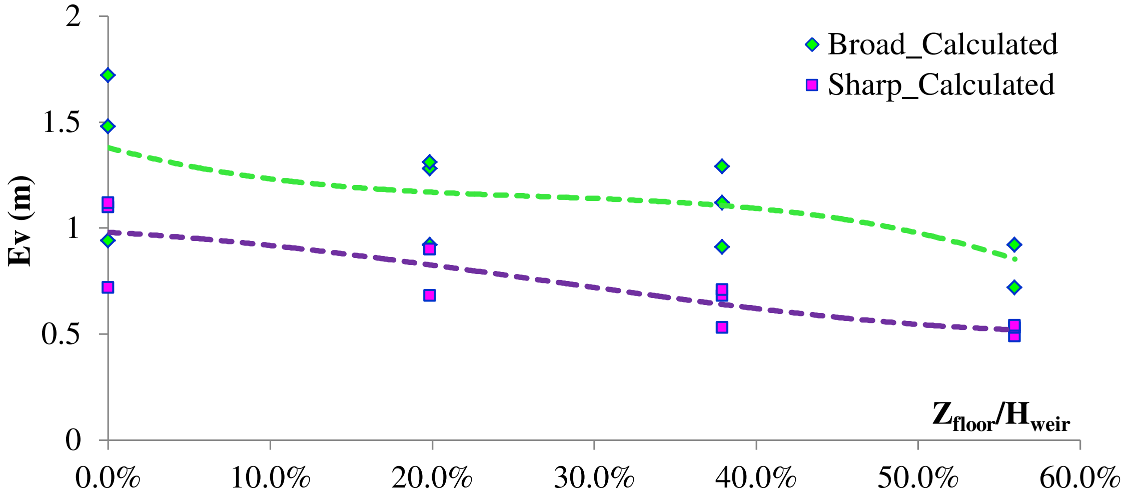

Figure 6-11: Effect of the crest length on the vortex extension

In conclusion, the visual observations were found to overpredict the extension of the vortex. The reason for this fact could be found in the methodology followed to visually identify the extension of the vortex. Visual observations determined the end of the vortex as the furthest downstream location where air bubbles are vertically dragged into the surface without showing recirculation towards the weir. This point would represent the end of the vortex along its horizontal axis, but not along the free surface. The vortex axis, represented by the green line in Figure 6-12, corresponds to depths at which the horizontal velocity is 0. The visual method would predict the vortex extension along its axis (E_v'), while the calculated method would give the extension along the surface (E_v), specifically at the elevation where the propeller meter was placed

Figure 6-12 highlights the differences between the visual and calculated method and graphically represents the reasons behind the overprediction of the former one to determine the end of the submerged roller.

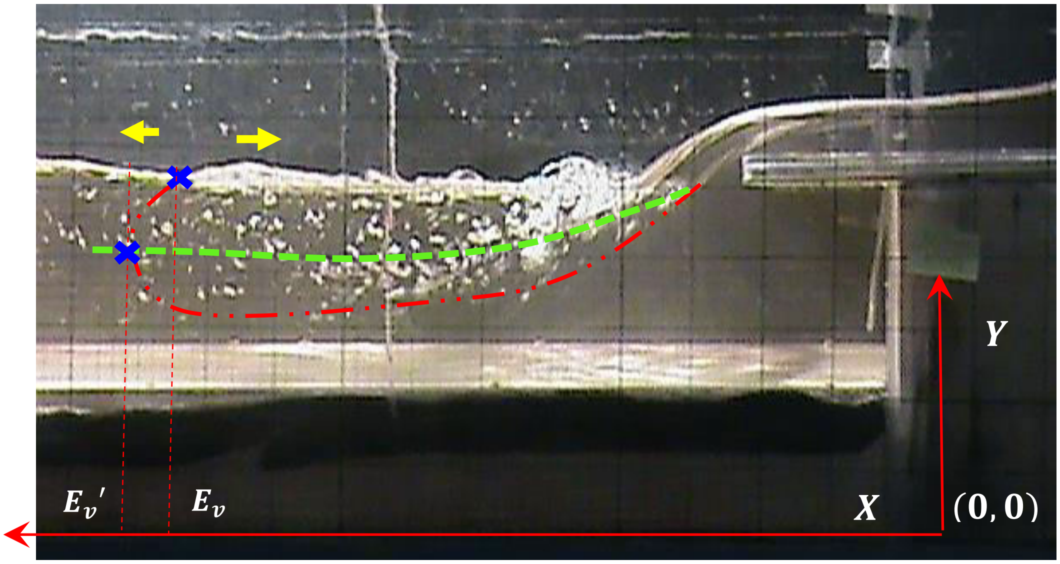

Figure 6-12: Visual identification of the region affected by the vortex; visual method (E_v') and calculated method (E_v)

6.5.4 Non-dimensional vortex extension

This section presents an analysis using the non-dimensional roller lengths, which is introduced in order to estimate the maximum length of the vortex. The maximum vortex extension was 1.8 meters for broad-crested weir and 1.0 meter for sharp-crested weir. In this section the calculated method is used to predict the end of the vortex (E_v), because of its independence from subjective interpretation of the visual observations.

The roller extension is ultimately affected by the depth of water over the crest. Therefore the vortex is expressed as a function of the ratio $E_v/(Y_0\text{-}H_{weir})$. This ratio is compared against the non-dimensional floor elevation Z_{floor}/H_{weir} .

The vortex extension reaches a maximum of 12 times the flow depth over the crest or 'freeboard' (Y_0-H_{weir}) for the broad-crested weir. This value is reduced to approximately 10 times the 'freeboard' for an elevated apron. The parallelism between trend lines seen for the several discharge (seen in Figures 6-13-a and 6-13-b), indicates that the roller extension is not sensitive to flow rate.

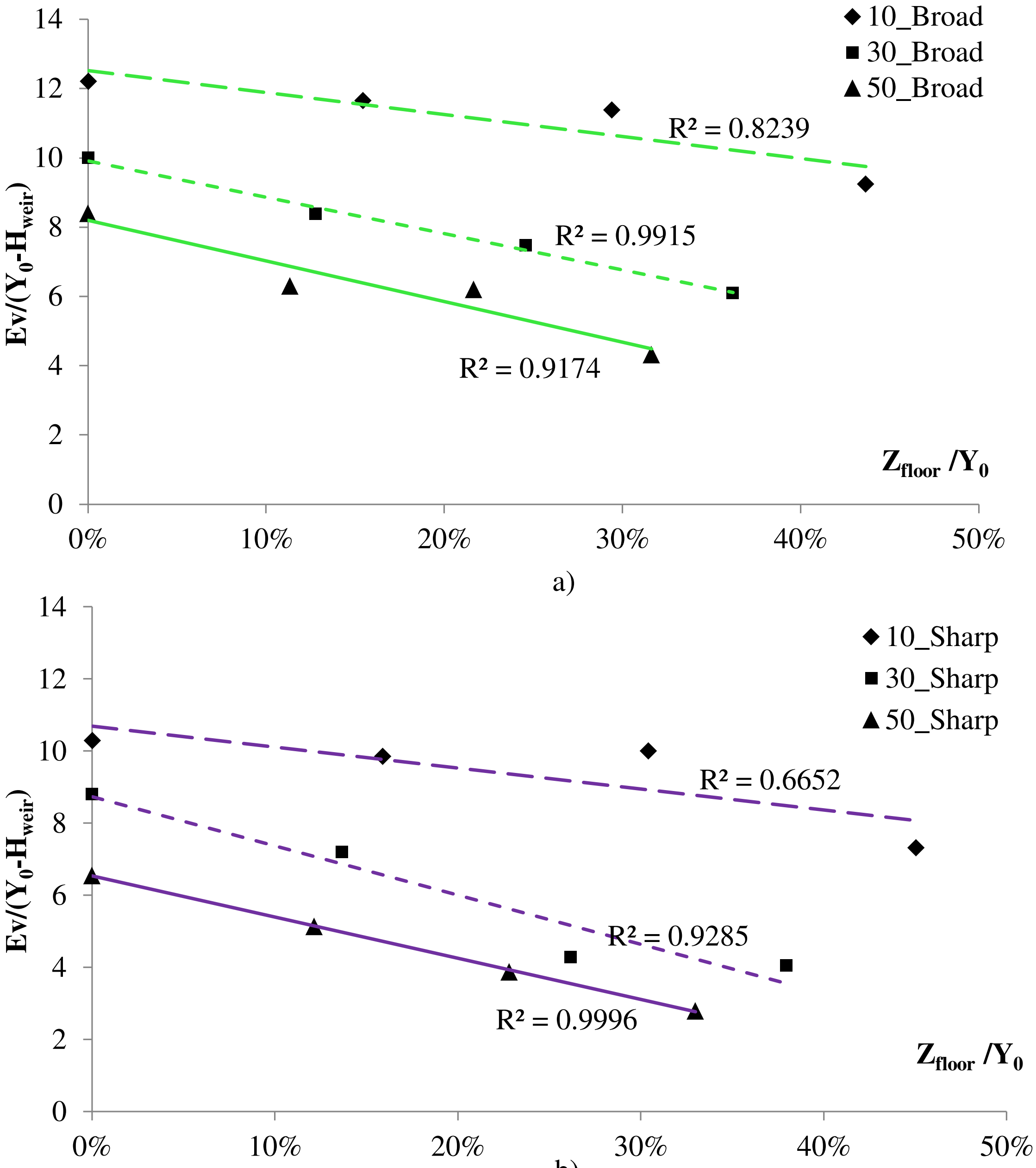

a)

b)

Figure 6-13: Non-dimensional vortex extension as a function of the floor elevation for low-, medium- and high- flow conditions: a) Broad-crested weir, b) Sharp-crested weir.

For sharp crests the vortex extension is approximately 10 times the flow depth over the crest, which could be potentially reduced about 20% by installing an elevated floor. As the discharge increases, the vortex extension benefits the most from the installation of an elevated floor, as revealed by trend curves which become steeper as the flow rate decreases (Figure 6-13-b). In the best case, the vortex could be potentially reduced up to 50% if an elevated floor is installed under high flow conditions.

6.6 Water Density – Air entrainment

The severity of the risk created by low-head dams is closely related to the amount of air entrained by the falling nappe. Air entrainment translates into a reduction of the density of the air-water mixture immediately downstream. Therefore, the buoyancy of anything or anybody entrapped by the vortex would be reduced in the same proportion, impeding their ability to surface.

The theoretical approach to measure air entrainment is intricate since many variables affect the concentration of air bubbles, the maximum depth reached by the air packets, or even the condition for air entrainment. An empirical relation to estimate the amount of air entrained by a high velocity water jet impacting the water surface was proposed by Van Sande and Smith (1973). One of their most important findings is that for lower velocity jets (as it would be in our case), the air entrainment is more irregular and highly dependent on the shape of the jet and the interaction between the jet and the receiving surface.

In 1995, Chanson obtained a first approximation to the air-water flow properties in turbulent shear flows, including the case of a plunging flow and a ‘free’ hydraulic jump. He used a conductivity probe connected to an air bubble detector to estimate the air concentration. The conductivity probe was improved in later studies, developing from a single-tip to a dual-tip probe, by implementing the principle of different electrical resistance between air and water (Murzyn & Chanson, 2007). This study provided the void fraction, bubble count rate (or bubble frequency) and other properties of the air-water flow for free hydraulic jump.

In this study, the density of the air-water mixture has been investigated by using the technique proposed by Vaideliene and Tervydis (2013). The water density reduction is a direct consequence of the air entrainment below the surface and therefore, the air concentration is directly related to the presence of bubbles within the water mass. The method proposed by Vaideliene and Tervydis for air bubble measurement is a simple technique which relies on a simple code which was implemented in Python by the author.

The proposed digital image processing had three stages: (i) to convert the colour image into a grey-scale image, (ii) to convert the grey-scale image into a binary image and (iii) to count the black and white pixels in order to estimate their ratio. This technique, was implemented on a code fully developed in MATLAB and which is included in Appendix D. Two individual routines were developed for this purpose:

Filtering Routine: The original image taken in colour is first, translated into a grey scale and second, translated into a binary image. A pixel threshold is selected for the purpose of transforming the greyscale image into a binary scale. This threshold value is defined as an independent variable in the MATLAB code, and is modified depending on the illumination sources (value and location). The output from this initial stage is an image in black and white, where black pixels indicate air and white pixels water.

Counting Routine: Once the image is filtered and converted into a binary image (black and white), the region outside of the roller's domain is discarded. This process was done case by case manually. This stage is essential, since the calculation relies on a pixel count function, which compares the pixels associated to each phase (i.e. air and water). Finally, the air entrainment (C_a) is calculated according to expression (6.2):

$$C_{air} = \frac{V_a}{V_{total}} = \frac{V_a}{V_w + V_a} = \frac{P_{black}}{P_{black} + P_{white}} \tag{6.2}$$

Where (V_a) refers to the volume of air, which in the image is represented by black pixels (P_{black}). The variable V_{total} refers to the total area considered which corresponds to the total region affected to the vortex, or the sum of volume occupied by air and water. These two amounts are represented by black and white pixels respectively. The density of the air-water mixture (ρ_{mix}) is formulated as:

$$\rho_{mix} = \frac{M_{total}}{V_{total}} = \frac{V_w * \rho_w + V_a * \rho_a}{V_w + V_a} \tag{6.3}$$

Which expressed in terms of pixel values leads to the expression:

$$(6.4) \qquad \rho_{mix} = \frac{P_{black} * \rho_{water} + P_{white} * \rho_{water}}{P_{black} + P_{white}}$$

Finally, the reduction of density in percentage terms (ρ_{red}) associated to the air-water mixture is calculated according to:

$$(6.5) \qquad \rho_{red}(\%) = \frac{P_{black} * \rho_{water} + P_{white} * \rho_{water}}{P_{black} + P_{white}}$$

This method offers a quantitative analysis of the air entrainment problem in the submerged hydraulic jump phenomenon. The idea behind this approach is quite simple however it has been proven to offer results which are comparable to more complex methods (Vaideliene & Tervydis, 2013).

6.6.1 Void Fraction

The amount of air entrained by the hydraulic jump and its effects on density change within the flow is studied in this section. Despite intensive study, many characteristics of the internal flow, the momentum transfer between the liquid-gas phases, and the air-water flow regions definition still remains uncertain for the hydraulic jump phenomenon. This topic has been physically investigated by authors such as Resch and Leutheusser in 1972, and later in 2000 by Chanson and Brattberg.

Moreover, the submerged hydraulic jump presents a very complex scenario for identification of flow regions and accurate prediction of the void fraction. The air concentration range for different hydraulic jump types was determined by Valle and Pasternack (2006) by field measurements, within the frame of natural streams. In a comparative analysis, the air concentration for 'free' hydraulic jump was found to be larger (26 to 48%) than for submerged jumps (7-24%). The range of variability accounted for the different typology of natural hydraulic jumps encountered in natural settings. These authors pointed out the air concentration attenuation along the cross-stream section as well as along the downstream section.

6.6.2 Air-water flow regions

The identification of the air-water flow regions was fully documented for a ‘free’ hydraulic jump (Chanson & Brattberg, 2000). Two main regions were identified:

- The “advective turbulent shear” region, where the moment transfer occurs between the impinging flow and the region recirculating region, located along the upper boundary. The air is entrained at the impingement point and in this region is characterized by a large amount of small bubbles.

- The ‘recirculating’ flow region, located on the upper zone is characterized by strong unsteady recirculation, high levels of turbulence, and a large amount of air entrained in the nature of large bubbles and air pockets which become foam near the free surface.

Several authors agree on the fact that air concentration distribution shows a peak in the turbulent shear region (Resch & Leutheusser, 1972), (Chanson & Brattberg, 2000). Chanson (2007) describes the air entrainment process in hydraulic jumps generated at the contact of the upstream jet and the roller, which coincides with the impingement point; air is entrained through this contact as air bubbles and air packets. The larger air bubbles are broken into very small bubbles and get entrained in the shear region, which is characterized by the maximum air concentration and bubble count rate as seen in Figure 6-14. Once entrained, the air bubbles are advected into regions of lesser shear where bubbles collide, coalescing and forming air cavities of larger dimensions. These larger entities are driven towards the free surface by a combination of buoyancy and turbulent advection into the recirculation region, where eventually are returned to the air phase through the free surface.

A third region is identified in Figure 6-14; the supercritical flow passing through the sluice gate corresponds to the “developing boundary layer”, located in between the “advective turbulent shear” region and the channel bed. In this region the flow regime resembles a plane “wall jet” typology.

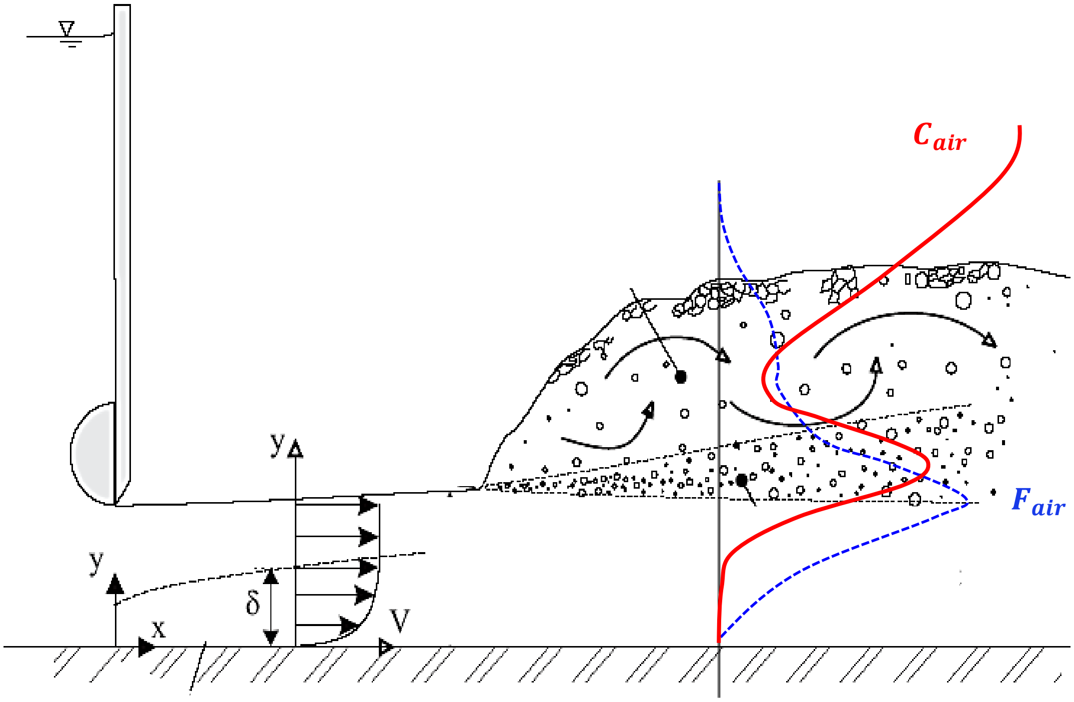

Figure 6-14: Region definition in the free hydraulic jump, as a function of the air entrainment concentration and distribution (Chanson, 2007)

The relation between the air concentration (C_{air}), the bubble frequency (F_{air}), and the 'free' hydraulic jump areas is seen in Figure 6-14. This image clearly shows the two main regions in the 'free' hydraulic jump aforementioned. The "advective turbulent shear" layer's lower limit corresponds to the minimum depth at which air bubbles are entrained. Right above this lower boundary the maximum of the bubble count rate (F_{air}) or maximum frequency of bubbles is found. The maximum concentration of air (C_{air}) is found in the middle of the "shear turbulent" layer where the peak of the (C_{air}) function is identified.

Those observations are transferred to the submerged type hydraulic jump, which is the focus of this study, in order to investigate the similarity between the regions existing in a 'free' and in a 'submerged' hydraulic jump.

Figure 6-15 compares the binary images obtained after MATLAB processing using the code developed (see Appendix D) with the original image.

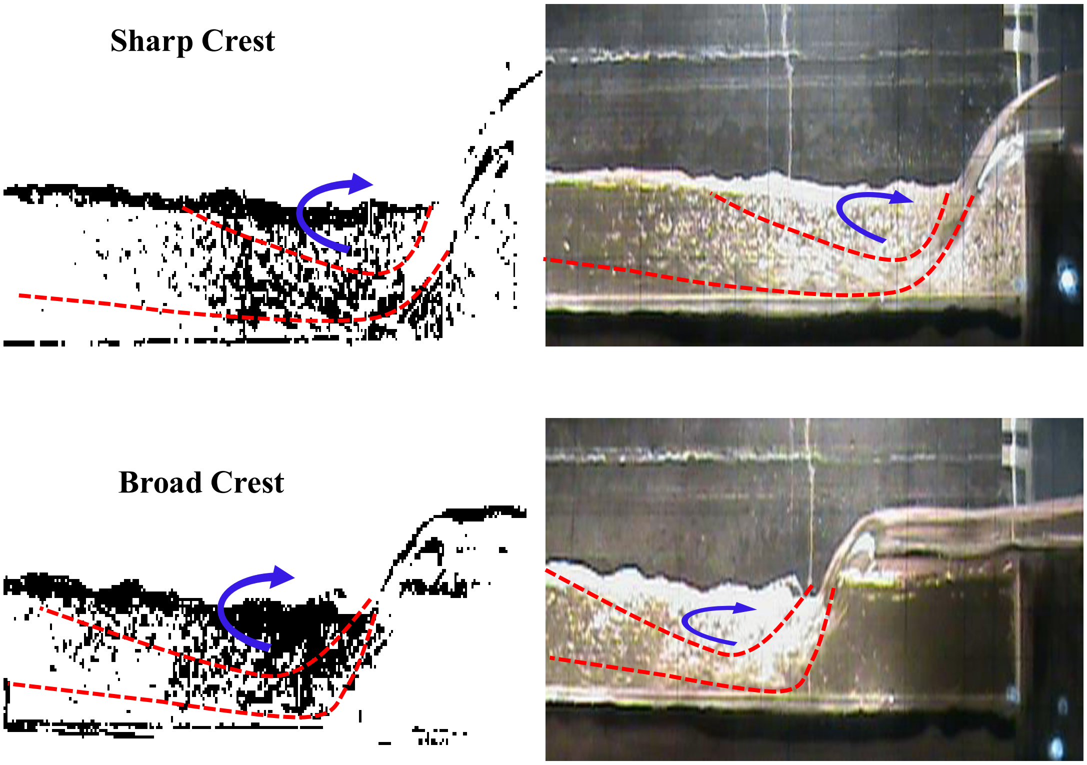

a) b)

Figure 6-15: Processed images using the developed MATLAB code. a) Processed images. b) Digital raw images.

This is a 2D estimate of the air entrainment at the wall, which is dependent on the pixel value (filter) selected to differentiate air from water. The limits of the "advective turbulent shear" layer described by Chanson in 1999 for a 'free' hydraulic jump generated by a sluice gate, can be associated to the 'lower' and 'upper' limits of the falling nappe in the case of a submerged hydraulic jump created by an overflow structure, as seen in Figure 6-15. The air is entrained because of the falling nappe strikes the downstream water body, opening two routes for air entrainment: the first one located above the nappe, and the second one below the falling nappe. Therefore, the momentum transfer between the falling nappe and the downstream pool occurs within this shear turbulent region.

The nature of the free surface counter-current is not fully understood at this stage, however its nature slightly differs from the 'recirculation' region proposed by Chanson. In submerged jumps, the 'recirculation' region shows an organized current which develops in a medium characterized by high levels of turbulence and entrained air. The explanation for the existence of an organized surface current in the submerged jump, in comparison with the ‘free’ type is related to the existence of an imposed tailwater depth.

The “developing boundary layer” located between the “advective shear turbulent” layer and the channel bed is acting as a plane “wall jet”. This supercritical bed current is deflected vertically by the imposed downstream conditions, at the boil point or end location of the vortex (E_v). It is presumed that this deflection ultimately induces the vortex recirculation and it is responsible for the development of the surface reverse current.

In conclusion, the submerged hydraulic jump is a phenomenon which is highly affected by the downstream conditions, and the development of an organized surface current is highly affected by an imposed local tailwater depth which is larger than the sequent depth for a classical hydraulic jump. Moreover, the two regions described in 1999 by Chanson for ‘free’ hydraulic jump were identified in the submerged case. The “advective shear turbulent” layer in ‘free’ and ‘submerged’ hydraulic jumps share the same characteristics, however the recirculation region differ between both phenomena. In the submerged roller, the chaotic flow characteristic of the ‘recirculation’ region becomes organized because of the presence of a higher water level downstream, which induces a recirculation pattern.

6.6.3 Density reduction within the submerged vortex

The air concentration distribution and magnitude were observed to be dependent on the crest length and the discharge over the structure. The visualization of air bubbles within the submerged roller revealed that the air-water regions (“advective turbulent shear” layer and ‘recirculation’ layer), are ultimately affected by the angle of incidence of the falling nappe.

The digital image processing method produced the results shown in Table 6-3 associated to the induced changes in density of the air-water mixture. This table shows a density reduction ranging between 20% and 50%. A preliminary observation of these values reveals that the averaged density reduction reached by the digital data post-processing method is much larger than expected.

As previously discussed, this methodology enables a quantitative analysis comparing the performance of different crest profiles and apron elevations under several discharges. The data series did not reveal any pattern regarding the impact of these variables on the quantity of air entrained. Therefore, it is ultimately suspected that the digital image processing technique is an approximate method, which is useful to assess the effect of different variables (crest length, apron elevation and discharge) on the air-water structure but not reliable to estimate the amount of air entrained. The 2D approach (at the wall) and the high dependency on the threshold pixel value selected to filter the images represent the sources of error of the method.

Table 6-3: Air concentration and density reduction for several combinations of flow rate, crest length and apron elevation

Floor elevation (cm)	Flow rate (l/s)	**BROAD**			**SHARP**		
		C_{air} (%)	ρ_{mix} (Kg/m^3)	$\rho_{reduction}$ (%)	C_{air} (%)	ρ_{mix} (Kg/m^3)	$\rho_{reduction}$ (%)
0	10	27.26	727.01	27.23	50.35	497.10	50.24
	30	27.08	728.85	27.04	40.46	595.30	40.41
	50	25.45	745.11	25.42	19.74	802.05	19.72
5.5	10	47.72	522.83	47.67	32.77	672.03	32.73
	30	34.08	659.02	34.04	10.47	894.59	10.46
	50	33.38	665.94	33.35	23.66	763.03	23.63
10.5	10	26.06	739.01	26.03	33.88	661.00	33.84
	30	39.11	608.87	39.08	22.36	775.97	22.33
	50	49.09	509.24	49.03	26.75	732.17	26.72
15.5	10	27.04	729.28	27.01	14.87	850.67	14.86
	30	39.42	605.70	39.37	12.28	876.55	12.26
	50	48.23	517.82	48.17	30.76	692.12	30.72

In conclusion, this method offers a simplified procedure to estimate the air concentration expected for submerged hydraulic jumps. In average, a density reduction of 30% is expected within the roller. However these results have several sources of inaccuracy, derived from the method selected for the analysis. Digital image analysis provides with a time-averaged value for the density reduction, neglecting the temporal variability. Additionally, the density calculated is a bulk density reduction for the entire roller, but as demonstrated by previous studies (Murzyn & Chanson, 2007), the air concentration frequency and quantity are a function of the position along the downstream and the vertical directions. In any case, these results would correspond to the maximum expected density reduction within the vortex and represent the worst case scenario, from a safety standpoint.

6.7 Conclusions

The vortex characteristics have been assessed studying (i) the spatial distribution of time-averaged bed and surface velocities, (ii) the downstream extension affected by the vortex, (iii) changes induced in the nappe's angle, and (iv) the air entrainment within the roller's domain.

The degree of submergence did not affect the maximum value of the counter-current velocity, but affected the spatial dissipation of the surface velocity.

A direct positive relation between the discharge and the vortex characteristics was found: larger flow rates created vortices which occupied a larger downstream extension and which were characterized by higher velocities. The minimum thickness of the bed current (Y_b) is ultimately responsible for feeding the submerged roller by transferring the bed current's momentum to the downstream.

The crest length revealed a high impact on the vortex dynamics. Broad-crested weirs produced submerged vortices characterized by higher velocities, larger downstream extensions and a quasi-horizontal vortex's axis. The hydraulics conditions identified for the sharp crest design served to judge this structure as a safer configuration than the broad crest configuration.

The effect of the apron's elevation on the vortex showed a linear behavior; the dynamic characteristics of the vortex are minimized when the downstream floor is elevated.

By elevating the downstream floor, the vortex extension can be potentially reduced to a minimum of two thirds of the original vortex extension. Two methods were used to assess the vortex's length: a visual method based on observations, and a calculated method based on velocity measurements. The visual observations were found to overpredict the vortex extension.

A digital image processing technique was used to evaluate the air entrainment at the vortex's core. The calculated air entrainment using this technique predicts values in the 30% mark, which is a high value in comparison with results obtained by other researchers (Valle & Pasternack, 2006).

A parallelism between the air-water regions identified for 'free' hydraulic jumps induced by a sluice gate (Chanson H. , 1999), (Chanson & Brattberg, 2000), and those identified for a submerged jump was observed. The "advective turbulent shear" layer, where the transfer of momentum between air and water occurs, share the same characteristics in 'free' and 'submerged' jumps, however the 'recirculation' region differ between both jump typologies.

The 'recirculation' region is not fully understood. However, it is believed that a vertical deflection of the "developing boundary layer", associated to the bed's current, is induced by the imposed tailwater conditions. This is the cause of the development of a surface current which characterizes the submerged roller.

Chapter 7. Results of numerical experiments

This chapter provides the results of the numerical model, assessing its performance against the experimental results. A base case was selected to assess the ability of the numerical model to simulate the submerged roller, by evaluating the spatial and temporal evolution of the free surface and the bed and surface velocities. A study of the performance of the numerical model for different arrangements is pursued to assess the impact of the crest length, flow rate and apron elevation on the numerical results. The analysis focuses on the comparison of the experimental and numerical results between a set of selected experimental tests, which are summarized in Table 7-1. Additional findings associated to the vertical velocity component, the kinetic energy and the energy dissipation rate are included. The stationary nature of the roller is also discussed.

Table 7-1: Details of the experimental runs considered for quantitative comparison.

Experimental Run Label	Q (l/s)	C_l (m)	z_{floor} (m)	y_t (m)	Variable
M-130715_2	50	0.06	0	0.300	Base case
M-130722_1	50	0.55	0	0.300	Crest length
M-130610_1	10	0.06	0	0.153	Flow rate
M-130628_1	30	0.06	0	0.236	
M-130827_1	50	0.06	0.055	0.330	Apron elevation
M-130807_1	50	0.06	0.105	0.376	
M-130816_2	50	0.06	0.155	0.414	

7.1 Base case

This section presents the numerical result associated to the base case, whose experimental characteristics are described in Table 7-1. The experimental arrangement associated to the base case coincided with the geometry of actual barriers without any of the implementations (i.e. broad crest or elevated apron), which are assessed in this study. Therefore a non-elevated apron, a sharp crest and the maximum flow rate represent this base case. The evaluation of the numerical model is accomplished by assessing the accuracy of the results at simulating: (i) the formation process of the submerged roller, (ii) the temporal evolution of the bed and surface velocities at specific control points, and (iii) the spatial distribution of the bed and surface velocities, which are shown for several downstream control sections.

7.1.1 Vortex Formation

The experimental results were obtained as a time-average measurement, collected on vortices which were already formed. On the numerical experiments, it is necessary to allow some time to achieve this condition. By allowing sufficient simulation time ($t_{sim} > 40s$), it was possible to achieve the fully formed vortex. This is associated to the definition of the model, which considers as initial condition water only behind the weir. This water eventually overflows the weir as a result of a constant discharge imposed at the inlet condition on the upstream.

Therefore, the submerged vortex was simulated by imposing an inflow on the weir's upstream and by controlling the downstream tailwater level by means of a vertical gate. As soon as the supercritical current reaches the downstream gate a reverse wave, which travels from this location towards the upstream, forms. This time period prior to the formation of the roller $[0\ s \leq t_{sim} < 26\ s]$ is seen in Figure 7-1. The advancing wave meets the upstream face of the dam after 26 seconds of simulation, as seen in Figure 7-2, which represents the period immediately after the formation of the roller $[26\ s \leq t_{sim} < 37.5\ s]$, in which it adapts and evolves in order to materialize the transition between the upstream and the downstream conditions. Finally, the vortex becomes stable for $t_{sim} \geq 37.5\ s$ seconds of simulation, as seen in Figure 7-3.

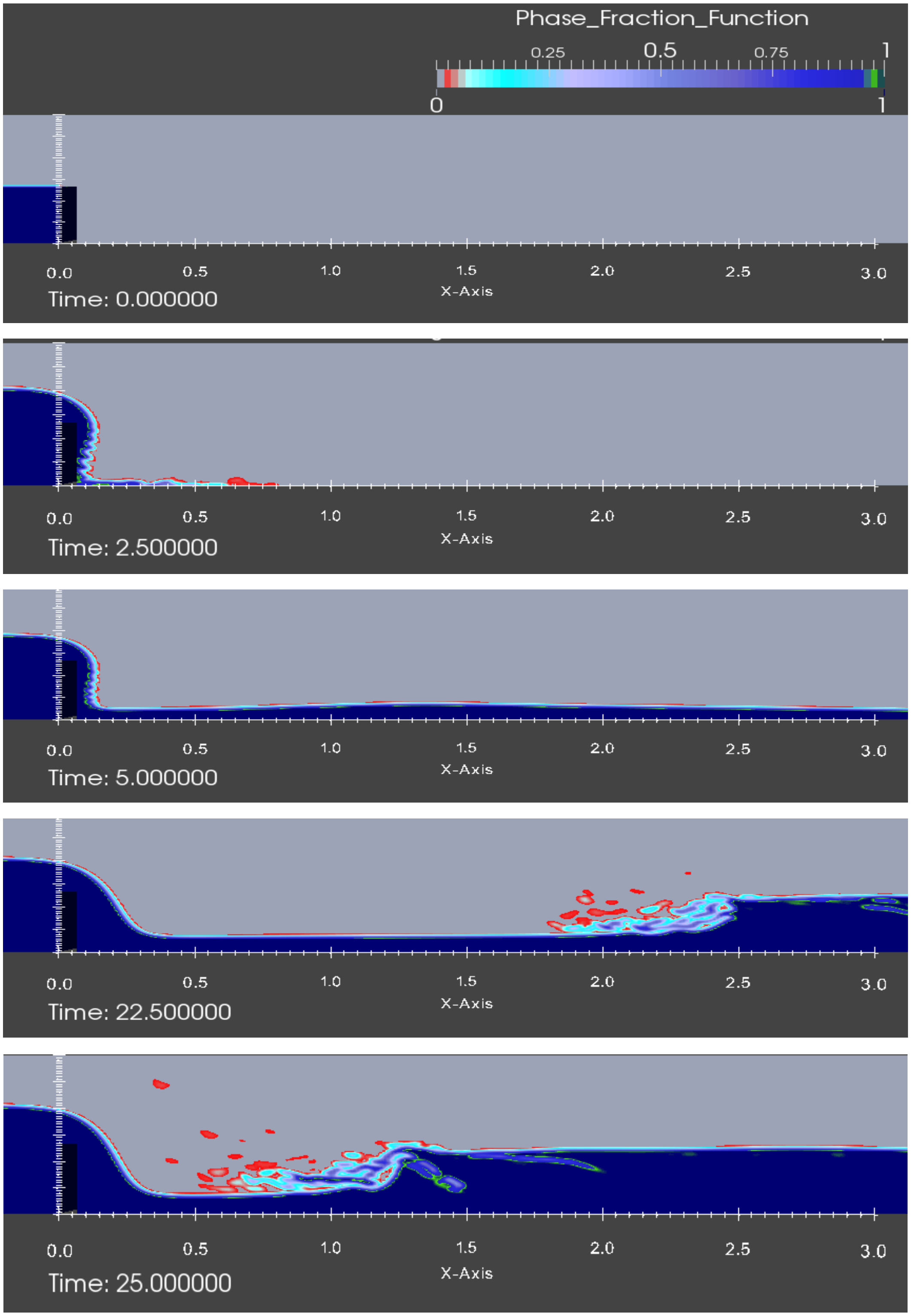

Figure 7-1: Spatial distribution of the phase fraction function (α) for time steps between $t_{sim} = 0\ s$ and $t_{sim} = 25\ s$, representing the stage prior to the roller formation.

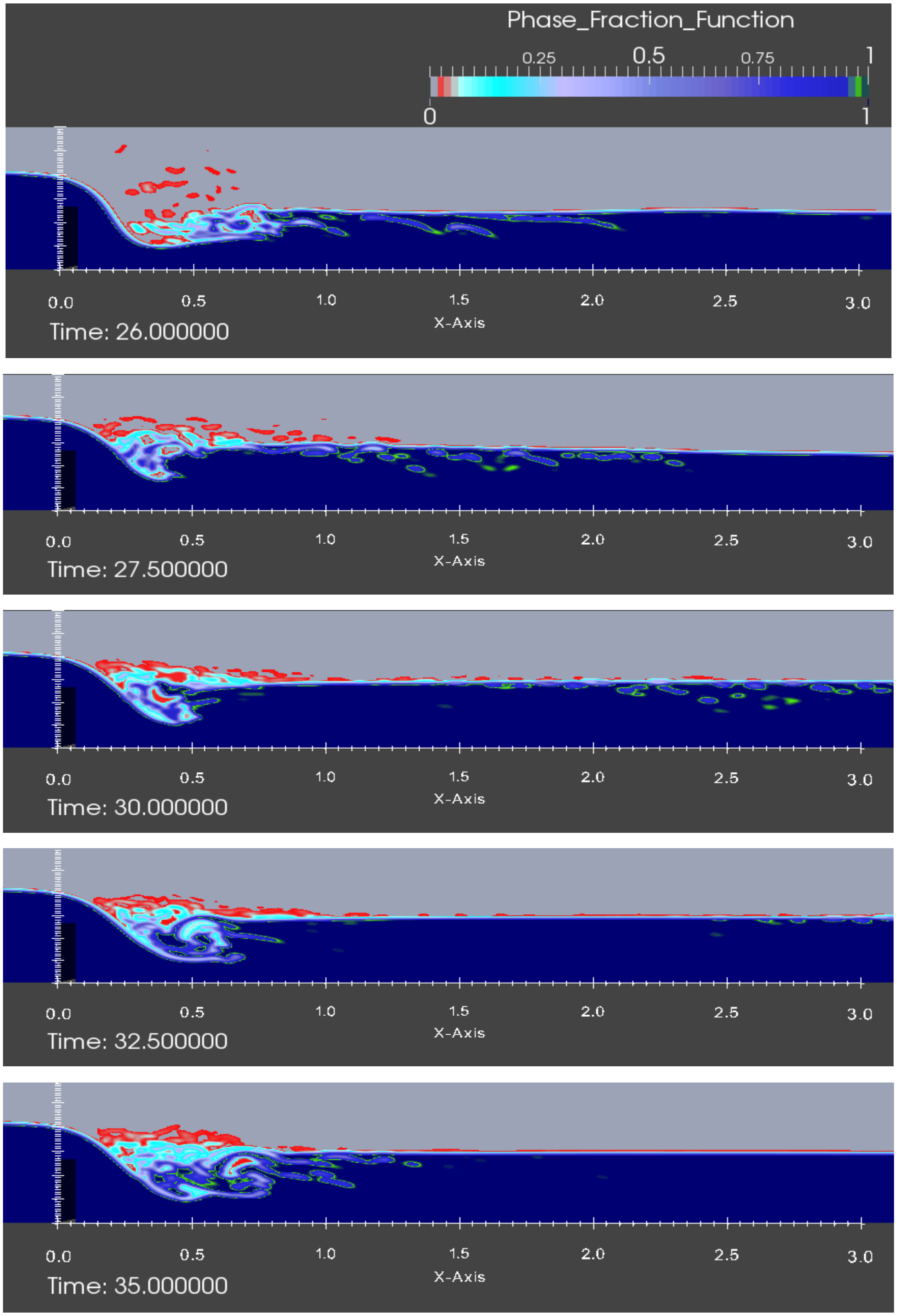

Figure 7-2: Spatial distribution of the phase fraction function (α) for time steps between $t_{sim} = 26\ s$ and $t_{sim} = 35\ s$, representing the stage posterior to the roller formation.

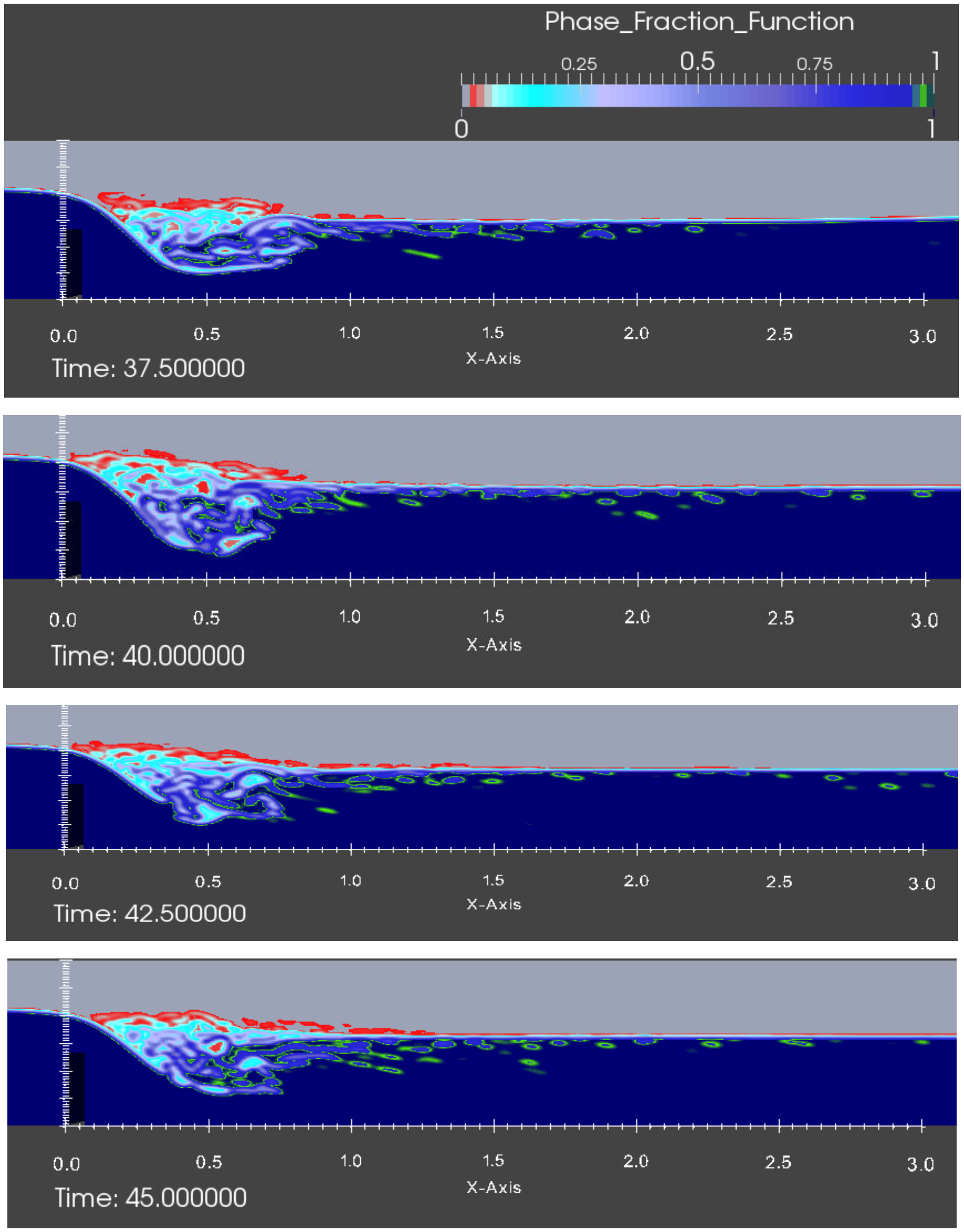

Figure 7-3: Spatial distribution of the phase fraction function (α) for time steps between $t_{sim} = 37.5\ s$ and $t_{sim} = 45\ s$, representing the stage associated to a fully developed submerged vortex.

When the vortex becomes stable, its extension increases, shedding air bubbles further downstream, as seen in Figure 7-3, in comparison with the stage when it is still forming, shown in Figure 7-2. The visualization presented of the roller formation process provides with additional information about the internal structure of the air-water mixture within the core of the vortex. Once stability is reached (Figure 7-3), the vortex expands to accommodate the amount of air within its core. As a result, the foamy top layer, characterized by large amounts of air (red colour in the figures), is elevated for this stage, increasing the total water depth. Additionally, it is observed that the vortex achieves an elongated shape along the streamwise direction, materialized by a large ‘tail’ of small bubbles (green colour in the figures), which affect far downstream locations in a continuous fashion. These characteristics represent the geometry of the submerged hydraulic jump formed by overtopping of hydraulic structures.

7.1.2 Longitudinal bed velocity

The bed velocity was measured in the experimental phase with an ADV and a propeller meter at 3 centimeters measured above the apron’s surface, at the control sections which are spaced every 0.2 meters along the longitudinal direction. The time-history of the bed velocities for control sections located in the downstream extension immediately after the weir is shown in Figure 7-4. The vortex formation stages are described as follows:

- Pre-vortex stage: Prior to the formation of the vortex $[0\ s \leq t_{sim} < 26s\ ]$. The bed velocity is associated to the supercritical flow advancing to the downstream.
- Post-vortex stage: Immediately posterior to the formation of the vortex $[26\ s \leq t_{sim} < 37.5\ s]$. The bed velocity decays once the advancing wave meets the falling nappe. This stage is associated to the adaptation of the vortex, leading to large velocity fluctuations.
- Formed-vortex stage: Stabilized vortex $[t_{sim} \geq 37.5\ s]$. The bed velocity shows an independence from time as a result of the stationary nature of the phenomenon.

The three coloured regions included in Figure 7-4 are associated to the aforementioned stages. Pre-vortex stage is represented in yellow, post-vortex stage is represented in red and finally, the blue region is associated to formed-vortex stage.

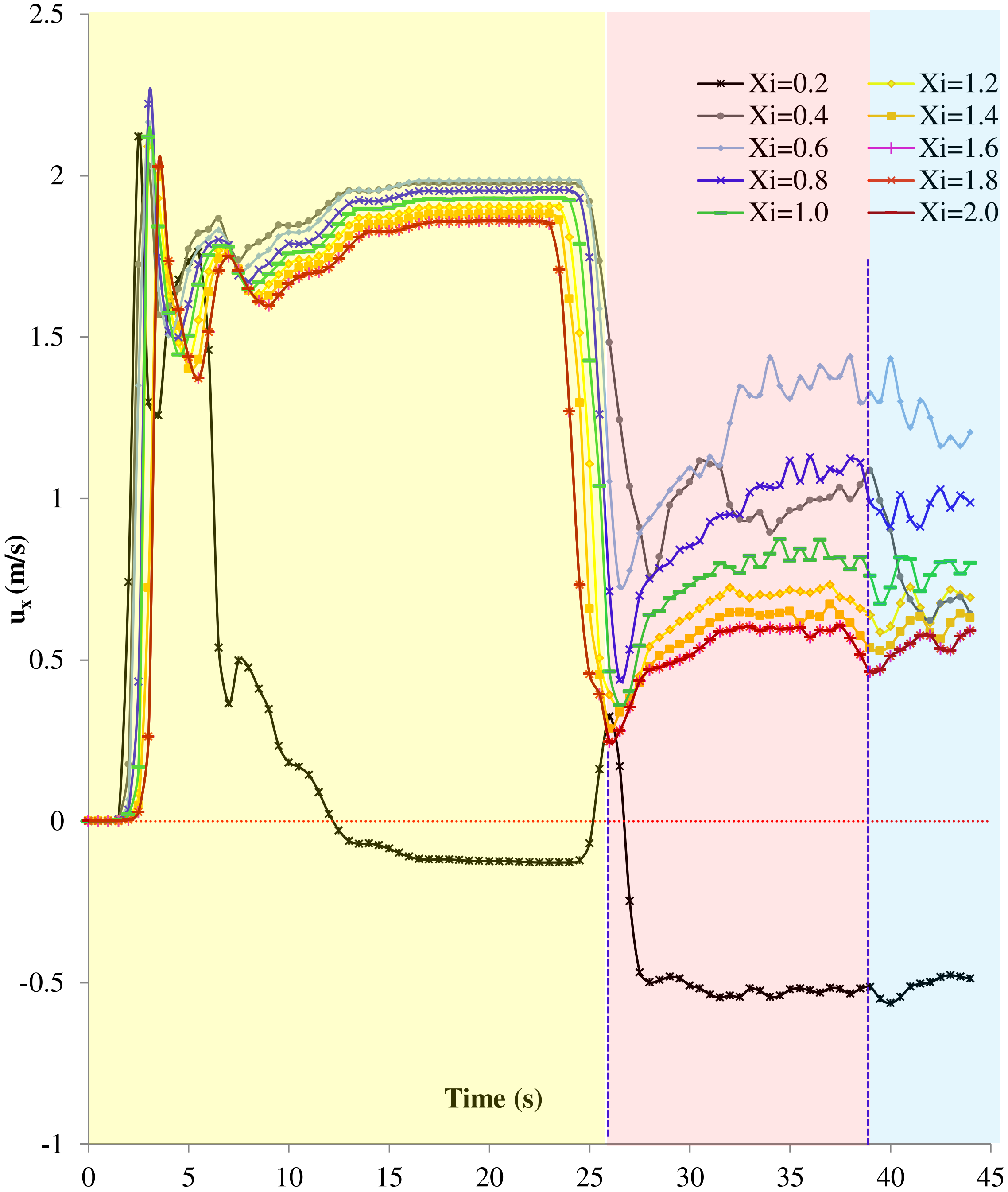

Figure 7-4: Time-history of the longitudinal bed velocity for control sections spaced 0.2 meters on the streamwise direction in the range [0.2m-2.0m].

It is observed that the control section $X_i = 0.2m$ shows a different velocity pattern than the rest of the sections. For the base case, this section is located between the downstream face of the weir and the falling nappe. At the post-vortex stage a secondary roller, which recirculates clockwise, forms in this region giving origin to the negative bed velocities.

It is also noticed that the bed-velocity is reduced, as the control section's abscissa increases. This observation is related to the loss of the kinetic energy due to friction with the bottom wall. For control points located further downstream, the velocity is exchanged for an increment of the water depth, satisfying the mass conservation principle. This differentiation of the bed velocity between control sections is especially noticed once the reverse wave reaches the falling nappe $[t_{sim} \geq 26s]$. At this point the bed velocity is largely affected by the presence of the submerged roller, with frictional/viscous effects being less significant. Higher bed velocities are induced at the sections which are affected by the presence of the roller. The bed velocity decreases as the abscissa increases, transitioning towards the downstream bed velocity value found at locations not affected by the roller existence, as seen in Figure 7.5.

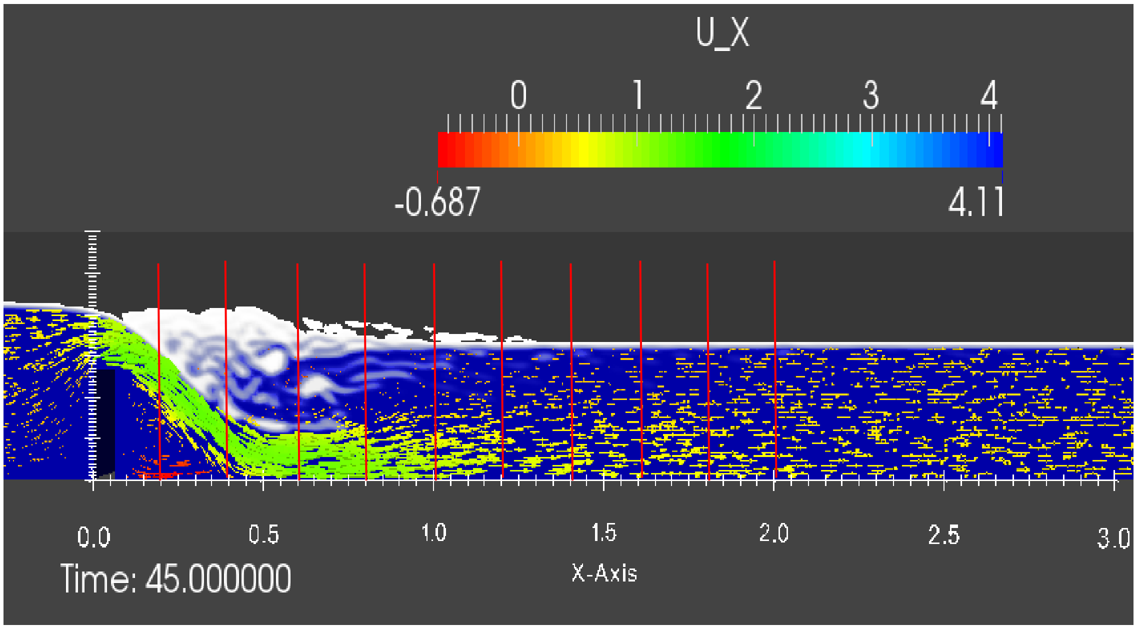

Figure 7-5: Spatial distribution of longitudinal velocity patterns for a vortex

The largest variations of the bed velocity for fully formed vortices (blue shaded region), are found in the initial sections, which are affected by the stationary vortex, as seen in Figure 7-6. The time–history for the bed velocity for the last three control sections

$X_i = 1.6\ \text{m}, 1.8\ \text{m}$ and $X_i = 2.0\ \text{m}$ show little variation from one to the next, revealing that these sections are totally outside of the region affected by the submerged roller as represented in Figure 7-7.

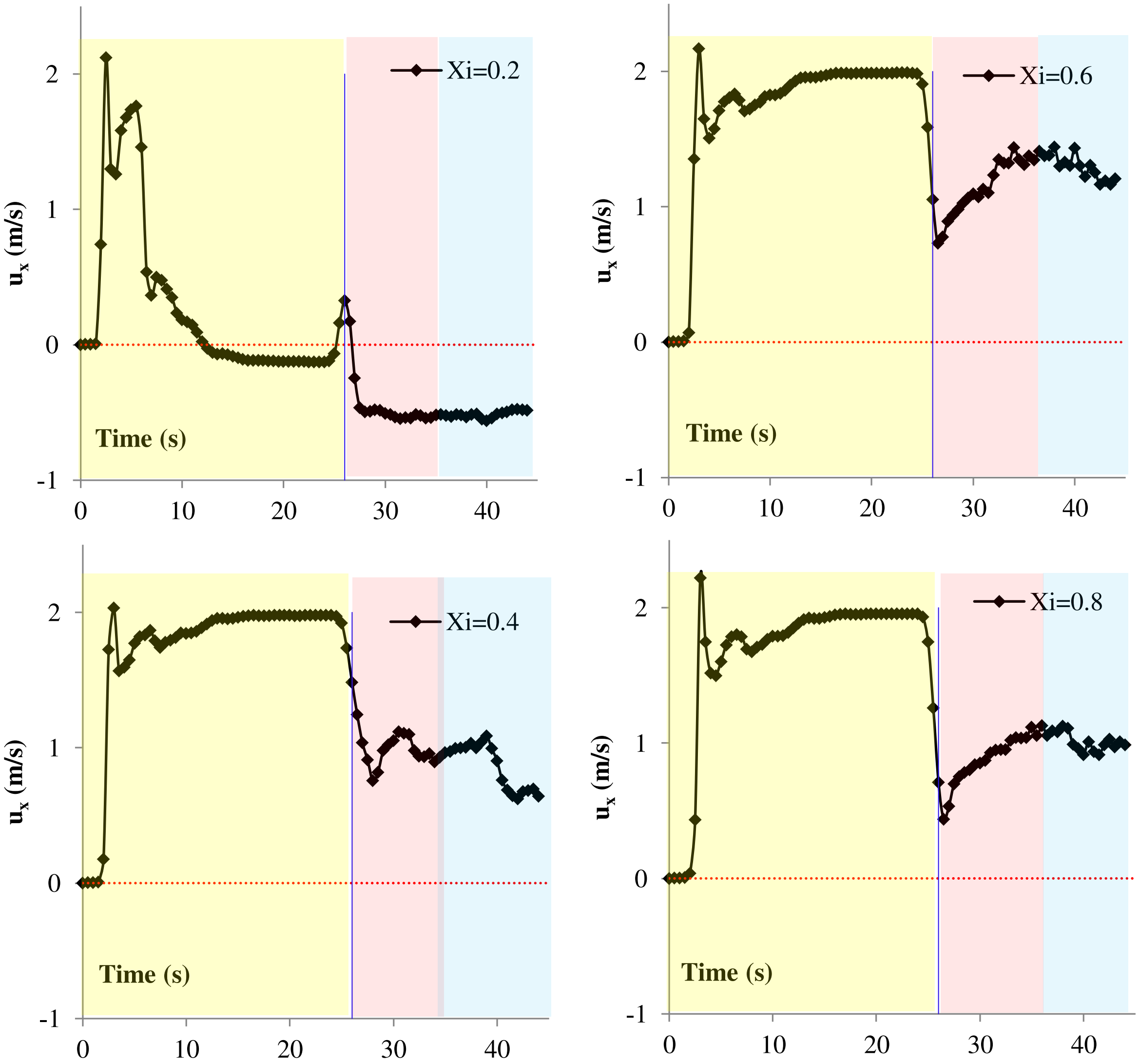

Figure 7-6: Time-history of the longitudinal bed velocity for control sections in the downstream range [0.2m-0.8m].

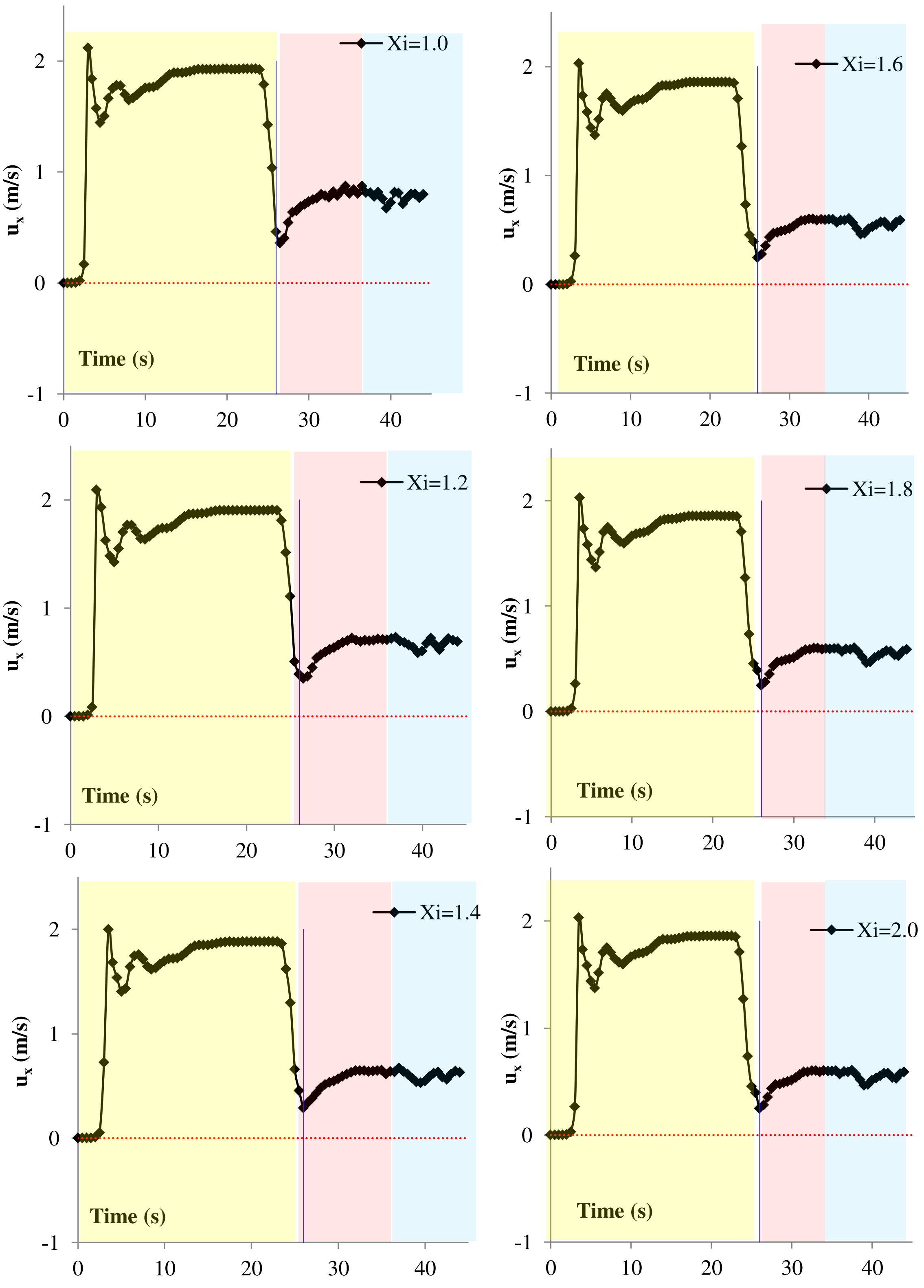

Figure 7-7: Time-history of the longitudinal bed velocity for control sections in the downstream range [1.0m-2.0m].

In order to extract the time-series shown in Figure 7-6 and Figure 7-7, the post-processing ParaView application was used. The data were extracted by slicing the entire domain with two planes perpendicular to the X and Y axes, respectively, which were defined at the coordinate of the point of interest. Afterwards, the point was manually selected and the time series for all the computed variables at that specific location was extracted.

7.1.3 Longitudinal surface velocity

The surface velocity was experimentally collected by the propeller meter measurement device, which provided the time-averaged velocity at specific control points placed 1.5 centimeters below the water surface. One of the main differences between surface and bed locations is that the surface cells are filled with either air, water, or an air-water mixture (foam). The indicator function for cells located along the surface, medium, and bottom depths is shown in Figure 7-8, 7-9 and 7-10, respectively, reaching values of 0 if fully occupied by air and 1 if full of water.

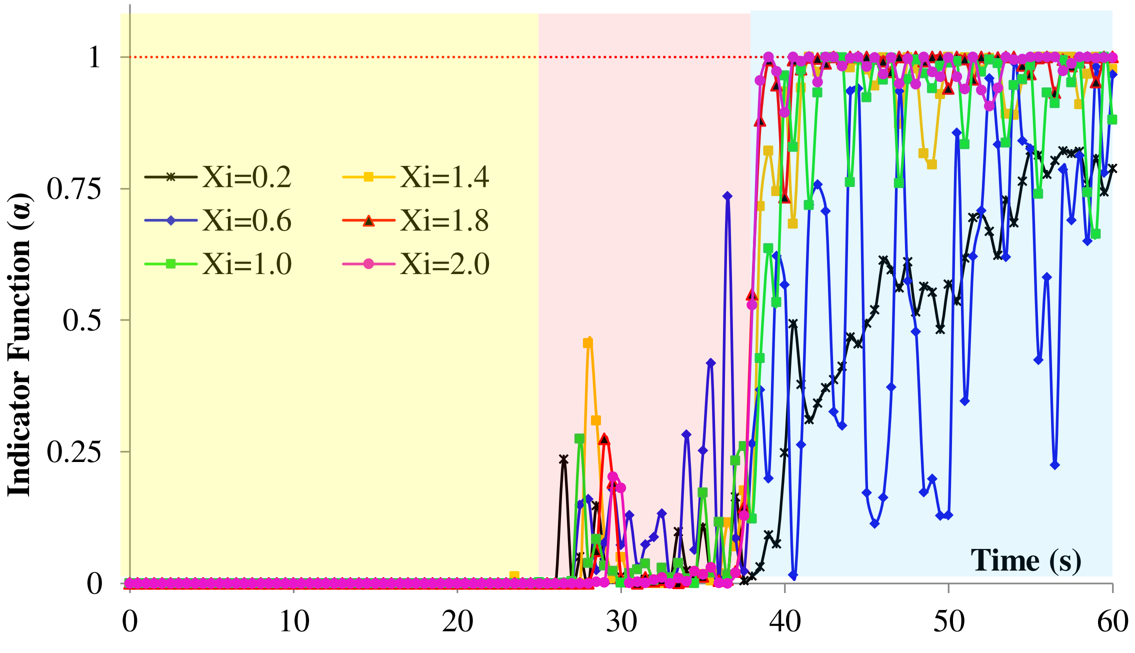

Figure 7-8: Time-history of the indicator function along the free surface (Y = 0.3m)

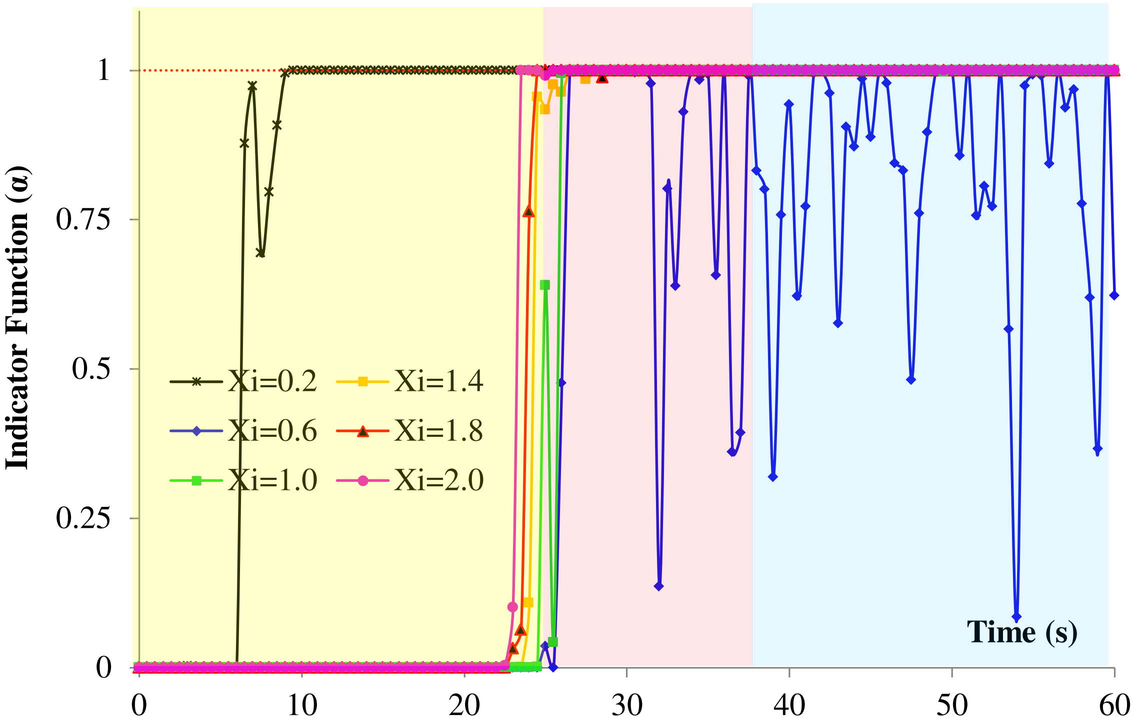

Figure 7-9: Time-history of the indicator function along the middle depth (Y = 0.16m)

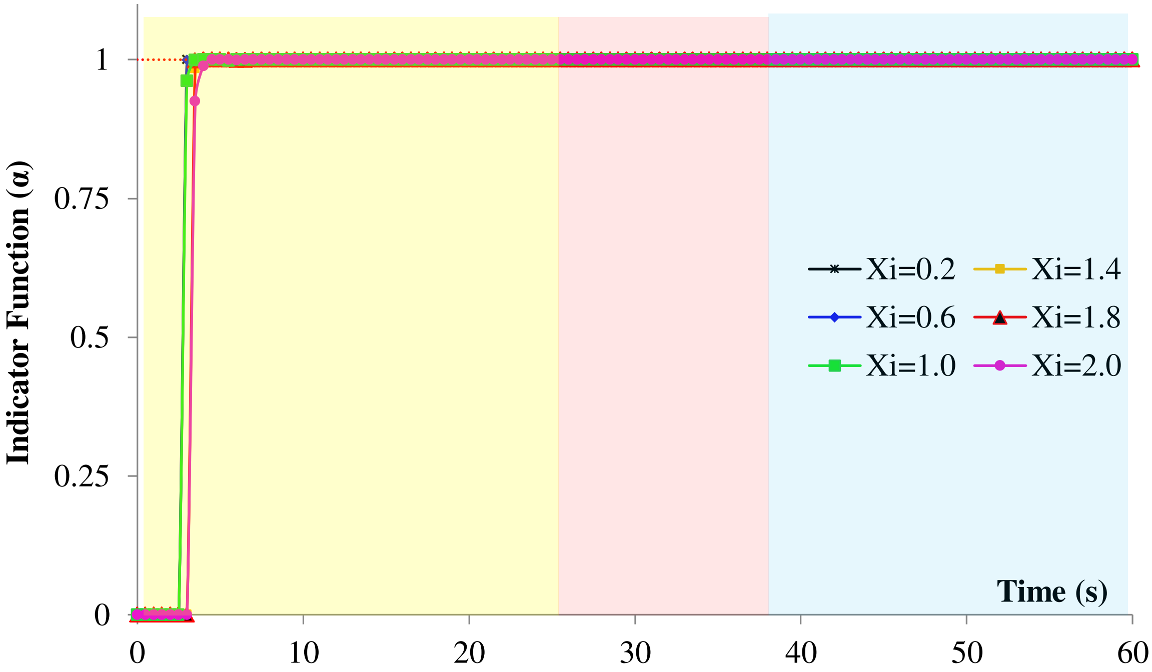

Figure 7-10: Time-history of the indicator function along the bed (Y = 0.03m)

The surface velocities presented in Figure 7-11 do not correspond necessarily to water, but to the fluid, which at each time step occupies the corresponding cell. For the formed-vortex stage the cell is full by water mainly, as seen in Figure 7-8. This reveals the stability of the vortex at this stage in comparison with the post-vortex stage.

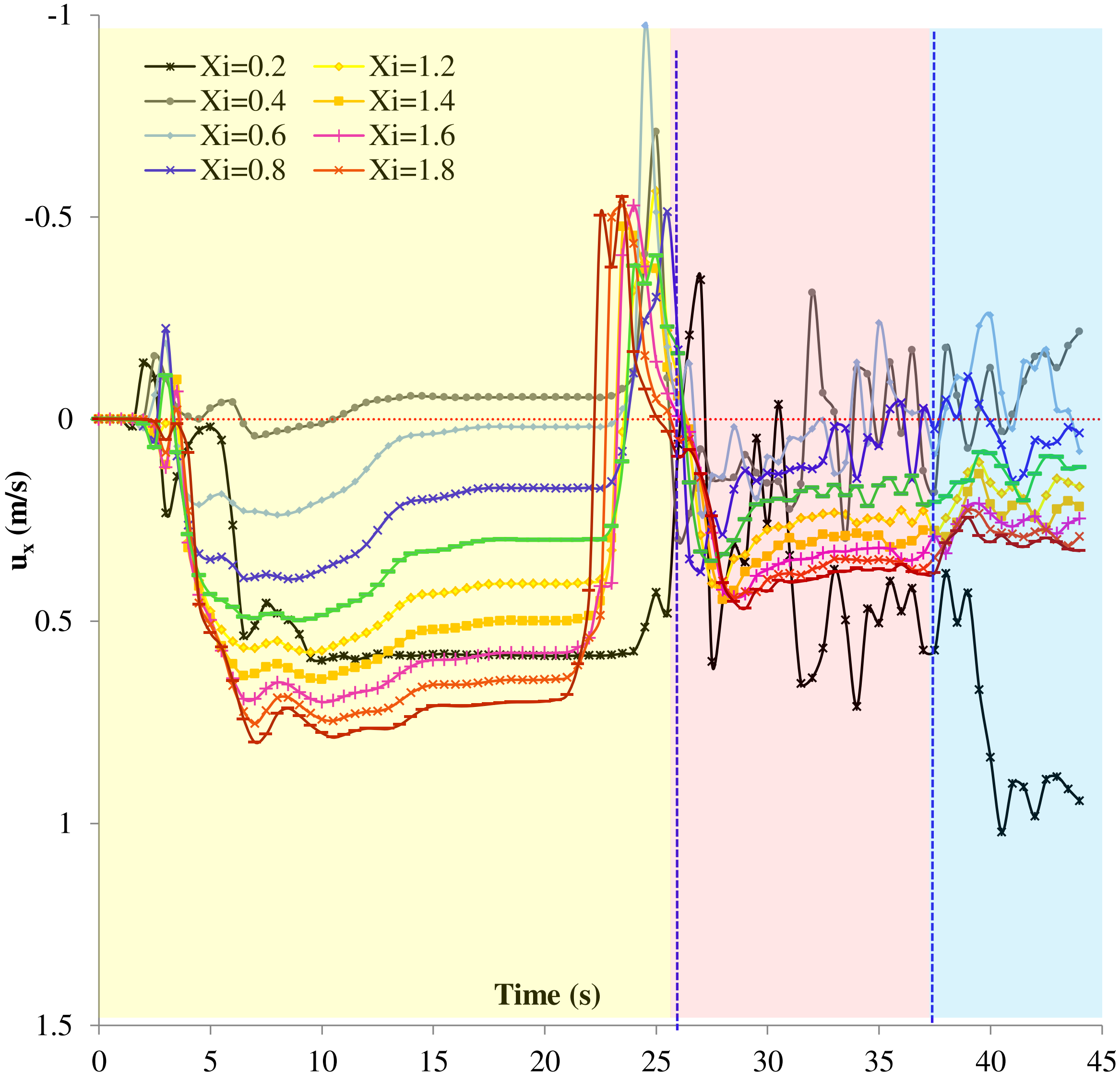

Figure 7-11: Time-history of the longitudinal surface velocity for control sections spaced 0.2 meters on the streamwise direction in the range [0.2m-2.0m].

The velocity peak along the surface occurs at the time step when the reverse wave passes though the section of interest, reaching a maximum value of -0.97 m/s at the section $X_i = 0.6$ m. Figure 7-11 shows that the surface velocity is positive in the stage prior to the vortex formation. There is a negative peak associated to the reverse wave passing through the section of analysis (i.e the peak affects first the 2.0 m section, followed by the 1.8 m, 1.6 m… up to the 0.2 m section). The peak is delayed in time as the abscissa decreases, indicating that the reverse wave slows down as it approaches to the weir. The surface velocity is displayed for each individual section in the range 0.2 to 2.0 m in Figure 7-12 and Figure 7-13.

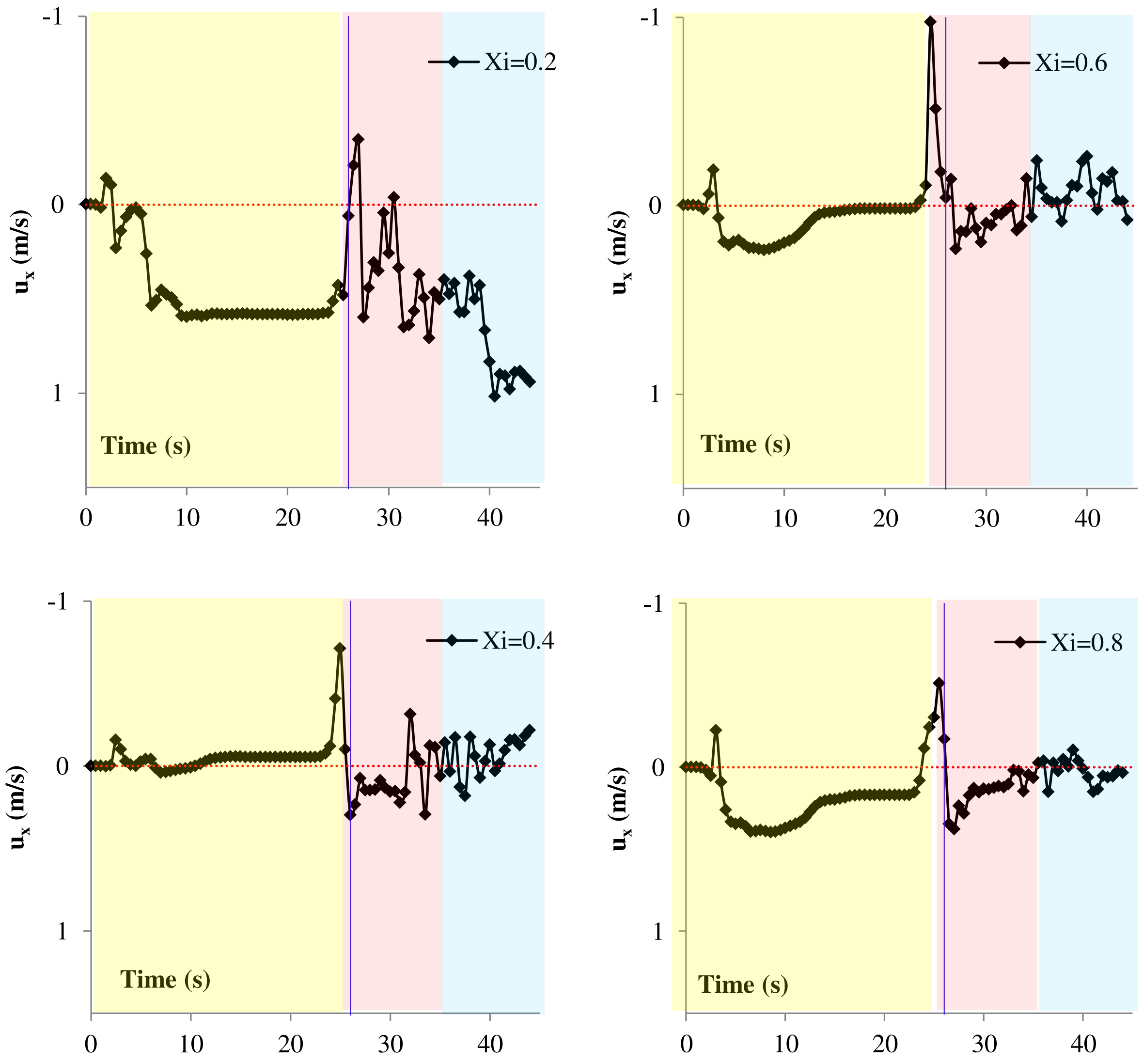

Figure 7-12: Time-history of the longitudinal surface velocity for control sections in the downstream range [0.2m-0.8m].

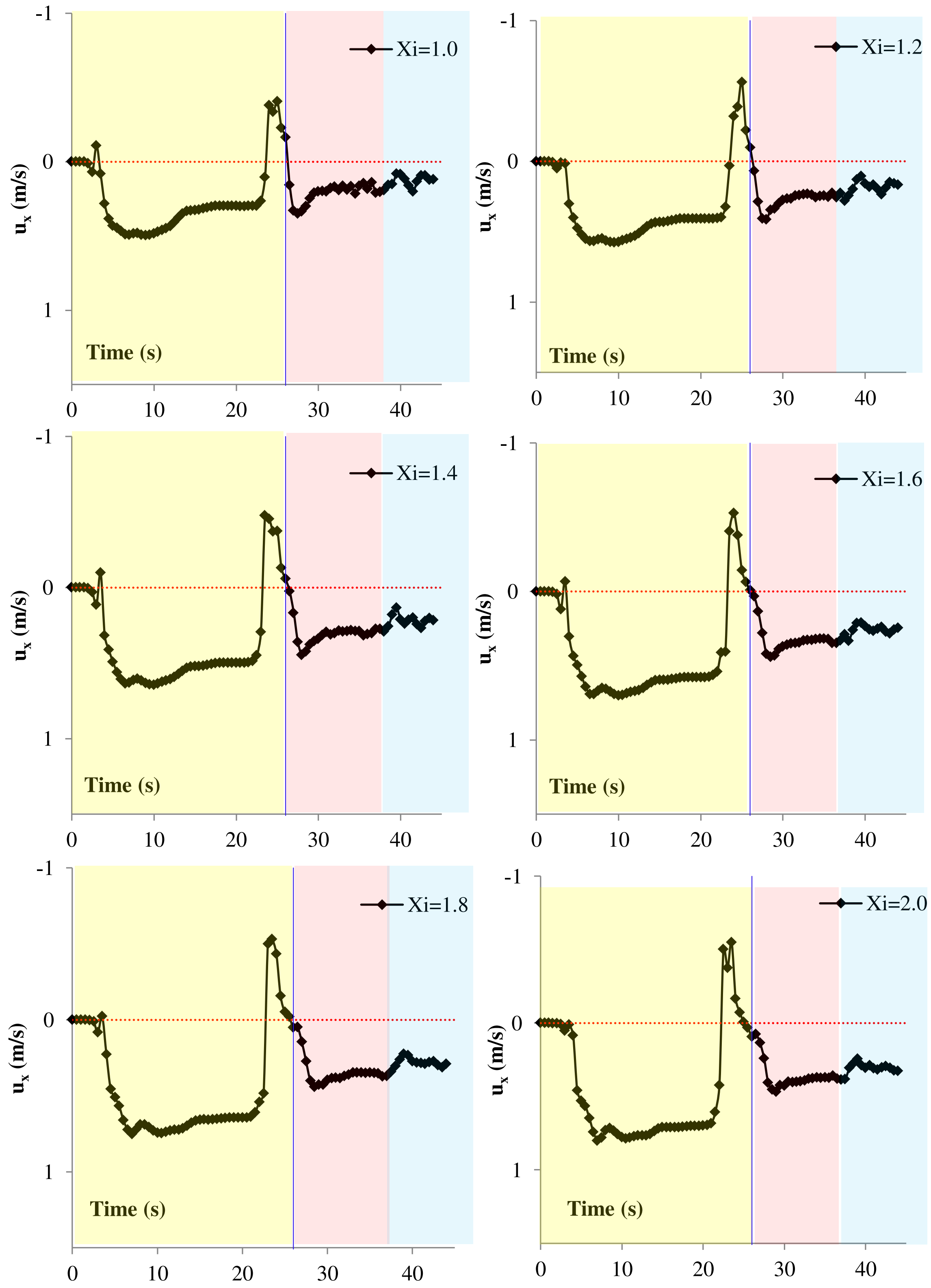

Figure 7-13: Time-history of the longitudinal surface velocity for control sections in the downstream range [1.0m-2.0m].

The 0.4, 0.6 and 0.8 m sections record negative velocities values in the post-vortex and formed-vortex stages, indicating than the submerged roller extension affects less than a meter in the downstream. As in the case of the bed velocity, the last three profiles (1.6, 1.8 and 2.0 m) show the same surface velocity pattern, indicating that these locations are completely outside of the area affected by the submerged roller.

7.2 Crest length validation

The base case (6 cm sharp crest) was compared with the 55 cm broad-crested case, in terms of bed and surface longitudinal velocities. The results of the numerical model are summarized in Figure 7-14. The bed velocities for the broad-crested weir achieve a peak which is characterized by a larger magnitude and is deferred in space, in comparison with the base case. This longitudinal offset between bed velocity peaks results from the physical extent of the broad crest design, which chutes the nappe at a larger downstream abscissa, as seen in Figure 7-15. The free surface counter-current, associated to the segment in which negative surface velocities are predicted, seems to be more intense for the broad-crested design reaching a peak value of $U_s = 0.25\ \mathrm{m/s}$ in comparison with the $U_s = 0.12\ \mathrm{m/s}$ predicted for the 6 cm crest.

The segment where negative bed velocities are predicted (at low abscissas), is associated to the secondary vortex which is being created below the falling nappe. The secondary vortex is characterized by surface velocities which are larger than those obtained for the primary vortex. The positive peak predicted for the surface velocity, occurring at low abscissas as well, is associated to downstream locations which directly receive the falling nappe.

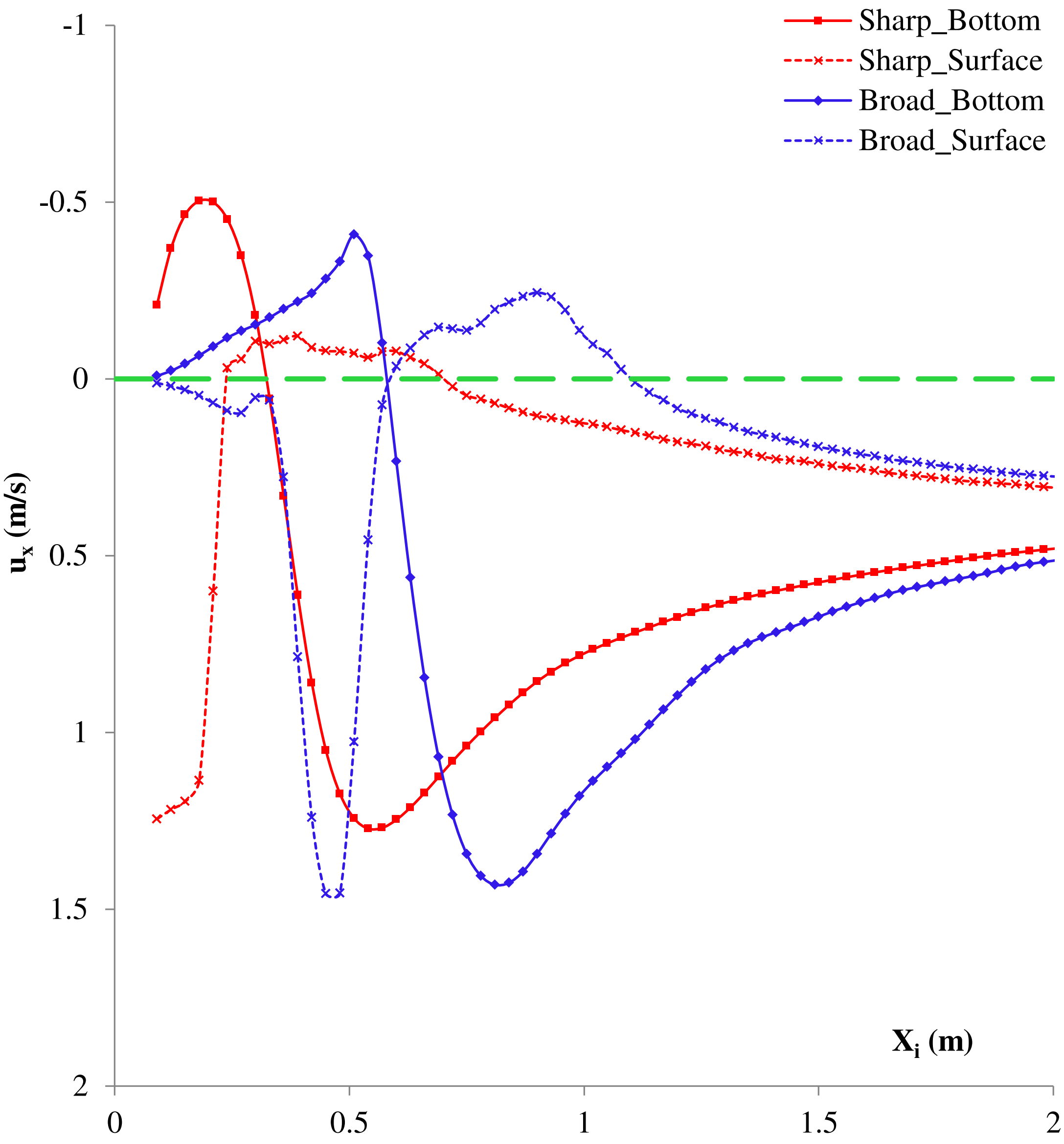

Figure 7-14: Spatial distribution of bed and surface velocities for sharp- and broad- crest conditions.

The spatial distribution of the phase fraction function is seen in Figure 7-15, for $t_{sim} = 45$ s associated to the formed vortex stage. It is observed than the broad crest affects a larger downstream extension and entrains a larger amount of air in the core of the roller. A larger recirculation is expected, resulting into a more significant vortex's tail for the broad crest, as seen in Figure 7-15.

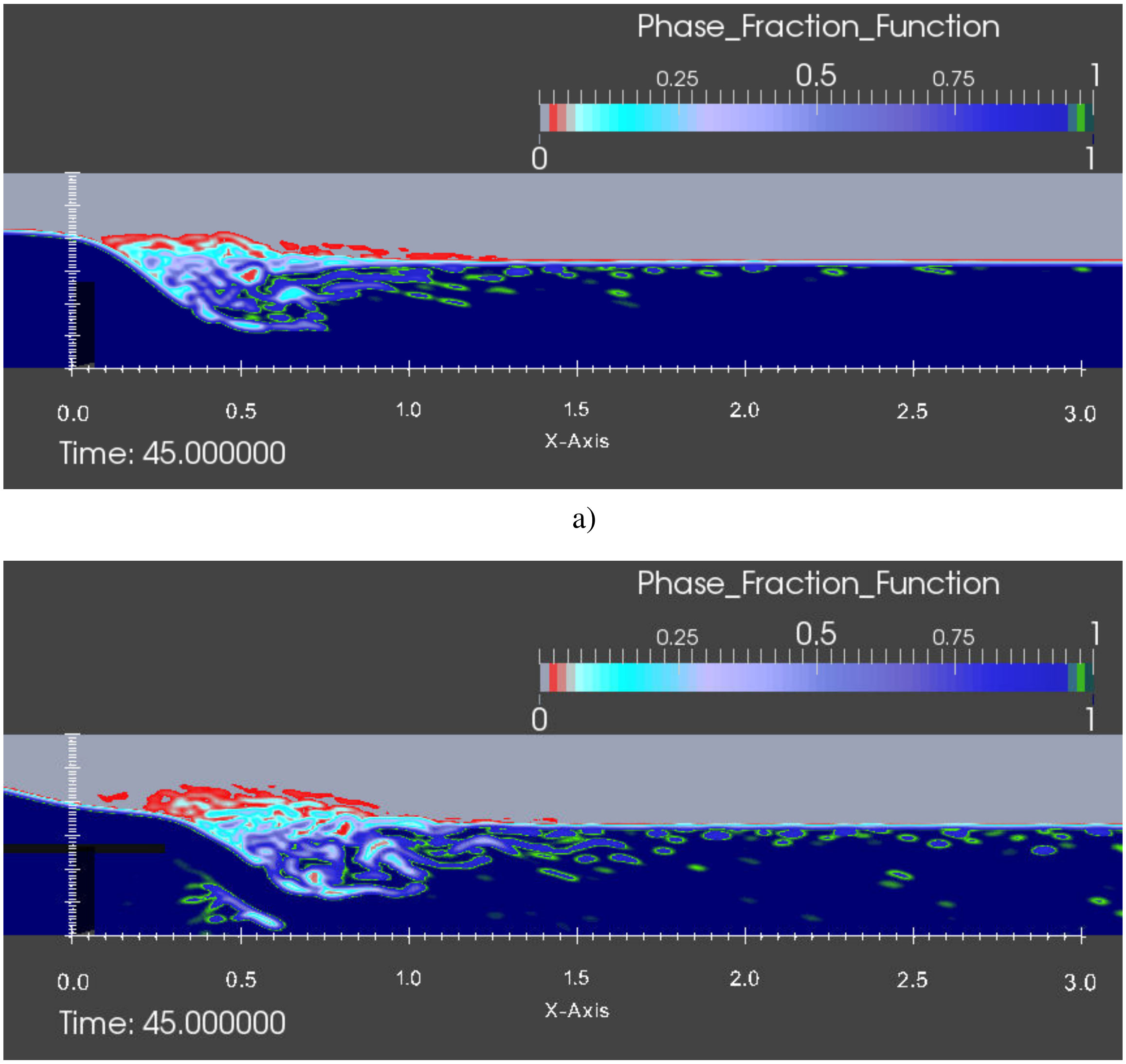

a)

b)

Figure 7-15: Spatial distribution of the phase fraction function (0 value for cells full of air and 1 for cells full of water): a) sharp crest; b) broad crest

The secondary roller generated in between the falling nappe and the downstream dam's face is largely influenced by the crest design. Air entrainment in the secondary vortex is observed in Figure 7-15-b), associated with the broad crest. The spatial distribution of bed and surface longitudinal velocities achieved by the experimental results were discussed in Section 6.3 and are summarized in Figure 7-16 for both: sharp- and broad- crests. Pictures indicative of each condition are included in Figure 7-17.

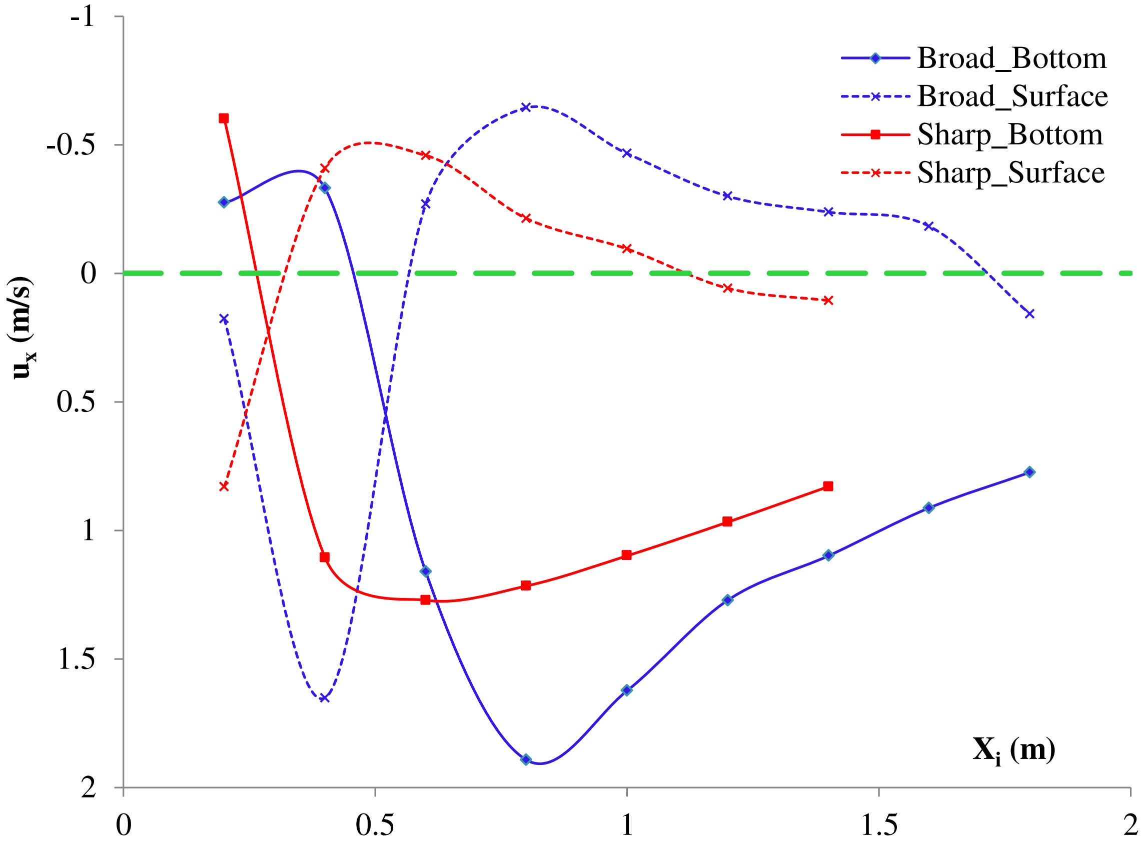

Figure 7-16: Experimental bed and surface velocities for sharp- and broad- crests.

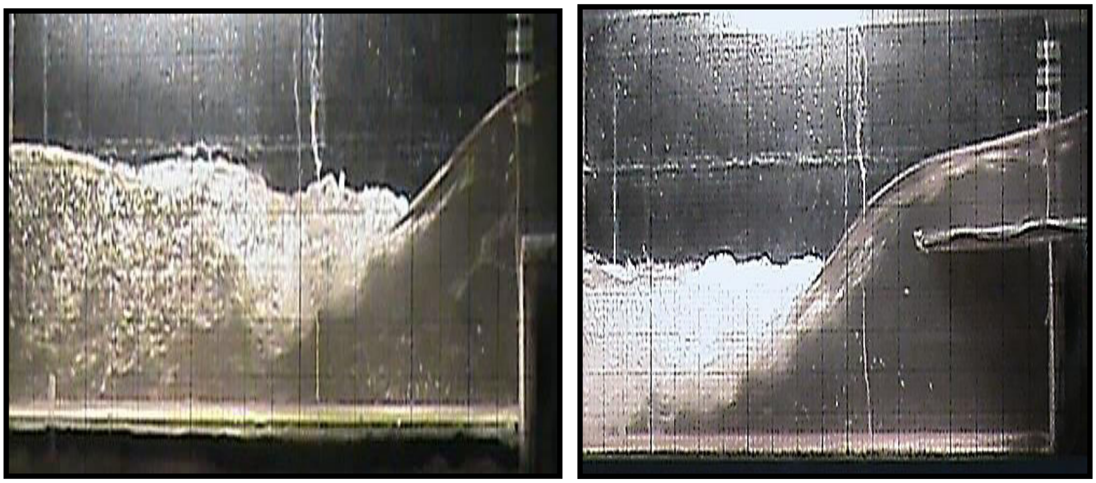

Figure 7-17: Images of the physical conditions. a) Sharp crest; b) Broad crest

When the experimental and the numerical results are compared, it is noted that the numerical simulation always under predicts the experimental results. Out of the two velocities series further studied, bed and surface, the numerical model did not seem to fully capture the surface-current. Therefore, the output for the surface velocity generated by the numerical model, predicted a surface velocity which was approximately two times smaller than the experimental results, as seen in Figure 7-18. The bed velocity peak is well captured but its spatial dissipation is accelerated. Therefore it appears that there is more dissipation in the model. As a result, a reduced extension of the vortex is predicted by the numerical simulation, in comparison to the experimental results.

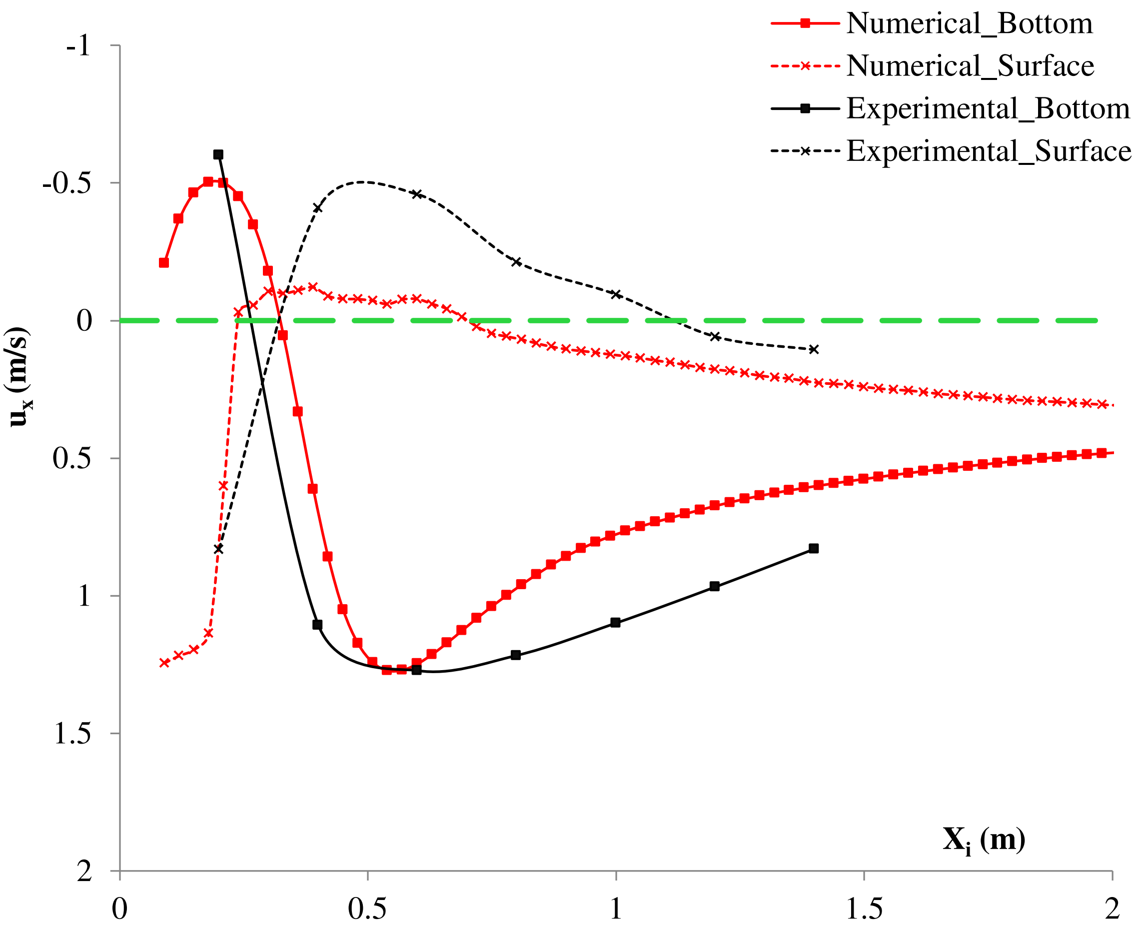

Figure 7-18: Comparison between physical and experimental bed and surface velocities for sharp-crested weir.

For the broad crest arrangement, the numerical model achieves a high accuracy on the spatial distribution velocity curves. However, in agreement with the 6 cm case, the velocity magnitude is under predicted, as seen in Figure 7-19. The numerical simulation of the 55 cm condition is judged to be more successful than for the sharp-crested one. The inclusion of the extended crest, associated to the broad crest design, forced the model to recreate the secondary vortex. Therefore, the global hydraulic system was better captured, simulating better the dynamics of the primary submerged roller.

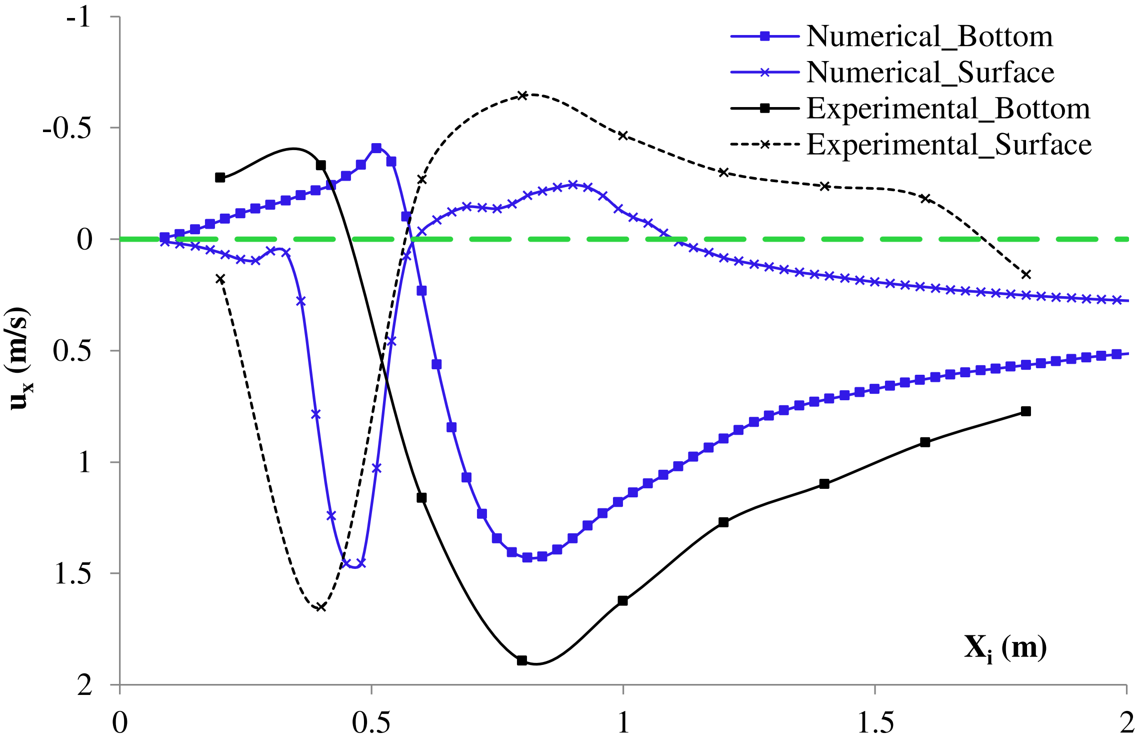

Figure 7-19: Comparison between physical and experimental bed and surface velocities for broad-crested weir.

7.3 Flow rate validation

The numerical results for the low, medium and high flow rate conditions are compared in Figure 7-20. The model performed very well at predicting the vortex velocities for the three discharges. As the flow rate increased the vortex is pushed further downstream. In addition, the peak velocity values are reduced as the discharge decreases. Furthermore, it is observed that the velocity curves for the medium flow condition $(Q = 30\,\mathrm{l/s}$ or $q = 80\,\mathrm{l/s\,.\,m})$ is located closer to the low than to the high flow condition, even though the numerical value is exactly in between.

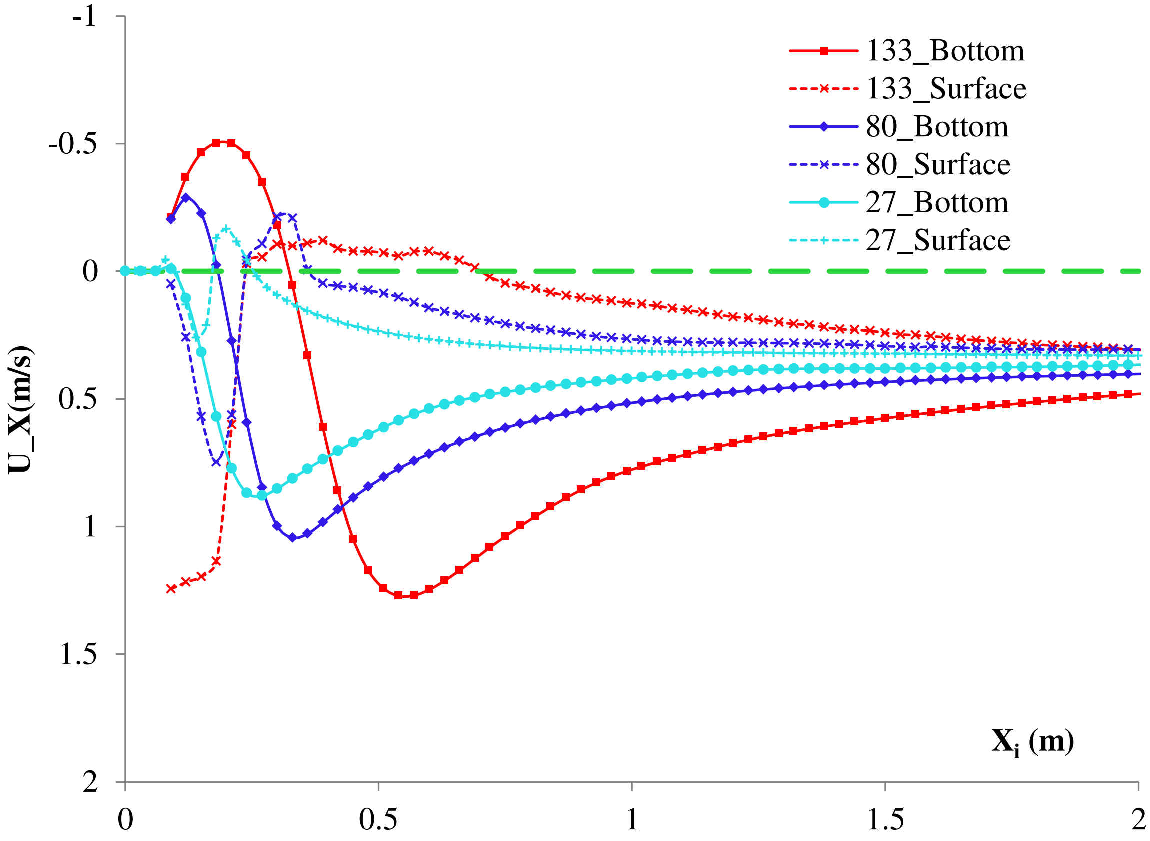

Figure 7-20: Numerical spatial distribution of bed and surface velocities for low (27 $l/s.m$), medium (80 $l/s.m$) and high (133 $l/s.m$) flow conditions.

The roller formed by the low flow condition (Figure 7-21-a) does not appear as a fully formed vortex and seems attached to the falling nappe, observation which is in common with the medium discharge condition (Figure 7-21-b). The vortex mechanism displayed for the high discharge (Figure 7-21-c) differs from the previous two cases, showing a vortex which is fully detached from the nappe. In the experimental investigations the detachment was always forced by adding an air tube which connected the atmosphere to the region below the falling nappe. This feature was not considered in the numerical model and might be the source of disagreement between numerical and experimental results for low- and medium- flow rates.

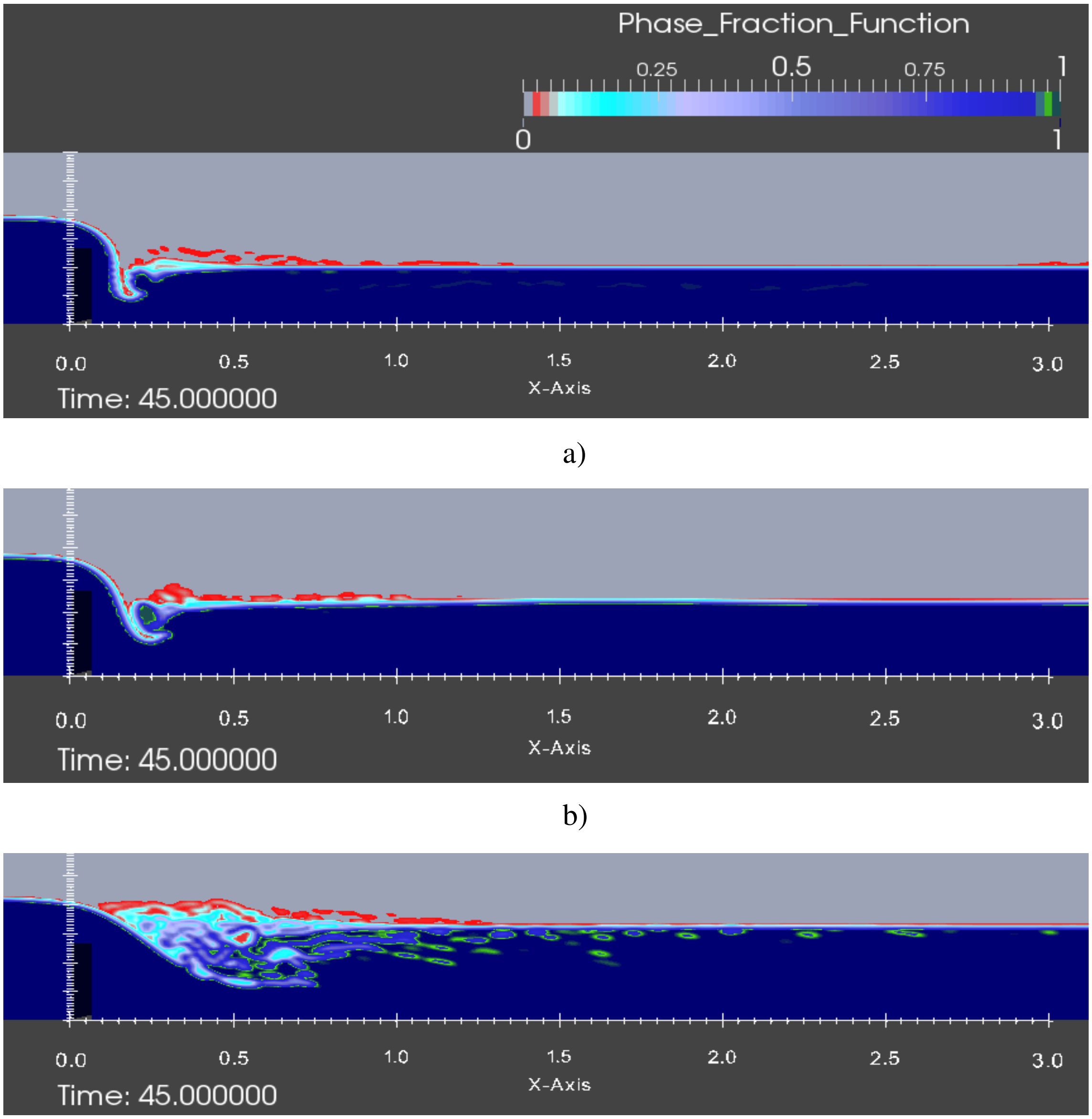

a)

b)

c)

Figure 7-21: Spatial distribution of the phase fraction function (0 value for cells full of air and 1 for cells full of water) a) low flow; b) medium flow: c) high flow

The spatial distribution of the experimental bed and surface velocities are included in Figure 7-22. As the unitary flow rate increases, the bed and surface velocities increase, respectively. The existence of the secondary vortex is only properly captured by the high discharge condition ($Q = 50\ \mathrm{l/s}$ or $q = 133\ \mathrm{l/s.m}$). By looking at the surface velocity curves, the vortex start point, represented by the intersection of the free surface velocity curve with the zero velocity line, was not obtained experimentally for either the low or the medium flow condition. The collection devices were not able to be placed closer to the weir and consequently, these points were not recorded.

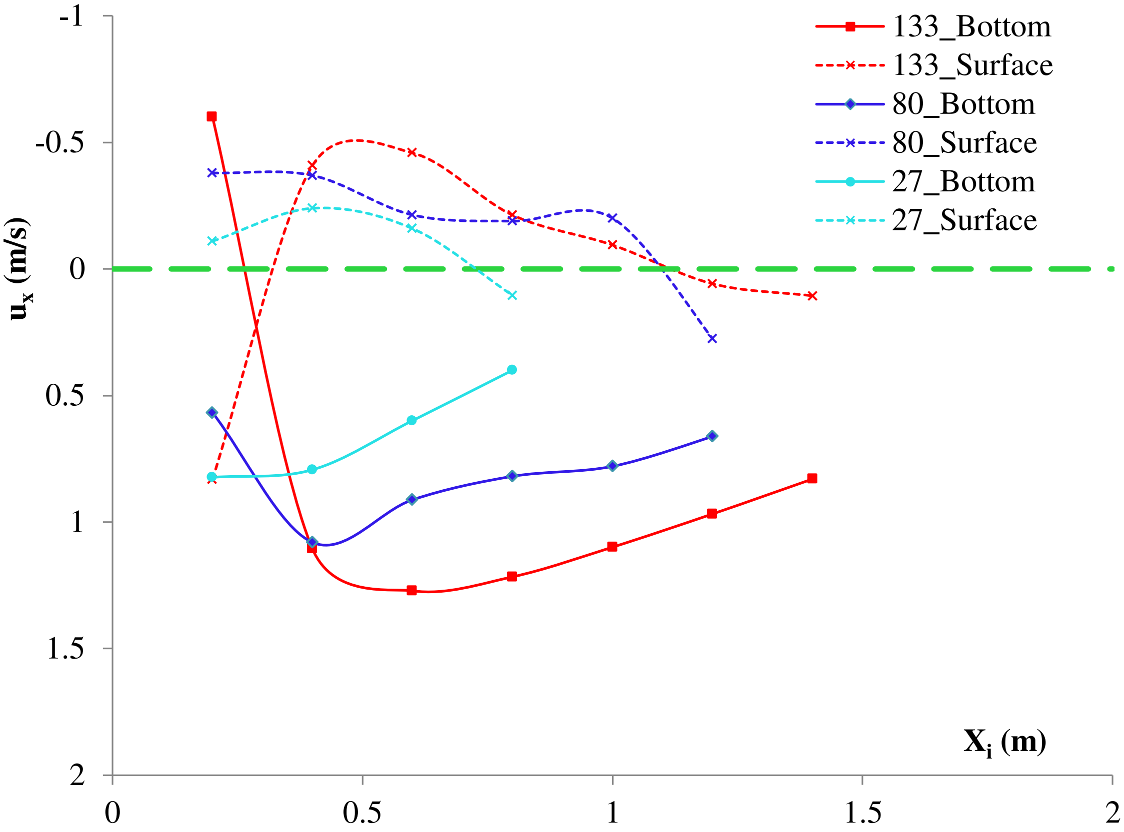

Figure 7-22: Experimental bed and surface velocities for low $(q = 27\ \mathrm{l/s.m})$, medium $(q = 80\ \mathrm{l/s.m})$, and high $(q = 133\ \mathrm{l/s.m})$ flow rate conditions.

For the high flow rate condition, the numerical simulation provided velocities which were very close to the experimental data, as seen in Figure 7-23. However the numerical model predicts surface currents which are smaller in magnitude and extension, in comparison with the experimental results. In agreement with the previous discussions regarding the model’s performance, the numerical model tends to underestimate the submerged roller. The bed velocity peak is perfectly captured by the numerical model revealing agreement, in magnitude and location terms, with the experimental results.

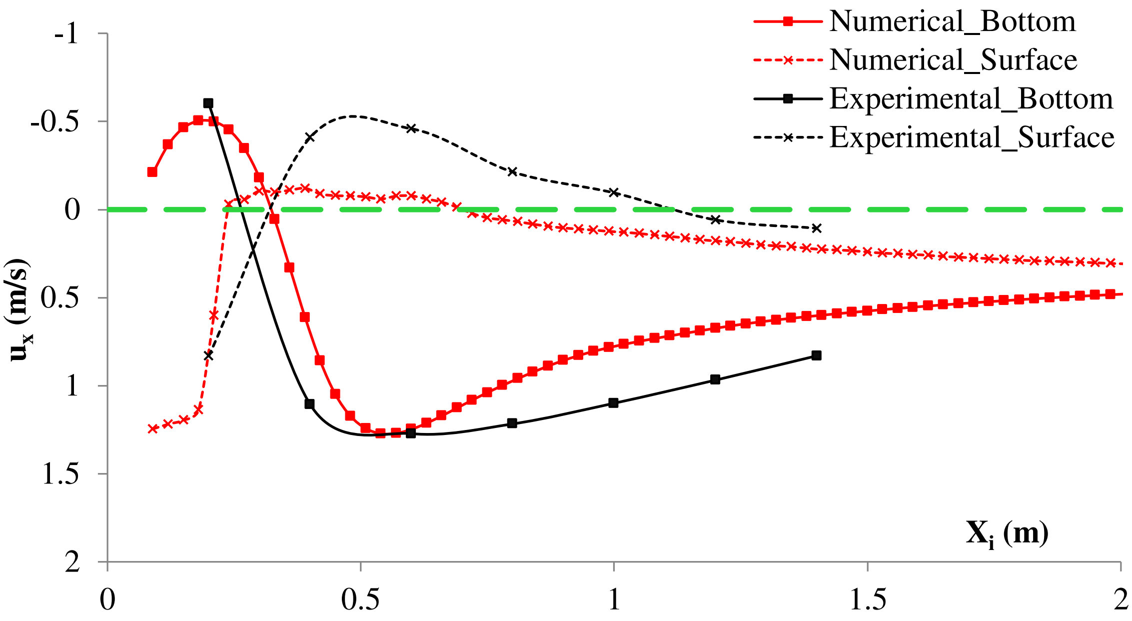

Figure 7-23: Comparison between physical and experimental bed and surface velocities for high flow condition ($q = 133\ \mathrm{l/s.m}$).

The performance of the numerical model against the experimental results for medium and low flow conditions is included in Figure 7-24 and Figure 7-25, respectively. It is observed that as the flow rate decreases the bed velocity peak shifts towards lower abscissas. The quality of the experimental data seems to decrease with the discharge. As a result, it is perceived that the disagreement between experimental and numerical results increases as the discharge decreases. This disagreement is explained in part as low accuracy of the experimental measurements at low flow conditions, and the inability of the numerical model to properly scale the air entrainment.

Taking into consideration the complexity of the submerged roller problem, it is concluded that the results of the numerical and experimental studies do show agreements within the frame of each approach's limitations. Therefore both methods complement each another and the results are considered valid when the limitations of each method are understood.

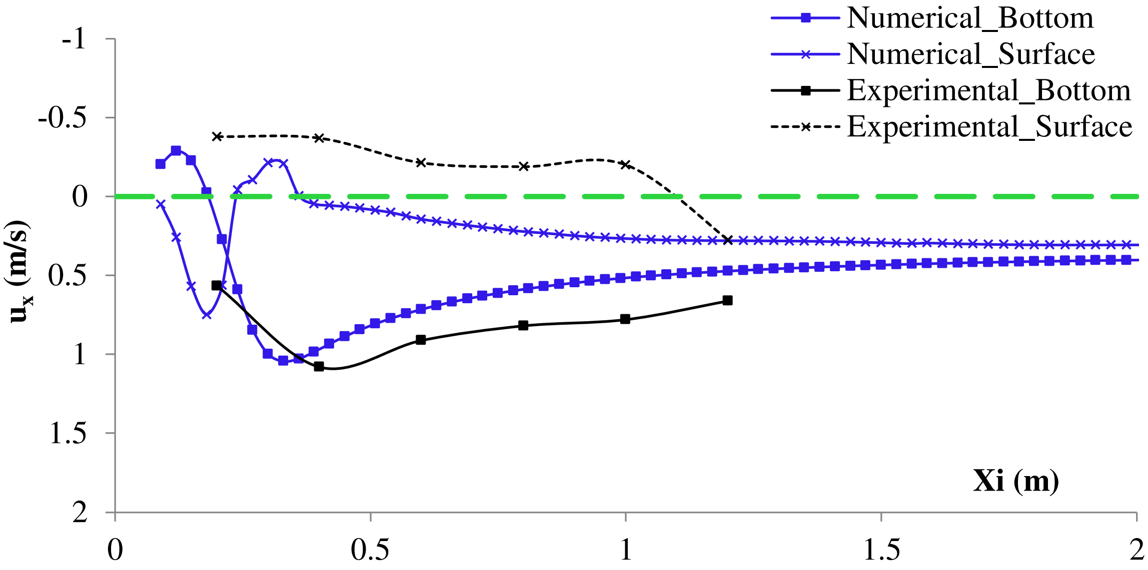

Figure 7-24: Comparison between physical and experimental bed and surface velocities for medium- flow condition ($q = 80\ \mathrm{l/s.m}$).

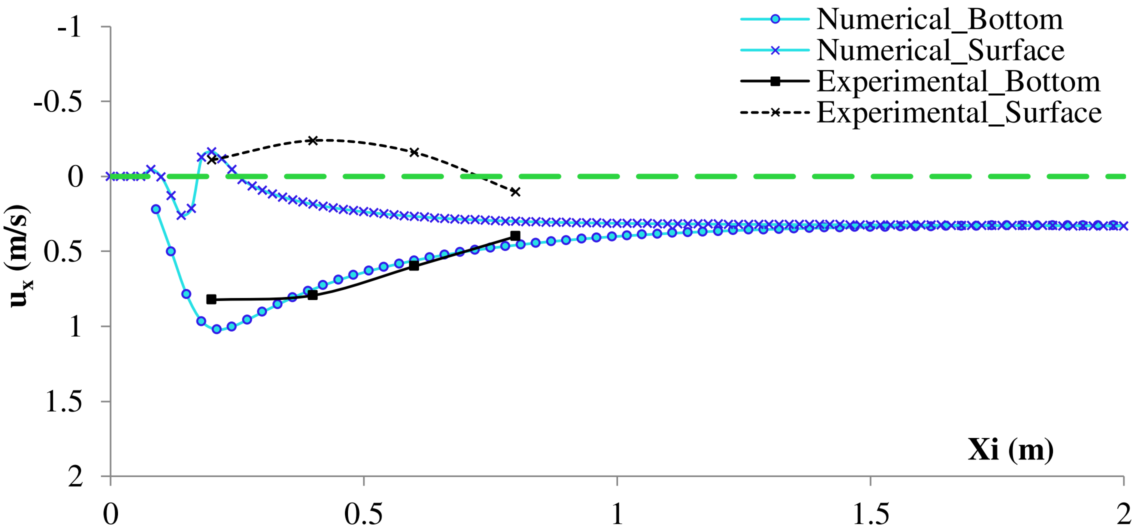

Figure 7-25: Comparison between physical and experimental bed and surface velocities for low- flow condition ($q = 27\ \mathrm{l/s.m}$).

7.4 Apron elevation validation

The numerical results for the downstream apron elevations tested during the experimental stage are presented in Figure 7-26. The numerical model provided with results which are coherent with the observations and the expectations. As the downstream floor is raised, the formed vortex becomes shorter (in extension), and the region affected by the downstream roller reduces. Moreover, Figure 7-26 reveals that as the apron is elevated, the bed velocity tends to decrease. In addition, the angle of the nappe and the inflow bed current are highly affected by the apron elevation, as seen in Figure 7-27. As the floor rises, the nappe angle becomes milder and the depth of the current along the bed thickens. This explains the decrement of the bed velocity as a result of an elevated apron.

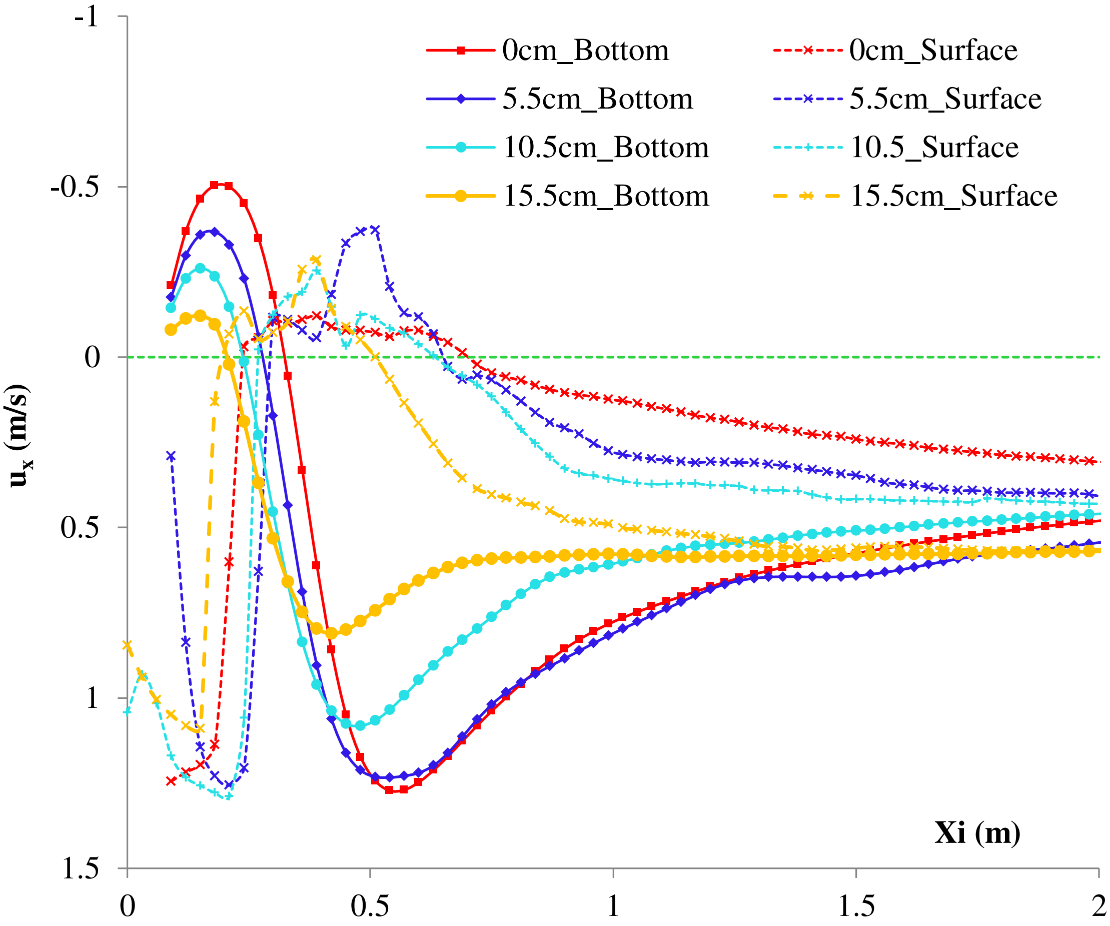

Figure 7-26: Spatial distribution of bed and surface velocities obtained with the numerical model for 0cm, 5.5cm, 10.5cm and 15.5cm apron elevations.

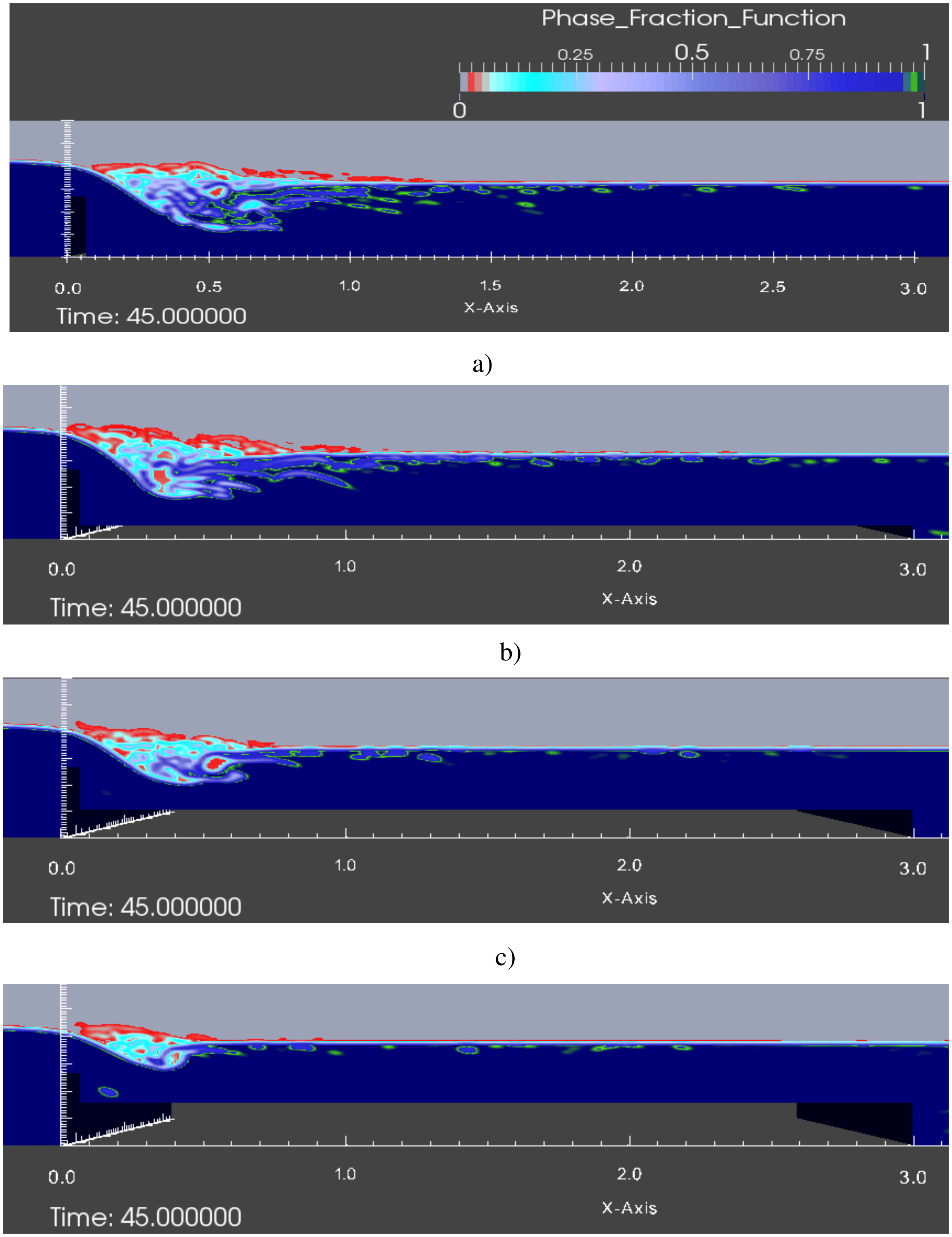

a)

b)

c)

d)

Figure 7-27: Spatial distribution of the phase fraction function (0 value for cells full of air and 1 for cells full of water) for several downstream apron elevations a) 0 cm; b) 5.5 cm c) 10.5 cm; d)15.5 cm

The velocity of the bed and surface currents obtained by the experimental procedures are compared in Figure 7-28 for several apron elevations. The general trend presented in the figure below reveals that as the apron is elevated, the bed and surface velocities are reduced. There is a slight discrepancy observed between the series corresponding to $z_i = 0$ cm and $z_i = 5.5$ cm conditions. This disagreement is explained in terms of a tailwater level imposed in the channel, which resulted into a different degree of submergence than for the rest of conditions. It is believed that the tailwater level for the $z_i = 5.5$ cm condition was too low, achieving a degree of submergence which was lower than the rest of the experimental series.

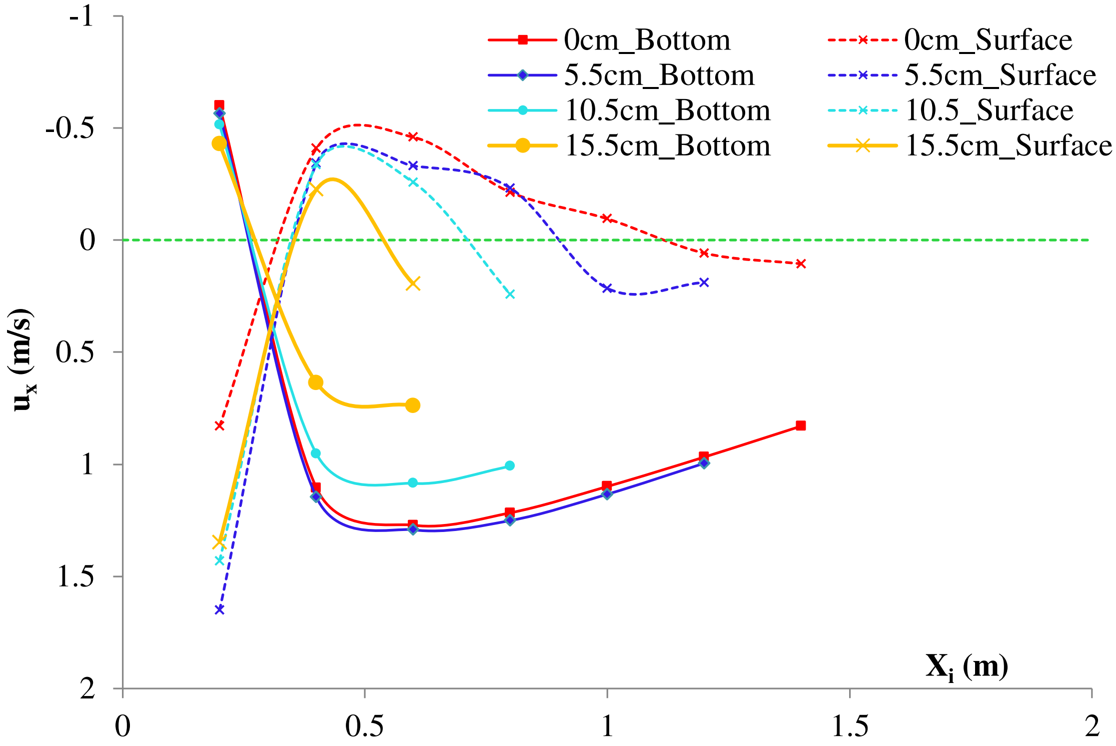

Figure 7-28: Experimental bed and surface velocities as a function of the downstream floor elevation for 0cm, 5.5cm, 10.5cm and 15.5cm apron's elevations

Figures 7-29 to 7-32 show the numerical and experimental spatial distribution of the surface and bed velocities, performed with a sharp-crested weir, a unitary flow discharge of $q = 133\ \mathrm{l/ms}$, and a changing elevation of the apron. Although generally good agreement is observed, the dissipation process of the bed velocity after its positive peak (located at abscissas corresponding to approximately X_i = 0.5m) shows the same issues than previous simulations. It seems that the numerical model predicts a faster dissipation of the roller's effect length-wise. Therefore the restoration of the velocity towards the average tailwater values is achieved at lower abscissas by the numerical simulation. On the other hand, another discrepancy related to the surface velocity is noticed between the experimental and the numerical model. It is observed that the surface counter current is not fully captured by the numerical model, and therefore, the superficial negative velocity is under predicted.

As experimental velocity measurements, other than the bed and surface velocity at discrete points, were not fully reliable for the amount of air entrained, digital imagery observations were employed to study the nature of the vortex. From the observed movement of the surface current, tracked by the entrained air bubbles, the flow velocity along the surface seemed to be slower than the experimental data collected by the propeller meter. The disagreements found between the numerical and experimental results could be explained in terms of a slight overprediction of the surface velocity. Therefore, it is believed that the numerical model is simulating the submerged roller phenomenon with high levels of accuracy in regards to the prediction of velocity peaks, and dynamics of the roller.

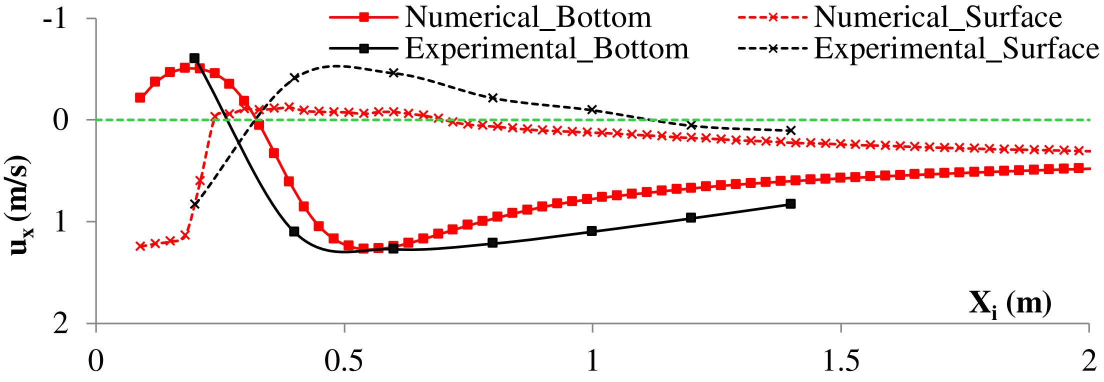

Figure 7-29: Comparison of numerical and experimental bed and surface velocities for non-elevated downstream apron (z_i = 0 cm).

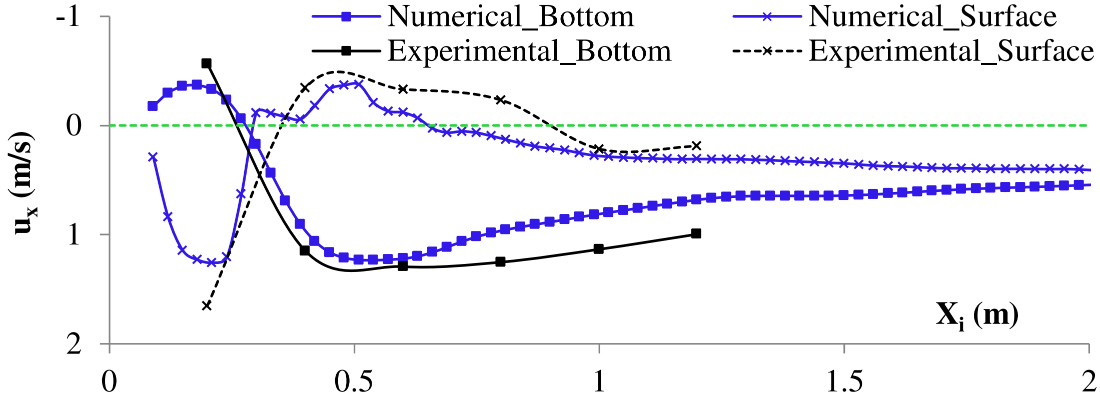

Figure 7-30: Comparison of numerical and experimental bed and surface velocities for low-elevated downstream apron ($z_i = 5.5$ cm).

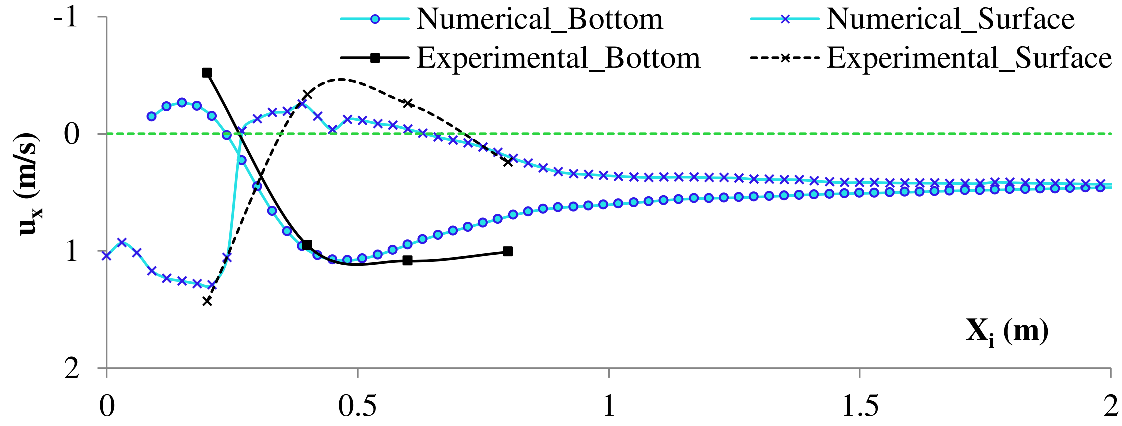

Figure 7-31: Comparison of numerical and experimental bed and surface velocities for mid-elevated downstream apron ($z_i = 10.5$ cm).

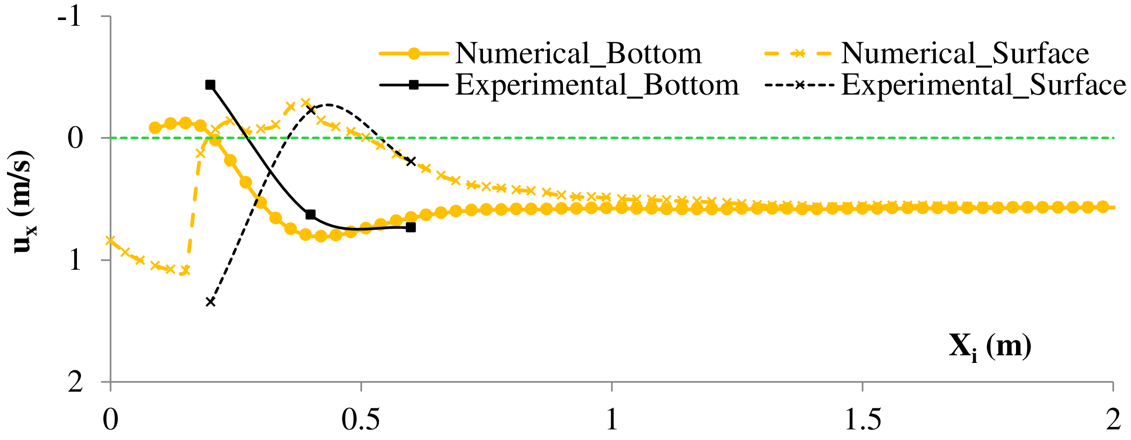

Figure 7-32: Comparison of numerical and experimental bed and surface velocities for high-elevated downstream apron ($z_i = 15.5$ cm).

7.5 Vertical velocity

A comparison of the time-history of the surface horizontal and vertical velocity components is included in Figure 7-33, for a set of control sections. The vertical component is associated to the direction along which the flow depth is measured. The time at which the velocity peak is reached ultimately depends on the downstream location. The furthest downstream section ($X_i = 2$ m) is reached by the velocity peak, associated to the pass of an advancing reverse wave, at an earlier time frame than the sections closer to the structure ($X_i = 0.2$ m).

This figure also reveals that there is a strong correlation between the horizontal and vertical components of the velocity; the vertical velocity peak is delayed in time for a given section. The vertical velocity component is in charge of lifting the water particles from the bottom towards the surface, inducing the recirculating pattern characteristic of the submerged roller. The reverse wave passing though the sections translate into a posterior vertical velocity induced at the control section. The vertical velocity peaks reduce in magnitude as the abscissa decreases.

For the time stage associated to the formed-vortex stage ($t_{sim} \geq 37.5$ s), there is a residual component of the vertical velocity at the control sections located at $X_i <$ 0.8 m. Consequently, the existence of this vertical velocity is responsible for the recirculation of water particles, which characterizes the vortex. Moreover, the aforementioned downstream locations ($X_i < 0.8$ m), are associated to the existence of a negative surface velocity, as seen in Figure 7.33-a), which reveals the existence of a surface counter current.

The residual vertical component of the velocity on the sections affected by the roller explains its stationary nature. Therefore the vortex remains as a stationary phenomenon if the inflow and downstream conditions are maintained constant.

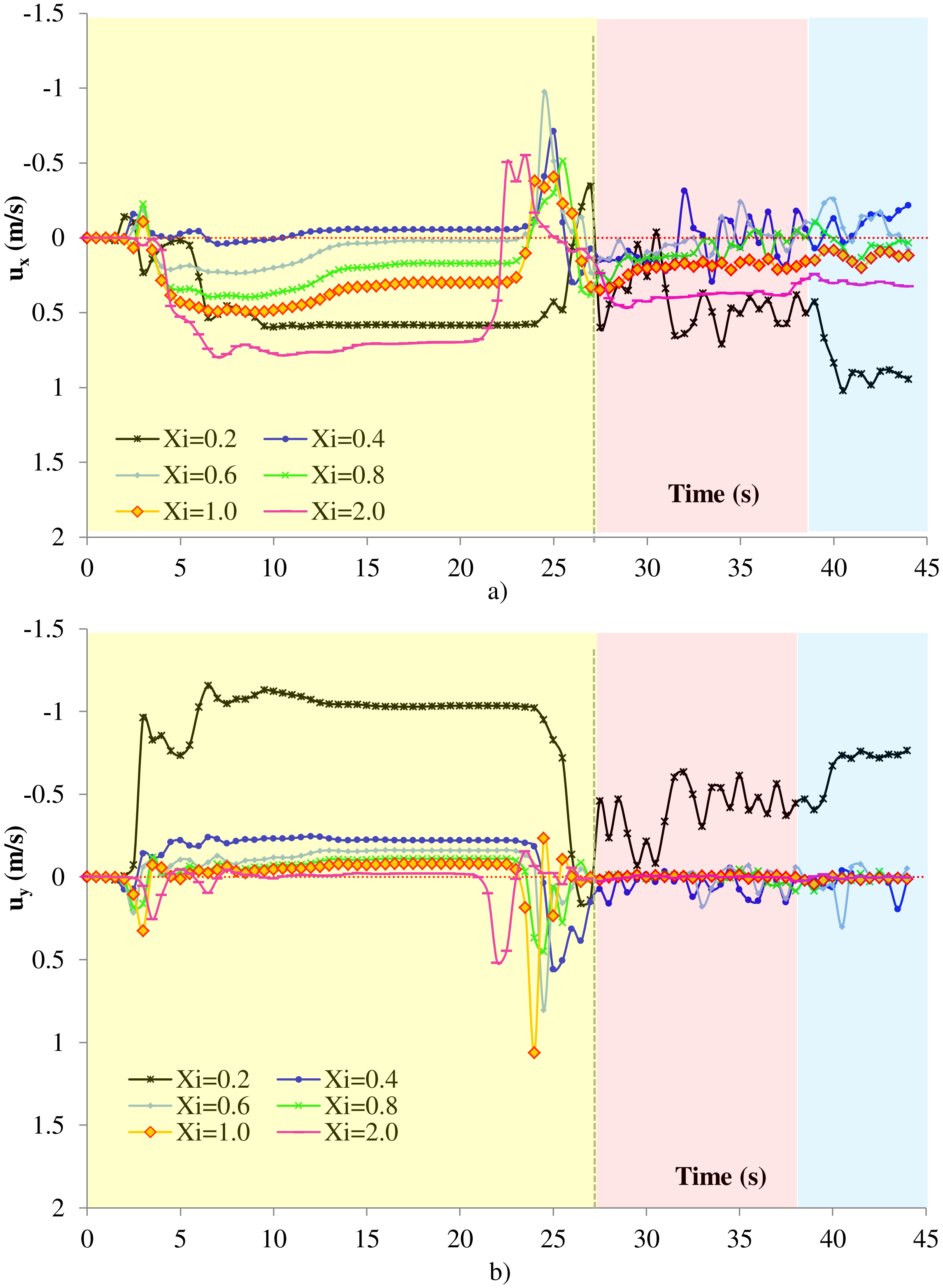

a)

b)

Figure 7-33: Comparison between the time history of the horizontal (u_x) and vertical (u_y) velocities along the free surface for different control sections (X_i)

7.6 Turbulent kinetic energy

The time-history of the turbulent kinetic energy adds up information to the problem of understanding the nature of submerged hydraulic jumps. It is observed that the turbulent kinetic energy follows the pattern for several cells located along the free surface, as seen in Figure 7-34. The magnitude of this energy is however dependent on the section of interest.

Both, the turbulent kinetic energy and horizontal velocity peaks occur at the same time instant. Therefore, the turbulent energy peak identified on the distribution coincides with the time frame at which the counter-current passes through the section. It is observed that as the abscissa decreases, the magnitude of the kinetic energy decreases. The energy decay is explained in terms of the energy lost through the vortex formation process, resulting into a decay of the advancing wave's kinetic energy as it approaches to the weir. The turbulent dissipation rate is presented in Figure 7-35. For a given section, the turbulent dissipation rate's peak identified in the distribution, coincides in time with that identified for the kinetic energy.

In the post-vortex temporal stage, shaded in red in Figures 7-34 and 7-35, there are significant residual values of the turbulent kinetic energy for control sections in the range $0.2 \leq X_i \leq 1$ m, which is indicative of a highly turbulent region. The energy drastically drops after 37.5 s of simulation, coinciding with the start of the formed-vortex stage.

For time steps corresponding to the formed-vortex stage ($t_{sim} \geq 37.5$ s), the remaining level of turbulent kinetic energy at surface cells located within the submerged vortex's domain, are responsible for the existence of a surface current. The remaining turbulent energy is independent on the time variable, which is associated to a stationary vortex.

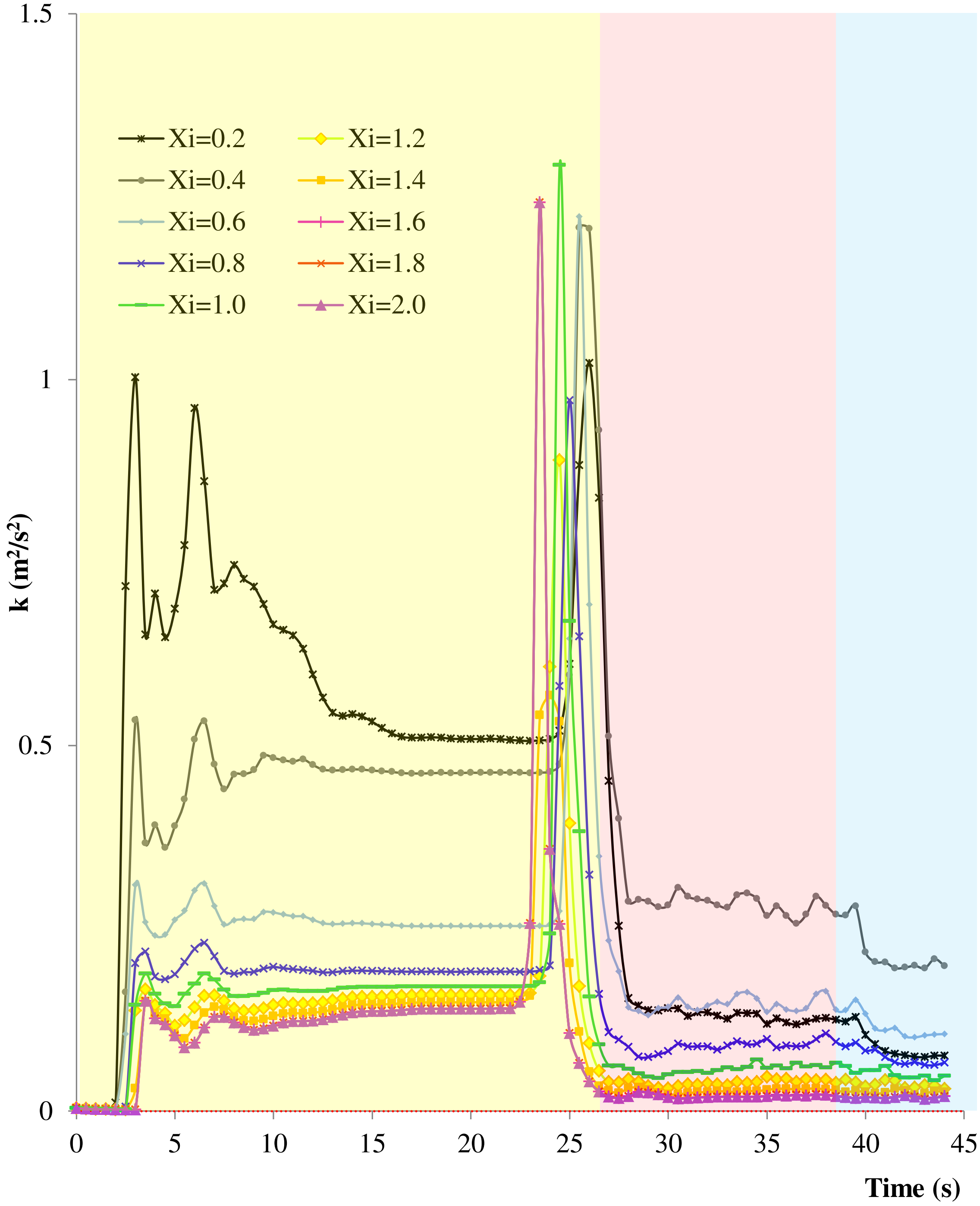

Figure 7-34: Time-history of the turbulent kinetic energy along the free surface line at different control sections (X_i)

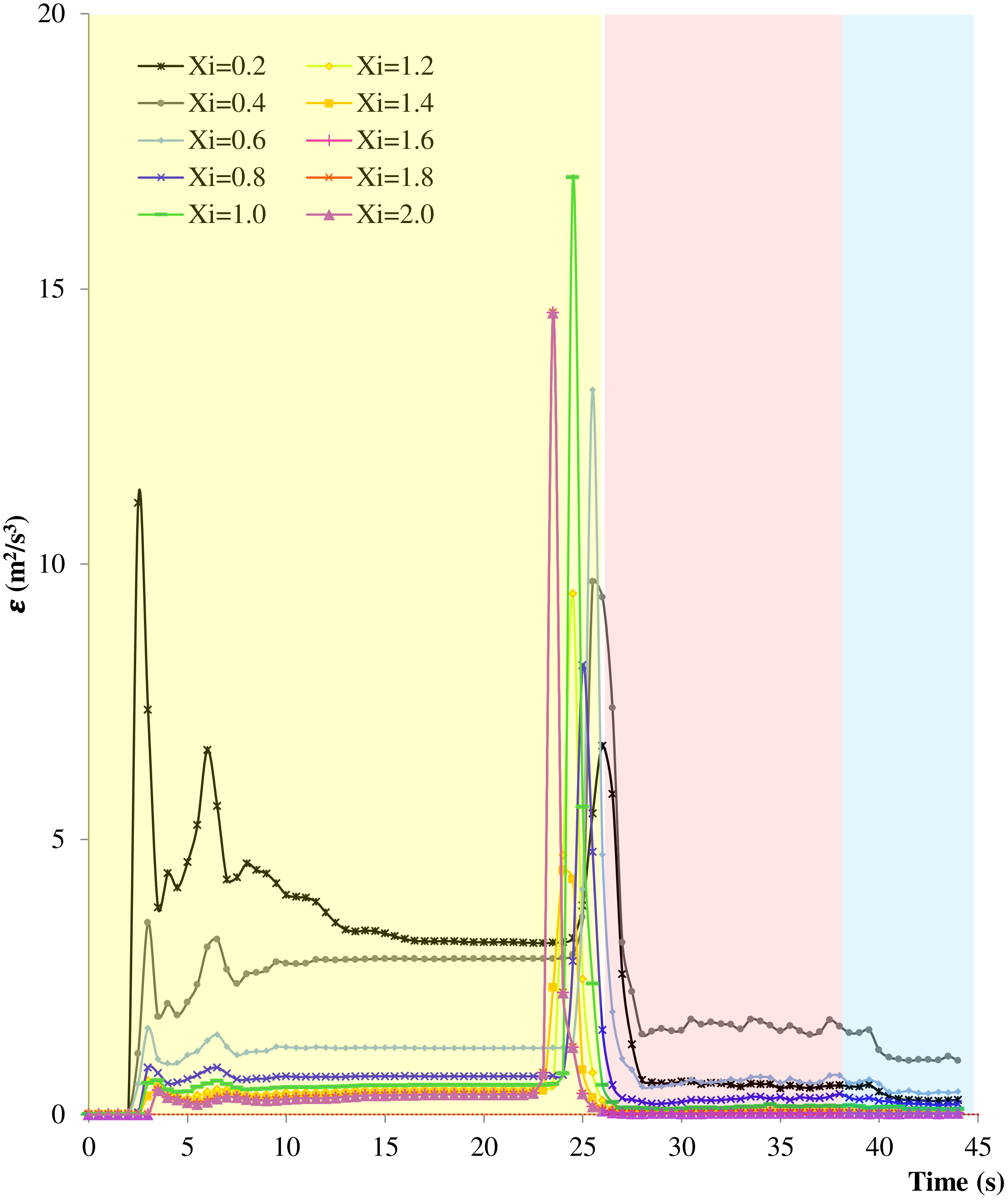

Figure 7-35: Time-history of the turbulent dissipation rate along the free surface line at different control sections (X_i)

7.7 Conclusions

The quantitative comparison of the numerical and physical results performed in this chapter demonstrates the stability of the model, the robustness of the solver interFoam and the endless possibilities of the OpenFOAM toolbox. The numerical model was used in this chapter to study the effect of changing flow rate, crest length, and downstream floor elevation on the dynamic characteristics of the submerged roller.

A base case was selected to assess the model performance. Three temporal stages were identified: (i) pre-vortex stage associated to the time period prior to the formation of the roller $[0\text{ s} \leq t_{sim} < 26\text{ s}]$. This stage corresponds with the existence of a supercritical bed current and a reverse advancing wave which moves towards the weir. (ii) The post-vortex stage, which represents the period immediately after the formation of the roller $[26\text{ s} \leq t_{sim} < 37.5\text{ s}]$, in which it adapts and evolves, and (iii) the formed-vortex stage which corresponds to a fully formed and stable vortex, occurring at $t_{sim} \geq 37.5\text{ s}$.

For points located along the bed channel, the passage of the advancing wave moving from the downstream towards the weir coincides with the time instant at which the horizontal bed velocity peak is recorded. For points located along the free surface, the horizontal surface velocity and turbulent kinetic energy showed peaks at the exact same time than the reverse wave was passing through the point. The vertical velocity peak was slightly delayed in time in comparison with those associated to the horizontal velocity and turbulent energy. At the formed-vortex stage, it was observed some residual turbulent kinetic energy at sections located within the vortex's domain. This energy is ultimately responsible for the stationary nature of the vortex. Residual vertical and horizontal velocities at points located within the same domain are indicative of the existence of the free surface current.

The numerical model performed well when the crest length, the apron elevation and the discharge were altered. The numerical and experimental results showed good agreement. In general terms, the numerical model tends to predict very well the bed velocity peak (in magnitude and location), and moderately well its spatial dissipation. It was observed that the numerical model predicts a faster decay of the bed velocity in comparison with the experimental results.

Moreover the surface counter current is not fully captured by the numerical model and therefore, the surface velocity is underestimated. This disagreement might be related to the inability of the model to properly scale air entrainment processes. The underprediction of the surface velocity might be the result of a simulated free-surface current as a very foamy layer (large amount of air entrained), in comparison to the experimental observations, resulting into a loss of momentum and an under estimation of the surface velocity.

In addition, it is also believed that there might be some errors in the data acquisition of the surface velocity by the propeller meter. The large amount of air and the fluctuating free surface might be responsible for compromising the inaccuracy of the velocity measurements. Taking into consideration the complexity of the submerged roller problem, the results of the numerical and experimental studies show a good agreement within the frame of each approach's limitations. It is therefore concluded that both methods complement each another and the results are considered valid when the limitations of each method are understood.

Chapter 8. Conclusions and Recommendations

8.1 Conclusions

This thesis presents the results of a comprehensive experimental and numerical study of submerged hydraulic jumps which occur immediately downstream from low-head dams. Such hydraulic structures are employed, for instance, as artificial barriers against migration of invasive species as sea lampreys. The impact of the weir crest length and of the downstream apron elevation on the submerged roller, in terms of the vortex formation and its hydrodynamic characteristics, has been investigated. The main conclusions of this work are summarized as follows:

- Overflow hydraulic structures operating at subcritical regimes are prone to the development of a submerged hydraulic jump forming immediately downstream from the structure. This hydraulic jump is characterized by large amounts of entrained air, intense turbulence and, depending on the geometry and flow conditions, the formation of a submerged roller, which can constitute a deadly combination for swimmers or boaters entrapped in the recirculation region.
- The minimum tailwater level associated with the formation of a submerged roller represents the transition from 'free' to 'submerged' types of hydraulic jump. A mathematical expression was proposed in this study to predict this lower boundary (Y_l), as a function of the upstream depth over the crest (Y_{crest}) and the downstream apron elevation (z_{floor}). The effect of the crest length did not significantly influence the location of the lower boundary.
- The submerged jump's upper boundary (Y_u) corresponds to the maximum water level associated with the formation of the submerged roller. Two equations were proposed to predict the upper boundary: (1) a simple power relation which is a

function of the upstream depth (Y_0) only and which is model-specific, and (2) a mathematical expression which improves the accuracy of the predicted upper boundary by incorporating a factor which accounts for the geometry of the weir, including the crest length. Broad-crested weirs required reduced flow depths to reach the upper boundary compared to the sharp-crested ones, thereby impacting the net tailwater range $(Y_u - Y_l)$ associated with the occurrence of submerged hydraulic jumps. The apron elevation affected slightly the magnitude of the upper boundary (maximum water level), by raising it as the apron is elevated.

- The original definition of the degree of submergence (S), which compares the local tailwater depth to the subsequent depth of the vortex, was found to be inaccurate. The degree of submergence is redefined in Section 5.3 and is now expressed in normalized terms, by comparing the local tailwater depth (Y_t) to the dangerous tailwater range associated with the formation of the submerged hydraulic jump $(Y_{u+} - Y_l)$.
- The degree of submergence did not affect the maximum value of the counter-current velocity, but did influence the reduction of the surface velocity. As the degree of submergence increased, the downstream region affected by the vortex increased, up to submergence values of 50%. The minimum depth of the bed current (Y_b) is ultimately responsible for feeding the submerged roller by transferring the bed current's momentum to the downstream water body. Therefore, a direct relation between the discharge, the bed current's depth, and the dynamic characteristics of the vortex was found and is presented in Section 6.2.1.
- The crest length impacted significantly the hydrodynamic characteristics of the vortex: broad-crested weirs generated submerged vortices characterized by high velocities and longer downstream extension induced by the quasi-horizontal vortex axis. The apron elevation also affected the roller characteristics: elevated downstream aprons induced vortices characterized by lower velocities and shorter downstream extension. Therefore, safer hydraulic conditions for potential

swimmers or boaters can be achieved by installing sharp-crested weirs in combination with elevated downstream aprons.

- Digital image processing techniques were developed to evaluate the air entrainment at the vortex's core. The calculated air entrainment using this technique outlined values of 30% of air volume within the vortex, which is a relatively high value compared to results obtained by other researchers (Valle & Pasternack, 2006).

- A parallelism between the air-water regions identified for 'free' hydraulic jumps induced by a sluice gate (Chanson H., 1999), and those identified for a submerged jump was observed. The "advective turbulent shear" layer where the transfer of momentum between entrained air and water occurs, share the same characteristics in both 'free' and 'submerged' jumps. However, the 'recirculation' region differs between both jump types. The author concluded that a vertical deflection of the "developing boundary layer" associated to the bed's current is induced by the imposed tailwater conditions, ultimately inducing a surface current which accompanies the submerged roller.

- The proposed numerical model demonstrates the capability of the OpenFOAM toolbox to reproduce complex flow problems involving air entrainment and intense turbulence. The quantitative comparison between the numerical and physical tests' results indicate that the numerical model tends to satisfactory predict the downstream bed velocity peak, in terms of magnitude, at specific locations. However, the numerical model does not accurately simulate the spatial dissipation of the bed velocity peak, predicting its faster decay compared to the experimental results. Moreover, the surface velocity is underpredicted as a result of a simulated surface current, which is more foamy and aerated than observed during the experimental investigations.

- For a fully-formed vortex ($t_{sim} > 37.5$ s), the numerical model showed some residual turbulent kinetic energy at locations within the vortex's domain. This turbulent energy is ultimately responsible for the stationary (steady-state) nature of the submerged roller. Residual vertical and horizontal velocities at points located within the vortex extension are indicative of the existence of the free surface current, which was also observed during the experimental tests.

These research findings demonstrate that the broad-crested design is effective in minimizing the tailwater range associated with the formation of a submerged roller. However, if a submerged roller forms, its hydrodynamic characteristics are more dangerous than those occurring in the case of a sharp-crested weir. An objective-specific evaluation is required to assess the desired design: either using a broad crest to minimize the occurrence of the submerged roller, or employing a sharp crest to minimize the velocities and vortex extension. An elevated apron will minimize both the vortex occurrence and its hydrodynamic characteristics.

It is believed that the disagreement between the experimental and the numerical results are associated to inherent errors in the data acquisition of the surface velocity and theoretical simplifications and limitations of the numerical model. Although reasonable accuracy in the estimation of the surface velocities was obtained, the large amount of entrained air and the fluctuating free surface might be responsible for some errors in the velocity measurements. Therefore, the experimental and numerical investigations complemented each other and helped identify areas of improvement for future studies.

8.2 Recommendations for Future Work

The findings obtained in this study helped identify several areas for potential improvements for future numerical and experimental investigations:

- Future experimental work focusing on measuring air entrainment within the submerged hydraulic jump is required to better understand its spatial and temporal distribution within the vortex' structure. A dual tip probe has been successfully used (Chanson & Brattberg, 2000) to measure the air bubble entrainment and its spatial distribution. The author recommends its incorporation in future investigation of the submerged rollers.

- Although surface velocity measurements provided reasonable accuracy, the propeller meter used in the experimental tests did not provide sufficient spatial definition and accuracy. Alternative devices or techniques should be investigated for recording velocities under such special conditions.

- The proposed redefinition of the degree of submergence suggested in this study is one of the highlights of this research work. The further validation of the proposed formulation by using a wider range of weir heights and geometric models with different scales would augment the confidence in the proposed formulation.

- In the numerical experiments, the refinement of the computational mesh was shown to significantly affect the accuracy of the numerical results. Future investigations with refined grid size may better capture the surface velocity peak.

- The search of alternative crest designs to minimize both the occurrence and the characteristics of the roller is encouraged. It is believed that a broad-crested design featuring a set of indentations would successfully accomplish both goals.

References

---

[1] AASHTO, I. C. (2005). A summary of Existing Research on Low-Head Dam Removal Projects. Transportation Research Board (TRB).

[2] Applegate, V. C. (1950). *Natural History of the Sea Lamprey, Petromyzon Marinus, in Michigan.* United States Department of the Interior. Fish and Wildlife Service.

[3] Borland-Coogan, F. P. (Director). (1980). *The Drowning Machine* [Motion Picture].

[4] Boussinesq, J. V. (1887). Cours d'analyse infinitésimale en vue des applications mécaniques et physiques. Paris: Gauthier-Villars.

[5] Caretto, L. S., Gosman, A. D., Patankar, S. V., & Spalding, D. B. (1972). Two calculation Procedures for Steady, Three-Dimensional Flows with Recirculation. *Third International Conference on Numerical Methods in Fluid Mechanics*, *2*, pp. 60-68.

[6] Castillo, L. G., Carrillo, J. M., Garcia, J. T., & Vigueras-Rodriguez, A. (2014). Numerical Simulations and Laboratory Measurements in Hydraulic Jumps. *11th International Conference on Hydroinformatics, HIC 2014.* New York City, USA.

[7] Chanson, H. (1993). Self-Aerated Flows on Chutes and Spillways. *Journal of Hydraulic Engineering, 119*(2), 220-243.

[8] Chanson, H. (1995). Air entrainment in two-dimensional turbulent shear flows with partially developed inflow conditions. *International Journal of Multiphase Flow*, 1107-1121.

[9] Chanson, H. (1999). *The Hydraulics of Open Channel Flow.* 338 Euston Road, London, UK: Arnold.

[10] Chanson, H. (2007). Bubbly flow structure in hydraulic jump. *European Journal of Mechanics B/Fluids, 26*, 367-384.

[11] Chanson, H., & Brattberg, T. (2000). Experimental study of the air-water shear flow in a hydraulic jump. *Int. Journal Multiphase Flow, 26*(4), 583-607.

[12] Cheng, Y., Lien, F. S., Yee, E., & Sinclair, R. (2003). A comparison of large Eddy simulations with a standard k-e Reynolds-averaged Navier-Stokes model for the prediction of a fully developed turbulent flow over a matrix of cubes. *Journal of Wind Engineering and Industrial Aerodynamics, 91*, 1301-1328.

[13] Chow, V. T. (1959). *Open-Channel Hydraulics.* New York: McGraw-Hill.

[14] Committe on Small Dams. (2011). Small Dams - Design, Surveillance and Rehabilitation, Bulletin. ICOLD.

[15] Crowe, R. (1975). *Great Lakes Fisheries Commission: History, program and progress.* Ann Arbor, Michigan: Great Lakes Fisheries Commission.

[16] Ferrari, A. (2010). A SPH simulation of free surface flow over sharp-crested weir. *Advances in Water Resources, 33*, 270-276.

[17] Govinda Rao, N. S., & Muralidhar, D. (1963). Discharge characteristics of weirs of finite crest width. *Houille Blanche, 18*(5), 537-545.

[18] Govinda Rao, N. S., & Rajaratnam, N. (1963). The submerged hydraulic jump. *Journal of Hydraulic Division, 89*, 139-162.

[19] Habibzadeh, A. (2013). Experimental Study of Submerged Hydraulic Jumps with Baffle Blocks. Edmonton, Alberta: University of Alberta.

[20] Hager, W. H., & Schwalt, M. (1994). Broad-Crested Weir. *Journal of Irrigation and Drainage Engineering*, pp. 120-13:26.

[21] Hirt, C. W., & Nicols, B. D. (1981). Volume of fluid (VOF) method for the dynamics of free boundaries. *J. Computational Physics, 39*, 201-225.

[22] Hotchkiss, R. H., & Comstock, M. (1992). Drownproofing of low overflow structures (Discussion). *Journal of Hydraulic Engineering, 118*, 1586-1589.

[23] Hughes, S. A. (1993). Physical models and laboratory techniques in coastal engineering (Vol. 7). World Scientific Publications.

[24] Hunn, J. B., & Youngs, W. D. (1980). Role of physical barriers in the control of sea lamprey (Petromyzon marinus). *Can. J. Fish. Aquat. Sci., 37*, 2118-2122.

[25] Issa, R. A. (1986). Solution of implicitly discretized fluid flow equations by operator splitting. *Journal of Computational Physics, 62*(1), 40-65.

[26] Jones, W. P., & Launder, B. E. (1972). The prediction of laminarization with a two equation model of turbulence. *International Journal of Heat and Mass Transfer, 15*, 301-314.

[27] Khatsuria, R. M. (2005). *Hydraulics of Spillways and Energy Dissipators.* New York: Marcel Dekker.

[28] Launder, B. E., & Spalding, D. B. (1974). The numerical computation of turbulent flows. *Computer Methods in Applied Mechanics and Engineering*(3), 269-289.

[29] Lavis, D. S., Hallett, A., Koon, E. M., & McAuley, T. C. (2003). History of advances in barriers as an alternative method to suppress Sea Lampreys in the Great Lakes. *J. Great Lakes Research, 29*, 362-372.

[30] Leutheusser, H. J. (1988). Dam Safety Yes, But What About Safety at Dams? *1988 National Conference, ASCE, Hyd. Div.*, (pp. 1091-1096). Colorado Springs, CO.

[31] Leutheusser, H. J., & Birk, W. M. (1991). Drownproofing of low overflow structures. *Journal of Hydraulic Engineering, 117*(2), 205-213.

[32] Leutheusser, H., & Fan, J. (2001). Backward flow velocities of submerged hydraulic jumps. *J. Hydraulic Engineering*(127), 514-517.

[33] Long, D., Rajaratnam, N., & Steffler, P. M. (1991). Structure of flow in hydraulic jumps. *J. Hydraulic Research, IAHR, 29*(2), 207-218.

[34] Long, D., Steffler, P. M., & Rajaratnam, N. (1990). LDA study of flow structure in submerged hydraulic jump. *Journal of Hydraulic Research, 28*(4), 437-460.

[35] Long, D., Steffler, P., & Rajaratnam, N. (1991). A numerical study of submerged hydraulic jumps. *Journal of Hydraulic Research, 29*(3), 293-308.

[36] Lv, X., Zou, Q. P., Reeve, D. E., & Zhao, Y. (2009). A novel coupled level set and volume of fluid method for sharp interface capturing on 3D tetrahedral grids. *Journal of Computational Physics, 229*(7), 2573-2604.

[37] Lv, X., Zou, Q., & Reeve, D. (2011). Numerical simulation of overflow at vertical weirs using a hybrid level set/VOF method. *Advances in Water Resources, 34*, 1320-1324.

[38] Ma, F., Hou, Y., & Prinos, P. (2001). Numerical calculation of submerged hydraulic jumps. *Journal of Hydraulic Research, 39*(5), 493-503.

[39] Madsen, P. A., & Svendsen, I. A. (1983). Turbulent Bores and Hydraulic Jumps. *Journal Fluid Mechanics, 129*, 1-25.

[40] Marquez Damian, S. Description and utilization of interFoam ´ multiphase solver. http://infofich.unl.edu.ar/upload/3be0e16065026527477b4b948c4caa7523c8ea52.pdf

[41] McCorquodale, J., & Khalifa, A. (1983). Internal Flow in a Hydraulic Jump. *Journal of the Hydraulics Division, ASCE, 106*, 355-367.

[42] McLaughlin, R. L., Hallett, A., Pratt, T. C., O'Connor, L. M., & McDonald, D. G. (2007). Research to Guide Use of Barriers, Traps, and Fishways to Control Sea Lamprey. *Journal Great Lakes Research, 33*(Special Issue (2)), 7-19.

[43] Millar, M., & Ross, I. (2000). *Sea lamprey barrier life cycle and operation protocols.* Great Lakes Fisheries Commission.

[44] Montes, J. S., & Chanson, H. (1998). Characteristics of undular hydraulic jumps: experiments and analysis. *Journal of Hydraulic Engineering, 124*(2), 192-205.

[45] Morman, R. H., Cuddy, D. W., & Rugen, P. C. (1980). Factors influencing the Distribution of Sea Lamprey (Petromyzon marinus) in the Great Lakes. *Sea Lamprey International Symposium (SLIS).* Marquette, Michigan, July 3 0- August 8.

[46] Murzyn, F., & Chanson, H. (2007). *Free-surface, bubbly flow and turbulence measurement in hydraulic jumps.* Brisbane, Australia: Div. of Civil Engineering, The University of Queensland.

[47] Ohtsu, I., Yasuda, Y., & Ishikawa, M. (1999). Submerged Hydraulic Jumps below Abrupt Expansions. *Journal of hydraulic Engineering, 125*(5), 492-499.

[48] OpenFOAM, U. G. (2014). *The Open Source CFD Toolbox. Version 2.3.0.* OpenFOAM FUNDATION.

[49] Patankar, S. V., & Spalding, D. B. (1972). A calculation procedure for heat, mass and momentum transfer in three-dimensional parabolic flows. *International Journal of Heat and Mass Transfer, 15*(10), 1787-1806.

[50] Peterka, A. J. (1978). *Hydraulic design of stilling basins and energy dissipaters.* (Vol. Engineering Monograph No. 25). Denver, Colorado, USA.

[51] Prandtl, L. (1925). Z. angew. *Math. Mech., 5*(1), 136-139.

[52] Prashun, A. L. (1992). *Fundamentals of hydraulic engineering.* Oxford University Press.

[53] Qingchao, L., & Drewes, V. (1994). Turbulence characteristics in free and forced hydraulic jumps. *Journal of Hydraulic Research, 32*(4), 877-898.

[54] Qu, J., Ramamurthy, A. S., Tadayon, R., & Chen, Z. (2009). Numerical simulation of sharp-crested weir flows. *Canadian Journal of Civil Engineering, 36*, 1530-1534.

[55] Rajaratnam, N. (1967). *Hydraulic jumps in advances in Hydroscience* (Ed. 4 ed.). New York: Academic Press.

[56] Rajaratnam, N. (1990). Skimming flow in stepped spillways. *Journal of Hydraulic Engineering, 116*(4), 587-590.

[57] Rajaratnam, N., & Muralidhar, D. (1969). Flow below deeply submerged rectangular weirs. *Journal of Hydraulic Research, 7*(3), 355-373.

[58] Rehbock, T. (1929). Wassermessung mit scharfkantigen Ueberfallwehren. *Z. VDI, Bd. 73, Nr. 27,*, 817-823.

[59] Resch, F. J., & Leutheusser, H. J. (1972). Le ressaut hydraulique: measure de turbulence dans la region diphasique. *La Houille Blanche, 4*, 279-293.

[60] Reynolds, O. (1903). *Papers on Mechanical and Physical Subjects* (Vols. III: The Sub-Mechanics of the Universe). Cambridge: Cambridge: University Press.

[61] Romagnoli, M., Portapila, M., & Morvan, H. (2009). Simulacion computacional del resalto hidraulico. *Mecanica Computacional, XXVIII*, 1661-1672.

[62] Rouse, J., Siao, T. T., & Nagaratnam, R. (1958). Turbulence characteristics of the hydraulic jump. *Journal of the Hydraulic Division, ASCE, 84*.

[63] Rusche, H. (2002). *Computational fluid dynamics of dispersed two-phase flow at high-phase fractions.* Imperial College of Science, Technology and Medicine, London, England: Ph.D. thesis.

[64] Sawyer, A. J. (1980). Prospects for integrated pest management of the sea lamprey (Petromyzon marinus). *Canadian Journal Fisheries and Aquatic Sciences*(37), 2081-2092.

[65] Smith, B. R., & Tibbles, J. J. (1980). Sea lamprey (Petromyzon marinus) in Lakes Huron, Michigan and Superior: history of invasion and control, 1936-78. *Canadian Journal of Fisheries and Aquatic Sciences, 37*, 1780-1801.

[66] Tschantz, B., & Wright, K. (2011). Hidden Dangers and Public Safety. Low-head Dams. *Journal of Dam Safety, 9*(1), 8-17.

[67] USBR, U. S. (1960). *Design of Small Dams.* United States Department of the Interior.

[68] Vaideliene, A., & Tervydis, P. (2013). Measurement of Air Bubbles Concentration in the water by means of Digital Image Processing. *Elektronika ir Elektrotechnika, 19*(4), 1392-1215.

[69] Valle, B. L., & Pasternack, B. (2006). Air concentrations of submerged and unsubmerged hydraulic jumps in a bedrock step-pool channel. *Journal of Geophysical Research, 3*.

[70] Van de Sande, E., & Smith, J. M. (1973). Surface entrainment of air by high-velocity water jets. *Chemical Engineering Science, 28*, 1161-1168.

[71] Villemonte, J. R. (1947). Submerged-weir discharge studies. *Engineering News Record*, 54-57.

[72] Vischer, D. L., & Hager, W. H. (1995). *Energy dissipators - Hydraulic design considerations.* Rotterdam, Netherlands: IAHR Hydraulic Structures Design Manual No.9.

[73] Wigley, R. L. (1959). Life history of the sea lamprey of Cayuga Lake, New York. *Fishery Bulletin, 59*, 561-617.

[74] Wright, K. R., Kelly, J. M., Houghtalen, R. J., & Bonner, M. R. (1995). Emergency Rescues at Low-Head Dams. *12th Annual Conference Association of State Dam Safety Officials.* Atlanta.

[75] Wu, S., & Rajaratnam, N. (1996). Submerged flow regimes of rectangular Sharp-Crested weirs. *Journal of Hydraulic Engineering, 122*(7), 412-414.

[76] Wu, S., & Rajaratnam, N. (1998). Impinging jet and surface flow regimes at drop. *Journal of Hydraulic Research, 36*(1), 69-74.

[77] Youngs, W. D. (1979). Evaluation of barrier dams to a adult sea lamprey mitigation. Michigan, USA: Ann Arbor.

Publications

The following are publications that were written during the completion of this thesis based on its content.

[1] Lopez-Egea, M., Nistor, I. Townsend, R., Paudel, B., Sullivan, P., (2014). A laboratory study of the impact of crest length on the characteristics of downstream submerged hydraulic jumps on low-head dam structures, *CSCE Annual Conference,* Halifax.

[2] Lopez-Egea, M., Nistor, I., (2014). *Modification of sea lamprey barrier's crest shape to mitigate hazardous hydraulic conditions*. Technocal Report prepared for the Sea Lamprey Control Centre - Department of Fisheries and Oceans, Sault-Ste, Marie, Canada.

[3] Lopez-Egea, M., Nistor, I. Townsend, R., (2014). An experimental study of the impact of crest width on the characteristics of downstream submerged hydraulic jumps on low-head dam structures. 1st Prize - Civil Engineering Section. *Research Poster Paper Competition- Faculty of Engineering Research Day,* University of Ottawa.

[4] Lopez-Egea, M., Nistor, I. Townsend, R., Paudel, B., Sullivan, P., (2015). An experimental and numerical study of submerged hydraulic jumps forming at low-head dams, *36th IAHR World Congress.* Delft-The Hague. (Accepted)

[5] Lopez-Egea, M., Nistor, I., (2015). *Numerical simulation of submerged hydraulic jump forming downstream from sea lamprey barriers.* Technical Report for the Sea Lamprey Control Centre - Department of Fisheries and Oceans, Sault-Ste, Marie, Canada.

Appendix A: Vortex Formation; experimental data

Table A- 1: Lower boundary (Y_l) associated to the transition from ‘free’ to ‘submerged’ hydraulic jump

Date	Test #	Q (l/s)	C_L (cm)	Z_{floor} (m)	Yo (m)	Y_{bed} (cm)	Y_t (m)
130510	1	10	6	0	0.34	8	0.095
130510	3	10	12	0	0.349	6	0.09
130510	11	10	16	0	0.35	10.5	0.1125
130510	14	10	20	0	0.344	9.8	0.108
130510	17	10	24	0	0.35	8	0.1
130513	1	20	6	0	0.375	10	0.135
130513	2	20	8	0	0.38	13.3	0.15
130513	3	20	12	0	0.38	13	0.14
130513	4	20	12	0	0.39	14.2	0.155
130513	5	20	16	0	0.386	14.5	0.157
130513	16	20	20	0	0.391	15	0.154
130513	17	20	24	0	0.388	14.5	0.15
130513	18	30	6	0	0.396	16.3	0.188
130513	19	30	8	0	0.4	16.7	0.185
130513	20	30	12	0	0.407	17.6	0.187
130513	21	30	16	0	0.412	17	0.188
130513	22	30	20	0	0.42	16	0.192
130513	23	30	20	0	0.418	17	0.194
130513	40	30	24	0	0.42	18	0.192
130514	1	40	6	0	0.423	18	0.204
130514	2	40	8	0	0.429	19.5	0.22
130514	3	40	12	0	0.434	19.5	0.226
130514	4	40	16	0	0.441	20	0.23
130514	5	40	20	0	0.445	19.5	0.22
130514	6	40	24	0	0.45	19.5	0.228
130514	7	50	6	0	0.444	21.5	0.258
130514	8	50	8	0	0.448	23	0.252
130514	9	50	12	0	0.454	22.5	0.26
130514	10	50	16	0	0.46	23.5	0.27
130514	11	50	20	0	0.47	24	0.275
130514	12	50	24	0	0.469	22	0.252
130524	1	10	30	0	0.347	10.3	0.111
130524	2	10	35	0	0.349	10.8	0.115
130524	3	20	30	0	0.385	14.5	0.154
130524	4	20	35	0	0.388	14.3	0.152
130524	5	30	30	0	0.419	15.5	0.195
130524	6	30	35	0	0.425	17	0.19
130524	7	40	30	0	0.445	19.5	0.232
130524	8	40	35	0	0.453	19.3	0.231
130524	9	50	30	0	0.47	22.5	0.26
130524	10	50	35	0	0.478	22.5	0.268
130614	1	10	35	0	0.344	10.6	0.109
130614	4	10	45	0	0.348	10.6	0.11
130614	7	10	55	0	0.35	11.5	0.117
130618	1	20	45	0	0.39	16.1	0.162
130618	4	30	45	0	0.424	19.3	0.196
130618	7	40	45	0	0.455	23.6	0.238
130618	10	50	45	0	0.479	26.2	0.262
130618	13	20	55	0	0.394	16	0.162
130618	13	50	55	0	0.484	25.5	0.256
130618	16	30	55	0	0.425	19.9	0.201

Date	Test #	Q (l/s)	C_L (cm)	Z_{floor} (m)	Yo (m)	Y_{bed} (cm)	Y_t (m)
130618	19	40	55	0	0.457	23.3	0.235
130725	1	10	6	0.105	0.345	9.7	0.204
130725	4	10	35	0.105	0.354	10	0.208
130725	7	10	45	0.105	0.352	11.2	0.22
130725	10	10	55	0.105	0.359	10.5	0.214
130725	13	30	6	0.105	0.4	15.5	0.276
130725	16	30	35	0.105	0.424	17.5	0.293
130726	3	10	8	0.105	0.348	9.5	0.204
130726	6	10	12	0.105	0.351	9.9	0.207
130726	9	10	16	0.105	0.352	10.5	0.213
130726	12	10	20	0.105	0.351	10	0.211
130726	15	10	24	0.105	0.353	10.2	0.213
130726	18	10	30	0.105	0.349	10.3	0.213
130730	1	30	12	0.105	0.413	17.2	0.293
130730	4	30	24	0.105	0.424	18.3	0.294
130730	7	30	45	0.105	0.43	18.4	0.295
130731	1	30	55	0.105	0.429	19	0.3
130731	4	50	6	0.105	0.45	22.4	0.342
130801	1	50	12	0.105	0.461	23.3	0.347
130801	4	50	24	0.105	0.475	23.5	0.348
130801	7	50	35	0.105	0.483	24.5	0.356
130801	10	50	45	0.105	0.48	23.5	0.351
130801	13	50	55	0.105	0.486	23.9	0.354
130808	1	10	6	0.155	0.343	8.6	0.256
130809	1	10	12	0.155	0.351	9	0.26
130809	4	10	24	0.155	0.355	9.4	0.266
130809	7	10	35	0.155	0.353	9.7	0.266
130809	10	10	45	0.155	0.354	9.5	0.267
130809	13	10	55	0.155	0.353	9.2	0.261
130809	16	30	6	0.155	0.405	15.5	0.334
130809	19	30	12	0.155	0.42	15.9	0.334
130812	1	30	24	0.155	0.421	16.2	0.335
130812	4	30	35	0.155	0.421	15.7	0.336
130812	7	30	45	0.155	0.42	16.2	0.331
130812	10	30	55	0.155	0.43	17.2	0.336
130812	13	50	6	0.155	0.46	20.8	0.389
130812	16	50	12	0.155	0.462	21.5	0.385
130813	1	50	24	0.155	0.473	22	0.39
130813	4	50	35	0.155	0.478	22.1	0.387
130813	7	50	45	0.155	0.487	22.6	0.397
130813	10	50	55	0.155	0.486	22	0.39
130819	1	10	6	0.055	0.345	10.4	0.163
130819	4	10	12	0.055	0.351	11	0.167
130819	7	10	24	0.055	0.351	11.2	0.167
130819	10	10	35	0.055	0.351	10.6	0.165
130819	13	10	45	0.055	0.35	10.6	0.163
130819	16	10	55	0.055	0.355	10.9	0.166
130821	1	30	6	0.055	0.398	18	0.243
130821	4	30	12	0.055	0.411	18.5	0.241
130821	7	30	24	0.055	0.42	18.4	0.245
130821	10	30	35	0.055	0.424	19.3	0.248
130821	13	30	45	0.055	0.43	19	0.251
130821	16	30	55	0.055	0.429	18.9	0.246
130821	19	50	6	0.055	0.444	23.3	0.295
130822	1	50	12	0.055	0.458	23.6	0.303
130822	4	50	24	0.055	0.476	25.1	0.319
130822	7	50	35	0.055	0.477	24.8	0.312
130822	10	50	45	0.055	0.481	24.5	0.304
130822	13	50	55	0.055	0.485	24.3	0.306

Table A- 2: Upper boundary (Y_{u+}) associated to the transition from ‘submerged’ to ‘undular’ hydraulic jump

Date	Test #	Q (l/s)	C_L (cm)	Z_{floor} (m)	Yo (m)	Y_{bed} (cm)	Y_t (m)
130510	2	10	6	0	0.345	NA	0.287
130510	7	10	8	0	0.345	NA	0.305
130510	9	10	12	0	0.353	NA	0.295
130510	12	10	16	0	0.35	31	0.3
130510	15	10	20	0	0.351	31.8	0.301
130510	18	10	24	0	0.35	30	0.297
130513	2	20	6	0	0.39	36.5	0.35
130513	3	20	8	0	0.385	35	0.338
130513	4	20	12	0	0.385	33.5	0.3265
130513	5	20	12	0	0.391	34.8	0.335
130513	6	20	16	0	0.388	33	0.32
130513	17	20	20	0	0.392	32	0.315
130513	18	20	24	0	0.392	31.8	0.314
130513	19	30	6	0	0.409	36.8	0.357
130513	20	30	8	0	0.415	36.5	0.358
130513	21	30	12	0	0.413	37.7	0.356
130513	22	30	16	0	0.415	36	0.343
130513	23	30	20	0	0.423	34.8	0.339
130513	24	30	20	0	0.423	36.4	0.346
130513	41	30	24	0	0.422	34.5	0.333
130514	2	40	6	0	0.454	41.5	0.395
130514	3	40	8	0	0.448	39	0.386
130514	4	40	12	0	0.445	40.5	0.39
130514	5	40	16	0	0.448	39.5	0.38
130514	6	40	20	0	0.453	38.5	0.37
130514	7	40	24	0	0.454	37.5	0.37
130514	8	50	6	0	0.473	41.5	0.403
130514	9	50	8	0	0.47	40.5	0.395
130514	10	50	12	0	0.465	41	0.393
130514	11	50	16	0	0.468	41	0.39
130514	12	50	20	0	0.476	41.5	0.39
130514	13	50	24	0	0.48	40.5	0.378
130524	14	10	30	0	0.349	30.7	0.294
130524	15	10	35	0	0.35	31.7	0.303
130524	16	20	30	0	0.386	33	0.318
130524	17	20	35	0	0.39	32.5	0.313
130524	18	30	30	0	0.42	34.5	0.338
130524	19	30	35	0	0.424	34	0.331
130524	20	40	30	0	0.448	36	0.366
130524	21	40	35	0	0.455	36.5	0.358
130524	22	50	30	0	0.473	39.2	0.38
130524	23	50	35	0	0.48	38.8	0.383
130614	2	10	35	0	0.345	30.4	0.296
130614	5	10	45	0	0.348	29.9	0.286
130614	8	10	55	0	0.348	32.8	0.31
130618	2	20	45	0	0.39	32.5	0.305
130618	5	30	45	0	0.424	33.6	0.324
130618	8	40	45	0	0.455	36.2	0.347
130618	11	50	45	0	0.48	38.2	0.366
130618	14	20	55	0	0.394	33.1	0.309
130618	14	50	55	0	0.485	39.1	0.375
130618	17	30	55	0	0.423	34.7	0.328
130618	20	40	55	0	0.457	35.5	0.353
130725	2	10	6	0.105	0.347	22.3	0.315
130725	5	10	35	0.105	0.349	20.5	0.301
130725	8	10	45	0.105	0.353	19.5	0.295
130725	11	10	55	0.105	0.354	20.4	0.298
130725	14	30	6	0.105	0.42	28.2	0.375
130726	1	30	35	0.105	0.423	24.7	0.35
130726	4	10	8	0.105	0.35	21	0.314
130726	7	10	12	0.105	0.354	20.8	0.308

Date	Test #	Q (l/s)	C_L (cm)	Z_{floor} (m)	Yo (m)	Y_{bed} (cm)	Y_t (m)
130726	10	10	16	0.105	0.349	20.6	0.313
130726	13	10	20	0.105	0.351	20.5	0.302
130726	16	10	24	0.105	0.354	20.2	0.297
130726	19	10	30	0.105	0.351	19.6	0.304
130730	2	30	12	0.105	0.42	28.2	0.375
130730	5	30	24	0.105	0.43	24.5	0.368
130730	8	30	45	0.105	0.426	25.8	0.344
130731	2	30	55	0.105	0.435	25.2	0.353
130731	5	50	6	0.105	0.485	33.6	0.443
130801	2	50	12	0.105	0.48	33.6	0.439
130801	5	50	24	0.105	0.477	32.5	0.416
130801	8	50	35	0.105	0.48	31.5	0.407
130801	11	50	45	0.105	0.482	30.5	0.402
130801	14	50	55	0.105	0.486	31.7	0.402
130808	2	10	6	0.155	0.354	17	0.332
130809	2	10	12	0.155	0.355	15	0.319
130809	5	10	24	0.155	0.353	13.9	0.31
130809	8	10	35	0.155	0.349	13.6	0.303
130809	11	10	45	0.155	0.352	13.5	0.298
130809	14	10	55	0.155	0.354	13.6	0.308
130809	17	30	6	0.155	0.425	23.4	0.392
130809	20	30	12	0.155	0.425	22.5	0.391
130812	2	30	24	0.155	0.422	22.2	0.372
130812	5	30	35	0.155	0.428	22	0.368
130812	8	30	45	0.155	0.425	21	0.362
130812	11	30	55	0.155	0.429	21.5	0.364
130812	14	50	6	0.155	0.504	31.5	0.475
130812	17	50	12	0.155	0.491	30.3	0.463
130813	2	50	24	0.155	0.485	29	0.445
130813	5	50	35	0.155	0.483	27	0.421
130813	8	50	45	0.155	0.479	25.5	0.416
130813	11	50	55	0.155	0.484	26.5	0.417
130819	2	10	6	0.055	0.353	28.3	0.327
130819	5	10	12	0.055	0.355	26.5	0.324
130819	8	10	24	0.055	0.351	25	0.303
130819	11	10	35	0.055	0.354	25.2	0.299
130819	14	10	45	0.055	0.355	23.8	0.301
130819	17	10	55	0.055	0.357	24.5	0.293
130821	2	30	6	0.055	0.413	32.5	0.364
130821	5	30	12	0.055	0.416	32.8	0.361
130821	8	30	24	0.055	0.422	30.5	0.34
130821	11	30	35	0.055	0.427	28.5	0.345
130821	14	30	45	0.055	0.428	28	0.333
130821	17	30	55	0.055	0.427	28	0.335
130821	20	50	6	0.055	0.48	37.5	0.425
130822	2	50	12	0.055	0.472	37.5	0.414
130822	5	50	24	0.055	0.474	35	0.394
130822	8	50	35	0.055	0.48	35	0.385
130822	11	50	45	0.055	0.48	33	0.378
130822	14	50	55	0.055	0.488	35	0.386

Table A- 3: Upper boundary (Y_{u-}) associated to the transition from ‘undular’ to ‘submerged’ hydraulic jump

Date	Test #	Q (l/s)	C_L (cm)	Z_{floor} (m)	Yo (m)	Y_{bed} (cm)	Y_t (m)
130510	3	10	6	0	0.345	NA	0.23
130510	8	10	8	0	0.346	NA	0.26
130510	10	10	12	0	0.353	25.7	0.267
130510	13	10	16	0	0.35	24.5	0.255
130510	16	10	20	0	0.348	25.1	0.26
130510	19	10	24	0	0.35	24.6	0.254
130513	18	20	20	0	0.392	26.5	0.284
130513	19	20	24	0	0.392	25.7	0.277
130513	20	20	6	0	0.375	26.7	0.285
130513	20	30	6	0	0.402	27.9	0.308
130513	21	20	8	0	0.38	27.5	0.29
130513	21	30	8	0	0.405	28	0.307
130513	22	20	12	0	0.386	25	0.273
130513	22	30	12	0	0.409	26.9	0.3
130513	23	20	12	0	0.39	25	0.275
130513	23	30	16	0	0.414	26.5	0.299
130513	24	20	16	0	0.385	24.5	0.27
130513	24	30	20	0	0.423	27.9	0.307
130513	25	30	20	0	0.419	27.3	0.304
130513	42	30	24	0	0.421	28.4	0.308
130514	43	40	6	0	0.435	31.9	0.347
130514	44	40	8	0	0.438	31.3	0.34
130514	45	40	12	0	0.437	21.5	0.34
130514	46	40	16	0	0.445	30.5	0.336
130514	47	40	20	0	0.45	29.7	0.33
130514	48	40	24	0	0.452	29.3	0.327
130514	49	50	6	0	0.462	34.2	0.366
130514	50	50	8	0	0.462	34.3	0.369
130514	51	50	12	0	0.46	34	0.368
130514	52	50	16	0	0.466	32.5	0.359
130514	53	50	20	0	0.475	34	0.365
130514	54	50	24	0	0.474	32.8	0.35
130524	55	10	30	0	0.349	26.1	0.269
130524	56	10	35	0	0.351	26.3	0.269
130524	57	20	30	0	0.388	26.4	0.285
130524	58	20	35	0	0.39	26.7	0.288
130524	59	30	30	0	0.42	39.2	0.315
130524	60	30	35	0	0.424	27.9	0.306
130524	61	40	30	0	0.448	31	0.34
130524	62	40	35	0	0.454	29.7	0.331
130524	63	50	30	0	0.473	31.3	0.35
130524	64	50	35	0	0.48	31.4	0.345
130614	3	10	35	0	0.349	24.9	0.258
130614	6	10	45	0	0.348	24	0.247
130614	9	10	55	0	0.346	25	0.249
130618	3	20	45	0	0.39	27.1	0.267
130618	6	30	45	0	0.424	29.2	0.296
130618	9	40	45	0	0.454	32.1	0.323
130618	12	50	45	0	0.48	33.8	0.341
130618	15	20	55	0	0.394	27	0.276
130618	15	50	55	0	0.483	34.5	0.348
130618	18	30	55	0	0.425	29	0.294
130618	21	40	55	0	0.456	31.6	0.32
130725	3	10	6	0.105	0.344	17.3	0.283
130725	6	10	35	0.105	0.352	15.4	0.272
130725	9	10	45	0.105	0.356	16.2	0.268
130725	12	10	55	0.105	0.358	16.1	0.271
130725	15	30	6	0.105	0.41	24.5	0.356
130726	2	30	35	0.105	0.425	22.1	0.337
130726	5	10	8	0.105	0.344	17.1	0.285
130726	8	10	12	0.105	0.354	17.2	0.283

Date	Test #	Q (l/s)	C_L (cm)	Z_{floor} (m)	Yo (m)	Y_{bed} (cm)	Y_t (m)
130726	11	10	16	0.105	0.348	16.6	0.277
130726	14	10	20	0.105	0.352	16.4	0.276
130726	17	10	24	0.105	0.356	16.2	0.274
130726	20	10	30	0.105	0.351	15.4	0.267
130730	3	30	12	0.105	0.416	24.4	0.355
130730	6	30	24	0.105	0.425	23.1	0.341
130730	9	30	45	0.105	0.428	22.8	0.339
130731	3	30	55	0.105	0.428	22.6	0.339
130731	6	50	6	0.105	0.479	32	0.427
130801	3	50	12	0.105	0.471	30.8	0.415
130801	6	50	24	0.105	0.476	28.5	0.4
130801	9	50	35	0.105	0.48	28.4	0.398
130801	12	50	45	0.105	0.483	28	0.391
130801	15	50	55	0.105	0.485	28.8	0.397
130808	3	10	6	0.155	0.347	13	0.3
130809	3	10	12	0.155	0.355	12.6	0.298
130809	6	10	24	0.155	0.354	12.5	0.293
130809	9	10	35	0.155	0.353	12.3	0.291
130809	12	10	45	0.155	0.352	11.7	0.285
130809	15	10	55	0.155	0.357	11.5	0.284
130809	18	30	6	0.155	0.42	21	0.379
130809	21	30	12	0.155	0.422	20.4	0.377
130812	3	30	24	0.155	0.426	19.4	0.366
130812	6	30	35	0.155	0.425	19.2	0.359
130812	9	30	45	0.155	0.43	19.4	0.36
130812	12	30	55	0.155	0.428	19.5	0.36
130812	15	50	6	0.155	0.482	27.5	0.444
130812	18	50	12	0.155	0.48	27	0.441
130813	3	50	24	0.155	0.477	25.5	0.418
130813	6	50	35	0.155	0.48	24.8	0.412
130813	9	50	45	0.155	0.485	23.4	0.405
130813	12	50	55	0.055	0.484	24	0.411
130819	3	10	6	0.055	0.345	22	0.278
130819	6	10	12	0.055	0.354	20.3	0.264
130819	9	10	24	0.055	0.351	20.2	0.265
130819	12	10	35	0.055	0.354	20.1	0.262
130819	15	10	45	0.055	0.351	19.3	0.255
130819	18	10	55	0.055	0.354	20	0.264
130821	3	30	6	0.055	0.405	27.2	0.338
130821	6	30	12	0.055	0.417	27.3	0.339
130821	9	30	24	0.055	0.421	25.9	0.318
130821	12	30	35	0.055	0.424	25.7	0.317
130821	15	30	45	0.055	0.43	25.3	0.314
130821	18	30	55	0.055	0.429	25.8	0.318
130821	21	50	6	0.055	0.47	34.1	0.4
130822	3	50	12	0.055	0.468	33.5	0.397
130822	6	50	24	0.055	0.475	30.8	0.372
130822	9	50	35	0.055	0.48	30.5	0.365
130822	12	50	45	0.055	0.481	29.8	0.362
130822	15	50	55	0.055	0.486	30.1	0.373

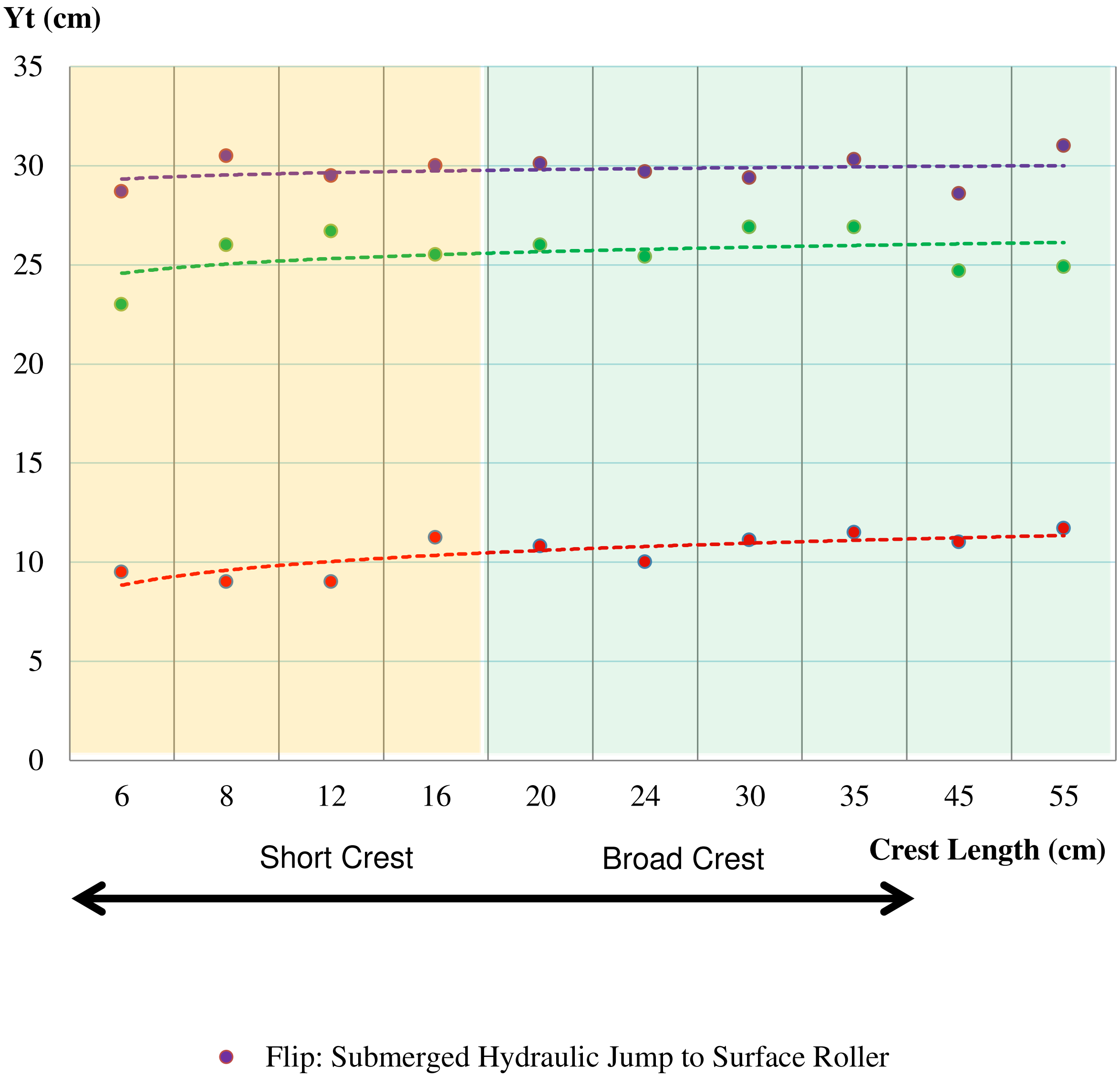

Figure A- 1: Transitional water depths for C_L=6 cm, Q=10 l/s and z_{floor}=0 cm

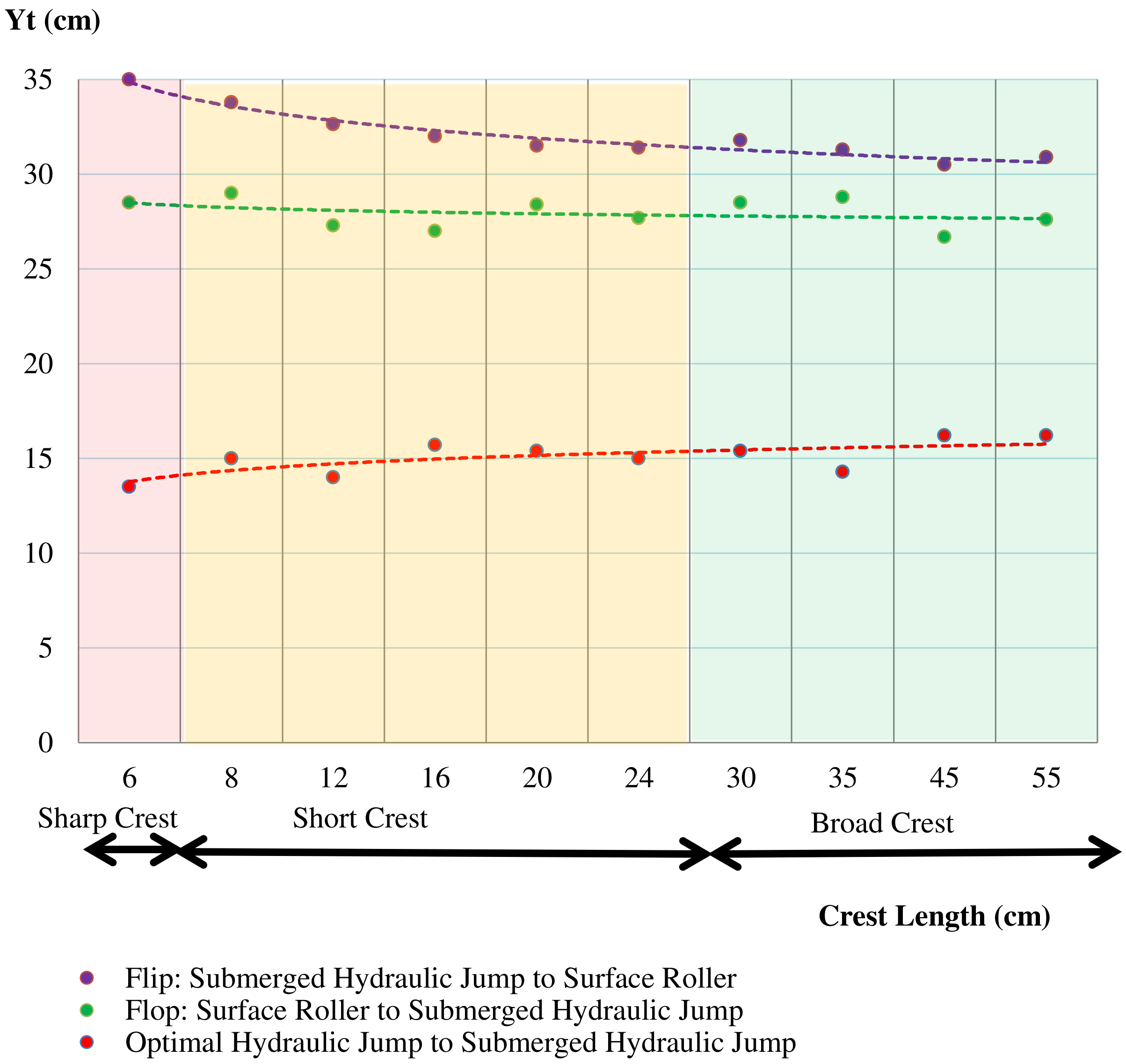

Figure A- 2: Transitional water depths for C_L=6 cm, Q=20 l/s and z_{floor}=0 cm

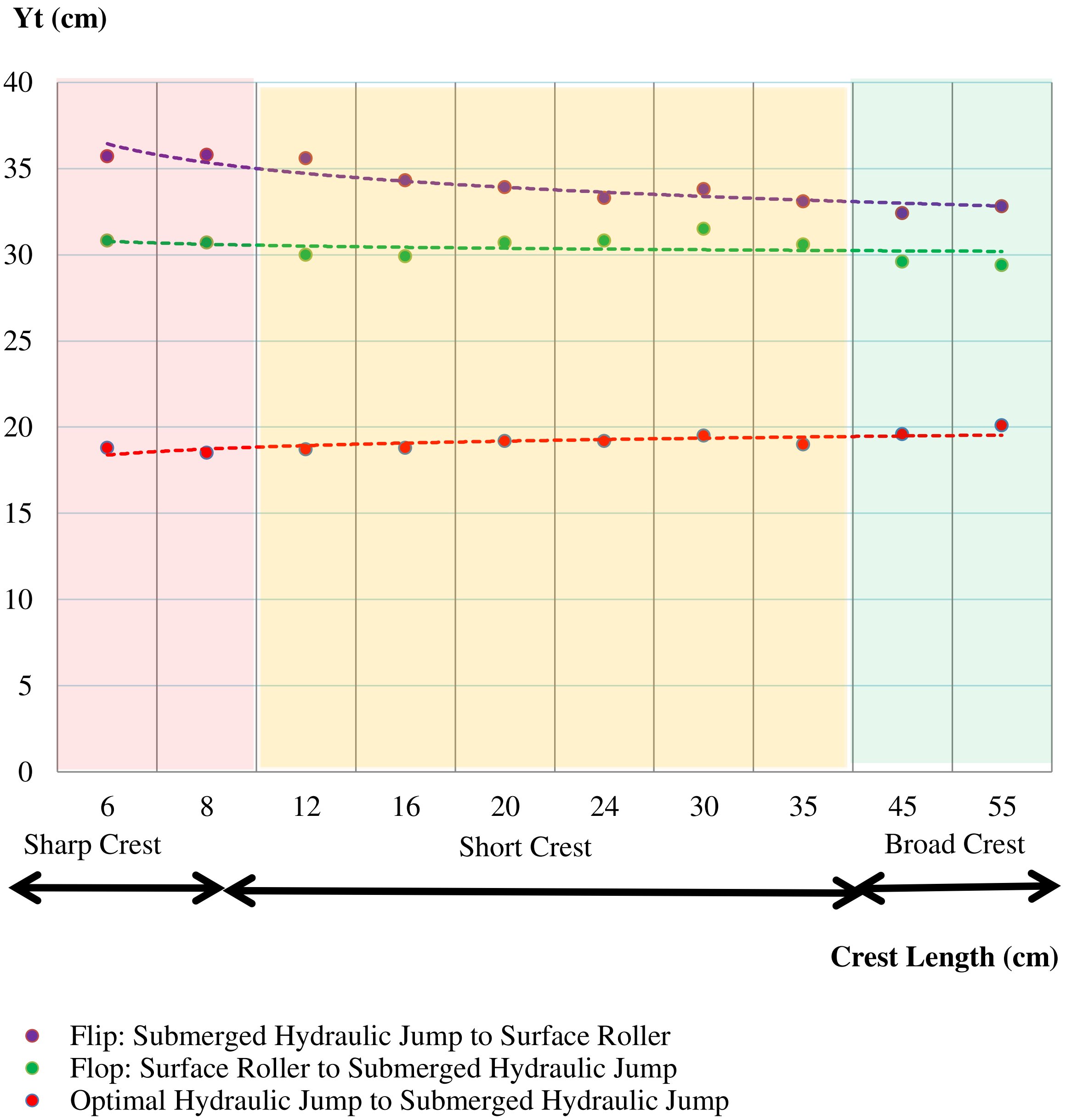

Figure A- 3: Transitional water depths for C_L=6 cm, Q=30 l/s and z_{floor}=0 cm

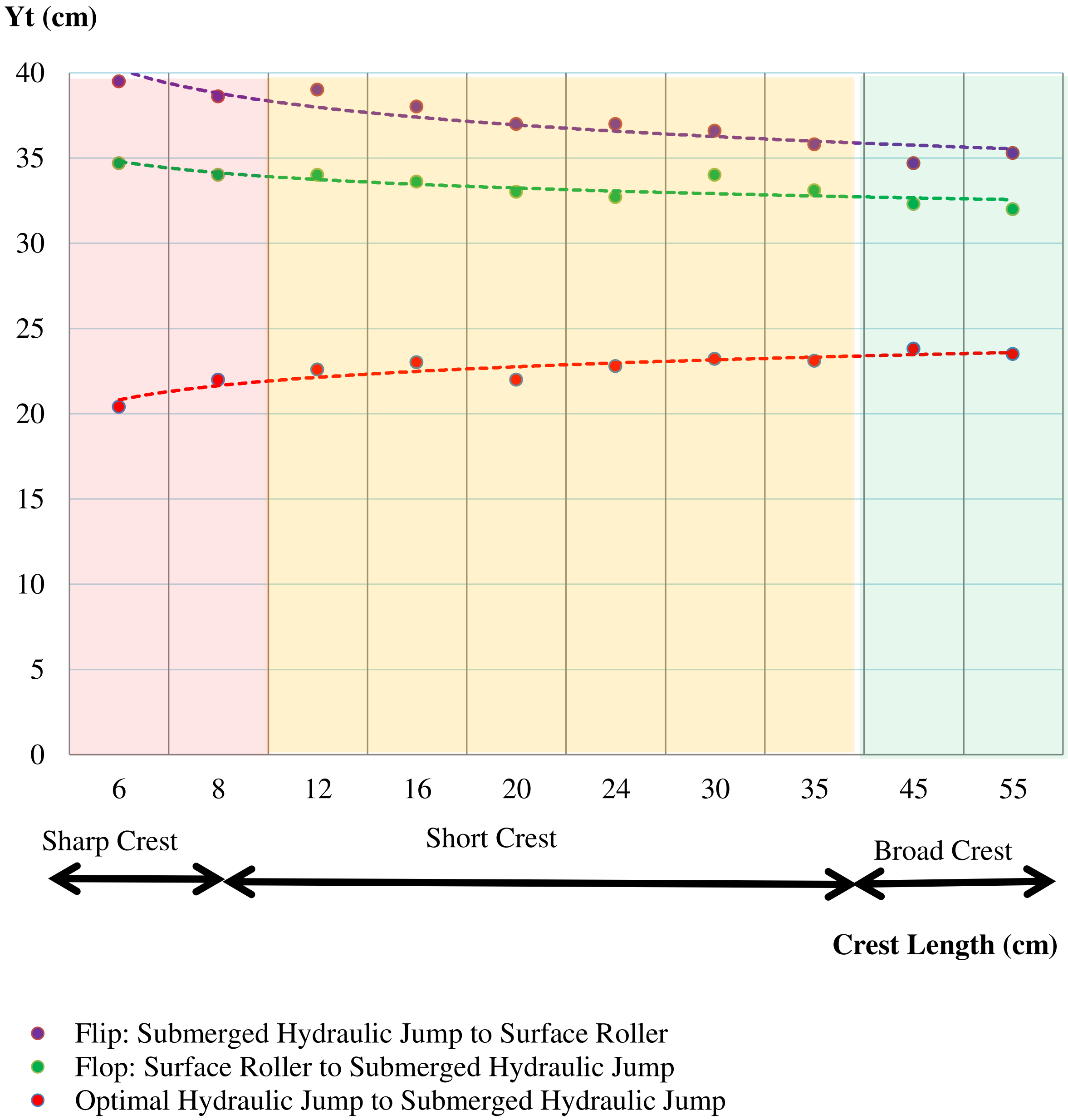

Figure A-4: Transitional water depths for C_L=6 cm, Q=40 l/s and z_{floor}=0 cm

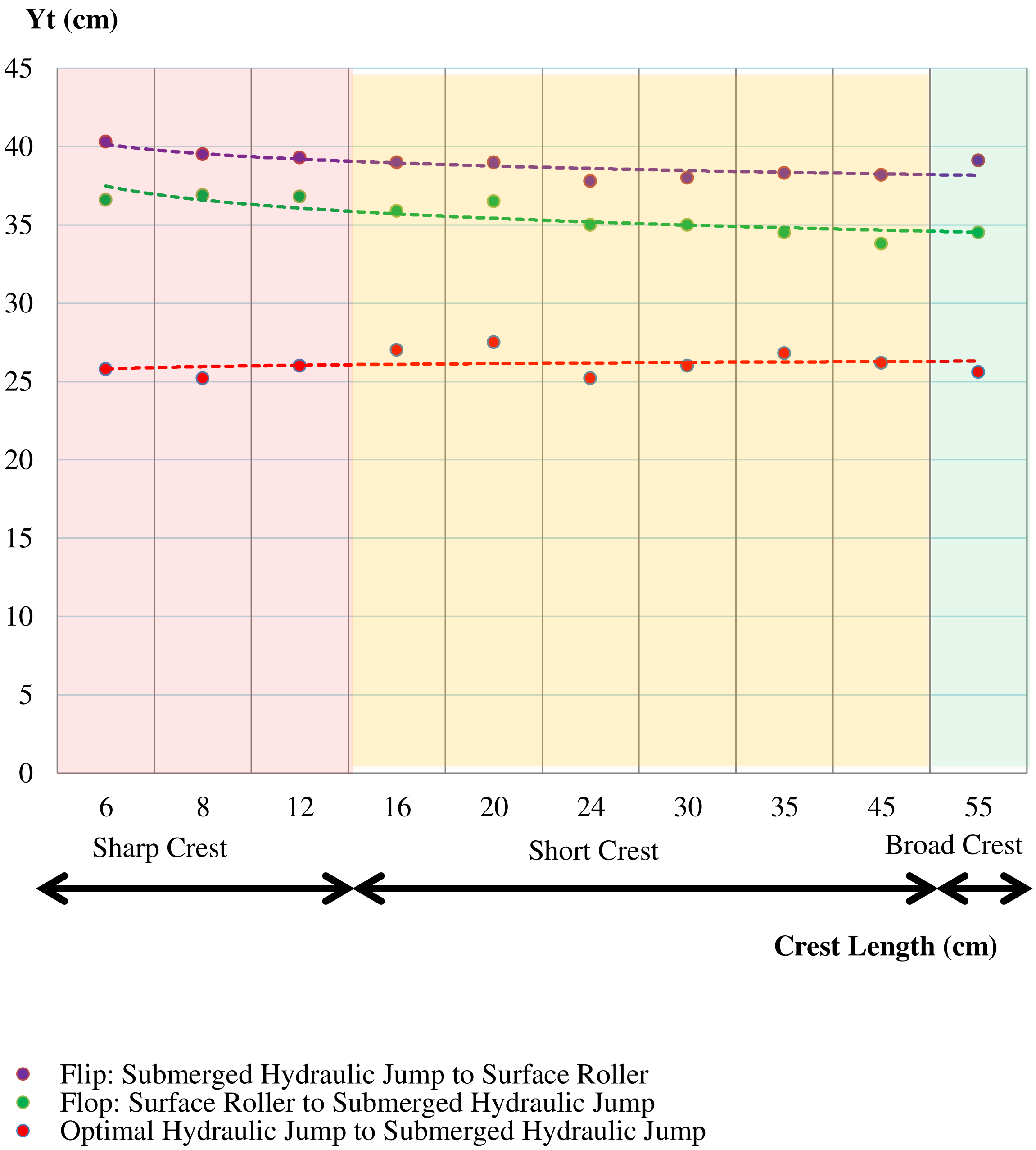

Figure A-5: Transitional water depths for C_L=6 cm, Q=50 l/s and z_{floor}=0 cm

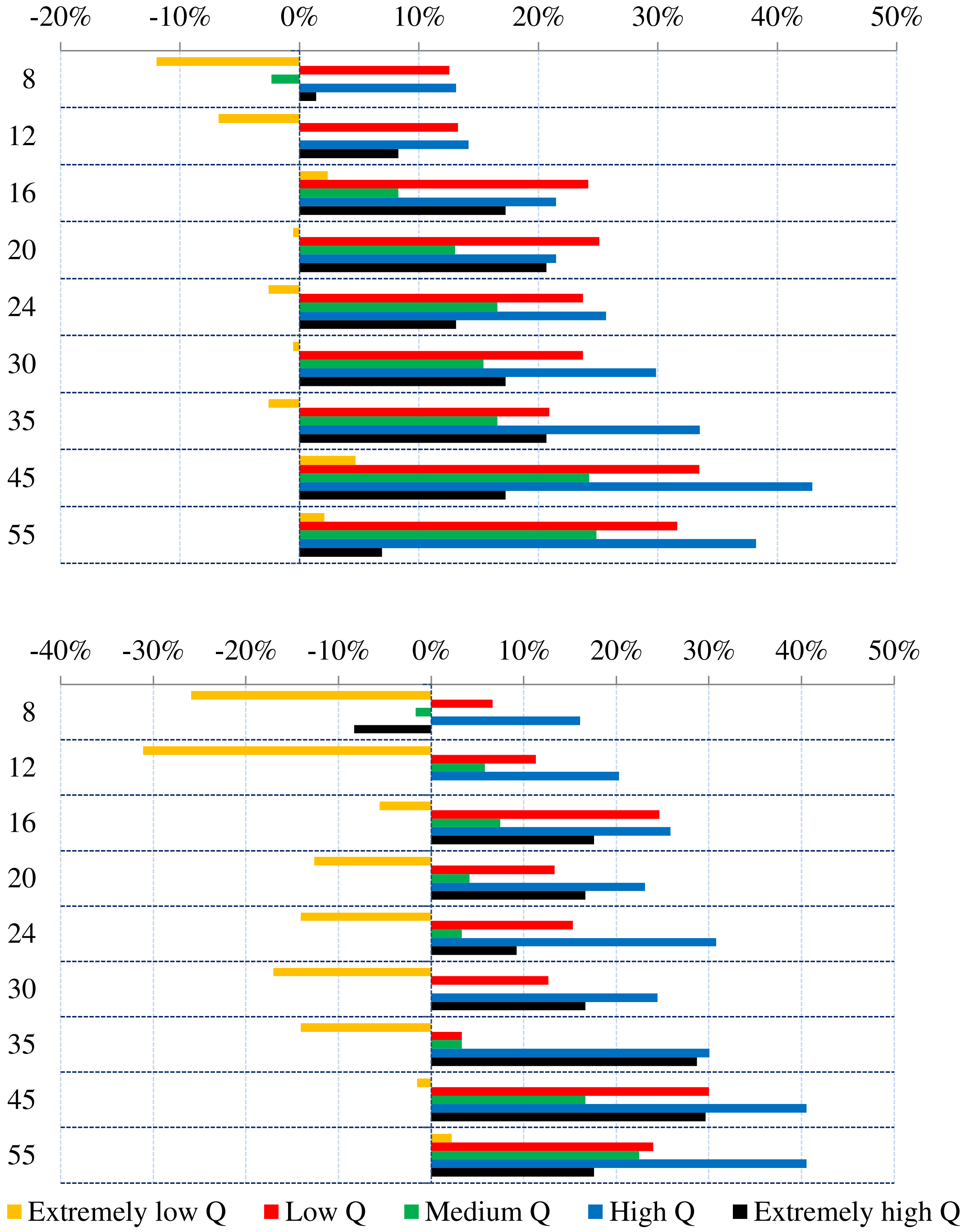

Figure A-6: Impact of the crest length at reducing the range of dangerous tailwater level $(Y_u - Y_l)$, in comparison with the 6cm sharp crest design; a) For raising tailwater level; b) For decreasing tailwater level

Appendix B: Vortex Characteristics; experimental data

									WATER LEVELS									
Date	Test #	Z_{floor} (m)	Q (l/s)	C_L (cm)	Yo (cm)	Yt (cm)	Iv (cm)	θ (°)	Xi=0.2 (m)	Xi=0.4 (m)	Xi=0.6 (m)	Xi=0.8 (m)	Xi=1.0 (m)	Xi=1.2 (m)	Xi=1.4 (m)	Xi=1.6 (m)	Xi=1.8 (m)	Xi=2.0 (m)
130607	**1**	0	10	6	34.4	12.3	15.5	54	9.8	11.8	12.2	12.7	NA	NA	NA	NA	NA	NA
130610	**1**	0	10	6	34.7	15.3	14	56	13.2	13.5	14.7	15.3	NA	NA	NA	NA	NA	NA
130611	**1**	0	10	6	34.6	20.2	11.5	58	18.7	18.8	19	19.4	19.7	NA	NA	NA	NA	NA
130611	**2**	0	10	6	34.4	24.9	8.5	54	24	24.1	24.2	24.7	25	NA	NA	NA	NA	NA
130612	**1**	0	10	35	34.9	11.4	26	65	9.8	8.5	10.8	11.3	NA	NA	NA	NA	NA	NA
130612	**2**	0	10	35	34.5	16.4	22	70	15.5	14.8	15.8	16	16.2	NA	NA	NA	NA	NA
130613	**1**	0	10	35	34.9	21.4	19	54	20	20.3	20.7	21.1	21.4	NA	NA	NA	NA	NA
130613	**2**	0	10	35	34.7	26.6	17.5	37	25.7	26	26.1	26.2	26.3	26.5	26.5	26.6	NA	NA
130620	**1**	0	10	45	35	12	39	65	11.8	8.5	10.8	11.8	11.9	NA	NA	NA	NA	NA
130624	**1**	0	10	45	35.2	16.5	34	62	16.4	14.9	15.2	16	16.4	NA	NA	NA	NA	NA
130625	**1**	0	10	45	35	22	29	70	24.5	21	21.1	21.6	21.8	21.9	NA	NA	NA	NA
130625	**2**	0	10	45	34.9	27.5	28	30	28	26.5	26.7	26.7	26.8	27	27.2	27.3	27.4	NA
130626	**1**	0	10	55	35.5	11.7	42	65	11.2	7.5	10.8	11.5	11.6	NA	NA	NA	NA	NA
130626	**2**	0	10	55	35.4	16.9	37	67	17.4	15.4	16	16.7	16.8	16.9	NA	NA	NA	NA
130627	**1**	0	10	55	35.6	21.9	38	55	23.5	20.9	20.9	21.3	21.7	21.9	NA	NA	NA	NA
130627	**2**	0	10	55	35.8	27	34	36	35	25.7	25.8	25.8	26	26.5	26.7	26.8	NA	NA
130628	**1**	0	30	6	40.2	23.6	18	58	18.8	19	20.8	21.8	22.3	23	NA	NA	NA	NA
130628	**2**	0	30	6	40.6	33.4	13	27	31.1	31.5	31.6	31.8	32.1	32.5	32.7	32.9	33	33.2
130702	**1**	0	30	35	42.3	23.8	27	53	27.4	18.2	19.8	21.5	22.2	23.1	23.5	23.5	NA	NA
130704	**1**	0	30	35	42.2	31.7	28	25	30.5	29	29.8	30	30.3	30.7	31.1	31.3	31.5	NA
130704	**2**	0	30	45	42.6	24.6	38	44	32.9	19	19.5	20.8	22.3	22.8	23.4	23.5	NA	NA
130705	**1**	0	30	45	42.3	31.5	38	20	33.8	27	29	30	30.5	30.7	31	31.3	31.5	NA
130710	**1**	0	30	55	42.5	24.6	41	50	31.8	22	19.5	19.9	21.3	22.7	23.5	24.3	NA	NA
130715	**1**	0	30	55	42.6	31.4	42	20	33.8	28	28.6	29	29.5	29.9	30.2	30.6	31	NA

									WATER LEVELS									
Date	**Test #**	**Z_{floor} (m)**	**Q (l/s)**	**C_L (cm)**	**Yo (cm)**	**Yt (cm)**	**Iv (cm)**	**θ (°)**	**Xi=0.2 (m)**	**Xi=0.4 (m)**	**Xi=0.6 (m)**	**Xi=0.8 (m)**	**Xi=1.0 (m)**	**Xi=1.2 (m)**	**Xi=1.4 (m)**	**Xi=1.6 (m)**	**Xi=1.8 (m)**	**Xi=2.0 (m)**
130715	**2**	0	50	6	44.8	30	22	45	24.5	23	25	26.5	27.5	28.2	28.6	NA	NA	NA
130716	**1**	0	50	6	46.9	38.5	20	20	35	35.5	36	36.3	36.8	37.6	37.8	38	38.1	38.2
130716	**2**	0	50	35	48	30	35	38	32.4	21.3	22	24.3	26	26.7	27.5	28.4	NA	NA
130717	**1**	0	50	35	47.8	36.5	30	20	34.6	32	33	33.5	33.8	34.4	35	35.7	36	NA
130718	**1**	0	50	45	48	29.1	46	39	35.7	24.2	20.3	22.5	25	25.6	26.7	27.8	NA	NA
130719	**1**	0	50	45	48.2	34.5	43	20	36.5	28.8	29.8	30.7	31.2	31.8	32.2	32.5	33	33.4
130722	**1**	0	50	55	48.2	29.5	48	40	36.2	27.3	20.7	21.8	24	26.3	26.9	27.4	28.2	NA
130722	**2**	0	50	55	48.1	36.1	49	18	37	32.1	31.5	32.6	33.2	33.4	33.8	34.5	35.1	35.7
130802	**1**	0.105	10	55	35.7	23.7	36	55	24	20	22	23.2	23.5	NA	NA	NA	NA	NA
130802	**2**	0.105	10	6	34.5	24.1	11	68	21.8	22.8	23.5	24	NA	NA	NA	NA	NA	NA
130806	**1**	0.105	30	6	40.1	30.8	16	40	24.7	26.3	28.3	29.7	NA	NA	NA	NA	NA	NA
130806	**2**	0.105	30	55	42.7	31.3	42	35	33.5	26	26	28.8	30	30.7	NA	NA	NA	NA
130806	**3**	0.105	50	55	48.5	37.2	46	20	36.9	32	30.5	32.5	34	35.6	36.5	NA	NA	NA
130807	**1**	0.105	50	6	46	37.6	21	36	31.5	31.8	33.7	34.7	35.6	NA	NA	NA	NA	NA
130815	**1**	0.155	10	55	35.5	27.7	41	40	30.5	23.8	26.7	27	NA	NA	NA	NA	NA	NA
130815	**2**	0.155	10	6	34.4	27.9	9	43	25.3	25.8	27.5	NA	NA	NA	NA	NA	NA	NA
130815	**3**	0.155	30	6	40.8	35.4	14	30	30.8	32.7	34	NA	NA	NA	NA	NA	NA	NA
130815	**4**	0.155	30	55	42.8	34.6	43	25	34.3	29	30	32.8	33.5	NA	NA	NA	NA	NA
130816	**1**	0.155	50	55	49	39.8	50	20	37.6	32.8	31.8	35.2	37.7	NA	NA	NA	NA	NA
130816	**2**	0.155	50	6	47	41.4	21	24	35.5	36.8	38.7	NA	NA	NA	NA	NA	NA	NA
130823	**1**	0.055	10	55	35.6	20.7	35	65	22.7	18.8	19.3	20.4	20.7	NA	NA	NA	NA	NA
130823	**2**	0.055	10	6	34.6	21	11	67	19	19.2	20.3	20.8	NA	NA	NA	NA	NA	NA
130823	**3**	0.055	30	6	40.2	28.7	16	48	24.2	24.5	26.8	27.7	28.2	28.5	NA	NA	NA	NA
130826	**1**	0.055	30	55	43	27.6	43	40	33.6	23	21.3	23.7	25	26.3	27.2	NA	NA	NA
130826	**2**	0.055	50	55	48.5	33.1	49	35	36.7	29.5	25	26.8	29	31.4	32.2	32.8	NA	NA
130827	**1**	0.055	50	6	45.2	33.3	22	35	27.2	25.8	28.5	30	30.7	31.6	NA	NA	NA	NA

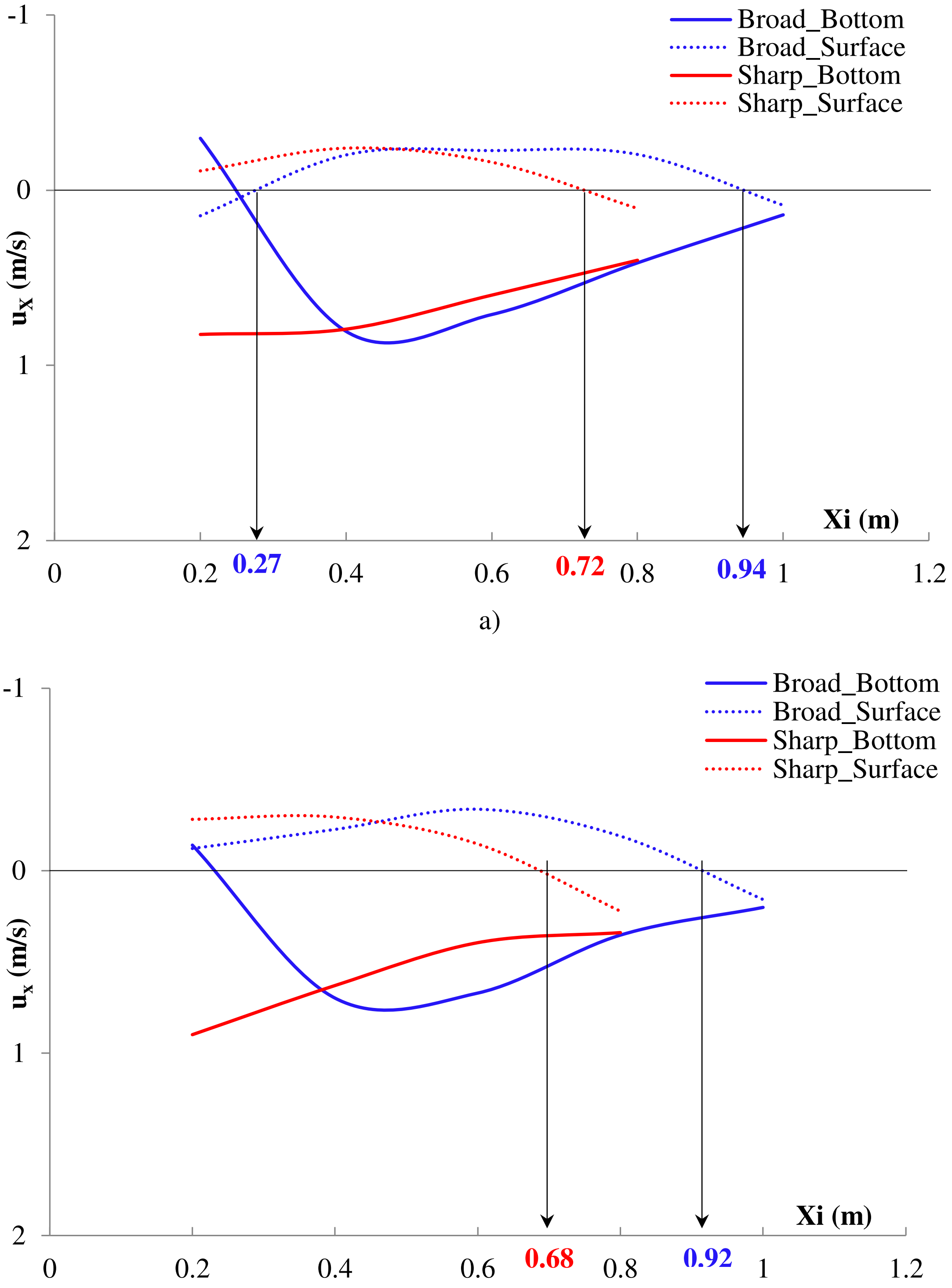

Figure B-1: Vortex start and end locations for Q = 10 l/s;

a) z_{floor}=0 cm; b) z_{floor}=+5.5 cm

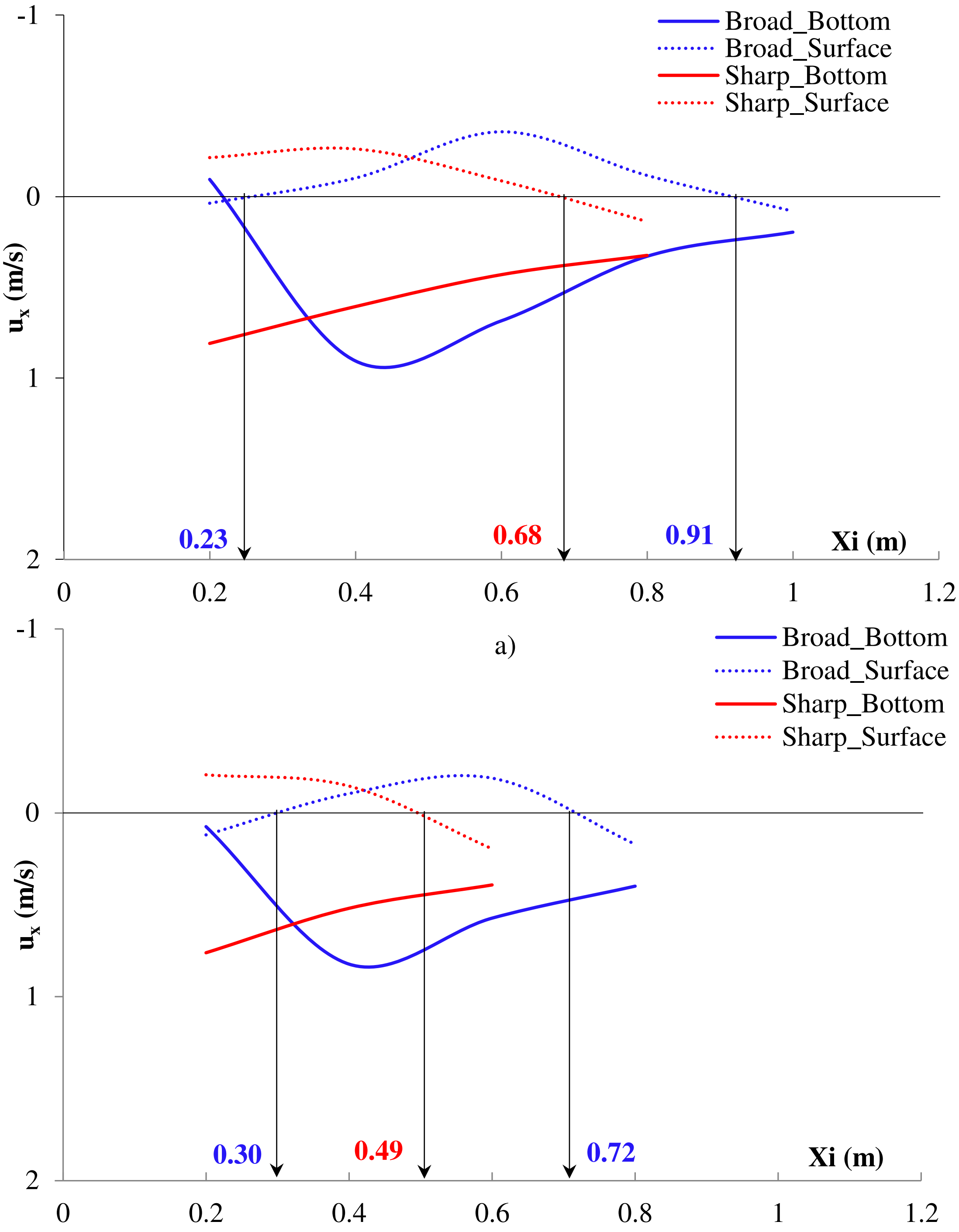

a)

b)

Figure B-2: Vortex start and end locations for Q = 20 l/s;

a) z_{floor}=+10.5 cm; b) z_{floor}=+15.5 cm

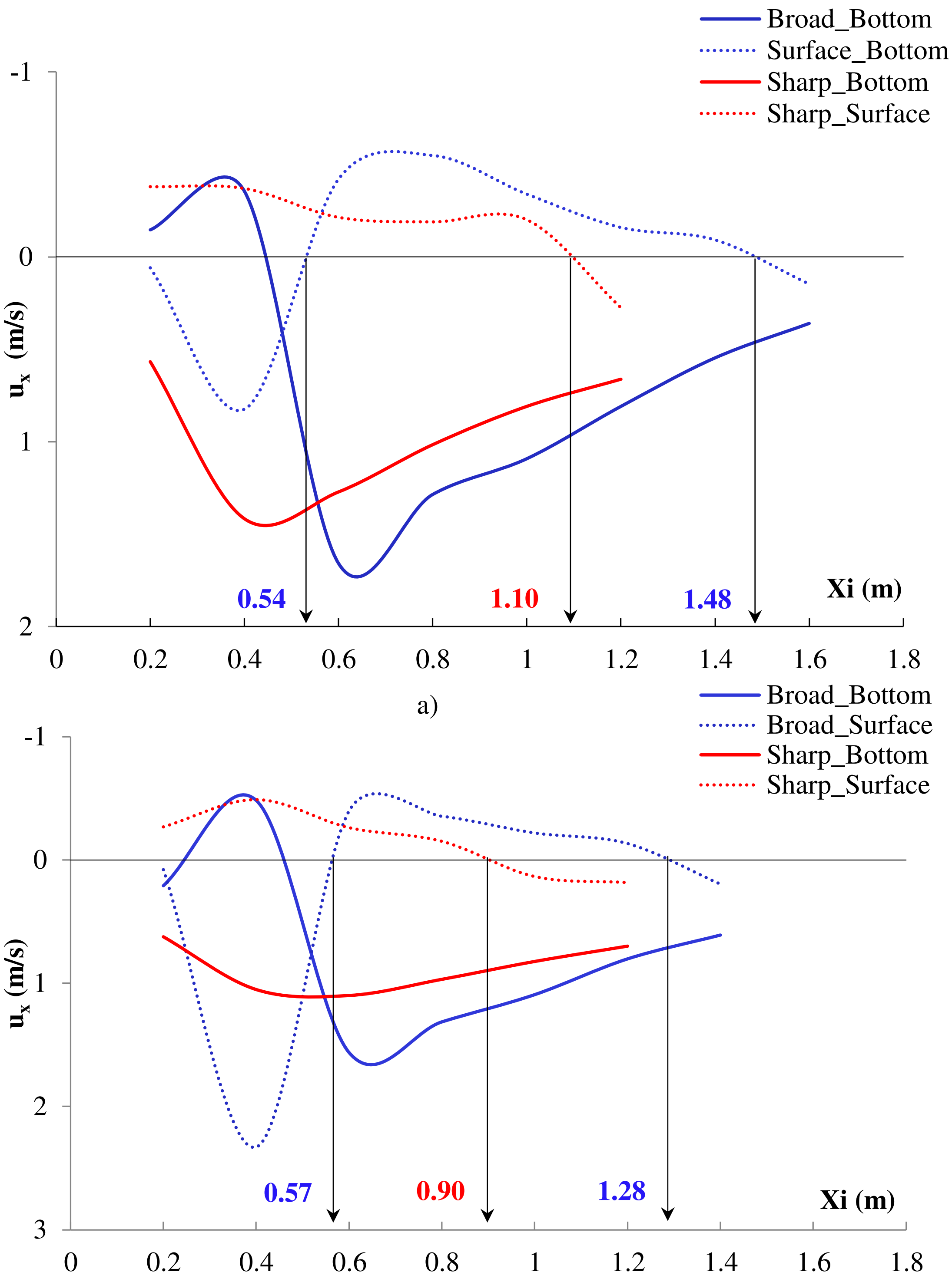

a)

b)

Figure B- 3: Vortex start and end locations for Q = 30 l/s;

a) z_{floor}=0 cm; b) z_{floor}=+5.5 cm

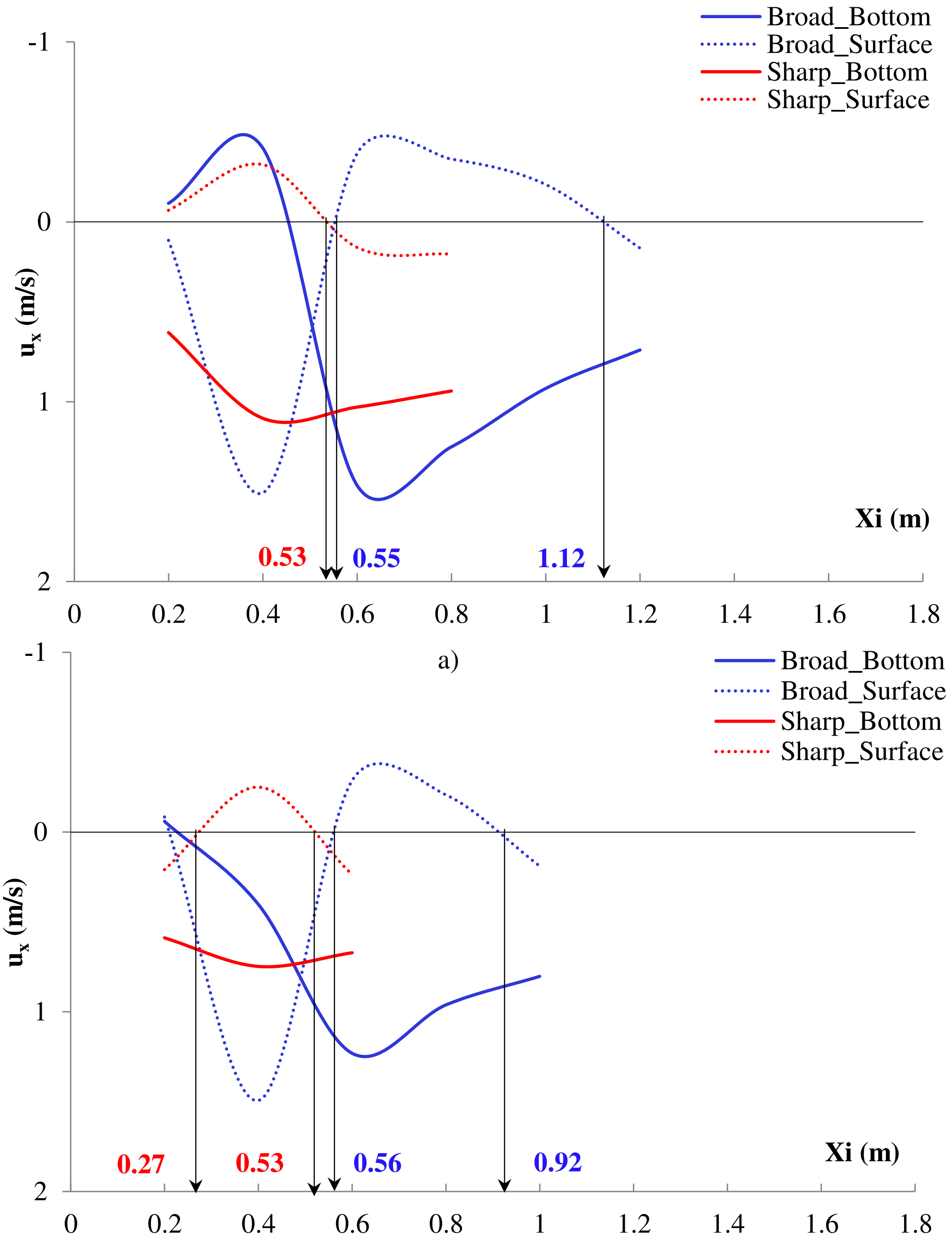

a)

b)

Figure B-4: Vortex start and end locations for Q = 30 l/s;

a) z_{floor}=+10.5 cm; b) z_{floor}=+15.5 cm

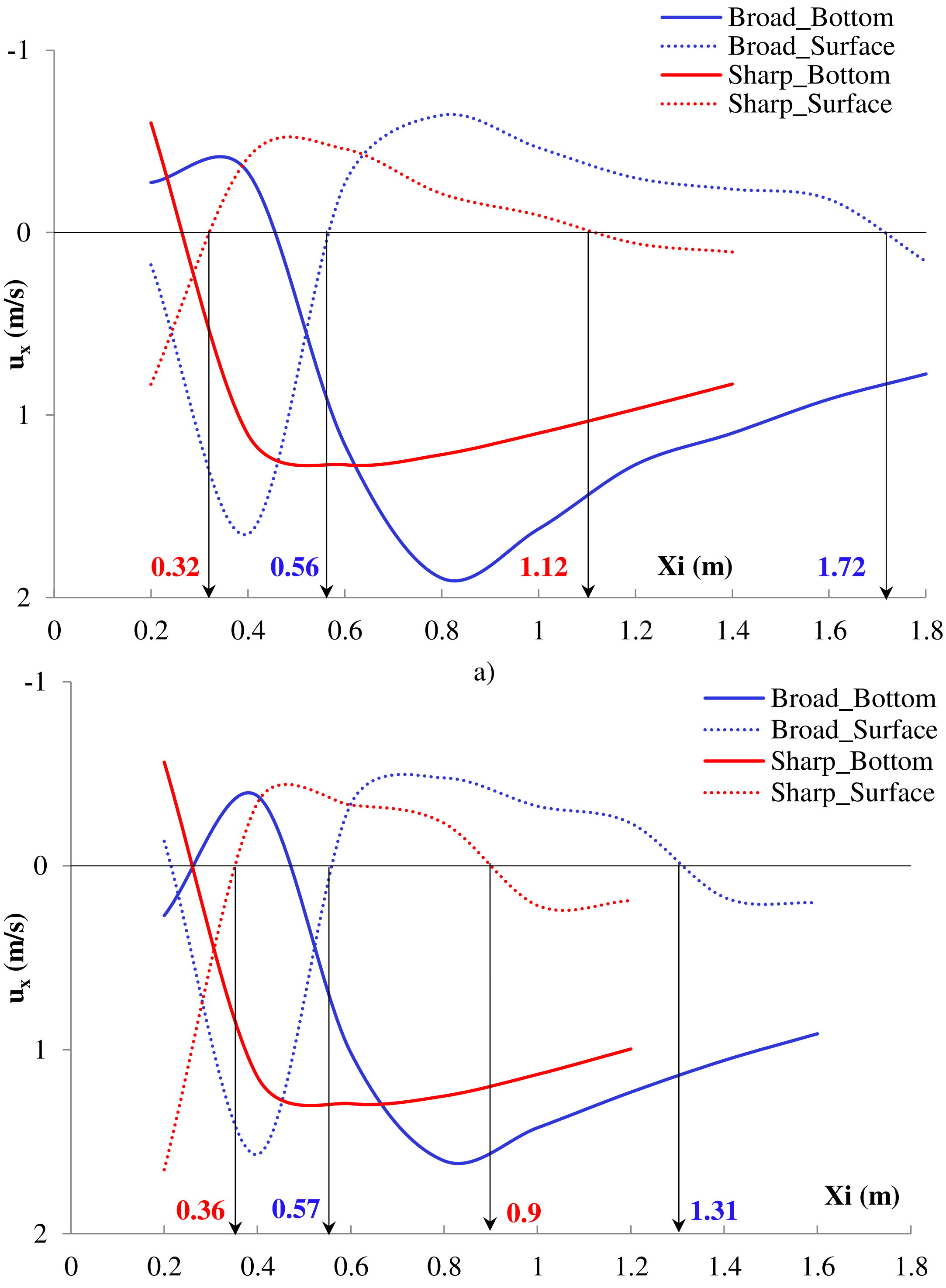

a)

b)

Figure B-5: Vortex start and end locations for Q = 50 l/s;

a) z_{floor}=0 cm; b) z_{floor}=+5.5 cm

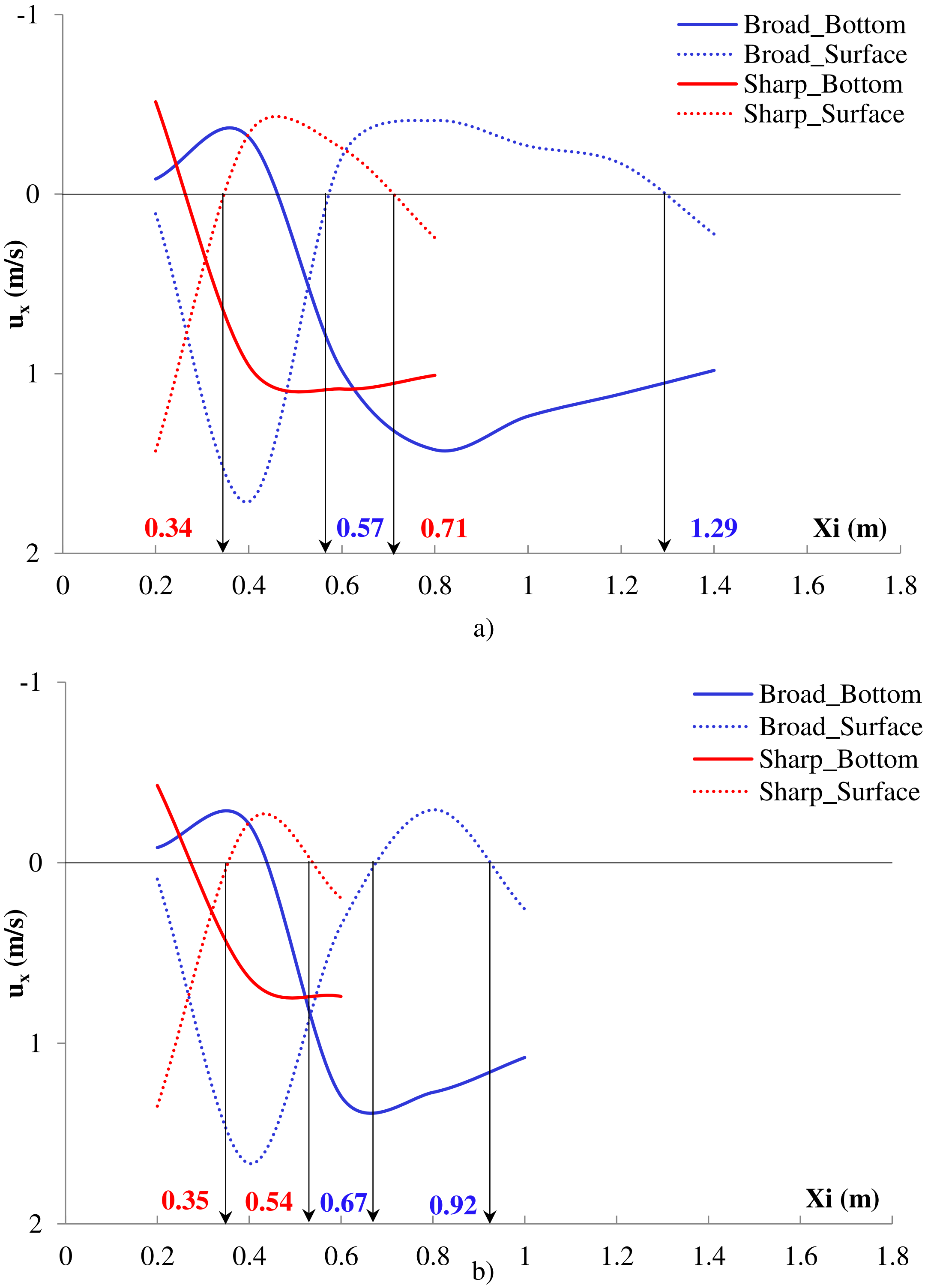

a)

b)

Figure B- 6: Vortex start and end locations for Q = 50 l/s;

a) z_{floor}=+10.5 cm; b) z_{floor}=+15.5 cm

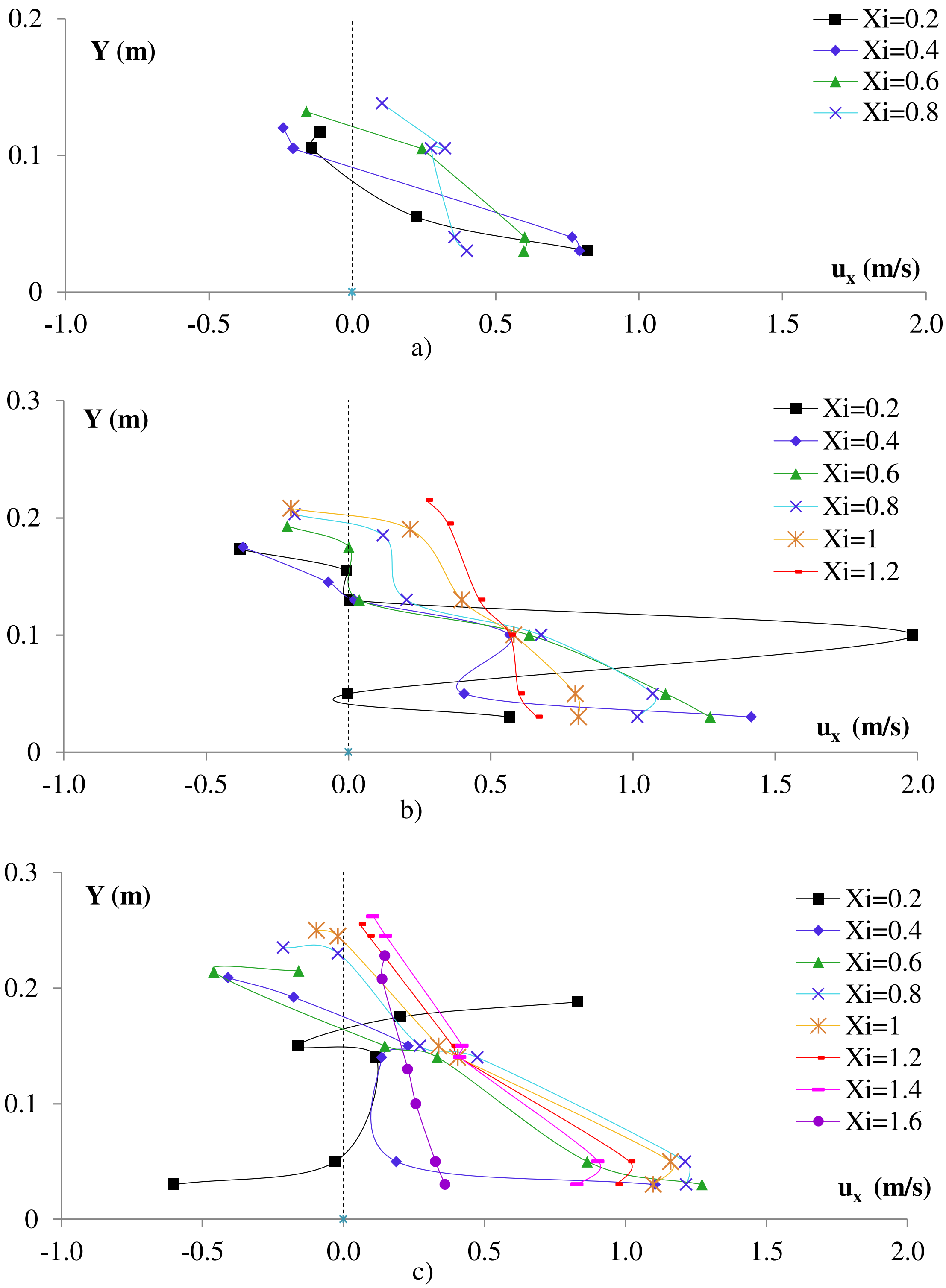

Figure B-7: Vertical evolution of the velocity profiles for sharp crest design (C_L=6 cm) and non-elevated floor (z_{floor}=0cm); a) Q=10 l/s; b) Q=30 l/s; c) Q=50 l/s.

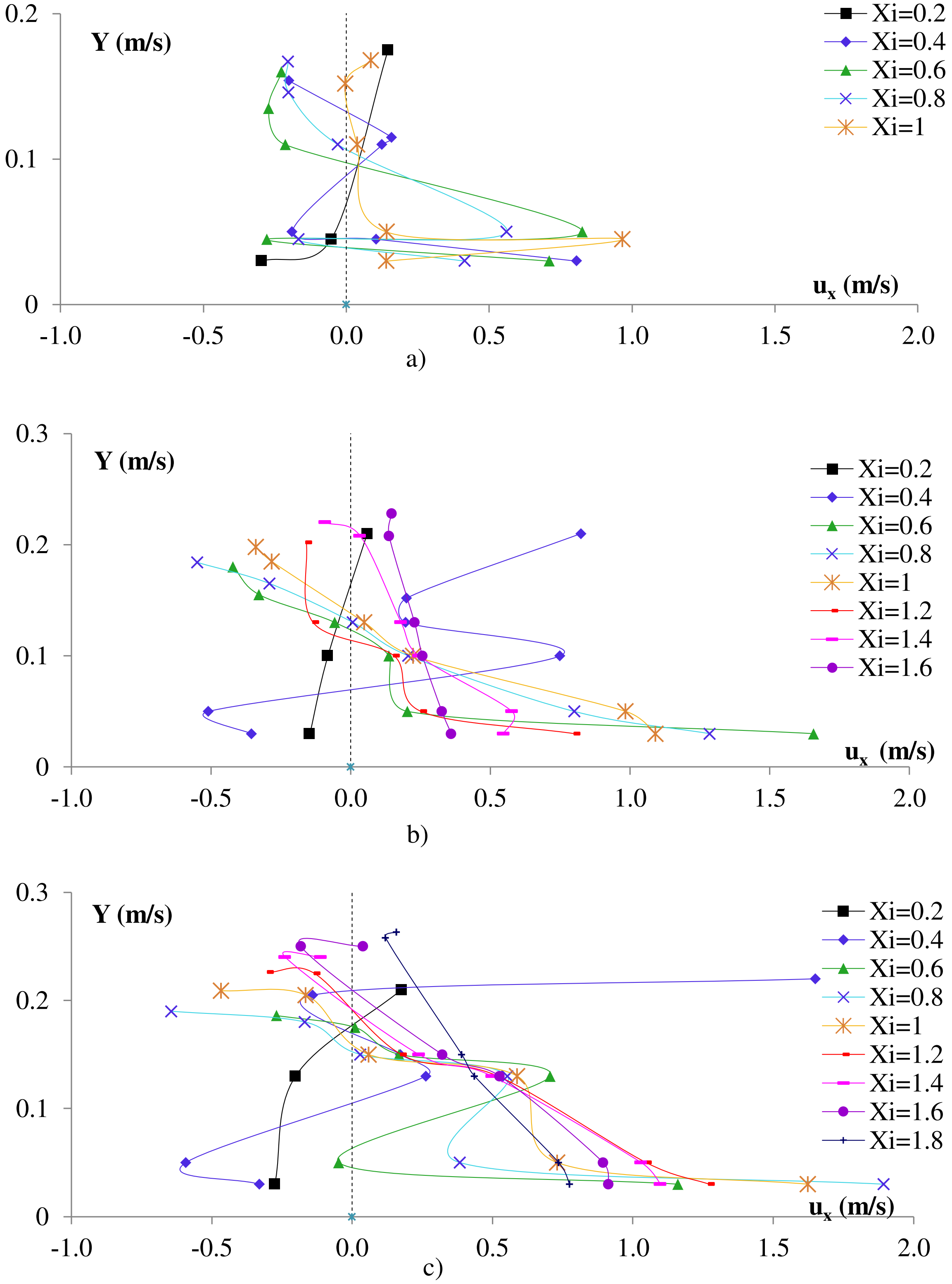

Figure B -8: Vertical evolution of the velocity profiles for broad crest design (C_L =55 cm) and non-elevated floor (z_{floor}=0cm); a) Q=10 l/s; b) Q=30 l/s; c) Q=50 l/s

Appendix C. Estimation of vortex extension

This appendix presents a comparison between the calculated and visual methods to predict the submerged vortex extension. The low flow rate condition, which was presented in section 6.5.3, represents the start point for this analysis.

For medium flow rates ($Q = 30\ \mathrm{l/s}$) it is observed, in agreement with low flow rates, that as the apron rises, the extension affected by the vortex reduces. This fact reveals that as the discharge over the weir increases, the benefits derived from installing an elevated apron increase. The results corresponding to this flow condition are summarized in Table C- and Figure C-, respectively.

For medium discharges, the observed vortex extension is overestimated. The shape of the curve provided by the visual and calculated methods show agreement, but the visual observations overpredict the extension of the roller by 25%. The roller extension was minimized by installing aprons elevated more than 20% the dam height, with an optimal value reached by floors elevated 40%. The benefits derived from installing an elevated floor were more remarkable for sharp-crested arrangements.

Table C-1: Experimental data concerning the vortex extension for Q=30 l/s

Condition			**Calculated**			**Observed**		
Z_{floor}	Crest	Z_{floor}/H_{weir}	I_v	E_v	L_v	I_v	E_v	L_v
0	B	0.0%	0.54	1.48	0.94	0.95	1.50	0.55
0	S	0.0%	<0.2	1.10	>0.9	1.12	1.44	0.32
5.5	B	19.9%	0.57	1.28	0.71	0.83	1.26	0.43
5.5	S	19.9%	<0.2	0.90	>0.7	1.0	1.16	0.16
10.5	B	37.9%	0.55	1.12	0.57	0.8	1.22	0.42
10.5	S	37.9%	<0.2	0.53	>0.33	0.5	0.66	0.16
15.5	B	56.0%	0.56	0.92	0.36	0.8	1.23	0.43
15.5	S	56.0%	0.27	0.53	0.26	0.5	0.64	0.14

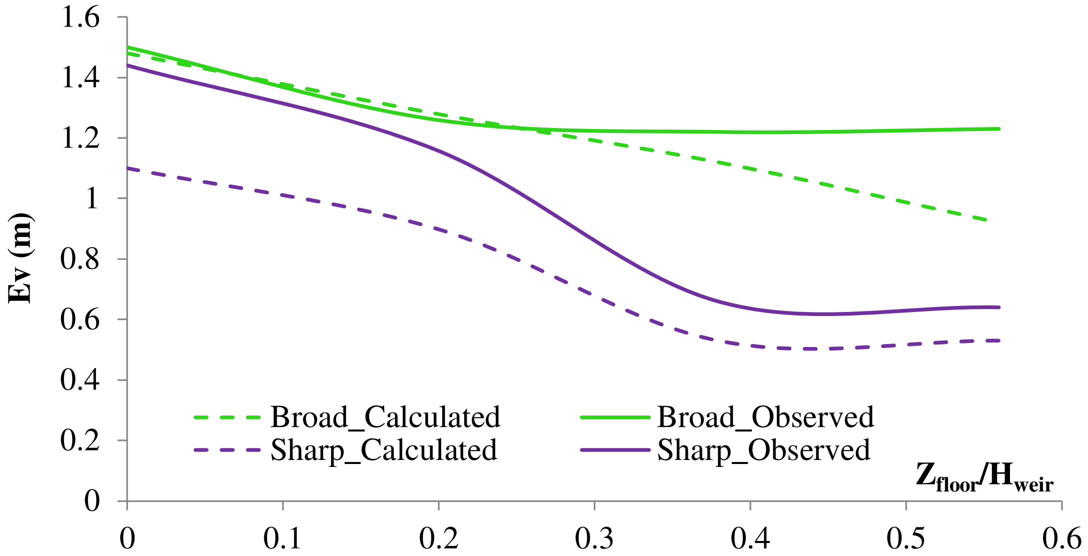

Figure C-1: Vortex extension vs. non-dimensional apron elevation for Q=30 l/s

For high flow rate condition ($Q = 50\,\mathrm{l/s}$), the results agree with those found for low and medium discharges. The calculated method underestimated vortex extension once more. The results associated to this condition are summarized in Table C-2 and Figure C-2.

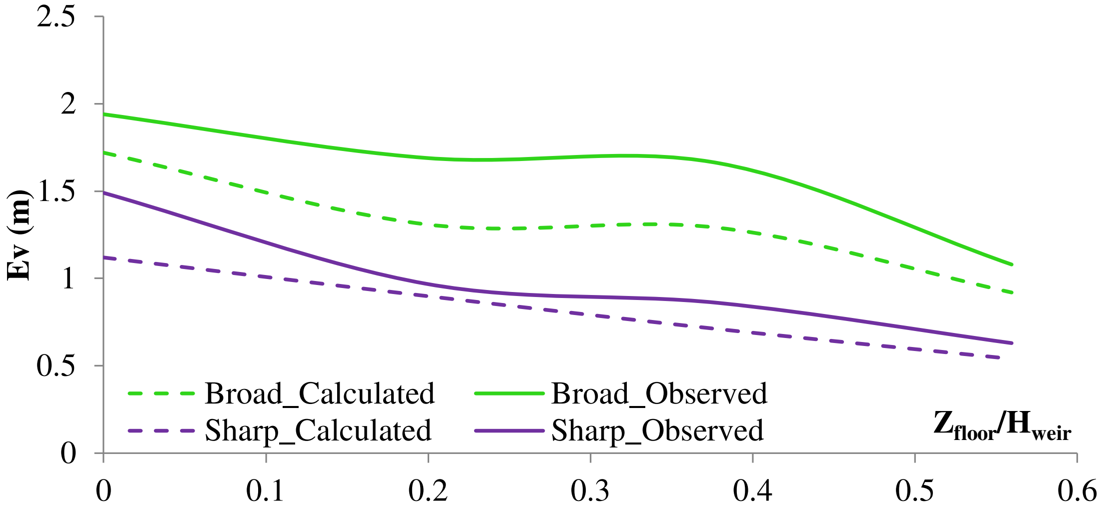

Figure C-2: Vortex extension vs. non-dimensional apron elevation for Q=50 l/s

Table C-2: Experimental data concerning the vortex extension for Q=50 l/s

Condition			**Calculated**			**Observed**		
Z_{floor}	Crest	Z_{floor}/H_{weir}	I_v	E_v	L_v	I_v	E_v	L_v
0	B	0.0%	0.56	1.72	1.16	0.67	1.94	1.27
0	S	0.0%	0.32	1.12	0.8	0.41	1.49	1.08
5.5	B	19.9%	0.57	1.31	0.74	0.49	1.69	1.20
5.5	S	19.9%	0.36	0.9	0.54	0.22	0.97	0.75
10.5	B	37.9%	0.57	1.29	0.72	0.46	1.66	1.2
10.5	S	37.9%	0.34	0.71	0.37	0.21	0.86	0.65
15.5	B	56.0%	0.67	0.92	0.25	0.5	1.08	0.58
15.5	S	56.0%	0.35	0.54	0.19	0.21	0.63	0.42

Appendix D. Air entrainment estimation

This appendix contains the code developed in MATLAB to predict the air entrainment. The air concentration has been calculated by using digital image processing, as recommended by (Vaideliene & Tervydis, 2013). The air entrainment was evaluated a posteriori in order to calculate the volume of air entrainment and the density of the water. The water and ambiance temperatures were controlled during the experiments and the averaged values are presented below with the associated density are presented below:

T_a=20C, $\rho = 1.2$ kg/m^3

T_w=15C, $\rho = 999.1$ kg/m^3

The code allows modify these variables in order to adequate to different scenarios. Once the program finish the calculations, a binary figure (include below) is obtain as a result of the subroutine. This figure shows the original image (transformed into a grey scale) and the binary figure, where black pixels represent air and white pixels represent water. Highly dependent on illumination (light absorbers installed, light settings and reflectance of the free surface.)

Several tests were performed in order to identify the right pixel threshold, which allowed a clear identification of the phases (air and water, respectively). It was found that a threshold of 0.7 performed good in most of the cases, and allowed a relative good comparison of scenarios.

```
%Modified code by Marta de los Dolores Lopez Egea,
University of Ottawa, 2013
%based on Philippe St-Germain, University of Ottawa, 2012
%The author makes no warranty or guarantee, expressed or
%implied, as to the accuracy and reliability of the results
%derived from the use of this code. Its free distribution
%does not constitute any such warranty or guarantee. No
%responsibility or liability is assumed by the author.


% perform thresholding by logical indexing
my_image = im2double(imread('test.png'));
my_image = my_image(:,:,1);
% perform thresholding by logical indexing.
Air_pixel=0.7
image_thresholded = my_image;
image_thresholded(my_image>Air_pixel) = 0;
image_thresholded(my_image<Air_pixel) = 256;
% display result
figure()
subplot(1,2,1)
imshow(my_image,[])
title('original image')
subplot(1,2,2)
imshow(image_thresholded,[])
```

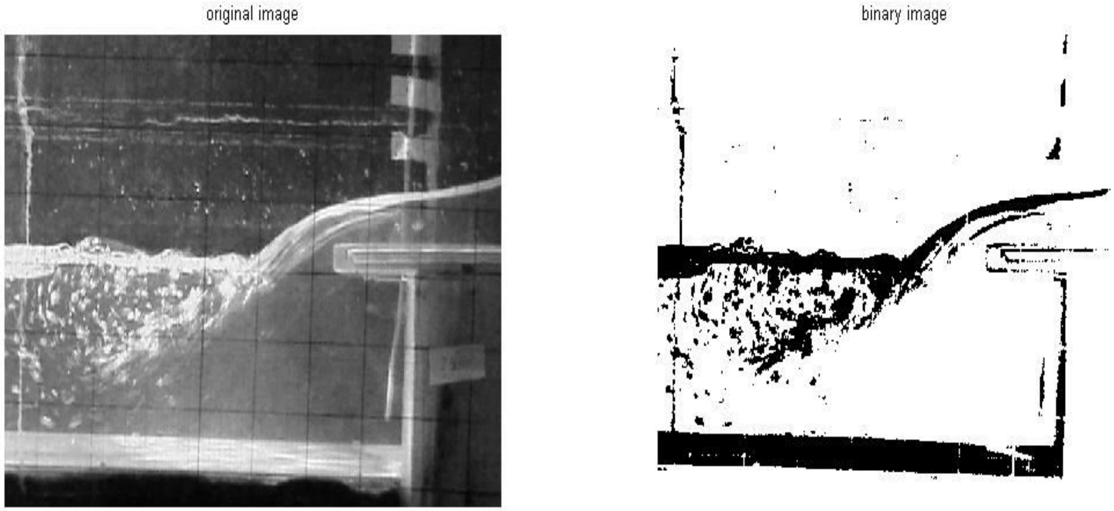

a)

b)

Figure D-1: a) Original image; b) Binary processed image

```
% Water density. Air temperature assumed 20 degrees and
Water temperature 15
% degrees Celsius

VAir=0;
VWater=0;
BW     = im2bw(my_image);
vAir = sum(BW(:));
vWater= numel(BW) - vAir;
cAir=((vAir/(vAir+vWater))*100);
display(cAir)
% Water density.
dAir=1.2041;
dWater=999.1026;
dMix=((dAir*vAir+dWater*vWater)/(vAir+vWater));
display(dMix)
```